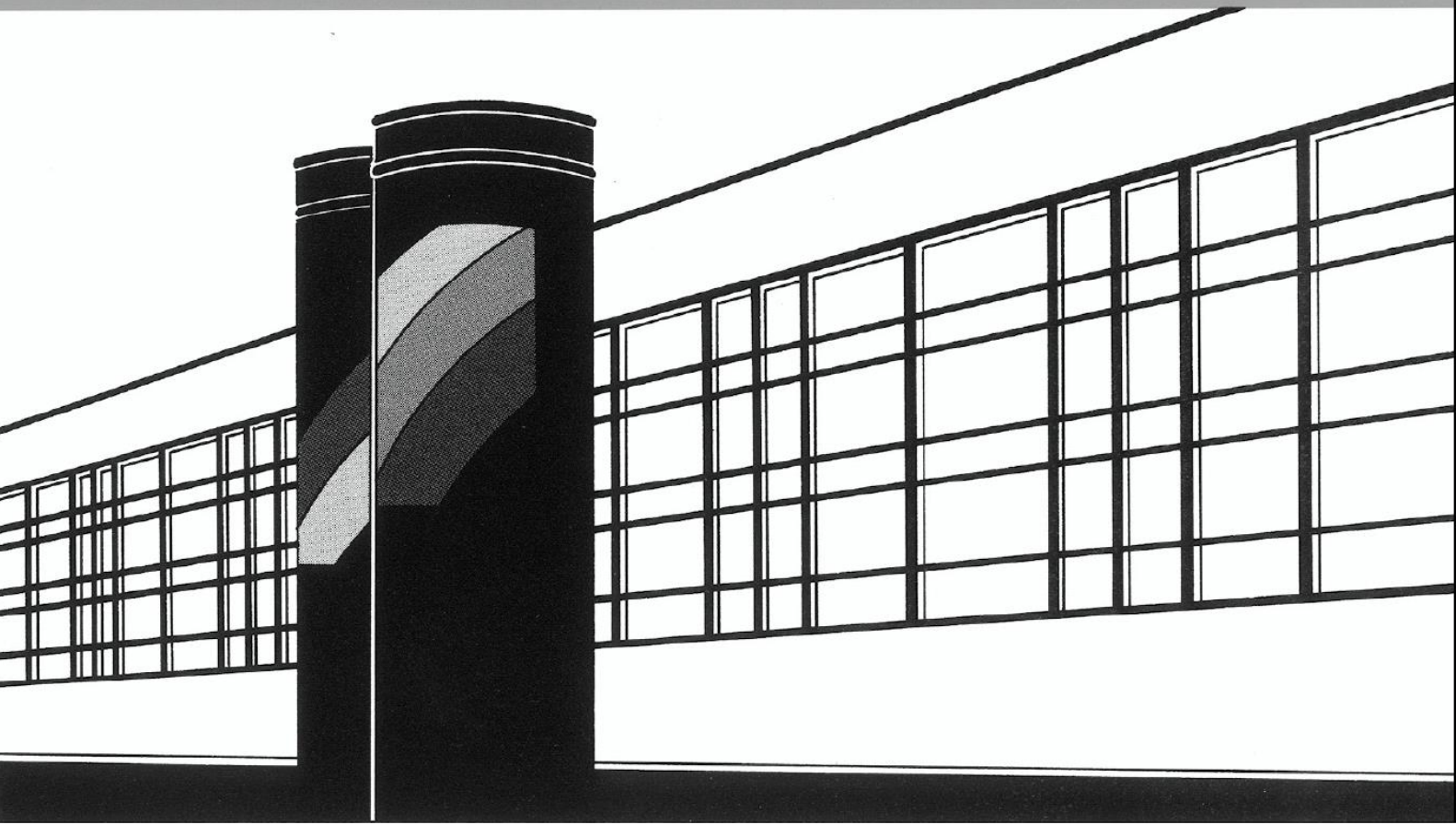


Universität Stuttgart



Institut für Wasser- und Umweltsystemmodellierung

Mitteilungen



Heft 251 Alexander Kissinger

Basin-Scale Site Screening and
Investigation of Possible Impacts of
CO₂ Storage on Subsurface Hydrosystems

Basin-Scale Site Screening and Investigation of Possible Impacts of CO₂ Storage on Subsurface Hydrosystems

von der Fakultät Bau- und Umweltingenieurwissenschaften der
Universität Stuttgart zur Erlangung der Würde eines
Doktor-Ingenieurs (Dr.-Ing.) genehmigte Abhandlung

vorgelegt von
Alexander Kissinger
aus Heilbronn

Hauptberichter: apl. Prof. Dr.-Ing. Holger Class

Mitberichter: Prof. Dr. Michael Kühn

Mitberichter: Prof. Dr.-Ing. Rainer Helmig

Tag der mündlichen Prüfung: 17.10.2016

Institut für Wasser- und Umweltsystemmodellierung
der Universität Stuttgart
2016

Heft 251 **Basin-Scale Site Screening
and Investigation of Possible
Impacts of CO₂ Storage on
Subsurface Hydrosystems**

von
Dr.-Ing.
Alexander Kissinger

D93 Basin-Scale Site Screening and Investigation of Possible Impacts of CO₂ Storage on Subsurface Hydrosystems

Bibliografische Information der Deutschen Nationalbibliothek

Die Deutsche Nationalbibliothek verzeichnet diese Publikation in der Deutschen Nationalbibliografie; detaillierte bibliografische Daten sind im Internet über <http://www.d-nb.de> abrufbar

Kissinger, Alexander:

Basin-Scale Site Screening and Investigation of Possible Impacts of CO₂ Storage on Subsurface Hydrosystems, Universität Stuttgart. - Stuttgart: Institut für Wasser- und Umweltsystemmodellierung, 2016

(Mitteilungen Institut für Wasser- und Umweltsystemmodellierung, Universität Stuttgart: H. 251)

Zugl.: Stuttgart, Univ., Diss., 2016
ISBN 978-3-942036-55-9

NE: Institut für Wasser- und Umweltsystemmodellierung <Stuttgart>: Mitteilungen

Gegen Vervielfältigung und Übersetzung bestehen keine Einwände, es wird lediglich um Quellenangabe gebeten.

Herausgegeben 2016 vom Eigenverlag des Instituts für Wasser- und Umweltsystemmodellierung

Druck: Document Center S. Kästl, Ostfildern

Danksagung

Zuerst möchte ich mich beim Bundesministerium für Bildung und Forschung (BMBF) und bei der Deutschen Forschungsgemeinschaft (DFG) bedanken, welche große Teile dieser Arbeit im Rahmen des Forschungsprojekts CO2BRIM finanziell gefördert haben.

Besonderer Dank gilt meinem Hauptberichter Holger Class für die große Unterstützung und das mir entgegengebrachte Vertrauen. Er hat mich auf dem ganzen Weg von der Studienarbeit, über die Diplomarbeit bis hin zu meiner Promotion betreut und mir stets viele Freiräume bei der Umsetzung meiner Arbeit gelassen. Sein fachlicher Input war dabei immer sehr wertvoll und von seiner gelassenen und ruhigen Art Probleme anzugehen, konnte ich viel lernen. Bei Rainer Helmig möchte ich mich, neben der Übernahme des Mitberichts, auch für viele lehr- und hilfreiche Diskussionen bedanken sowie für die einzigartige und sehr positive Stimmung am Lehrstuhl, die er maßgeblich zu verantworten hat. Michael Kühn möchte ich danken, dass er den Mitbericht übernommen hat und mich auch fachlich unterstützte.

Mein Dank gilt auch den CO2BRIM Kollegen Stefan Knopf, Wilfried Konrad, Vera Noack und Dirk Scheer. Die Arbeit mit ihnen hat mir sehr viel Spaß gemacht. Ich denke, wir verdienen wirklich das Prädikat interdisziplinär. Lena Mahl möchte ich zum einen danken, dass sie mich während der Studien- und Diplomarbeit betreut hat und viel dazu beigetragen hat, dass ich mich für die Promotion hier entschieden habe. Zum anderen auch für die tolle Zeit im CO₂ Büro. Bei Bernd Flemisch möchte ich mich vor allem dafür bedanken, wie er die DuMu^x Entwicklung vorantreibt und leitet. Es hat viel Spaß gemacht Teil des Entwicklerteams zu sein. Christoph Grüninger, Vishal Jambhekar und Emna Mejri möchte ich für die produktive Kelleratmosphäre danken. Pru Lawday und Maria Costa gebührt viel Dank für die Hilfe, die sie mir bei der Bewältigung von verwaltungstechnischen Angelegenheiten geleistet haben. Ned Coltman danke ich für seine sprachlichen Korrekturen an der Arbeit und Simon Scholz und Marcel Wirth für ihre wertvollen Beiträge, welche aus ihren Bachelor-Arbeiten hervorgingen. Allen Kollegen aus der Arbeitsgruppe möchte ich für die tolle Atmosphäre hier am Lehrstuhl danken. Ich werde immer gerne auf Veranstaltungen wie den Georgenhof (-burg), Lehrstuhlexkursionen, Weinproben, Karaokeabende, etc. zurückblicken.

Weiterhin möchte ich der sog. Spalter-Gruppe danken, bestehend aus meinen Freunden Lydia Seitz, Tobias Mosthaf, Julian Mehne, Michael Sinsbeck und Johannes Hommel. Wenn ich bei der Arbeit grübelte, halfen unsere gemeinsamen Mensagänge mich wieder auf andere Gedanken zu bringen. Meinen Eltern und meinem Bruder Thomas möchte ich für alles, was sie über die Jahre für mich getan haben, danken. Insbesondere meinem Bruder, der mich am Anfang des Studiums immer darin bestärkte diesen Weg zu gehen. Last and most möchte ich mich bei meiner Lebensgefährtin Melanie bedanken. Deine Unterstützung und Dein Rückhalt während der letzten Jahre und vor allem in der Schlussphase der Promotion waren unheimlich wichtig.

Contents

List of Figures	V
List of Tables	XI
Notation	XIII
Abstract	XIX
Zusammenfassung	XXIII
1. Introduction	1
1.1. Motivation and Aims	1
1.2. Literature Review	5
1.2.1. Site-Screening Methods for CO ₂ Storage on the Basin Scale	5
1.2.2. Assessment of Large-Scale Brine Displacement due to CO ₂ Storage	7
1.3. Structure of this Thesis	9
2. Fundamentals of Porous-Media Flow	11
2.1. Spatial Scales and the Continuum Approach	11
2.2. Local Thermodynamic Equilibrium	13
2.3. Properties of the Porous Medium	13
2.3.1. Porosity and Compressibility of the Porous Medium	13
2.3.2. Permeability	14
2.4. Brine and CO ₂	15
2.4.1. Components and Phases	15
2.4.2. Mole and Mass Fractions	16
2.4.3. Density	16
2.4.4. Dynamic Viscosity	17
2.5. Multi-Phase Flow	19
2.5.1. Saturation	19
2.5.2. Capillary Pressure	19
2.5.3. Relative Permeability	21

2.6. Transport Processes	23
2.6.1. Advection	23
2.6.2. Diffusion	24
2.6.3. Mechanical Dispersion	24
2.7. Variable-Density Flow	25
3. Model Concepts	27
3.1. Balance Equations	27
3.1.1. Momentum Balance Equation	27
3.1.2. Mass Balance Equations	28
3.2. Analytical Methods	35
3.2.1. Analytical Solution for Estimating the Volumetric CO ₂ Storage Efficiency	36
3.2.2. Single-Phase Injection in a Multi-Layer System with a Fault Zone . .	37
3.3. Numerical Implementation	42
3.3.1. Numerical Simulator DuMu ^x	42
3.3.2. Spatial Discretization: The Box-Method	43
3.3.3. Temporal Discretization: The Implicit Euler Scheme	46
3.3.4. The Newton-Raphson Method	46
3.3.5. Fault-Zone Representation Using a Discrete-Fracture Approach	47
3.3.6. Infinite-Aquifer Boundary Conditions	52
4. Basin-Scale Screening for CO₂ Storage Efficiency	55
4.1. The Gravitational Number as a Qualitative Indicator for Storage Efficiency .	56
4.2. Available Data	59
4.3. Numerical Model Setup	62
4.4. Results	63
4.4.1. Basin-Scale Application of the Gravitational Number	64
4.4.2. Comparison of the Gr-Criterion and the Okwen-Method with Respect to Storage Efficiency	64
4.4.3. Testing the Significance of the Gr-Criterion with Respect to Residual Trapping	69
4.4.4. Testing the Significance of the Gr-Criterion with Respect to Porosity and Reservoir Thickness	70
4.5. Discussion	73
4.6. Conclusion	74
5. Large-Scale Investigation of Brine Displacement	77
5.1. Uncertainty Categorization and Brine Displacement	78
5.2. Available Data	79

5.3. Numerical Model Setup	82
5.3.1. Boundary and Initial Conditions for the Numerical Models	83
5.3.2. Fault Zone Representation Using a Discrete-Fracture Model	85
5.4. Numerical Model Reliability	85
5.4.1. Large-Scale Pressure Propagation During Injection	85
5.4.2. Upconing with Variable Brine Density: The Saltpool Experiment	88
5.5. Results	92
5.5.1. Definition of Target Variables	92
5.5.2. Scenario Uncertainty	94
5.5.3. Model Uncertainty (Recognized ignorance)	104
5.6. Discussion	112
5.7. Conclusion	116
6. Summary and Outlook	119
6.1. Summary	119
6.2. Outlook	124
Bibliography	129
A. Further Information for Simulations in Chapter 4	139

List of Figures

2.1.	A porous medium in the micro (left), and macro-scale perspective (right) (Nuske, 2014).	11
2.2.	The fluctuation of a physical property over the considered volume. The consideration as an REV is possible if fluctuations are sufficiently small. Figure from Helmig (1997), modified by (Nuske, 2014).	12
2.3.	The density of brine over temperature for different salinities (left) at a pressure of 100 bar. The density of CO ₂ over pressure for different temperatures (right).	17
2.4.	The viscosity of brine over temperature for different salinities (left) at a pressure of 100 bar. The viscosity of CO ₂ over pressure for different temperatures (right).	18
2.5.	Capillary pressure-saturation relationship for $p_e = 0.1$ bar, $\lambda_{BC} = 2.0$, $S_{rw} = 0.3$, and $S_{rn} = 0.0$. Note that the curve is regularized with a linear function at $S_w = 0.31$ to avoid unrealistically high capillary pressures.	20
2.6.	Relative permeability-saturation relationship for $\lambda_{BC} = 2.0$, $S_{rw} = 0.3$, and $S_{rn} = 0.0$	23
3.1.	Injection of CO ₂ in a confined aquifer. The vertical pressure distribution is assumed hydrostatic for the sharp interface model.	32
3.2.	Multi-layer system with n aquifers coupled through a fault zone, modified after Scholz (2014). The bottommost layer is the injection horizon. Each layer is split into two regions coupled through the fault zone.	38
3.3.	Schematic overview of the solution procedure for the Zeidouni-Method, modified after Scholz (2014). For numerically inverting the Laplace transform the Stehfest algorithm is used (Stehfest, 1970).	41
3.4.	Box constructed on a finite-element grid (left). Basis and weighting function for a node i (right). For 2D quadrilaterals the basis function is bilinear, and for 3D cubes it is trilinear. Figure modified after Darcis (2012).	43

3.5.	Grid with variable vertical discretization length and a fault zone shown in red. Note that the width of the fault zone (w_{ij}) may be greater than the vertical discretization length. The bottom shows a zoom on a fracture element face, containing the nodes i and j from the above grid, in x and y direction. The fault-zone width w_{ij} is an input parameter of the fracture model. d_{ij} is the distance between nodes i and j , and h_{ij} is the distance between the midpoint of the line connecting nodes i and j and the center of the element face. Both d_{ij} and h_{ij} are calculated from the geometry of the element face.	48
3.6.	An inner domain within the red frame is surrounded by an outer domain with radius R_o	53
4.1.	Unpublished depth grid for the base of the Upper Buntsandstein (equivalent to the top of the Middle Buntsandstein) with depths recorded in meters below mean sea level (bmsl). Figure from Kissinger et al. (2014).	59
4.2.	The interpolated distribution of the geothermal gradient for the area of interest (based on (LIAG, 2012)). Figure from Kissinger et al. (2014).	60
4.3.	The CO ₂ density as a function of pressure and temperature (top left), the CO ₂ viscosity as a function of pressure and temperature (top right), the brine density as a function of salinity and temperature (bottom left) and the brine viscosity as a function of salinity and temperature (bottom right). The red points are the data points from the database. They are not plotted with the brine density (bottom left) as they are a function of pressure, salinity and temperature and would therefore not fit on the brine density surface shown here. Figure modified after Kissinger et al. (2014).	62
4.4.	Schematic setup of the model domain for the numerical simulations. Due to symmetry reasons only a small part of the radially symmetric problem is simulated. Figure from Kissinger et al. (2014).	63
4.5.	Distribution of Gr for the Middle Buntsandstein rock unit in the North German Basin. The numbers refer to the areas selected in Sec. 4.4.4 (Area 1 = low Gr, Area 2 = medium Gr, Area 3 = high Gr). Figure from Kissinger et al. (2014).	65
4.6.	Left: Simulation results in terms of storage efficiency (SE) for 49 data points over Gr. Right: The same simulation results plotted over storage efficiency obtained from the Okwen-Method using Eq. 3.37 and 4.7. Figure modified after Kissinger et al. (2014).	67
4.7.	Left: Simulation results for two injection rates (0.1 and 1.0 Mt per year) plotted over Gr. Note the logarithmic scaling of Gr. Right: The same simulation results plotted over storage efficiency (SE) obtained from the Okwen-Method using Eq. 3.37 and 4.7. Figure modified after Kissinger et al. (2014).	68

4.8.	Comparison of storage efficiency (SE) and the residually trapped CO ₂ mass (also given in terms of storage efficiency, i.e. kg/m ²). Figure modified after Kissinger et al. (2014).	70
4.9.	Left: Storage efficiency over Gr. The cross marker represents the mean storage efficiency and the bars indicate the standard deviation. Right: Mean storage efficiency for the three areas with constant Gr for all areas (black curve) and area-specific Gr (red curve). Note: the three means for the area-specific case (red cross marker) on the right plot are identical to the three means on the left plot (red cross marker). Figure modified after Kissinger et al. (2014).	72
5.1.	Levels of uncertainty after Walker et al. (2003), modified by Walter et al. (2012).	78
5.2.	Top of the Solling injection horizon discontinuous where the salt wall penetrates the layer. The top of the Zechstein salt is displayed with a blue mesh. The injection point at the flank of the anticlinal structure in about 1651 m depth is projected on top of the Solling injection horizon. Vertical exaggeration is 2:1. Figure from Kissinger et al. (2017).	79
5.3.	Top of the Rupelian clay barrier with discontinuities where Cretaceous sediments penetrate the Rupelian clay barrier. The top of the Cretaceous is displayed as blue mesh. Vertical exaggeration is 2:1. Figure from Kissinger et al. (2017).	80
5.4.	Top view on the groundwater table. The rivers are highlighted in blue. The elevation values are normalized to the minimum elevation of the groundwater table. Figure from Kissinger et al. (2017).	81
5.5.	Perspective view on the 3D geological model with zoom in on the anticlinal structure showing the mesh of the 3D volume model. Vertical exaggeration 2:1. Here Quaternary 1 and 2 are combined in the Quaternary layer. Figure from Kissinger et al. (2017).	81
5.6.	Boundary and initial conditions of the domain. Also shown is the position of the fault zone situated on the flank of the salt wall in red.	83
5.7.	a) Cross-section of the domain showing the lateral and top boundary conditions as well as the injection well and the fault zone (modified after Scholz (2014)). b) Top view on the upper aquifer showing the inner domain (30 km × 25 km) in blue and the domain extension with an outer radius of 100 km in red. Due to the symmetry of the line connecting the injection and the fault zone only half of the domain is simulated.	86
5.8.	Comparison of domain radii for 50, 100 and 150 km. Left: Neumann case with the upper aquifer closed on top. Right: Dirichlet case where the top aquifer has a constant pressure (very large diffusivity).	87

5.9.	Comparison of different horizontal discretization lengths for 150, 300 and 450 m. Left: Neumann case with the upper aquifer closed on top. Right: Dirichlet case where the top aquifer has a constant pressure (very large diffusivity).	88
5.10.	Setup of the saltpool benchmark.	89
5.11.	a) and b) : diagonal vertical cross-sections between inlet and outlet showing the salinity after 9000 s. Also shown are the 10 % and 50 % isolines for the low (0.01) and high (0.1) salinity case. c) and d) : salinity at outlet over time for the low (0.01) and high (0.1) salinity case, with 50^3 , 100^3 and 125^3 elements.	91
5.12.	a) Top view on the Rupelian clay barrier. Also shown are the two hydrogeological windows in the Rupelian clay barrier and the salt wall piercing through the barrier layer. The fault zone on the salt wall is highlighted in red. b) shows a cross-section (vertical exaggeration 4:1) along line A-B with approximate locations of the injection point (IP) and the two measurement points for pressure (M1 and M2).	93
5.13.	(a): Initial salt distribution for the reference scenario before the initialization run along the cross-section shown in Fig. 5.12 (vertical exaggeration 4:1). (b): Salt distribution for the reference scenario after an initialization run of 300 000 years. Six concentration isolines are shown which correspond to the entries in the legend (0.01, 0.1, 1, 10, 100 and 300). The permeability of the different layers is also shown. Please note the logarithmic scale of concentration and permeability.	96
5.14.	Top row: View on top of the Rupelian clay barrier for three different scenarios low, medium and high with increasing initial salt gradients. The results show the salt concentration increase after 50 years of injection. Concentration increases below 0.01 g/L are not shown. Bottom row: View on top of the Post-Rupelian for the three scenarios. Also see Fig. 5.12 for orientation. Note the different scales for the top and bottom row.	97
5.15.	Total salt flow into target aquifers (top left) over the injection and post-injection period split into salt flow over fault zone (top right), salt flow over hydrogeological windows (bottom left) and salt flow over the intact Rupelian clay barrier (bottom right).	98
5.16.	The cumulative salt flow for a period of 100 years (injection + post injection) into the Tertiary Post-Rupelian layer (a), Quaternary 2 layer (b) and Quaternary 1 layer (c) with and without injection. The scenario numbers along with short explanations of the varied parameters are given in (d).	99
5.17.	Left: Total mass flow into the target aquifers normalized by the injection rate. Right: Mass flow over fault zone into the target aquifers.	100

5.18.	Mass flow normalized by the brine injection rate into the target aquifers, for different permeabilites of the Upper Buntsandstein barrier. The upper right scenario with a permeability of $1 \times 10^{-18} \text{ m}^2$ corresponds to the reference scenario.	101
5.19.	Maximum mass flow reached after 50 years of injection normalized by the brine injection rate into the target aquifers over the fault zone permeability, for two different permeabilites of the Upper Buntsandstein barrier. Left: High barrier permeability, high diffuse migration over barrier; right: Low barrier permeability, high focused migration over fault zone.	102
5.20.	Left: Volumetric flow normalized by injection rate into target aquifers through the fault zone. Right: Salt flow into target aquifers through fault zone.	103
5.21.	Top: Volume flow over time into the target aquifers for the 1p1c and the 1p2c model. Bottom: Pressure increase due to injection at M1 and M2.	105
5.22.	Volume flow over time into the target aquifers for the 2p3c and the 1p2c model.	106
5.23.	Cross-section of the complex and generic geometry (vertical exaggeration 4:1) along the same cross-section, as shown in Fig. 5.12.	107
5.24.	Volume flow normalized by the injection rate over time into the target aquifers for the generic and the complex model.	108
5.25.	Model setup for the Zeidouni-Method with two permeable layers (injection horizon and intermediate aquifers) and the target aquifers with infinite diffusivity.	110
5.26.	Top row: Total volume flow into target aquifers (left) and volume flow over fault zone (right) for an Upper Buntsandstein barrier permeability of $1 \times 10^{-18} \text{ m}^2$. Bottom row: Total volume flow into target aquifers (left) and volume flow over fault zone (right) for an Upper Buntsandstein barrier permeability of $1 \times 10^{-20} \text{ m}^2$. Also shown in the right figure is the Zeidouni-Method for the case of a high injection horizon diffusivity.	111

List of Tables

3.1.	List of fully discretized equations. Note that in this work the 2p model is not used in combination with the fracture module, hence the equations for the 2p model only account for matrix flow. The matrix and fracture weighting factors (W_m and W_f) are only implemented for the component balance equations of salt in the 1p2c and 2p3c model.	49
3.1.	List of fully discretized equations. Note that in this work the 2p model is not used in combination with the fracture module, hence the equations for the 2p model only account for matrix flow. The matrix and fracture weighting factors (W_m and W_f) are only implemented for the component balance equations of salt in the 1p2c and 2p3c model.	50
3.1.	List of fully discretized equations. Note that in this work the 2p model is not used in combination with the fracture module, hence the equations for the 2p model only account for matrix flow. The matrix and fracture weighting factors (W_m and W_f) are only implemented for the component balance equations of salt in the 1p2c and 2p3c model.	51
4.1.	The initial fluid properties of seven different data points as well as Gr and the storage efficiency obtained from the simulations.	66
4.2.	The characteristics of the three different areas. Note that for Area 1 and 3 there are only ranges of a minimum and maximum value for porosity and thickness. For Area 2 the data points are listed in the the appendix in Table A.1. The values for pressure, temperature, salinity and Gr are the mean values for each area and are used as initial conditions for the simulations.	71
5.1.	Properties of the model layers according to Larue (2010); Reutter (2011); Schäfer et al. (2011); Noack et al. (2013).	82
5.2.	Input parameters for the analytical and the numerical model. * denotes parameters only relevant for the numerical simulation.	87
5.3.	Input parameters for the saltpool benchmark as given in Oswald and Kinzelbach (2004).	90

5.4.	List of parameters for the 1p2c model for the reference scenario. The two-phase flow specific parameters are additionally required for the 2p3c model.	94
5.5.	Averaged values for the permeability, porosity, viscosity and diffusivity of the injection horizon and the intermediate aquifer for the Zeidouni-Method. . . .	109
5.6.	Fluid volumes displaced into the target aquifers during 50 years of injection over different vertical pathways. The volumes are normalized by the injected volume. Two scenarios are considered: (i) High diffuse leakage through the Upper Buntsandstein barrier (UBS) ($k = 10^{-18} \text{ m}^2$) and (ii) low diffuse leakage through the UBS ($k = 10^{-20} \text{ m}^2$). The values in brackets for the 1p1c model are the displaced volumes obtained when deducting the base flow.	112
A.1.	9 data pairs of porosity and reservoir thickness for Area 2. Note: for the simulations an average is taken, where value ranges are given.	139
A.2.	Initial conditions and results of the simulations in Sec. 4.4.2.	140

Notation

The following table shows the significant symbols used in this work. Local notations are explained in the text.

Symbol	Definition	Dimension
Greek Letters:		
α	Solute expansion coefficient	-
α_l	Longitudinal dispersivity	m
α_t	Transversal dispersivity	m
β	Product of parameters that require upwinding	$\text{m}^2 \text{s}^{-1}$
Γ	Dimensionless gravitational number	-
Γ_G	Variable of integration for domain boundary	m^2
Γ_{V_i}	Variable of integration for boundary of finite volume or box	m^2
ϵ	Mass balance error	kg or mol s^{-1}
η	Dimensionless space	-
θ	Weighting coefficient ($0 \leq \theta \leq 1$) for temporal discretization scheme	-
λ	Mobility ratio $\lambda = \frac{\lambda_n}{\lambda_w}$	-
λ_α	Molility of phase α , $\lambda_\alpha = \frac{k_{r\alpha}}{\mu_\alpha}$	$\text{Pa}^{-1} \text{s}^{-1}$
λ_{BC}	Brooks and Corey shape parameter	-
λ_t	Total molility $\lambda_t = \lambda_n + \lambda_w$	$\text{Pa}^{-1} \text{s}^{-1}$
ρ	Mass density	kg m^{-3}
ρ_α	Mass density of phase α	kg m^{-3}
ρ_α^m	Molar density of phase α	mol m^{-3}
μ	Dynamic viscosity	Pa s
μ_α	Dynamic viscosity of phase α	Pa s

τ	Dimensionless time	-
ϕ	Effective Porosity	-
ϕ_{dp}	Drainable porosity	-
χ	Ratio of dimensionless time and space, $\chi = \frac{\eta}{\tau}$	-

Latin Letters:

a	Distance between fault zone and injection well	m
A_α	Cross-sectional area of phase α	m^2
A_{IP}	Area of sub-control volume face at integration point <i>IP</i>	m^2
C_s	Compressibility of the solid matrix	Pa^{-1}
C_t	Total compressibility of the fluid and the solid matrix	Pa^{-1}
C	Dimensionless factor $C = k_{rn}f_w$	-
Ca	Dimensionless capillary number	-
d	Characteristic grain diameter	m
d_{10}	Characteristic grain diameter whose size exceeds 10 % of the other diameters by weight	m
d_{ij}	Distance between nodes i and j	m
\mathbf{D}_{disp}	Mechanical dispersion tensor	$\text{m}^2 \text{s}^{-1}$
D_m^κ	Molecular diffusion of component κ	$\text{m}^2 \text{s}^{-1}$
D_{pm}^κ	Effective porous medium diffusion of component κ	$\text{m}^2 \text{s}^{-1}$
D_j	Diffusivity of aquifer j , $D_j = \frac{k}{\mu_w \phi C_t}$	$\text{m}^2 \text{s}^{-1}$
E	Volumetric CO ₂ storage efficiency	-
\mathbf{f}	Flux vector	$\text{kg or mol s}^{-1} \text{m}^{-2}$
\mathbf{f}_a	Advective flux vector	N m^{-1}
\mathbf{f}_d	Diffusive flux vector	$\text{kg or mol s}^{-1} \text{m}^{-2}$
\mathbf{f}_f	Fracture flux vector	$\text{kg or mol s}^{-1} \text{m}^{-2}$
f_α	Fractional-flow function of phase α , $f_\alpha = \frac{\lambda_\alpha}{\lambda_t}$	-
\mathbf{g}	Gravity acceleration vector	m s^{-2}
g	Scalar gravity acceleration $g = 9.81$	m s^{-2}
G	Model domain	m^3
Gr	Dimensionless gravitational number	-
h	Height of the CO ₂ front	m
h'	Dimensionless height of the CO ₂ front	-

h_{ij}	Distance from element center to midpoint of edge connecting nodes i and j	m
H	Aquifer thickness	m
\mathbf{K}	Intrinsic permeability tensor	m ²
k	Scalar permeability	m ²
k_f	Scalar permeability of fracture	m ²
$k_{fh,j}$	Horizontal fault permeability in aquifer j	m ²
$k_{fv,j}$	Vertical fault permeability in aquifer j	m ²
$k_{r\alpha}$	Relative permeability of phase α	-
l_{cr}	Characteristic length	m
L_j	Distance between midpoints of aquifers j and $j + 1$	m
$\overline{M_\alpha}$	Average molar weight of a phase α	kg mol ⁻¹
M^κ	Molar weight of a component κ	kg mol ⁻¹
\mathbf{n}	Unit normal vector of sub-control volume face	-
\mathbf{n}_{ij}	Unit normal vector of sub-control volume face between node i and j	-
\mathbf{n}_{IP}	Unit normal vector of sub-control volume face at integration point IP	-
N	Number nodes in a grid	-
N_i	Linear basis function, $N_i = N_i(\mathbf{x})$	-
p	Pressure	Pa
p_α	Pressure of phase α	Pa
p_c	Capillary pressure	Pa
p_e	Entry pressure	Pa
\hat{p}_c	Dimensionless capillary pressure	-
p_{cr}	Characteristic pressure	Pa
Δp_{j1}	Pressure change in aquifer j region 1	Pa
Δp_{j2}	Pressure change in aquifer j region 2	Pa
q	Source or sink term	kg or mol s ⁻¹ m ⁻³
q_α	Source or sink term of phase α	kg or mol s ⁻¹ m ⁻³
q^κ	Source or sink term of component κ	kg or mol s ⁻¹ m ⁻³
q_t	Total source or sink term of	kg or mol s ⁻¹ m ⁻³
$Q_{leakage}$	Volumetric leakage rate	m ³
Q_{well}	Volumetric injection rate	m ³
\mathbf{r}	Residual vector of whole domain	kg or mol s ⁻¹
r	Radial coordinate	m
r_i	Residual at node i	kg or mol s ⁻¹

R_o	Outer radius of domain	m
s	Storage term	kg or mol m ⁻³
s_f	Storage term of fracture	kg or mol m ⁻³
S_α	Saturation of phase α	-
S_{rn}	Residual non-wetting phase saturation	-
S_{rw}	Residual wetting phase saturation	-
t	Time	s
\hat{t}	Dimensionless time	-
Δt^n	Time step size of time step n	s
T	Temperature	K
\mathbf{u}	Primary variable vector as a function of space $\mathbf{u} = \mathbf{u}(\mathbf{x})$	-
$\tilde{\mathbf{u}}$	Interpolated primary variable vector as a function of space	-
\tilde{u}	Interpolated primary variable (scalar) as a function of space	-
$\tilde{\mathbf{u}}_{IP}$	Interpolated primary variable vector at integration point	-
$\hat{\mathbf{u}}$	Discrete primary variable vector of whole domain	-
$\hat{\mathbf{u}}_i$	Discrete primary variable vector at node i	-
\hat{u}_i	Discrete primary variable (Scalar) at node i	-
\hat{u}_D	Fixed Dirichlet value	-
\mathbf{v}	Specific volumetric flux vector, Darcy or filter velocity	m s ⁻¹
\mathbf{v}_α	Specific volumetric flux vector of phase α	m s ⁻¹
\mathbf{v}_a	average fluid velocity, per unit area of the fluid phase	m s ⁻¹
\mathbf{v}_f	Specific volumetric flux vector, Darcy or filter velocity	m s ⁻¹
\mathbf{v}_t	Specific volumetric total flux vector	m s ⁻¹
$\hat{\mathbf{v}}_t$	Dimensionless total velocity	-
v_{cr}	Scalar characteristic velocity	m s ⁻¹
$V_{f,i}$	Volume of fracture at node i	m ³
V_i	Box volume of node i	m ³
∂V_i	Boundary of a box i	m ³
w_f	Fault zone width	m
w_{ij}	Fracture width between nodes i and j	m
W_i	Weighting function of node i , $W_i = W_i(\mathbf{x})$	-
W_f	Weighting coefficient ($0 \leq W_f \leq 1$) of fracture storage term	-
W_m	Weighting coefficient ($0 \leq W_m \leq 1$) of matrix storage term	-

x	x-coordinate	m
\mathbf{x}	Coordinate vector	m
x^κ	Mole fraction of component κ	-
x_α^κ	Mole fraction of component κ in phase α	-
X_α^κ	Mass fraction of component κ in phase α	-
y	y-coordinate	m
Δy	Increment on y -axis	m
\hat{z}	Dimensionless z-coordinate	-

Subscripts:

α	Phase index
f	Fracture or fault zone
m	Matrix
h	Horizontal
v	Vertical
i	Node or box index
j	Node or box or aquifer index
IP	Index of integration point
upw	Upwinding index, either i or j
w	Wetting phase (brine phase)
n	Non-wetting phase (CO ₂ phase)
pm	Porous medium

Superscripts:

κ	Component index
n	Time step index
CO_2	CO ₂ component
H_2O	Water component
S	Salt (NaCl) component

Abstract

Carbon Dioxide, Capture and Storage (CCS) is considered to be a cost-effective technology for mitigating climate change in the near future. A necessary requirement for a successful implementation of CCS is the public acceptance of the technology. The affected public needs to be aware of, and accept the risks that are associated with the subsurface storage of CO₂. This demands the use of transparent and comprehensible criteria in a site-selection and characterization process.

Such a process comprises several levels. The first level should be a basin-scale screening using different criteria with the aim of identifying favorable areas and sites for CO₂ storage. Once potential sites have been identified, an exploration should be carried out to obtain site-specific data. The next step should comprise a site-specific investigation of the risks associated with CO₂ storage, covering such risks as the leakage of CO₂ from the reservoir and the risk of saltwater intrusion in freshwater aquifers. This work deals with two aspects of such a multi-level site-selection and characterization process. The first aspect is related to a basin-scale screening method, allowing for a qualitative ranking of different areas with respect to storage efficiency. The second aspect investigates the displacement of resident brine during the injection of CO₂, on the basis of a realistic, but not real large-scale site in the North German Basin. For both aspects, the relevant processes and parameters are analyzed, and models with varying complexity are compared for the target variables of interest.

Basin-Scale Screening for CO₂ Storage Efficiency An important requirement for a screening method is a low computational demand, as the screening has to be carried out over a large area. For this purpose, the dimensionless gravitational number (Gr), which has a negligible computational demand, is considered here as a screening criterion. Gr relates gravitational forces to viscous forces during CO₂ injection, and is therefore a qualitative indicator of how efficient a reservoir can be used (i.e. storage efficiency). The basin-scale database available in this work comprises regionalized data for depth, temperature conditions, and salt concentrations in the Middle Buntsandstein rock unit of the North German Basin. These data are sufficient to determine the initial fluid properties (viscosities and densities) of brine and CO₂. However, other relevant parameters like the permeability, the porosity, and the reservoir thickness are

not regionalized on the basin scale. Gr is therefore calculated based on the fluid properties at every data point of the database. The Gr-criterion allows only for a qualitative ranking of different sites, therefore numerical simulations are performed to test if there is a significant influence of the varying fluid properties on storage efficiency. Additionally, the influence of the parameters porosity and reservoir thickness, for which data are only available in selected areas, is compared to the influence of the varying fluid properties in these areas. The results suggest, that the influence of the fluid properties on the storage efficiency is notable but less important, than that of the parameters porosity and reservoir thickness. Still, the influence of the fluid properties can be in the same range as the other two parameters.

Additionally, the Gr-criterion is compared to the Okwen-Method, which is an analytical solution for estimating the storage efficiency. The main finding is, that both methods show an acceptable qualitative agreement with the simulation results for large parts of the considered range of depth, temperature conditions, and salt concentrations found in the Middle Buntsandstein rock unit.

To summarize, a screening method, such as the Gr-criterion or the Okwen-Method based on the available database of depth, temperature conditions, and salt concentrations can provide valuable information for identifying suitable areas for CO₂ storage. However, it becomes clear that these criteria can only be part of a larger set of criteria that have to be evaluated.

Large-Scale Investigation of Brine Displacement Brine displacement is considered to be a potential risk of CO₂ storage. A site selection process should therefore include a phase where the fate of the brine displaced by the injected CO₂ is investigated. For this purpose, different numerical and analytical models exist. This work investigates brine displacement in a realistic (but not real) CO₂ storage site in the North German Basin.

The geological model comprises, besides the injection horizon and its surrounding layers, the complete overburden up to the shallow freshwater aquifers. It therefore fully couples flow between deep and shallow layers. Several characteristics of the North German Basin are included in the geological model, such as a salt wall, which penetrates all layers up to the shallow freshwater aquifers, and the Rupelian clay barrier, which separates saltwater from freshwater aquifers. The Rupelian clay barrier is discontinuous at several locations, so-called hydrogeological windows, which allow for an exchange between saltwater and freshwater. The second important barrier in the geological model is the Upper Buntsandstein barrier, which is the main barrier preventing the CO₂ from migrating upwards. It is situated approximately 1300 m below the Rupelian clay barrier. A conservative assumption is made by assuming a permeable fault zone, at the flank of the salt wall. This fault zone directly connects the injection horizon to the freshwater aquifers, which are, in this work, referred to as target aquifers.

In a scenario study, different components of the geological model are varied, not in a statistical sense, but on the entire range of plausible values, thereby creating a span of possible results. This allows, to some extent, a generalization of the conclusions drawn here to other sites, at least within the North German Basin. The results presented in this work show first and foremost that notable, in the sense of non-negligible, increases in the salt concentration in the target aquifers are locally constrained to regions, where initially elevated concentrations are present prior to the injection, and where permeabilities are high enough to support sufficient flow (i.e. at the fault zone and the hydrogeological windows). Hence, the quality of the prediction of concentration changes strongly depends on how well the initial salt distribution is known. Another important parameter is the permeability of the Upper Buntsandstein barrier. It has a strong influence on the type of brine displacement, which can either be diffuse across the barrier or focused over the fault zone.

In a further study, models with varying complexity are compared. More complex models will increase the computational demand and require more data. In general, hydrogeological data are highly uncertain, therefore a risk analysis may require many realizations of a model (for example Monte-Carlo simulations). To limit the computational demand, while still being able to handle the uncertainties in the data, requires the use of simplified models. The main aim of this model comparison is to reduce the model uncertainty, by investigating the effects of the different model simplifications. The analysis on model simplification shows that the level, to which the complexity of a model can be reduced, depends on the target variable of interest. For example, when considering the volumetric leakage rate into the target aquifers as a target variable most of the model simplifications compared in this work show an acceptable agreement. However, when considering the pressure-buildup as a target variable the agreement between some of the considered model simplifications significantly worsens. The agreement between the different models has to be evaluated bearing in mind the uncertainty of the hydrogeological parameters, whose impact is expected to be much greater than the impact of most of the model simplifications treated here.

Overall, the analysis on brine displacement presented in this work, will help in the design of effective and efficient large scale models. A possible application could be a basin-scale model of the North German Basin considering multiple CO₂ injections.

Zusammenfassung

Die CO₂-Abscheidung und -Speicherung (CCS, engl. Carbon Dioxide Capture and Storage) wird als kosteneffiziente Technologie zur Minderung der anthropogenen Emissionen des Treibhausgases CO₂ in die Atmosphäre angesehen. Die CCS-Technologie könnte somit einen wichtigen Beitrag zur Abschwächung der Folgen des Klimawandels in naher Zukunft leisten. Eine erfolgreiche Umsetzung der CCS-Technologie, in einem klimarelevanten Maßstab, hängt stark von deren öffentlicher Akzeptanz ab. Die Risiken für Mensch und Umwelt, welche mit der unterirdischen Speicherung von CO₂ einhergehen, sollten daher offen kommuniziert und von einer betroffenen Öffentlichkeit akzeptiert werden. Deshalb ist es notwendig bei der Suche nach geeigneten Standorten transparente und nachvollziehbare Auswahlkriterien einzusetzen. Die Standortauswahl sollte in mehreren Stufen verlaufen. Zuerst können, durch ein großflächiges Screening, anhand verschiedener Kriterien, geeignete Gebiete für die CO₂-Speicherung identifiziert werden. Nach der Identifizierung von potentiellen Standorten, kann eine Erkundung folgen, mit deren Hilfe standortspezifische Daten erhoben werden können. In einem weiteren Schritt sollte eine standortspezifische Risikoanalyse durchgeführt werden, z.B. zum Risiko der Migration von CO₂ aus dem Speicherhorizont oder der Beeinträchtigung von Süßwasseraquiferen durch verdrängtes Salzwasser. Diese Arbeit befasst sich mit zwei Aspekten dieser mehrstufigen Standortauswahl. Der erste Aspekt beschreibt eine Screening-Methode zur großflächigen Untersuchung von geeigneten Gebieten in Bezug auf die CO₂-Speichereffizienz, wodurch eine qualitative Einteilung dieser Gebiete ermöglicht wird. Im zweiten Aspekt wird die Verdrängung der im Injektionshorizont vorhandenen Sole anhand eines realistischen, jedoch nicht realen Standorts innerhalb des Norddeutschen Beckens untersucht. Für beide in dieser Arbeit behandelten Aspekte werden Modelle mit unterschiedlicher Komplexität sowie die relevanten physikalischen Prozesse und Parameter untersucht.

Großflächiges Screening in Bezug auf die CO₂-Speichereffizienz Eine wichtige Voraussetzung für eine Screening-Methode ist ein möglichst geringer Rechenaufwand, da große Gebiete schnell und effektiv evaluiert werden müssen. Aus diesem Grund wird hier die Eignung der dimensionslosen Gravitationszahl (Gr-Zahl), die mit vernachlässigbar kleinem Rechenaufwand

bestimmt werden kann, als Screening-Kriterium untersucht. Die Gr-Zahl beschreibt das Verhältnis von Gravitationskräften zu viskosen Kräften, während der CO₂-Injektion und ist somit als qualitativer Indikator, für eine effiziente Ausnutzung des betrachteten Reservoirs (Speichereffizienz), einsetzbar. Die Datenbasis, welche für diese Analyse zur Verfügung steht, umfasst regionalisierte Tiefen-, Temperatur- und Salzkonzentrationsdaten des Mittleren Buntsandsteins im Norddeutschen Becken. Die Datenbasis ist somit ausreichend zur Bestimmung der im Injektionshorizont vorliegenden Fluideigenschaften (Viskosität und Dichte) von Sole und CO₂. Die Datenbasis für den Mittleren Buntsandstein enthält jedoch keine regionalisierten Daten zu den Permeabilitäten, den Porositäten und den Formationsmächtigkeiten. Die Gr-Zahl wird deshalb nur unter Berücksichtigung der Fluideigenschaften bestimmt. Die Bestimmung wird für jeden Datenpunkt der Datenbasis durchgeführt, so dass die Gr-Zahl regionalisiert vorliegt. Da das Gr-Kriterium nur eine qualitative Differenzierung von verschiedenen Gebieten zulässt, werden zusätzlich numerische Simulationen durchgeführt, um zu prüfen, ob die Variabilität in den regionalisierten Fluideigenschaften einen großen Einfluss auf die Speichereffizienz hat. Hierbei wird auch der Einfluss von Parametern wie der Porosität und der Formationsmächtigkeit untersucht, für die Daten nur in ausgewählten Gebieten verfügbar sind. Die Simulationsergebnisse zeigen, dass variable Fluideigenschaften, basierend auf den regionalisierten Daten von Tiefe, Temperatur und Salzkonzentrationen, eine wichtige Rolle spielen. Ihr Einfluss ist jedoch den Parametern Porosität und Formationsmächtigkeit untergeordnet, kann aber auch von der gleichen Größenordnung sein.

Weiterhin wurde das Gr-Kriterium mit der Okwen-Methode verglichen. Die Okwen-Methode ist eine analytische Lösung zur Bestimmung der Speichereffizienz. Die zentrale Schlussfolgerung dieses Vergleichs ist, dass beide Methoden eine passable qualitative Übereinstimmung mit den durchgeführten Simulationen zeigen für weite Teile der im Mittleren Buntsandstein vorliegenden Tiefen-, Temperatur- und Salzkonzentrationsdaten.

Zusammenfassend lässt sich zu dieser Untersuchung feststellen, dass sowohl das Gr-Kriterium als auch die Okwen-Methode wertvolle Informationen zur Identifizierung von geeigneten Gebieten für die CO₂-Speicherung liefern können, ausgehend von der verwendeten Datenbasis. Jedoch müssen beide Methoden Teil eines größeren Kriterienkatalogs sein, welcher zur Identifizierung von geeigneten Gebieten eingesetzt wird.

Großskalige Untersuchung der Sole-Migration an einem realistischen Standortmodell Die Verdrängung von Sole durch die Injektion von CO₂ ist eines der Risiken, welches mit der CO₂-Speicherung assoziiert wird. Aus diesem Grund sollten bei der Wahl eines geeigneten Standortes die Auswirkungen der Sole-Verdrängung untersucht werden. Hierfür stehen verschiedene analytische und numerische Modelle zur Verfügung. In dieser Arbeit wird die Verdrängung von Sole anhand eines realistischen, jedoch nicht realen Standorts zur CO₂-Speicherung im

Norddeutschen Becken untersucht.

Das hierfür verwendete geologische Modell umfasst, neben dem Injektionshorizont, das komplette Deckgebirge bis zu den oberflächennahen Süßwasseraquiferen. Somit ist die Grundwasserströmung zwischen tiefen und oberflächennahen Schichten voll gekoppelt. Das geologische Modell enthält weiterhin für das Norddeutsche Becken typische Merkmale, wie z.B. einen Salzwall, welcher alle Schichten bis zu den oberflächennahen Süßwasseraquiferen durchbricht oder die Barrierschicht Rupelton, welche Süß- und Salzwasseraquifere voneinander trennt. Der Rupelton ist an einigen Stellen unterbrochen, sog. Rupelfehlstellen, welche eine wichtige Rolle für den Austausch von Süß- und Salzwasser spielen. Die zweite wichtige Barriere ist der Obere Buntsandstein, welcher ca. 1300 m unterhalb des Rupeltons liegt und die eigentliche Barriere für das aufsteigende CO₂ darstellt. Weiterhin wird eine konservative Annahme getroffen, indem eine durchlässige Störungszone an dem Salzwall angenommen wird. Diese stellt eine direkte Verbindung zwischen dem Injektionshorizont und den oberflächennahen Aquiferen dar.

In einer Szenarienstudie werden verschiedene Komponenten und Parameter dieses geologischen Modells, zwischen plausiblen Ober- und Untergrenzen, variiert. Somit stellt sich eine Bandbreite von möglichen Ergebnissen ein. Dies erlaubt in gewissen Grenzen eine Generalisierung der Schlussfolgerungen, welche in dieser Szenarienstudie getroffen werden hin zu anderen Standorten, zumindest innerhalb des Norddeutschen Beckens. Die Ergebnisse dieser Studie zeigen, dass sich relevante Erhöhungen der Salzkonzentration nur dort ergeben, wo bereits vor der CO₂ Injektion erhöhte Konzentrationen aufgetreten sind und wo ausreichend hohe Permeabilitäten vorhanden sind, d.h. an den Rupelfehlstellen und an der Störungszone. Ein weiterer wichtiger Parameter ist die Permeabilität der Oberen Buntsandstein Barriere, welche die Art der Sole-Verdrängung – großflächig über die Barriere oder aber fokussiert über die Störungszone – kontrolliert.

In einer weiteren Studie werden verschiedene Modelle von unterschiedlicher Komplexität miteinander verglichen. Komplexere Modelle erhöhen im Allgemeinen den Rechenaufwand und haben einen größeren Datenbedarf. Da hydrogeologische Daten mit großen Unsicherheiten behaftet sind, bedarf es bei einer Risikoanalyse vieler Realisationen (z.B. Monte-Carlo Simulationen). Um den Rechenaufwand möglichst gering zu halten und trotzdem der hohen Unsicherheit in den Daten gerecht zu werden, benötigt man vereinfachte Modelle und Annahmen. Das Ziel dieser Vergleichsstudie ist die Gegenüberstellung von verschiedenen Modellvereinfachungen, zur Reduzierung der Modellunsicherheit. Ob man die Komplexität eines Modells reduzieren kann, hängt von der betrachteten Zielvariable ab. Ist z.B. der verdrängte Volumenfluss die Zielvariable, so zeigen die meisten der hier untersuchten Modellvereinfachungen eine passable Übereinstimmung untereinander. Wird hingegen der durch die Injektion hervorgerufene Druckanstieg als Zielvariable gewählt, so sind deutliche Unterschiede zwischen einigen der betrachteten Modellvereinfachungen erkennbar.

Zusammenfassend lässt sich feststellen, dass die Ergebnisse und Schlussfolgerungen der hier

präsentierten Szenario- und Modell-Vergleichsstudien zur Sole-Migration einen wichtigen Beitrag bei der Erstellung von effektiven und effizienten großskaligen Modellen leisten können. Ein Anwendungsbeispiel hierfür könnte die Erstellung eines Modells für das gesamte Norddeutsche Becken sein, unter Berücksichtigung mehrerer sich beeinflussender CO₂ Speicherstandorte.

1. Introduction

1.1. Motivation and Aims

According to the Intergovernmental Panel on Climate Change (IPCC) (IPCC, 2014), the globally averaged combined land and ocean surface temperatures have increased by $0.85\text{ }^{\circ}\text{C} \pm 0.20\text{ }^{\circ}\text{C}$ between 1850 and 2012. They further conclude that this change in temperature is due to an increase of greenhouse gas (GHG) concentrations in the atmosphere that is a result of human activity. The projected future risks of this global climate change on humans and the environment are manifold: risk of undermining food security, risk of increasing competition for water resources especially in dry sub-tropical regions, increased risk of extreme events such as floods, storms, drought, sea-level rise, and increase of extinction risk for species especially in highly vulnerable ecosystems such as polar regions or coral reefs.

The annual GHG emissions have almost doubled from 1970 (27 GtCO₂eq/year) to 2010 (49 GtCO₂eq/year). 78% of this increase in GHG emissions are attributed to CO₂ emitted from fossil-fuel combustion and industrial processes (IPCC, 2014). In 2010, the direct annual CO₂ emissions from the energy-supply sector (electricity and non-electricity, for example use of fossil fuels for transport) were about 30 GtCO₂/year making it the major contributor to GHG emissions. So-called baseline scenarios, predicting CO₂ emissions if no action is undertaken to reduce GHG emissions (i.e. business as usual), show that the annual CO₂ emissions will increase to about 55–70 GtCO₂/year by the year 2050 and 65–90 GtCO₂/year in the year 2100 (Bruckner et al., 2014). This would result in an estimated rise in temperature of about 3.5–4.8 °C in the year 2100 (IPCC, 2014), relative to the period from 1861-1880.

Many strategies for the reduction of CO₂ emissions in the energy sector exist, including both improvements of energy Efficiency, and low-GHG energy production technologies such as renewable energies, nuclear power and Carbon Dioxide Capture and Storage (CCS). CCS is a technology with the potential for strongly reducing CO₂ emissions from electricity production and industrial processes. CCS comprises three main steps:

- CO₂ capture, either from fossil fuel-fired power plants (coal, oil, and gas), or from industrial processes, where the generation of CO₂ is an inherent part of the production process,
- the liquefaction of the captured CO₂ and transport via pipeline or barge, and
- the storage of supercritical CO₂ in geological formations such as deep saline aquifers or in oil and gas reservoirs (either in depleted reservoirs, or in systems where injected CO₂ will enhance an ongoing oil or gas production operation).

The greatest potential for CCS lies in the reduction of CO₂ emissions from coal-fired power plants. Based on their literature review, Bruckner et al. (2014) estimate that CO₂ emission from a modern-to-advanced grade coal-fired power plant could be reduced from 710–950 gCO₂eq/kWh to 70–290 gCO₂eq/kWh by CCS. This reduction becomes especially important when considering that coal has been the largest and fastest growing source of primary energy in the past decade (IEA, 2012b). The main cost increase incurred when adding a CCS system to a conventional coal-fired power plant is attributed to the capturing of CO₂. Studies evaluated in IEA (2013) estimate that the cost increase related to CO₂ capture would range between 40–63%. This results in an increase in unit cost for energy created in these plants to around 100 USD/MWh. Bruckner et al. (2014) assume an additional 10 USD/MWh for transport and storage of CO₂ based on their literature review, leading to total costs of 110–130 USD/MWh for electricity generation with CCS from coal-fired power plants, for various capturing technologies. Although it is expected that costs will decrease due to learning curve effects once the deployment of CCS increases (IEA, 2013), CCS will always lead to additional costs in electricity generation. In order to make the technology economically feasible, these additional costs have to be compensated by a price on carbon emissions or direct financial support from governments (Bruckner et al., 2014).

To prevent an increase in concentrations of GHG in the atmosphere past the level of 430–530 ppm CO₂eq by the year 2100, a level which corresponds to an estimated rise in temperature of 0–2 °C (Clarke et al., 2014), Bruckner et al. (2014) state: “Improving the energy efficiencies of fossil power plants and/or the shift from coal to gas will not by itself be sufficient to achieve this. Low-GHG energy supply technologies are found to be necessary if this goal is to be achieved.” (p. 516). All cost-effective planning scenarios that reach low concentrations (430–530 ppm CO₂eq) predict a sharp rise in the deployment of the CCS technology in the near future. They predict an increase in storage from about 5 Mt/year being stored today to 1–7 Gt/year by 2030 and 15–60 Gt/year being stored annually in the year 2100 (Eom et al., 2015; Bruckner et al., 2014). Also considered in many scenarios is the combination of bioenergy with CCS (BECCS) which creates a net negative emission and may therefore help

in lowering CO₂ concentrations in the atmosphere. Eom et al. (2015) stress: “Our physical deployment measures indicate that the availability of CCS technology could play a critical role in facilitating the attainment of ambitious mitigation goals. Without CCS, deployment of other mitigation technologies would become extremely high in the 2030-2050 period. Yet the presence of CCS greatly alleviates the challenges to the transition particularly after the delayed climate policies, lowering the risk that the long-term goal becomes unattainable.” (p. 73). Also, the International Energy Agency stresses the importance of CCS as a bridging technology in the near future: in their 2DS Scenario aiming to keep the temperature rise below 2 °C, CCS accounts for 20 % of the cumulative CO₂ reductions by the year 2050 (IEA, 2012a). In the reports discussed above (Bruckner et al., 2014; IEA, 2012a) the importance of CCS as a cost-effective climate-change mitigation technology has been stressed, but the critical question remains: Is there enough storage capacity to meet the demand projected in the various scenarios?

Dooley (2013) determines the average demand for CO₂ storage capacity in the year 2100 from more than 122 peer-reviewed articles with low concentration targets (400–500 ppm CO₂eq) to be 1340 GtCO₂. To compare, Bruckner et al. (2014) give a lower estimate of 448–1000 GtCO₂. Dooley (2013) compares this value with the so-called practical global storage capacity, 3900 GtCO₂. With this value, obtained by summarizing the estimates of various literature sources, Dooley (2013) concludes that it is unlikely that insufficient storage capacity will pose restrictions on the deployment of CCS. The majority of this storage capacity is situated in the U.S. (about 2250 GtCO₂). As a comparison, and pertaining to the investigation outlined in this report, the estimated storage capacity for Germany is 10 GtCO₂ with 2.75 GtCO₂ in depleted oil and gas reservoirs and 6.3–12.8 GtCO₂ in saline aquifers (Knopf et al., 2010). However, it must be noted that the so-called matched storage capacity, which is the storage capacity obtained when matching large stationary CO₂ sources with suitable storage sites at an economic distance (Bachu et al., 2007), will probably be much smaller than the above estimates.

A climate-relevant implementation of CCS will require a major focus on CO₂ storage in deep saline aquifers of sedimentary basins, which provide the largest storage potential (e.g. Metz et al. (2005); Müller and Reinhold (2011); Dooley (2013); Knopf et al. (2010)). Finding suitable sites for CO₂ storage is a challenging task which has to be assessed on multiple levels. For example, in the Carbon Sequestration Atlas of the United States and Canada (NETL, 2010), the site characterization process is divided into three steps: site screening, site selection, and initial characterization. The site-screening step involves the evaluation of regional geologic and social criteria on a basin scale in order to rank a list of so-called “selected areas”. These areas are analyzed in more detail in the site-selection step, where qualified sites are defined. In the third step, the previously selected sites undergo an initial characterization.

Once areas or suitable sites are selected, the next level of site characterization should also include a more thorough area or site-specific analysis of the potential risks of CO₂ storage. Among the major risks associated with the storage of CO₂ are the potential for CO₂ leakage, the dissolution of heavy metals due to the acidification of groundwater in contact with CO₂, and saltwater leakage into freshwater aquifers due to pressure build-up within the storage formation (Bannick et al., 2008). The injection of supercritical CO₂ into deep saline aquifers inevitably leads to the displacement of resident brine. Hazardous situations may arise if brine migrates vertically through discontinuities, like permeable fault zones or abandoned wells, into shallow aquifer systems, where the brine may contaminate drinking-water resources. Salt concentrations at a drinking-water production well should not rise above the regulatory limits, which would eventually lead to a shutdown of production. CO₂ storage should therefore not interfere with water supply. This is especially true for Germany, as around 74% of the drinking water is obtained from essential public groundwater resources (Bannick et al., 2008).

Deployment of CCS is highly dependent on public acceptance of the technology. In Germany, CCS faced fierce opposition from environmental groups, public water suppliers, and an affected public. Therefore, the different levels of a site-selection process and the assessment of potential risks have to be communicated to stakeholders in order to avoid misconceptions on either side.

Making predictions during the different stages of a site-selection process, for example determining storage efficiency on the basin scale, or evaluating the displacement of saline water into freshwater aquifers for a specific site, will require the usage of analytical or numerical models. A wide range of models, with different complexities based on varying assumptions, exist for application in the context of CO₂ storage. Deciding on the appropriate level of model complexity is not an easy task. The choice of a model depends on multiple criteria, including:

- the physical processes which the model should be capable of handling,
- the computational demand,
- the data availability, and
- the uncertainty in these data.

Using the most complex model available may not necessarily be the best choice as both the computational demand and the data demand increase. If the computational demand is too high, it may become unfeasible to consider the large uncertainties in the data, inherent to hydrogeological systems, which require numerous realizations of the model. If there is not enough reliable data to justify the use of more complex models, the obtained results can be highly speculative. On the other hand, an oversimplified model may over- or underestimate target variables, when essential physical processes are neglected. Especially under site-specific

conditions, models verified only in an idealized environment may fail to produce reliable results. In order to reduce the uncertainty with regard to the model assumptions, different model types relying on different assumptions should be compared under realistic conditions.

This work puts the focus on two important aspects of a multi-level site characterization. For both aspects, the relevant processes and parameters are analyzed, and models with varying complexity are compared for the target variables of interest:

1. A possible site-screening approach, used to qualitatively evaluate different regions with regard to storage efficiency on the basin scale, is presented in this work (Chapter 4). It is applied to the Middle Buntsandstein rock unit in the North German Basin.
2. An analysis of different scenarios in order to identify relevant parameters controlling brine displacement due to CO₂ injection in a realistic conceptual site with characteristic features of the North German Basin is also presented in this work (Chapter 5). Additionally, different models are tested with the aim to find the right level of model complexity for evaluating brine migration.

1.2. Literature Review

In the following sections, literature regarding basin-scale site screening, the topic of Chapter 4, and literature related to brine displacement due to CO₂ storage, the topic of Chapter 5, will be reviewed.

1.2.1. Site-Screening Methods for CO₂ Storage on the Basin Scale

Finding suitable sites for CO₂ storage depends on many different criteria (technical, economical, legislative or social). Bachu (2003) describes a regional-scale suitability assessment for sedimentary basins. 15 different technical and economic criteria are used for ranking sedimentary basins according to their suitability for CO₂ storage. Among the criteria are depth, climate (mean surface temperature), and a geothermal characterization of the basin (warm, moderate, and cold basin), all of which are used to estimate the thermodynamic conditions (pressure and temperature) of the basin. Based on the thermodynamic conditions, fluid properties like the density and viscosity of brine and CO₂ can be determined. The fluid properties have an influence on the shape of the CO₂ plume in the reservoir and thus on the amount of CO₂ that can be stored in a given reservoir volume. Methods developed for screening in the context of CO₂ storage can consider one or several of the criteria defined for example in Bachu (2003).

Such methods are used either for a qualitative (ranking of areas or sites) or a quantitative (estimating the storage capacity of different sites) assessment.

Many methods for estimating storage efficiency have been published in the last 10 years. Most of them rely on simple and fast analytical or numerical models to estimate storage efficiencies. A comparison of different methods was carried out in Goodman et al. (2013) for saline aquifers. One of the major conclusions drawn in their report is that despite substantial differences in the underlying assumptions of the models considered, the variability of the hydrogeological parameters has a much greater effect on CO₂ storage estimates than the actual method used. One of the methods compared in Goodman et al. (2013) was the simple analytical method for laterally closed injection aquifers, proposed by Zhou et al. (2008). It relies on the assumption of a uniform pressure buildup within the injection aquifer, which is valid for high permeabilities ($>1 \times 10^{-14} \text{ m}^2$) and small domain radii. The storage efficiency is then calculated using the amount of CO₂ stored in the system until a maximum allowable pressure is exceeded, above which geomechanical degradation of the formation or barrier could occur. The storage efficiency is therefore constrained by pressure buildup. Szulczewski et al. (2012) point out that storage capacity is a dynamic quantity which is limited by pressure constraints as well as by the amount of CO₂ that can be trapped in an aquifer. The trapping mechanisms, which Szulczewski et al. (2012) consider are residual trapping of CO₂ due to capillary forces and solubility trapping due to the dissolution of CO₂ in the groundwater. They conclude that, at first, pressure constraints limits the CO₂ storage capacity due to a predicted high storage demand. When the storage demand curve declines, the maximum amount of CO₂ that can be trapped will limit the CO₂ storage capacity. Mathias et al. (2008, 2009) developed an analytical model to determine the maximum pressure buildup at different sites during injection with a specified rate in a laterally open injection aquifer. In their screening approach, Mathias et al. (2009) exclude sites where the maximum injection-induced pressure exceeds the pressure required to fracture the rock formation.

Okwen et al. (2010) present another simple analytical model that takes into account the mobility ratio of brine and CO₂ as well as a dimensionless gravitational number for estimating volumetric storage efficiency. Their method is based on the model derived by Nordbotten and Celia (2006). The method by Okwen et al. (2010) is considered in this work and will be discussed in more detail in Sec. 3.2.1. Another computationally inexpensive and efficient qualitative indicator for reservoir characterization with respect to the CO₂ storage potential is given by the dimensionless gravitational and capillary numbers as proposed by Kopp et al. (2009a,b). Using the U.S. National Petroleum Council public database (NPC, 1984), the authors test the effects of depth, temperature, capillary pressure absolute and relative permeability, and show that physically sound dimensionless numbers can be used to qualitatively rank reservoirs with

respect to their viscous, capillary and gravitational forces. The gravitational number defined in Kopp et al. (2009a) will be used as a qualitative criterion for storage efficiency in this work and is discussed in more detail in Sec. 3.1.2 and 4.1.

1.2.2. Assessment of Large-Scale Brine Displacement due to CO₂ Storage

As stated previously, the injection of supercritical CO₂ in deep saline aquifers will lead to the displacement of resident brine. In the case that this displaced brine migrates vertically, this can pose a threat to drinking-water resources. In the last decade, a large focus has been put on research in the field of brine migration, and new insights were gained by means of large-scale numerical and analytical models (Birkholzer et al., 2015). The extent of injection-induced pressure propagation was already the subject of several simulation studies. Model predictions have shown that the area for potential brine migration to occur is much larger than the actual extent of a CO₂-plume (2–8 km), as elevated pressures are predicted at radii up to 100 km from the injection well (Birkholzer et al., 2009; Birkholzer and Zhou, 2009; Schäfer et al., 2011). Schäfer et al. (2011) performed simulations in a realistic geological system consisting of aquifer and barrier formations bounded by a sealing fault zone. Birkholzer et al. (2009) considered a generic geometry in a multi-layered system consisting of a sequence of aquifers and barriers, thereby investigating both lateral and vertical pressure propagation. They conclude that leakage across barriers (diffuse leakage) needs to be considered for a realistic pressure propagation if the barriers have a permeability higher than $1 \times 10^{-18} \text{ m}^2$. However, they do not expect significant damage due to diffuse leakage across barrier layers, for cases where the barrier permeability is higher than $1 \times 10^{-18} \text{ m}^2$, unless vertical pathways such as permeable fault zones or abandoned wells exist where focused leakage may occur.

More recent studies focus on the simplification of the models used for quantifying brine migration and developing pressure-management tools for a large spatial scale. Brine leakage through abandoned wells was investigated in Celia et al. (2011) using a semi-analytical model described in Celia and Nordbotten (2009) and Nordbotten et al. (2009). A comparison of models of varying complexity on the basin scale with multiple injection wells was conducted by Huang et al. (2014). They concluded that single-phase numerical models (i.e. injection of brine into brine instead of CO₂ into brine) are sufficient for predicting the basin-scale pressure response. Analytical and semi-analytical solutions depending on superposition of solutions in time and space may not be accurate enough, as the variability of formation properties (heterogeneity and anisotropy) cannot be captured. Cihan et al. (2011) developed an analytical model capable of handling multi-layered systems considering diffuse leakage (through barrier layers) and focused leakage (abandoned wells and fault zones). The same analytical model is also applied in Birkholzer et al. (2012), where pressure management strategies are compared.

Zeidouni (2012) presented an analytical model for the determination of brine flow through a permeable fault zone into aquifers separated by impermeable aquitards. This model has a realistic description of the fault zone, as lateral and vertical transmissivity within the fault zone can be assigned independently of each other, thereby allowing a wide range of fault zone configurations. The analytical model developed by Zeidouni (2012) will also be considered in this work for (i) verifying a numerical model with regard to large-scale pressure propagation (Sec. 5.4), and (ii) as a simplified and therefore fast method to evaluate leakage in a complex geological setting (Sec. 5.5.3). A more detailed explanation of the underlying assumptions and equations of the model proposed by Zeidouni (2012) is given in Sec. 3.2.2.

The injection of CO₂ into saline aquifers and the possible leakage of the displaced brine across vertical pathways means that the analysis will include saline water at different depths. At these different depths, the fluid will flow under different conditions (temperature, salinity, and pressure). Temperature and salinity influence the flow field because of their effect on the density and the dynamic viscosity. Most of the models applied in Chapter 5 consider variable-density flow. Oldenburg and Rinaldi (2010) set up an idealized numerical model of two aquifers separated by an aquitard with a connecting permeable fault zone. They show that a new hydrostatic equilibrium may establish if salt water is pushed upwards through a fault zone due to an increase in pressure in the lower aquifer. The new equilibrium strongly depends on the salt concentration in the lower aquifer, where low concentrations may lead to continuous upward flow, as opposed to the case with high salt concentrations. Tillner et al. (2013) consider brine-migration scenarios for a potential storage site in northern Germany using a multi-phase (H₂O and CO₂) and multi-component (H₂O, NaCl and CO₂) model accounting for density differences due to variable salt concentrations. They included several fault zones which can be permeable or impermeable, thereby controlling leakage into overlying aquifers. Tillner et al. (2013) conclude that the choice of boundary conditions, Dirichlet conditions (open boundary) or Neumann conditions (closed boundary) for the lateral boundary has the highest impact on the observed brine migration, while the results are less sensitive to the fault permeability. The model for the deep subsurface used by Tillner et al. (2013) was further coupled (one-way coupling) to a model comprising more shallow freshwater aquifers (Kempka et al., 2013) using flow through the fault zones as boundary conditions for the shallow aquifer model. The results indicate that an increase in the salt concentration due to CO₂ injection is only recognizable in those areas, which already have a naturally elevated salt concentration. Walter et al. (2012, 2013) use a generic multi-layer system with a radially symmetric fault zone surrounding the injection at a certain distance. They also use a multi-phase (H₂O and CO₂) and multi-component (H₂O, NaCl, and CO₂) model to calculate the brine flow into a shallow aquifer. Walter et al. (2012) make a conservative assumption by specifying a high initial salinity of 0.1 kg salt/kg brine across the deep layers, while in Walter et al. (2013), a linear

increase of salt concentration with depth is assumed. The results show that the amount of salt entering the shallow aquifer varies significantly between these two assumptions, with more salt entering in the constant-concentration case. As a result, the prediction of salt transport into shallow aquifers is not only uncertain with respect to the boundary conditions and the hydrogeological parametrization, but in particular with respect to the initial salt distribution assumed in the system. This finding is confirmed by Tillner et al. (2016) where the initial salt distribution, the lateral boundary conditions, and the available pore space in the fault zone are identified as the key parameters influencing saltwater intrusion in shallow aquifers.

A realistic geological model with typical characteristics of the North German Basin will be considered in the evaluation of brine displacement in Chapter 5. A number of numerical studies have been conducted for modeling large-scale heat and salt transport in the North German Basin to determine regional flow fields. Magri et al. (2009a,b) model two-dimensional heat and salt transport near shallow salt structures piercing through a layered aquifer/aquitard system. They argue that topographically-driven flow, gravitational and thermohaline convection are the major mechanisms that lead to solute exchange between deep and shallow layers. Noack et al. (2013) model three-dimensional regional heat transport and find that temperature anomalies occur at hydrogeological windows in the Rupelian clay barrier (a barrier between deeper saline and shallower freshwater aquifers) where cooler water from shallow aquifers displaces the warmer formation water. Kaiser et al. (2013) extend this work by including salt transport in their model of the Northeast German Basin. Their simulations also confirm the important role of the hydrogeological windows in the Rupelian clay barrier, that connect saline aquifers with freshwater aquifers.

1.3. Structure of this Thesis

This thesis will follow up the topics discussed above and is structured as follows: Chapter 2 presents the fundamentals of flow through porous media required for understanding the analytical and numerical models used in this work. These models are then discussed in Chapter 3 along with additional implementations carried out in this work. In Chapter 4, a basin-scale screening method for storage efficiency is applied on the Middle Buntsandstein rock unit in the North German Basin. In Chapter 5, critical parameters and model assumptions controlling brine migration are identified in a realistic (but not real) CO₂ storage site in the North German Basin. Finally, a summary and overall conclusion is given in Chapter 6.

2. Fundamentals of Porous-Media Flow

2.1. Spatial Scales and the Continuum Approach

When analyzing the mechanics of flow through porous media, there are different scales on which momentum, mass, and energy transfer can be described. The molecular scale resolves the motion of individual molecules. The continuum approach uses a volume that contains a sufficient number of molecules, where an averaging of molecular parameters results in new parameters like pressure, temperature, concentrations, density and viscosity. These new parameters can then be described by continuous functions. If, during the averaging process, the number of molecules within the considered volume is too small, the parameters will fluctuate, and no continuum can be established. The scale resulting from the application of the continuum approach on the molecular scale is referred to as the micro-scale (Bear, 1988; Helmig, 1997). For describing momentum transfer on the micro-scale, the Navier-Stokes equations can then be used (Bear, 1988). On the micro-scale different phase geometries (solid, liquid, gas) are fully resolved (see Fig. 2.1). Describing flow in a porous medium on the

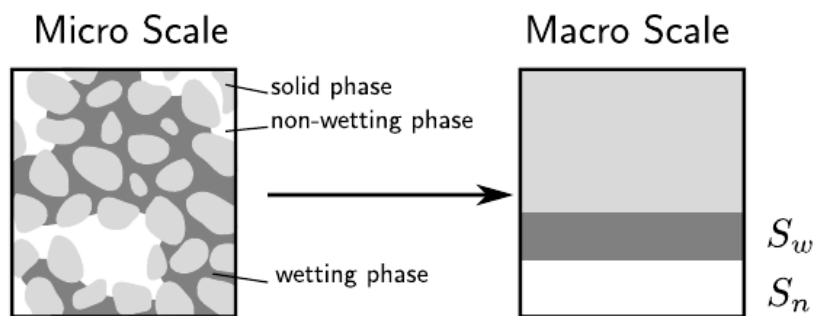


Figure 2.1.: A porous medium in the micro (left), and macro-scale perspective (right) (Nuske, 2014).

micro-scale is often not feasible, as the process of resolving the pore structure in simulations has an enormous computational demand. For small problems, simplifications of the pore and pore throat geometry may help in reducing the complexity of the problem enough such that calculations of small domains are possible. However, almost all practical applications in the

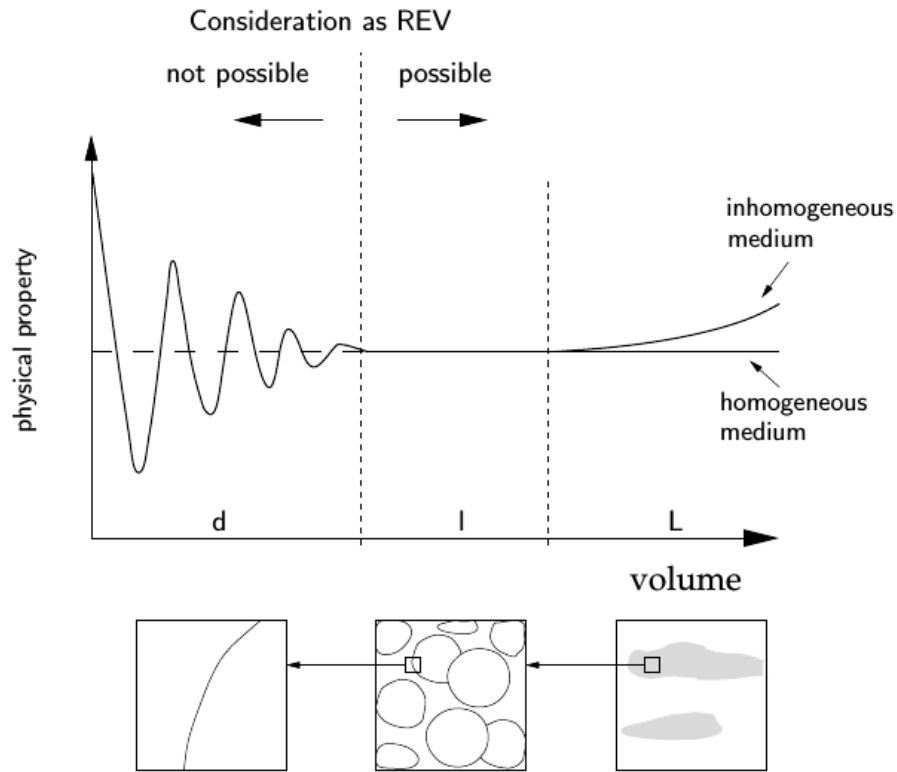


Figure 2.2.: The fluctuation of a physical property over the considered volume. The consideration as an REV is possible if fluctuations are sufficiently small. Figure from Helmig (1997), modified by (Nuske, 2014).

context of hydrogeology are solved on the so-called macro-scale. To obtain the macro-scale, the continuum approach is applied once more, averaging over a so called representative elementary volume (REV) (Bear, 1988), containing both solid and fluid phases, see Fig. 2.1. On the macro- or REV-scale, the pore geometry and the interfaces between solid and fluid phases are not longer resolved. Instead, averaged parameters such as porosity, permeability or phase saturation are introduced, and Darcy's law is often assumed to be a valid simplification of the momentum balance equation (see Sec. 3.1.1). Just as before, making the REV too small, for example in the range of a pore diameter, will lead to strong fluctuations of the REV-properties. On the other hand, if a large REV is chosen, the properties will start to change, due to heterogeneities in the porous-media system (for example layered system, fractures etc.). This is illustrated in Fig. 2.2. If heterogeneities are present, the domain can be split into different control volumes which are assumed to be valid REV's (Helmig, 1997).

2.2. Local Thermodynamic Equilibrium

As a result of averaging over the micro-scale, parameters like pressure, temperature, and concentration also have to be transferred to the macro-scale in order to describe flow and transport processes in porous media. The simplest and most common assumption here is to assume local thermodynamic equilibrium. Local thermodynamic equilibrium states that within an REV the following equilibria exist (Helmig, 1997):

- **Mechanical Equilibrium:** An equilibrium of forces is required, i.e. no resulting net force. For an REV this means that on the interface between two phases the considered forces should add up to zero. For a system with two fluid phases, the force balance contains the fluid phase pressures of the wetting (p_w), and non-wetting (p_n) phase, as well as the capillary pressure (p_c): $p_n = p_w + p_c$.
- **Thermal Equilibrium:** All temperatures of the different fluid (T_α), and solid phases (T_s) are the same, i.e. $T_s = T_\alpha = T$.
- **Chemical Equilibrium:** All components' rates of production are equal to their rates of destruction. For the distribution of a component between two phases n and w this implies that the fugacity of the component κ in each phase must be the same, i.e. $f_n^\kappa = f_w^\kappa$.

Using these assumptions greatly simplifies the solution of the resulting equations. If one were to include local non-equilibrium processes, this would require knowledge of the interfacial areas between the phases (i.e. information available only on the micro-scale). This is discussed in detail in Nuske (2014) and will not be treated further here.

2.3. Properties of the Porous Medium

2.3.1. Porosity and Compressibility of the Porous Medium

The most important characteristic of a porous medium on the macro-scale is the ratio of the volume of void space to the total volume. The resulting parameter is called porosity:

$$\phi = \frac{V_{pore}}{V_{total}}. \quad (2.1)$$

Considering only the void space that is accessible for flow leads to the definition of the so-called effective porosity. The effective porosity only considers the interconnected pores within V_{pore} (Bear, 1988). In this work, the porosity ϕ used is considered to be the effective porosity. In hydrogeology there are more definitions of porosity, such as the drainable porosity

or specific yield. In these definitions V_{pore} is the volume of water which can be drained due to gravitational forces, where a residual saturation S_{rw} of water is left behind. This value has to be equal to or smaller than the effective porosity. Defining ϕ_{total} with V_{pore} being the total void volume (interconnected and disconnected pores) the drainable porosity can be defined as (Bear, 1988):

$$\phi_{dp} = \phi_{total}(1 - S_{rw}). \quad (2.2)$$

A change in pressure may cause the bulk volume of a porous medium to change. The change can be attributed to the compressibility of the solid grains and the so-called pore compressibility (consolidation of the void space). Usually the compressibility of the solid grains is considered much smaller than the changes in porosity due to consolidation for hydrogeological problems (Bear, 1988). Hence, only the latter is considered here. The compressibility of the porous medium can be defined similar to the compressibility of a fluid:

$$C_s = \frac{1}{\phi} \frac{d\phi}{dp}. \quad (2.3)$$

Under the assumption that the compressibility C_s itself is not a function of pressure, the following dependence of porosity on pressure can be obtained after integration:

$$\phi(p) = \phi_{ini} e^{C_s(p-p_{ini})}, \quad (2.4)$$

where ϕ_{ini} and p_{ini} are the initial porosity and pressure. Using the Taylor series approximation to express the exponential function leads to the function used in this work:

$$\phi(p) = \phi_{ini} \left(1 + X + \frac{X^2}{2} \right) \quad \text{with } X = C_s(p - p_{ini}). \quad (2.5)$$

This is the same function used in Schäfer et al. (2011) for the determination of far-field pressure during long-term CO₂ storage.

2.3.2. Permeability

Flow in a porous medium at small Reynolds numbers encounters a resistive force both from the fluid and the porous medium itself. This resistive force is proportional to the specific volumetric flux. The reciprocal or inverse of the resistance caused by the porous medium is called permeability \mathbf{K} . The permeability \mathbf{K} is generally a tensor, as in most hydrogeological systems, which are often layered systems, the permeability in the lateral direction of a formation is usually much higher than the permeability in the vertical direction. This is known as anisotropy. If the permeability tensor is aligned with the coordinate axis of the system it has

a diagonal form. If isotropic conditions can be assumed, the permeability tensor reduces to a scalar value denoted here as k . If the permeability tensor varies with space, the porous medium is heterogeneous. The permeability can be obtained directly from small scale (lab experiments) or large scale (pumping test) measurements. The permeability can also be estimated from semi-empirical relations that relate porosity, and an effective grain size to the permeability (Bear, 1988).

2.4. Brine and CO₂

Mass/mole fraction, density, and viscosity are parameters obtained through averaging over the molecular scale. These parameters are used on the micro- as well as on the macro-scale. In this work, the relevant fluids are brine and CO₂. Generally, the term brine is used for saltwater with a salinity above 5 ‰. However, in this work the term brine or brine phase is also used for water with low salinities. For CO₂ injection, supercritical conditions are preferred, as CO₂ exhibits liquid- and gas-like properties. Under supercritical conditions, the density of CO₂ is greater than the density in the gaseous state, which decreases the buoyant drive, and increases storage safety. On the other hand, the viscosity is smaller than in the liquid state, which reduces the resistance during injection.

2.4.1. Components and Phases

A component is a chemically-independent species of a system, which means that its concentration cannot be determined from the presence of other independent components in the system. In this work, water (H₂O), carbon dioxide (CO₂), and salt (NaCl) are considered independent components.

On the micro-scale every point in space is occupied by a certain phase, either fluid or solid (see Fig. 2.1 left). Phases can be composed of a single component or several components. Fluid phases can be liquid or gaseous. Liquid phases always form a sharp interface with other phases, if they are not completely miscible. A gaseous phase on the other hand, does not form a sharp interface with other gaseous phases. The phases considered in this work are the liquid brine phase consisting of the components water and salt and the gaseous CO₂ phase, consisting only of the component CO₂.

2.4.2. Mole and Mass Fractions

The mole fraction x_α^κ is defined as the ratio of the number of molecules of a component κ to the total number of molecules within a phase α . A mole fraction can be converted to a mass fraction (ratio of the mass of a component κ to the total mass of a phase) through the following relation:

$$X_\alpha^\kappa = x_\alpha^\kappa \frac{M^\kappa}{\bar{M}_\alpha}, \quad (2.6)$$

where \bar{M}_α is the average molar mass of a phase. It is the weighted arithmetic mean of the molar masses M^κ of the components weighted by the mole fractions x_α^κ :

$$\bar{M}_\alpha = \sum_{\kappa} M^\kappa x_\alpha^\kappa. \quad (2.7)$$

Given $n - 1$ mole or mass fractions of a phase comprising n components the composition of the phase is defined, as the sum of the mole and mass fractions has to be one:

$$\sum_{\kappa} x_\alpha^\kappa = 1 \quad \text{and} \quad (2.8)$$

$$\sum_{\kappa} X_\alpha^\kappa = 1. \quad (2.9)$$

In this work, the term salinity is synonymous to the salt mass fraction X_w^S , where the component index S stands for salt, and the phase index w for the wetting phase brine.

2.4.3. Density

The density of a phase ϱ_α can be defined as its mass per volume. It can also be expressed in terms of moles per volume in which case it is denoted here as ϱ_α^m . If the density in terms of mass is known it can be converted to a molar density with the average molar mass:

$$\varrho_\alpha^m = \frac{\varrho_\alpha}{\bar{M}_\alpha}. \quad (2.10)$$

For the simulation of CO₂ sequestration, the density of brine is often considered a function of temperature, pressure, and the mass fractions of dissolved salt and CO₂ (Darcis, 2012; Bielinski, 2006). Assuming chemical equilibrium for the mass transfer of CO₂ and water between the brine and CO₂ phases, the mass fractions of CO₂ in brine are in the order of 1 to 6%, under relevant temperature and pressure conditions (see for example Darcis (2012)). Thus, the CO₂ mass fraction increases the brine density. This is important to consider for large time scales, where the dissolution of CO₂ is an important trapping mechanism, which

can be enhanced by convective mixing, due to density differences in the brine phase (see Sec. 2.7). However, for the applications presented in this work, where either short time scales are considered or the fate of the injected CO₂ is not the primary concern, the dissolution of CO₂ into the brine phase is not relevant, and therefore neglected.

The equation of state defined by Batzle and Wang (1992) is used for calculating the brine density. The brine density is shown in Fig. 2.3 (left). Here the brine density is shown with respect to temperature and salinity. The brine density decreases with increasing temperature. An increasing salinity has the opposite effect and increases the brine density. Although not

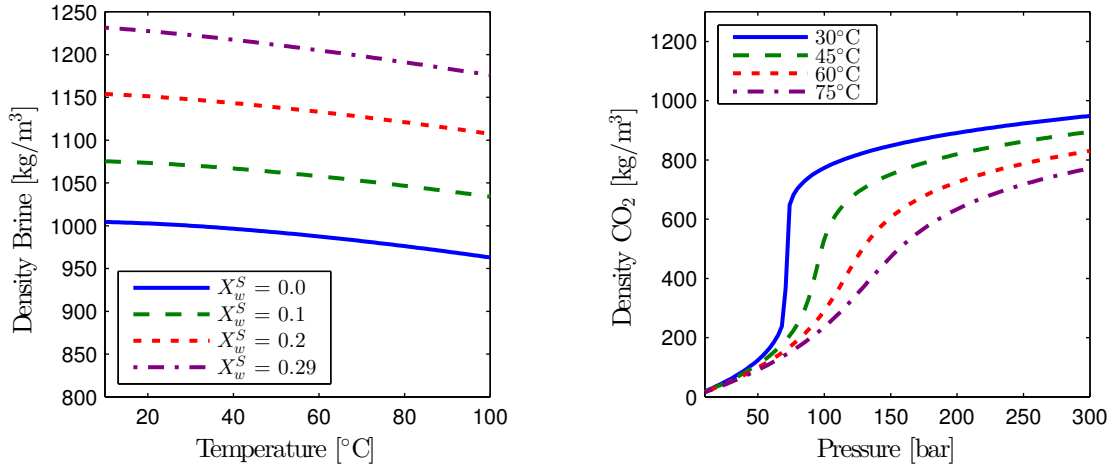


Figure 2.3.: The density of brine over temperature for different salinities (left) at a pressure of 100 bar. The density of CO₂ over pressure for different temperatures (right).

shown here the relation is, to a lesser extent, also dependent on pressure, which is important to consider, during the injection of CO₂. For this case, the increasing pressure leads to an increase of the brine density.

The CO₂ density is calculated according to the relation defined by Span and Wagner (1996). Figure 2.3 (right) shows the CO₂ density plotted over pressure for different temperatures. The density of CO₂ strongly increases close to the critical point ($T_{\text{crit}} = 31 \text{ °C}$, $p_{\text{crit}} = 7.39 \text{ MPa}$).

2.4.4. Dynamic Viscosity

The dynamic viscosity μ is the proportionality factor relating shear stress to the velocity gradient. It can be expressed as follows:

$$\tau_{yx} = \mu \frac{\partial v_x}{\partial y}, \quad (2.11)$$

where τ_{yx} is the shear stress in x-direction on a plane, whose outer normal is in y-direction, and $\frac{\partial v_x}{\partial y}$ is the velocity gradient. The dynamic viscosity will simply be referred to as viscosity from now on. For a Newtonian fluid the viscosity is not a function of the velocity gradient. Considering laminar flow in a tube, a linear relationship between the average velocity and the viscous force can be established. Similarly, for a porous medium on the macro-scale the viscous force is expressed as the resistance times the specific volumetric flux \mathbf{v} :

$$\text{Viscous Force} = \mu \mathbf{K}^{-1} \mathbf{v}, \quad (2.12)$$

where the previously introduced permeability \mathbf{K} depends on the porous medium and the viscosity depends on the fluid. For brine the viscosity is again calculated according to a relationship defined by Batzle and Wang (1992). Within this relationship the viscosity is considered to be a function of temperature and the salinity. The influence of pressure is neglected. The brine viscosity is shown in Fig. 2.4 (left). It is plotted over temperature for various salinities. The brine viscosity increases with increasing salinity and decreasing temperature. The viscosity of gases is lower than that of liquids. The viscosity of supercritical

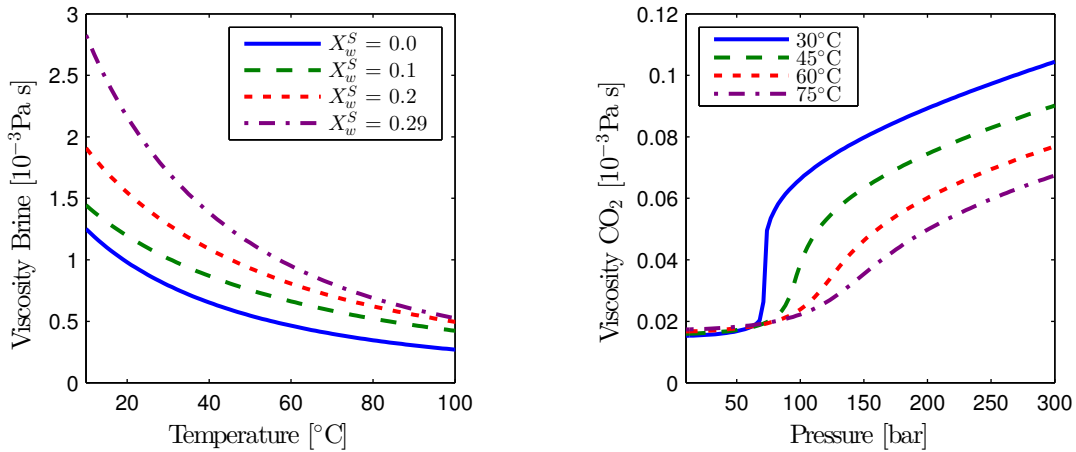


Figure 2.4.: The viscosity of brine over temperature for different salinities (left) at a pressure of 100 bar. The viscosity of CO₂ over pressure for different temperatures (right).

CO₂ is lower than the brine viscosity by roughly one order of magnitude. For CO₂ viscosity calculations, the relationship by Feghhour et al. (1998) is used. The CO₂ viscosity is plotted in Fig. 2.4 (right). A sharp increase of the CO₂ viscosity is observed close to the critical point. Temperature and pressure both have opposing effects on the CO₂ viscosity, similar to the CO₂ density. Therefore, both viscosity and density, above supercritical conditions, are almost constant over depth in hydrogeological systems, where temperature and pressure increase.

2.5. Multi-Phase Flow

2.5.1. Saturation

The pore space is filled with fluid of one or more phases. The phases can be liquid or gaseous, in this case liquid brine and supercritical CO₂. On the macro-scale, the amount of pore space occupied by a phase within an REV is called saturation S_α where α denotes the phase index:

$$S_\alpha = \frac{V_\alpha}{V_{pore}} \quad \text{with } 0 \leq S_\alpha \leq 1. \quad (2.13)$$

The sum of the saturations over all fluid phases present within an REV must be 1:

$$\sum_{\alpha} S_\alpha = 1. \quad (2.14)$$

If one phase is replaced by another phase, usually some amount of the displaced phase stays in the REV. This amount is referred to as the residual saturation $S_{r\alpha}$.

2.5.2. Capillary Pressure

The capillary pressure is defined as the pressure difference between two phases on the fluid-fluid interface:

$$p_c = p_n - p_w. \quad (2.15)$$

On the micro-scale, where the position of fluid-fluid and fluid-solid interfaces is known, a driving force evolves due to one phase's higher affinity to connect with the solid phase. The phase with the higher affinity is called the wetting phase. Considering a circular tube with water as the wetting phase (w) and air as the non-wetting phase (n), the wetting phase may rise against the gravitational force. On the micro-scale this driving force, i.e. the capillary pressure can be expressed by the Young-Laplace equation:

$$p_c = \frac{2\sigma \cos\alpha}{r}, \quad (2.16)$$

where σ is the surface tension between the two fluid phases, α is the contact angle between the wetting phase and the solid phase and r is the radius of the tube. With this equation it becomes clear that a decrease of the radius of the tube will lead to an increase in capillary pressure. To transfer the concept of capillary pressure to the macro-scale it is necessary to establish a relationship between capillary pressure and the previously introduced saturation.

One of the commonly used relations was introduced by Brooks and Corey (1964):

$$p_c = p_e \left(\frac{S_w - S_{rw}}{1 - S_{rw} - S_{rn}} \right)^{\lambda_{BC}}, \quad (2.17)$$

where p_e is the entry pressure, S_{rw} is the residual saturation of the wetting fluid and λ_{BC} is a parameter related to the pore-size distribution within the REV. The entry pressure is a threshold pressure at which the non-wetting phase can enter an REV initially saturated with the wetting phase. If the porous medium is regarded as a bundle of tubes with varying tube radii, the entry pressure can be interpreted as the capillary pressure corresponding to the largest tube radius. Figure 2.5 shows the capillary pressure-saturation relationship for the parameters also used in Sec. 4.4. Generally, the Brooks and Corey relationship is used to fit

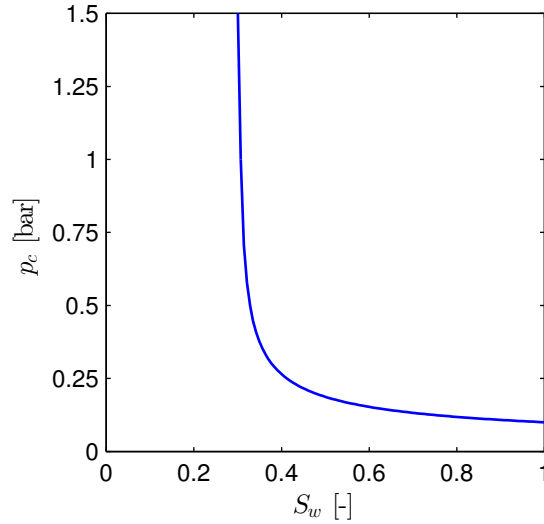


Figure 2.5.: Capillary pressure-saturation relationship for $p_e = 0.1$ bar, $\lambda_{BC} = 2.0$, $S_{rw} = 0.3$, and $S_{rn} = 0.0$. Note that the curve is regularized with a linear function at $S_w = 0.31$ to avoid unrealistically high capillary pressures.

experimental data. An experiment for the displacement of a wetting phase by a non-wetting phase in a column is a good example for explaining how a $p_c - S_w$ relationship evolves. At first, the column is fully saturated with the wetting fluid. A reservoir of wetting fluid is installed at one end and a reservoir of non-wetting fluid on the other end of the column. The pressure in the non-wetting reservoir is then increased by an increment Δp_n while the wetting pressure stays constant. If the difference between pressures is above the entry pressure, some of the non-wetting phase will enter the column, and some of the wetting phase will leave, given that the system has adequate time to equilibrate. From the amount of wetting phase leaving the column, the saturation can be obtained at a certain Δp_n . This procedure is then repeated several times until the saturation does not change anymore. With these conditions a $p_c - S_w$

relationship can be obtained, as shown in Fig. 2.5. The left over wetting phase within the column corresponds to the residual water saturation S_{rw} . If the obtained $p_c - S_w$ relationship is used as a constitutive relationship for a simulation an assumption of local capillary equilibrium or local mechanical equilibrium at all times is implicitly made. The process of the wetting phase being displaced by the non-wetting phase is called drainage. Wetting phase displacing the non-wetting phase is called imbibition. It has to be mentioned that the $p_c - S_w$ relationship is not a unique relationship. Depending on the direction of the process (imbibition or drainage) different curves will be obtained (hysteresis). Hysteresis can be important if imbibition or drainage both occur sequentially during a process for example:

- During CO₂ injection, drainage occurs. After the injection, brine will flow back towards the well (imbibition).
- Sub-surface methane storage requires injection and extraction of methane depending on supply and demand. Here drainage and imbibition follow sequentially.

For the applications considered in this work only, drainage is of importance, hence hysteresis is not considered. More information on the implementation of models accounting for hysteresis can be found for example in Papafotiou (2008).

2.5.3. Relative Permeability

When two or more phases are present in the pore space, the resistance to flow will increase compared to similar systems with only one phase. On the macro-scale, this additional resistance is integrated into the viscous force using the term relative permeability $k_{r\alpha}$. The relative permeability is a function of the phase saturation:

$$0 \leq \sum_{\alpha} k_{r\alpha}(S_{\alpha}) \leq 1. \quad (2.18)$$

On the micro-scale there are several effects that contribute to this resistance (Helmig, 1997):

- Simplifying the porous medium to a bundle of tubes, the relative permeability is proportional to the cross-sectional area available for each phase.
- Extending this analogy to a system of tubes of variable radius, either filled with wetting or non-wetting phase, the tubes with small radii are occupied by the wetting phase. Resistance against wetting phase flow is therefore increased by higher viscous forces, which

can be expressed as a function of the square of the tube radius after Hagen-Poiseuille (neglecting the gravitational force):

$$\frac{8\mu_w}{r^2}v_w = -\frac{\partial p_w}{\partial x}. \quad (2.19)$$

- Additionally, as the larger pores are occupied by the non-wetting phase the wetting phase has to flow around these large pores through smaller pores. This increases the flow path and therefore the tortuosity.

All the above micro-scale effects are represented on the macro-scale by the single parameter: relative permeability. In the general case, the relative permeability is an anisotropic tensorial quantity. Similar to the intrinsic permeability tensor, the relative permeability may change with direction, due to a heterogeneous distribution of the fluid phases. This leads to preferential flow paths. However, in most practical applications, the relative permeability of a phase is assumed to be a scalar related to the phase's saturation, as data for justifying a more complex description is usually not available. However, upscaling relative permeabilities from a highly resolved geological description to a coarse geological description, may also require the use of tensorial relative permeabilities, see for example Wolff (2013). There exist different $k_{r\alpha} - S_\alpha$ relationships, one of the most commonly used is the relationship by Brooks and Corey (1964):

$$\begin{aligned} k_{rw} &= (S_e)^{\frac{2+3\lambda_{BC}}{\lambda_{BC}}}, \\ k_{rn} &= (1 - S_e)^2 (1 - S_e)^{\frac{2+\lambda_{BC}}{\lambda_{BC}}}, \end{aligned} \quad (2.20)$$

with $S_e = \frac{S_w - S_{rw}}{1 - S_{rw} - S_{rn}}$.

The relationship is shown in Fig. 2.6 for the parameters used in Sec. 4.4. It can be seen that the relative permeability of each phase becomes zero, as the phase's residual saturation is approached. Further, k_{rw} shows a small slope for low values of S_w which can be attributed to the wetting phase occupying small pores at low saturation which contribute little to flow. By assuming that the non-wetting phase occupies the larger pores, and that the wetting phase occupies the smaller pores capillary equilibrium is implicitly assumed within an REV. The $k_{r\alpha} - S_w$ relationship is hysteretic in nature, just as the $p_c - S_w$ relationship is.

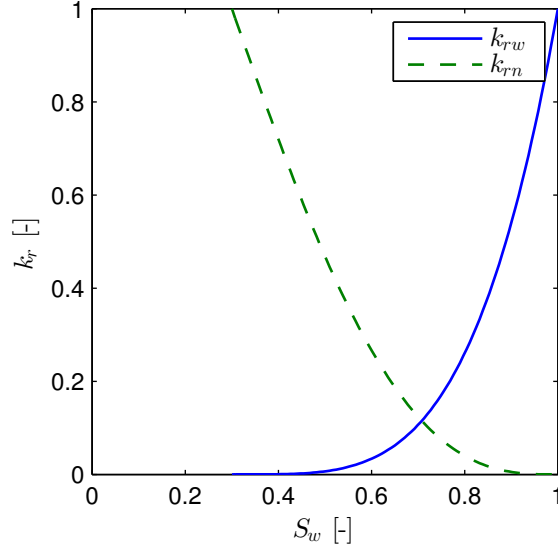


Figure 2.6.: Relative permeability-saturation relationship for $\lambda_{BC} = 2.0$, $S_{rw} = 0.3$, and $S_{rn} = 0.0$.

2.6. Transport Processes

In this section, the basic transport processes and their relevance for the further applications are presented.

2.6.1. Advection

If a fluid moves the components present in the fluid will also move with the fluid. This transport mechanism is known as advective transport or advective flow and can be expressed per unit area of a porous medium as:

$$\mathbf{J}_a^\kappa = \phi X^\kappa \varrho \mathbf{v}_a, \quad (2.21)$$

where X_κ is the mass fraction of a component, ϱ the density and \mathbf{v}_a is an average velocity of the fluid (per unit area of the fluid phase). This definition is also valid for multi-phase flow, where the components of a phase are being transported with a specific phase flux \mathbf{v}_α . In the context of CO_2 sequestration, the term advection is often used to describe the flow resulting from the injection of CO_2 , whereas the term buoyancy is used to describe gravity-induced flow, although this flow is strictly speaking also a form of advective flow.

2.6.2. Diffusion

Diffusion is a mass transport process which is caused by the Brownian motion of molecules. Considering a fluid with a dissolved component κ on the micro-scale the binary diffusive flux may be expressed in terms of a mole fraction gradient (Taylor and Krishna, 1995):

$$\mathbf{j}_{\text{diff}}^{\kappa} = -\varrho^m D_m^{\kappa} \mathbf{grad} x^{\kappa}, \quad (2.22)$$

where ϱ^m is the molar density and D_m is the molecular Diffusion coefficient. Note that the index of the solvent or fluid phase is omitted in this section. Equation 2.22 is known as Fick's law. Another common way to express Fick's law is to use the mass fraction gradient instead of a mole fraction gradient (Taylor and Krishna, 1995; Diersch and Kolditz, 2002; Bear, 2005). On the macro-scale, a diffusive flux per unit volume of the porous medium can be obtained by averaging Eq. 2.22 (Bear, 2005):

$$\mathbf{J}_{\text{diff}}^{\kappa} = \overline{\mathbf{j}_{\text{diff}}^{\kappa}} = -\phi \varrho^m \mathbf{T}(\phi) D_m^{\kappa} \mathbf{grad} x^{\kappa}, \quad (2.23)$$

where $\mathbf{T}(\phi)$ is the tortuosity tensor, defined by a function of the porosity ϕ . In this work, an isotropic medium is assumed and the tortuosity is simplified to ϕ . Finally, the macro-scale diffusion coefficient of the porous medium is defined as:

$$D_{pm}^{\kappa} = \phi^2 D_m^{\kappa}. \quad (2.24)$$

2.6.3. Mechanical Dispersion

Mechanical dispersion leads to the spreading of a dissolved component within a moving fluid in a porous medium. The term mechanical indicates that dispersion (spreading) only takes place if the fluid is moving with an average velocity \mathbf{v}_a (per unit area of the fluid phase). On the micro-scale the evolving velocity distribution of a fluid in a pore (parabolic in case of laminar flow) will lead to varying velocities in magnitude over the cross-section of the pore. Molecular diffusion will act mainly in the direction normal to the streamlines in order to equilibrate the arising concentration gradients. Additionally, the structure of the interconnected pore space will lead to deviations from the mean direction of flow. Both these effects lead to an increased spreading. When averaging over an REV, these effects lead to an additional so-called dispersive flux. Bear (2005) introduces another scale, larger than the macro-scale, to arrive at a new continuum, referred to as megascopic-scale. On this scale, the effects of macro-scale heterogeneities are described through macro dispersion. The formulation of dispersion on the megascopic-scale can be defined in the same way as for the macro-scale. The following

formulation of dispersive flux per unit area of porous medium is often used independent of the scale:

$$\mathbf{J}_{\text{disp}}^\kappa = -\phi \varrho^m \mathbf{D}_{\text{disp}} \mathbf{grad} x^\kappa, \quad (2.25)$$

where \mathbf{D}_{disp} is the hydrodynamic dispersion tensor. It can be formulated depending on the direction of the average fluid velocity \mathbf{v}_a :

$$\mathbf{D}_{\text{disp}} = \frac{\mathbf{v}_a \otimes \mathbf{v}_a}{|\mathbf{v}_a|} (\alpha_l - \alpha_t) + \mathbf{I} (\phi D_m^\kappa + \alpha_t |\mathbf{v}_a|), \quad (2.26)$$

where α_l and α_t are the longitudinal and transversal dispersivities, respectively. α_l is a measure for the scale of the heterogeneities of the problem. According to Bear (2005) the choice of this parameter thus depends on the scale of the problem, as the dimension of the “sub-scale“ heterogeneities, i.e. the heterogeneities not resolved, will increase if the scale of the problem increases. He states further that $\alpha_l = L/10$, where L is the size of the domain of interest, can be a first guess. Similarly, he roughly approximates α_t to be $\alpha_l/10$. Notice that in Eq. 2.26 the diffusive flux is already included.

2.7. Variable-Density Flow

In many applications, the density of a fluid phase cannot be considered uniform, within the domain of interest. This variability in density needs to be considered in the gravity or buoyancy term of the momentum balance. A system of equations describing single-phase, variable-density flow is generally fully coupled and non-linear, as the density and the viscosity are functions of temperature, salinity, and pressure. For example, the density of brine is mainly a function of temperature and salinity (see Fig. 2.3). This has the consequence that the bulk brine flow, depending on the brine density, cannot be treated independently from the transport of salt or heat.

Variable-density flow can be stable or unstable. Unstable situations arise if heavy fluid is situated above lighter fluid. In the context of CO₂ sequestration such situations may occur if brine, fully saturated with CO₂ at the CO₂ plume, is situated above lighter brine without dissolved CO₂, see for example Gläser (2011). If no other external forces act, which is the case after the injection is over, free convection may occur, where the fluid flow is driven entirely by density differences. However, if dispersive flow is large compared to the density-driven flow, the front can stabilize. The dimensionless Rayleigh Number describes the ratio of density-driven flow and dispersive flow. The Rayleigh number is used as a measure of stability (Diersch and

Kolditz, 2002):

$$Ra = \frac{dk\Delta\varrho g}{\mu D}, \quad (2.27)$$

where d is a characteristic system height. In a homogeneous horizontally aligned aquifer, a natural choice for d would be the aquifer thickness. D stands for the magnitude of dispersive fluxes arising either from thermal diffusivity or hydrodynamic dispersion of a dissolved component ($\|\mathbf{D}_{\text{disp}}\|$). The remaining term $\left(\frac{k\Delta\varrho g}{\mu}\right)$ can be interpreted as gravitationally induced flux, due to density differences.

In this work, stable conditions are assumed, where the brine density increases with depth, due to an increase of salinity. In the model presented in Chapter 5, a stable layering is combined with advective flow, caused by groundwater recharge and the injection of super-critical CO_2 . A similar situation is considered in the experiments conducted by Oswald and Kinzelbach (2004). They set up experiments, better known as the saltpool benchmark, whose results are widely used to validate numerical models (Bastian et al., 2001; Diersch and Kolditz, 2002; Johannsen et al., 2002). These experiments deal with upconing as a result of water extraction in an initially stably layered system, with freshwater on top and salt water below. The salinity of the bottom layer is varied. The higher the salinity in the bottom layer, the higher the non-linearities, and the more challenging the problem becomes for the numerical simulator. Results of this benchmark will be shown in Sec. 5.4.2. Besides the brine density, the viscosity of brine is also a function of salinity and the temperature, and therefore affects the flow field. Magri et al. (2009a) who consider a comparable hydrogeological system as in Chapter 5, state that the effect of a variable viscosity has a significant impact on the overall flow field.

3. Model Concepts

In this chapter, the balance equations and solution methods that are applied in Chapters 4 and 5 will be presented. To start, all relevant balance equations will be briefly introduced without thorough derivation (Sec. 3.1). Following this, analytical and numerical solution methods are explained in Sec. 3.2 and 3.3.

3.1. Balance Equations

The mass balance equations for a single-phase two-component model (1p2c), a two-phase model (2p) without component transport, and two-phase three-component model (2p3c) are shown in this section, along with the generalization of Darcy's law. Additionally, the fractional-flow formulation, and the sharp-interface formulation are derived from the 2p balance equations.

3.1.1. Momentum Balance Equation

The hydrogeological systems under consideration in this work are described as a porous-media system, assuming laminar flow throughout. The inertial force (convective and local) is assumed to be much smaller than the viscous force. Additionally, the viscous force (i.e. the resistive force opposite to the flow direction) is proportional to the specific volumetric flux. This type of flow is also known as creeping flow (Bear, 1988). The resulting momentum balance, also called Darcy's law, allows the explicit solution of the specific volumetric flux \mathbf{v}_f (per unit area of the porous medium):

$$\mathbf{v}_f = -\frac{\mathbf{K}}{\mu} (\mathbf{grad} p - \varrho \mathbf{g}). \quad (3.1)$$

\mathbf{v}_f is also referred to as the filter or the Darcy velocity. If ϱ and μ are assumed constant the relationship between the specific volumetric flux and the pressure gradient is linear, just as in a potential flow. This is advantageous, as the solution of a complex flow problem can be achieved by superimposing the solutions of simpler subproblems. Darcy's law was originally derived from 1D column experiments, thus Eq. 3.1 is a generalization of Darcy's law, which is applicable to 3D flow in anisotropic media in terms of pressure instead of hydraulic head (Bear,

1988). Whether Darcy's law is a valid assumption or not can be tested with the dimensionless Reynolds number, a ratio of inertial and viscous forces:

$$Re = \frac{\varrho d |\mathbf{v}_f|}{\mu}. \quad (3.2)$$

Here, d is defined as a characteristic grain diameter such as for example d_{10} , (i.e. the grain size exceeding 10 % of the other diameters by weight). Bear (1988) concludes that an effective upper limit of validity of Darcy's law, for the cases reported in literature, would be a Reynolds number between 1 and 10. It is assumed that this condition is fulfilled in this work. For convenience, the specific volumetric flux \mathbf{v}_f will be referred to as \mathbf{v} from now on. Equation 3.1 can be further extended to account for the flow of multiple mobile phases in the pore space (Helmig, 1997):

$$\mathbf{v}_\alpha = -\frac{k_{r\alpha} \mathbf{K}}{\mu_\alpha} (\mathbf{grad} p_\alpha - \varrho_\alpha \mathbf{g}). \quad (3.3)$$

Here, every phase has its own specific volumetric flux \mathbf{v}_α and the additional resistance caused by multiple phases present in the pore space is accounted for by the term relative permeability $k_{r\alpha}$, previously introduced in Sec. 2.5.3.

3.1.2. Mass Balance Equations

The following section will present the different mass balance equations that will be used in this work. The generalization of Darcy's law, described in the last section, is directly inserted into all mass balance equations.

One-Phase Two-Component Formulation (1p2c)

First the mole balance or continuity equation for a single phase without additional components is formulated:

$$\frac{\partial(\phi \varrho_w^m)}{\partial t} = \text{div} \left\{ -\varrho_w^m \frac{\mathbf{K}}{\mu_w} (\mathbf{grad} p_w - \varrho_w \mathbf{g}) \right\} + q_w. \quad (3.4)$$

The mole balance equation is written in terms of the brine phase (index w). ϱ^m is a molar density whereas ϱ denotes the mass density. In the storage term, the porosity ϕ as a function of pressure, is considered using Eq. 2.5. Further, the density of brine in the storage term is a function of pressure, temperature, and salinity, see Sec. 2.4.3. q_w represents a molar source or sink term for the brine phase.

Using Eq. 3.4 as a total mole balance, another equation is needed to describe the transport of the component salt:

$$\frac{\partial(\phi \varrho_w^m x_w^S)}{\partial t} = \text{div} \left\{ -\varrho_w^m x_w^S \frac{\mathbf{K}}{\mu_w} (\mathbf{grad} p_w - \varrho_w \mathbf{g}) - \phi \varrho_w^m \mathbf{D}_{\text{disp}} \mathbf{grad} x_w^S \right\} + q^S. \quad (3.5)$$

Here, x_w^S is the mole fraction of salt in the brine phase. The equation considers the advective transport of salt and includes a term accounting for dispersive fluxes, as discussed in Sec. 2.6.3. Equations 3.4 and 3.5 together form the 1p2c balance equations. Another equation is required to close the system (previously discussed in Sec. 2.4.2):

$$\sum_{\kappa} x_{\alpha}^{\kappa} = 1. \quad (3.6)$$

This equation relates the mole fractions within a phase and is valid for all compositional models.

Two-Phase Formulation (2p)

The mass balance equations for two-phase immiscible flow are formulated as follows:

$$\phi \frac{\partial(\varrho_{\alpha} S_{\alpha})}{\partial t} = \text{div} \left\{ -\varrho_{\alpha} \frac{k_{r\alpha}}{\mu_{\alpha}} \mathbf{K} (\mathbf{grad} p_{\alpha} - \varrho_{\alpha} \mathbf{g}) \right\} + q_{\alpha} \quad (3.7)$$

$$\alpha \in \{w, n\}.$$

They consist of two mass balance equations: one for the wetting phase brine (w) and one for the non-wetting phase CO₂ (n). The multi-phase flow extension of Darcy's law (Eq. 3.3) is used. Near the injection well, the total compressibility is dominated by the compressibility of CO₂. The 2p model will be used to describe the propagation of the CO₂ front near the injection well. Far-field pressure buildup is therefore less relevant (Chapter 4). Thus, the 2p model does not consider the compressibility of the porous medium, meaning that ϕ is not included in the time derivative of the storage term. q_{α} is a source or sink term for phase α . Here, two additional closing relations are required for relating wetting and non-wetting phase pressures through the capillary pressure:

$$p_n = p_w + p_c, \quad (3.8)$$

and for relating the wetting and non-wetting phase saturation:

$$\sum_{\alpha} S_{\alpha} = 1. \quad (3.9)$$

Two-Phase Fractional-Flow Formulation

The two-phase balance equations can be reformulated into a pressure and a saturation transport equation. For a more thorough derivation, see Helmig (1997).

Assuming incompressibility, which requires the division of Eq. 3.7 by the phase density ϱ_α and the summation of the wetting and non-wetting mass balances, the following equation is obtained:

$$\operatorname{div} \mathbf{v}_w + \operatorname{div} \mathbf{v}_n + q_w + q_n = 0. \quad (3.10)$$

Now a total phase flux \mathbf{v}_t can be introduced. This is the sum of the fractional fluxes, i.e. the individual phase velocities:

$$\mathbf{v}_t = \mathbf{v}_w + \mathbf{v}_n. \quad (3.11)$$

Hence, Eq. 3.10 becomes:

$$\operatorname{div} \mathbf{v}_t + q_t = 0, \quad (3.12)$$

where q_t is the sum of the wetting and non-wetting source terms. This equation is known as the pressure equation. The next step is to insert both phase velocities from Eq. 3.3 into Eq. 3.11. Using the closing relation $p_n = p_w + p_c$, one of the pressures can be replaced. In this case, p_n is replaced:

$$\mathbf{v}_t = -\mathbf{K} (\lambda_w + \lambda_n) \mathbf{grad} p_w + \lambda_n \mathbf{grad} p_c - (\lambda_w \varrho_w + \lambda_n \varrho_n) \mathbf{g}. \quad (3.13)$$

To simplify the notation, phase mobilities, $\lambda_w = \frac{k_{rw}}{\mu_w}$ and $\lambda_n = \frac{k_{rn}}{\mu_n}$, are introduced. Further, the total mobility $\lambda_t = \lambda_w + \lambda_n$ and the fractional flow function $f_\alpha = \frac{\lambda_\alpha}{\lambda_t}$ are defined. After several reformulation steps, the following relation for \mathbf{v}_t can be obtained:

$$\mathbf{v}_t = -\lambda_t \mathbf{K} \left(\mathbf{grad} p_w + f_n \mathbf{grad} p_c - (f_w \varrho_w + f_n \varrho_n) \mathbf{g} \right). \quad (3.14)$$

In order to obtain the saturation equations, the phase velocities \mathbf{v}_α have to be expressed in terms of the total velocity. To solve the system of equations with two unknowns (one phase pressure and one phase saturation) only one saturation equation is required together with the pressure equation. Here, the saturation equation for the wetting phase is derived. Solving Eq. 3.3 for $\mathbf{K} \mathbf{grad} p_w$ and inserting this into Eq. 3.14 yields:

$$\mathbf{v}_w = f_w \mathbf{v}_t - \lambda_n f_w \mathbf{K} \mathbf{grad} p_c - \lambda_n f_w (\varrho_w - \varrho_n) \mathbf{K} \mathbf{g}. \quad (3.15)$$

Inserting Eq. 3.15 into Eq. 3.7 and again assuming incompressibility results in the saturation equation:

$$\phi \frac{\partial S_w}{\partial t} = \text{div} \left\{ f_w \mathbf{v}_t - \lambda_n f_w \mathbf{K} \mathbf{grad} p_c - \lambda_n f_w (\varrho_w - \varrho_n) \mathbf{K} \mathbf{g} \right\} + q_w. \quad (3.16)$$

Equations 3.12 and 3.16 make up the fractional-flow formulation. In order to better distinguish the dominant driving forces, the dimensions are removed following the approach by Kopp et al. (2009a). At first, three independent characteristic values have to be defined:

- l_{cr} = system length or width of a saturation front,
- v_{cr} = characteristic Darcy velocity, and
- p_{cr} = capillary-pressure drop over the system length or width of a saturation front.

Using these characteristic values, the following terms are non-dimensionalized:

$$\widehat{\text{div}} = \text{div} l_{cr}, \quad \widehat{\mathbf{grad}} = \mathbf{grad} l_{cr}, \quad \hat{t} = \frac{t v_{cr}}{\phi l_{cr}}, \quad \hat{p}_c = \frac{p_c}{p_{cr}}, \quad \hat{\mathbf{v}}_t = \frac{1}{v_{cr}} \mathbf{v}_t. \quad (3.17)$$

Now the dimensions of the saturation equation (Eq. 3.16) are removed. Additionally, isotropic conditions are assumed and \mathbf{g} is replaced by $g \widehat{\mathbf{grad}} \hat{z}$:

$$\frac{\partial S_w}{\partial \hat{t}} = \widehat{\text{div}} \left\{ f_w \hat{\mathbf{v}}_t - \frac{\lambda_n f_w k p_{cr}}{v_{cr} l_{cr}} \widehat{\mathbf{grad}} \hat{p}_c - \lambda_n f_w (\varrho_w - \varrho_n) k g \widehat{\mathbf{grad}} \hat{z} \right\}. \quad (3.18)$$

Finally, the capillary (Ca) and gravitational numbers (Gr) along with another dimensionless parameter C are introduced:

$$Ca = \frac{k p_{cr}}{\mu_n v_{cr} l_{cr}}, \quad Gr = \frac{(\varrho_w - \varrho_n) g k}{\mu_n v_{cr}}, \quad C = k_{rn} f_w. \quad (3.19)$$

Ca and Gr will be discussed further in Chapter 4. Inserting these dimensionless numbers into the saturation equation yields:

$$\frac{\partial S_w}{\partial \hat{t}} = \widehat{\text{div}} \left\{ f_w \hat{\mathbf{v}}_t - C Ca \widehat{\mathbf{grad}} \hat{p}_c - C Gr \widehat{\mathbf{grad}} \hat{z} \right\}. \quad (3.20)$$

Note that Ca and Gr could also be defined with the brine viscosity term in the denominator, if C were defined as $C = k_{rw} f_n$. Similar to the saturation equation, the pressure equation (Eq. 3.12) can also be non-dimensionalized using the above dimensionless numbers. Further analysis on this topic can be found in Kopp et al. (2009a).

Two-Phase Sharp-Interface Formulation

Another formulation of the two-phase flow balance equations (Eq. 3.7) exists when assuming vertical equilibrium. Vertical equilibrium is based on the Dupuit assumption, where vertical fluxes are neglected. The assumption is valid if the lateral extent of a formation is much larger than its vertical extent. This is usually the case for saline aquifers, where CO_2 can be stored. An exception is the area close to the injection well, where the values of the gravitational number (Gr) are very low and the viscous forces dominate. If solved numerically, the main advantage of the vertical-equilibrium assumption is that the system is reduced to two dimensions. However, for specific cases as presented below, the formulation can be further reduced from a system of non-linear partial differential equations to a system of non-linear ordinary differential equations. The approach presented in Nordbotten and Celia (2006) is used for the derivation of a sharp-interface model. As the aim is to show the main assumptions and explain the resulting equations, the derivation will not be in full detail. For a more thorough derivation see Nordbotten and Celia (2006).

Due to the vertical-equilibrium assumption, the CO_2 is assumed to immediately gather below the top of the injection layer with two domains forming: the brine domain, and the CO_2 domain. Both domains are separated by a sharp interface. Such a system is shown in Fig. 3.1. The brine domain is fully saturated with brine, while the CO_2 domain contains both the

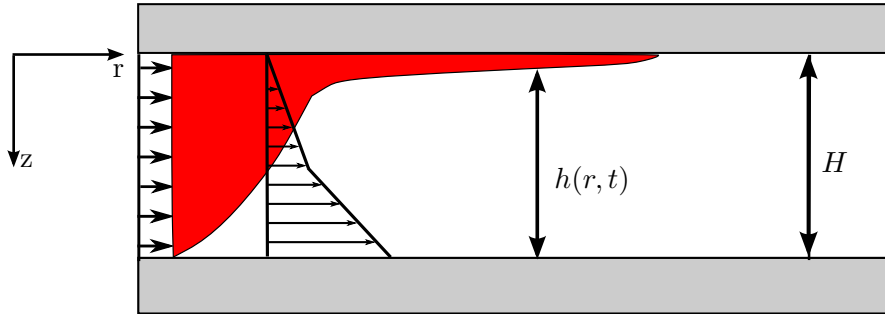


Figure 3.1.: Injection of CO_2 in a confined aquifer. The vertical pressure distribution is assumed hydrostatic for the sharp interface model.

CO_2 and the residual brine, i.e. $S_n = (1 - S_{rw})$. As saturations within the two domains are fixed, the relative permeabilities ($k_{r\alpha}$) are constant, considerably simplifying the problem. For simplifying Eq. 3.7 further, the following assumptions are made:

- a radially symmetric domain with an injection well at the center,
- the top and bottom of the injection formation are orthogonal to the gravity vector,
- the system is incompressible,

- and the material parameters are constant in the vertical direction, meaning no averaging procedure is required to determine effective parameters.

Vertically integrating Eq. 3.7, where each phase is integrated over its cross-sectional area A_α , leads to:

$$\phi(1 - S_{rw}) \frac{\partial A_\alpha}{\partial t} = \text{div}(A_\alpha \mathbf{v}_\alpha) + q_\alpha. \quad (3.21)$$

The term $\phi(1 - S_{rw})$ is found in both balance equations. Nordbotten and Celia (2006) define it similar to the drainable porosity ϕ_{dp} (see Sec. 2.3.1), namely as a measure of the pore space being invaded by a CO₂ front. Due to radial symmetry, the divergence operator can be replaced by $\frac{\partial}{\partial r}$ and A_α can be replaced by $r(H - h(r, t))$ for the wetting phase and $rh(r, t)$ for the non-wetting phase respectively. Additionally, \mathbf{v}_α is replaced by $-\lambda_\alpha k \frac{\partial p_\alpha}{\partial r}$ which yields:

$$-\frac{\partial h}{\partial t} = \frac{\lambda_w k}{\phi_{dp} r} \frac{\partial}{\partial r} \left\{ -r(H - h) \frac{\partial p_w}{\partial r} \right\} \quad \text{and} \quad (3.22)$$

$$\frac{\partial h}{\partial t} = \frac{\lambda_n k}{\phi_{dp} r} \frac{\partial}{\partial r} \left\{ -rh \frac{\partial p_n}{\partial r} \right\}. \quad (3.23)$$

Equations 3.22 and 3.23 form a system of partial differential equations with three unknowns h, p_w and p_n . To reduce the number of unknowns, a relation between the pressures p_w and p_n is needed. Here, Nordbotten and Celia (2006) again make use of the vertical-equilibrium assumption, which states that vertical fluxes are neglected. This means that a hydrostatic pressure distribution is established at all times (see Fig. 3.1). With this, only one pressure is required for any position r to reconstruct the wetting phase and the non-wetting phase pressures in vertical direction. The pressure used for reconstruction is chosen to be the wetting phase pressure (p_w) at the bottom of the domain ($h = H$). Choosing the non-wetting phase pressure p_n to be the pressure at the top ($h = 0$), results in the following equations:

$$p_w = p(r, t, H), \quad (3.24)$$

$$p_n = p(r, t, 0) = p_w - (H - h)\varrho_w g - h\varrho_n g \quad \text{and} \quad (3.25)$$

$$\frac{\partial p_n}{\partial r} = \frac{\partial}{\partial r} \left(p_w + (\varrho_w - \varrho_n) h g \right). \quad (3.26)$$

Inserting Eq. 3.26 into Eq. 3.23 leads to one less unknown:

$$\frac{\partial h}{\partial t} = \frac{\lambda_n k}{\phi_{dp} r} \frac{\partial}{\partial r} \left\{ -rh \frac{\partial}{\partial r} \left(p_w + (\varrho_w - \varrho_n) h g \right) \right\}. \quad (3.27)$$

Equation 3.27 includes the effect of buoyant forces on the propagation of the CO₂ tongue. This effect is referred to as the buoyant drive. If density differences are high, this will result in an increased front propagation velocity, and a thinner CO₂ tongue. Summing up Eq. 3.22 and

3.27 and integrating the resulting equation from 0 to r yields:

$$const = kr \left\{ (H - h)\lambda_w \frac{\partial p_w}{\partial r} + h\lambda_n \frac{\partial}{\partial r} (p_w + (\rho_w - \rho_n)hg) \right\}. \quad (3.28)$$

Here, the integration constant can be physically interpreted as a total flow in the radial direction. The assumption of a constant injection rate Q_{well} leads to the integration constant $-\frac{Q_{well}}{2\pi}$. Inserting the integration constant, solving the equation for $\frac{\partial p_w}{\partial r}$, and inserting it into Eq. 3.22 leads to the following equation:

$$\frac{\partial h}{\partial t} = \frac{\lambda_w k \Delta \rho g}{\phi_{dp} r} \frac{\partial}{\partial r} \left\{ \frac{r(H - h)h\lambda_n}{(H - h)\lambda_w + h\lambda_n} \frac{\partial h}{\partial r} + \frac{(H - h)Q_{well}}{2\pi k((H - h)\lambda_w + h\lambda_n)} \frac{1}{\Delta \rho g} \right\}, \quad (3.29)$$

which is a non-linear partial differential equation with the unknown h . In their derivation of a self-similar solution for $h(r, t)$, Nordbotten and Celia (2006) bring Eq. 3.29 into a dimensionless form. Further, they introduce a scaling variable χ which they use in order to find a stationary solution that satisfies a non-linear ordinary differential equation. The steps used to obtain this equation are not shown here. The presentation is restricted to showing the resulting equation:

$$0 = \chi - \left[1 + \Gamma \lambda \chi \frac{\partial (h')^2}{\partial \chi} \right] \frac{2\lambda}{(1 + (\lambda - 1)h'^2)} + 4\Gamma \lambda \frac{1 - h'}{1 + (\lambda - 1)h'} \left[h' + \chi \frac{\partial h'}{\partial \chi} + h' \chi \frac{\partial^2 h'}{\partial \chi^2} \left(\frac{\partial h'}{\partial \chi} \right)^{-1} \right]. \quad (3.30)$$

Within this equation the following dimensionless variables are defined:

$$\Gamma = \frac{2\pi \Delta \rho g k \lambda_w H^2}{Q_{well}}, \quad \lambda = \frac{\lambda_n}{\lambda_w}, \quad h' = \frac{h}{H}, \quad (3.31)$$

$$\tau = \frac{Q_{well} t}{2\pi H k \phi_{dp}}, \quad \eta = \frac{r}{\sqrt{k}}, \quad \chi = \frac{\eta}{\tau},$$

where Γ is a different formulation of the gravitational number and χ is the remaining independent variable which is the ratio of dimensionless space and time. Equation 3.30 is valid for $\left(\frac{\partial h'}{\partial \chi}\right) \neq 0$, which physically means that the CO₂ tongue has to become thinner (monolithically) for increasing χ . If Γ becomes small, for example due to a high injection rate, Eq. 3.30 can be solved explicitly for h' with:

$$h' = \begin{cases} 1 & \text{for } \chi \leq \frac{2}{\lambda}, \\ \frac{1}{\lambda-1} \left(\sqrt{\frac{2\lambda}{\chi}} - 1 \right) & \text{for } \frac{2}{\lambda} < \chi < 2\lambda, \\ 0 & \text{for } \chi \geq 2\lambda. \end{cases} \quad (3.32)$$

Here, the dimensionless height of the CO₂ front depends solely on the viscosity ratio. For large

Γ , the ordinary differential equation (Eq. 3.30) has to be solved numerically. This requires that the following boundary conditions are fulfilled:

- an outer radius r_{max} where $h = 0$ exists,
- and the volume balance:

$$\int_0^{r_{max}} \phi_{dp} h(r, t) 2\pi r dr = Q_{well} t \quad \text{or} \quad \int_0^{\chi_{max}} h'(\chi) d\chi = 2 \quad (3.33)$$

is satisfied.

Equations 3.30 and 3.33 are a system of non-linear ordinary differential equations that have to be solved for $h'(\chi)$ numerically.

Two-Phase Three-Component Formulation (2p3c)

The most complex model used in this work accounts for two-phase miscible flow and three-component transport. One mole balance equation for each of the three components is formulated:

$$\begin{aligned} \frac{\partial(\phi \sum_{\alpha} \varrho_{\alpha}^m x_{\alpha}^{\kappa} S_{\alpha})}{\partial t} = & \\ \sum_{\alpha} \text{div} \left\{ -\varrho_{\alpha}^m x_{\alpha}^{\kappa} \frac{k_{r\alpha}}{\mu_{\alpha}} \mathbf{K}(\mathbf{grad} p_{\alpha} - \varrho_{\alpha} \mathbf{g}) - \varrho_{\alpha}^m D_{pm, \alpha}^{\kappa} \mathbf{grad} x_{\alpha}^{\kappa} \right\} & \quad (3.34) \\ + q^{\kappa} & \\ \alpha \in \{w, n\} \quad \text{and} \quad \kappa \in \{H_2O, CO_2, S\}. & \end{aligned}$$

In this system, the fluid phases are brine (w) and CO₂ (n), and the components are water, CO₂, and salt. However, for the application in mind, the dissolution of CO₂ in brine and vice versa is neglected as the fate of the CO₂ is not the primary interest. Similarly, the salt component is only considered in the brine phase. As a result, the brine phase consists only of water and salt, and the CO₂ phase only of CO₂. The compressibility of the porous medium as well as the two fluid phases are considered. The flux term considers advection as well as molecular diffusion. Equations 3.6, 3.8 and 3.9 are required as closing relations.

3.2. Analytical Methods

In this section, analytical solutions for some of the formulations above are presented. These solutions are applicable when the physics and the geometry of a problem are significantly

simplified. On the one hand, they can be used for making fast predictions if the available data is not sufficient for more complex approaches, or if the computational demand is too high for numerical models. On the other hand, analytical solutions can be used to verify numerical models, i.e. to see if the implementation of a numerical model is correct.

3.2.1. Analytical Solution for Estimating the Volumetric CO₂ Storage Efficiency

Okwen et al. (2010) presented an analytical solution for calculating the volumetric storage efficiency of a radially symmetric reservoir with a vertical injection well, a constant injection rate, homogeneous permeability and porosity, and constant fluid parameters. This method will be referred to here as the Okwen-Method. The Okwen-Method is based on the previously introduced non-linear ODE (Eq. 3.30) derived by Nordbotten and Celia (2006). Therefore, the underlying assumption of a vertical equilibrium and a sharp interface between the CO₂ and brine phase (i.e. no capillary fringe and no mass transfer between the two phases) is also made here. The aim of this method is to determine the volumetric storage efficiency, which is defined as:

$$E = \frac{V_{\text{injected}}}{V_{\text{formation}}} = \frac{Q_{\text{well}}t}{\phi_{dp}2\pi H(r_{\text{max}})^2}. \quad (3.35)$$

Here V_{injected} is the injected volume of CO₂ and $V_{\text{formation}}$ is the available pore space in the reservoir. Okwen et al. (2010), like Nordbotten and Celia (2006), show that for small gravitational numbers the volumetric storage efficiency becomes independent of the gravitational number and depends only on the mobility ratio (λ) and the residual saturation of brine (S_{rw}). They use the definition of the gravitational number Γ shown in Eq. 3.31, defined by Nordbotten and Celia (2006), which includes the mobility of brine instead of CO₂. Inserting the definitions of dimensionless space (η) and time (τ) given in Eq. 3.31 into Eq. 3.35 yields:

$$E = \frac{(1 - S_{rw})\tau_{\text{max}}}{\eta_{\text{max}}^2} = \frac{(1 - S_{rw})}{\chi_{\text{max}}}. \quad (3.36)$$

As mentioned previously, χ_{max} can be calculated explicitly with Eq. 3.32 if Γ is sufficiently small. If gravitational forces cannot be neglected, Eq. 3.30 has to be solved numerically together with Eq. 3.33. To avoid this, the Okwen-Method uses a polynomial function with Γ and λ as independent variables to explicitly calculate the volumetric storage efficiency when gravitational forces are not negligible. For this, they solved the non-linear ordinary differential equation (Eq. 3.30) to obtain χ_{max} for different values of Γ ($0.5 \leq \Gamma \leq 50$) and λ ($5 \leq \lambda \leq 20$) and fitted the results with a polynomial.

The resulting equation for estimating storage efficiency E according to the Okwen-Method is:

$$E = (1 - S_{rw}) \frac{1}{\lambda} \quad 0 \leq \Gamma < 0.5,$$

$$E = \frac{2(1 - S_{rw})}{(0.0324\lambda - 0.0952)\Gamma + (0.1778\lambda + 5.9682)\Gamma^{1/2} + 1.6962\lambda - 3.0472}, \quad (3.37)$$

$$0.5 \leq \Gamma \leq 50.$$

Storage efficiency in terms of mass per volume can easily be obtained by multiplying E with the density of CO₂ under reservoir conditions.

3.2.2. Single-Phase Injection in a Multi-Layer System with a Fault Zone

In this section, an analytical solution for determining leakage, due to brine injection in a multi-layer aquifer system, whose layers are connected by a fault zone, is presented. The analytical solution is based on the solution presented by Shan et al. (1995) for a two layer system, and was extended by Zeidouni (2012) to account for the following conditions:

- a pressure jump across the fault plane,
- the inclusion of multiple aquifers above the injection layer.

The analytical solution will be referred to here as the Zeidouni-Method.

The set of governing equations is a simplification of Eq. 3.4. It is derived by assuming a constant brine density and viscosity, a constant aquifer thickness, and a homogeneous permeability and porosity in each aquifer. Vertical fluxes in the aquifers are neglected based on the Dupuit assumption, except for the fault zone where vertical leakage may occur. The fault zone itself is assumed to have no storage, and is aligned with the y -axis. The injection layer and each overlying aquifer is split into two regions for each side of the fault plane, see Fig. 3.2. The governing equations for the injection layer and the overlying aquifers are denoted by the first index j for the aquifer number, with $j = 1$ for the injection layer, and the second index

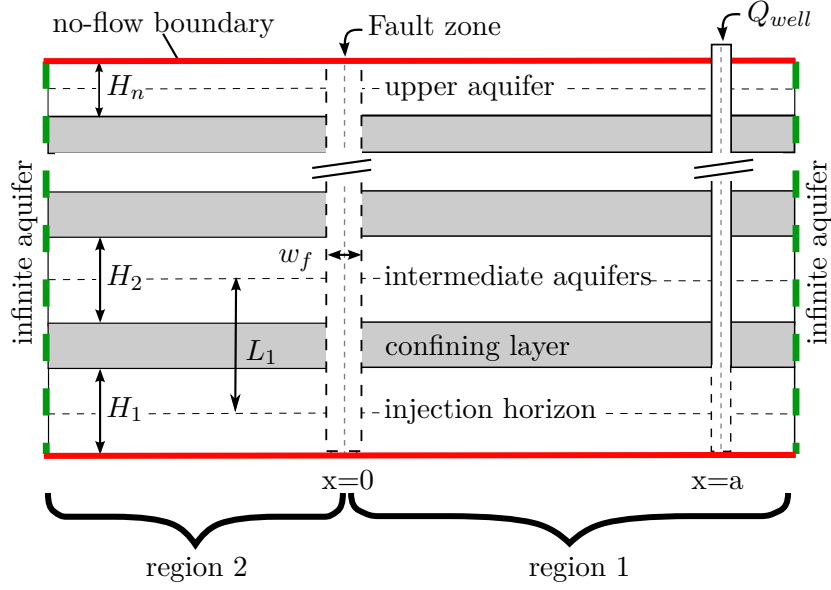


Figure 3.2.: Multi-layer system with n aquifers coupled through a fault zone, modified after Scholz (2014). The bottommost layer is the injection horizon. Each layer is split into two regions coupled through the fault zone.

denoting either region 1 or 2. For example, p_{j2} is the pressure in aquifer j , region 2:

$$\text{injection layer} = \begin{cases} \text{region 1 : } \frac{1}{D_1} \frac{\partial \Delta p_{11}}{\partial t} = \frac{\partial^2 \Delta p_{11}}{\partial x^2} + \frac{\partial^2 \Delta p_{11}}{\partial y^2} + \frac{Q_{well} \mu_1}{k_1 H_1} \delta(x-a) \delta(y), \\ \text{region 2 : } \frac{1}{D_1} \frac{\partial \Delta p_{12}}{\partial t} = \frac{\partial^2 \Delta p_{12}}{\partial x^2} + \frac{\partial^2 \Delta p_{12}}{\partial y^2}, \end{cases} \quad (3.38)$$

$$\text{upper aquifer } j = \begin{cases} \text{region 1 : } \frac{1}{D_j} \frac{\partial \Delta p_{j1}}{\partial t} = \frac{\partial^2 \Delta p_{j1}}{\partial x^2} + \frac{\partial^2 \Delta p_{j1}}{\partial y^2}, \\ \text{region 2 : } \frac{1}{D_j} \frac{\partial \Delta p_{j2}}{\partial t} = \frac{\partial^2 \Delta p_{j2}}{\partial x^2} + \frac{\partial^2 \Delta p_{j2}}{\partial y^2}, \end{cases} \quad (3.39)$$

where D_j is the diffusivity of the aquifer j defined as $D_j = \frac{k_j}{\mu_j \phi_j C_{t,j}}$ with $C_{t,j}$ being the total compressibility (porous medium and brine). Δp is the pressure change to an arbitrary initial pressure, Q_{well} is the volumetric injection rate, a is the distance between the injection point and the fault plane. The Dirac delta function δ has a value of 1 at the coordinates of the injection and 0 everywhere else. To complete the system of equations initial and boundary conditions have to be defined. Pressure changes at infinite distance and initial conditions are 0

for all aquifers and regions:

$$\Delta p_{j1}(x, y, 0) = \Delta p_{j2}(x, y, 0) = 0, \quad (3.40)$$

$$\Delta p_{j1}(x, \pm\infty, t) = \Delta p_{j2}(x, \pm\infty, t) = 0, \quad (3.41)$$

$$\Delta p_{j1}(\infty, y, t) = \Delta p_{j2}(-\infty, y, t) = 0. \quad (3.42)$$

Next, Neumann boundary conditions at the fault plane ($x = 0$) for each region of each aquifer are defined. Since it is assumed that the fault zone has no storage, the pressure gradients within the fault zone are linear. For the injection layer $j = 1$, the following flow balance arises for region 1 and 2:

$$\text{region 1 : } \left\{ \begin{array}{l} \underbrace{\frac{k_1 H_1}{\mu_1} \frac{\partial \Delta p_{11}(0, y, t)}{\partial x}}_{\text{flow from injection}} = \underbrace{\frac{k_{fh,1} H_1}{w_f \mu_1} (\Delta p_{11}(0, y, t) - \Delta p_{12}(0, y, t))}_{\text{flow to region 2}} \\ + \underbrace{\frac{k_{fv,1} w_f}{2L_1 \mu_1} (\Delta p_{11}(0, y, t) - \Delta p_{21}(0, y, t))}_{\text{flow to aquifer 2 region 1}} \end{array} \right. \quad (3.43)$$

$$\text{region 2 : } \left\{ \begin{array}{l} \underbrace{\frac{k_{fh,1} H_1}{w_f \mu_1} (\Delta p_{11}(0, y, t) - \Delta p_{12}(0, y, t))}_{\text{flow from region 1}} = \underbrace{\frac{k_1 H_1}{\mu_1} \frac{\partial \Delta p_{12}(0, y, t)}{\partial x}}_{\text{flow to region 2}} \\ + \underbrace{\frac{k_{fv,1} w_f}{2L_1 \mu_1} (\Delta p_{12}(0, y, t) - \Delta p_{22}(0, y, t))}_{\text{flow to aquifer 2 region 2}} \end{array} \right. \quad (3.44)$$

where $k_{fh,1}$ and $k_{fv,1}$ are the horizontal and vertical permeability of the fault zone in the injection aquifer respectively, w_f is the fault zone width, and L_1 is the distance of the midpoints of aquifer 1 and 2. The flow balance for an intermediate aquifer j has an additional term

accounting for flow from aquifer $j - 1$:

$$\begin{aligned}
 \text{region 1 : } & \left\{ \begin{aligned}
 & \frac{k_j H_j}{\mu_j} \frac{\partial \Delta p_{j1}(0, y, t)}{\partial x} = \frac{k_{fh,j} H_j}{w_f \mu_j} (\Delta p_{j1}(0, y, t) - \Delta p_{j2}(0, y, t)) \\
 & + \frac{k_{fv,j} w_f}{2L_j \mu_j} (\Delta p_{j1}(0, y, t) - \Delta p_{(j+1)1}(0, y, t)) \\
 & + \underbrace{\frac{k_{fv,j-1} w_f}{2L_{j-1} \mu_{j-1}} (\Delta p_{(j-1)1}(0, y, t) - \Delta p_{j1}(0, y, t))}_{\text{flow from aquifer } j-1 \text{ region 1}},
 \end{aligned} \right. \\
 \text{region 2 : } & \left\{ \begin{aligned}
 & \frac{k_{fh,j} H_j}{w_f \mu_j} (\Delta p_{j1}(0, y, t) - \Delta p_{j2}(0, y, t)) = \frac{k_j H_j}{\mu_j} \frac{\partial \Delta p_{j2}(0, y, t)}{\partial x} \\
 & + \frac{k_{fv,j} w_f}{2L_j \mu_j} (\Delta p_{j2}(0, y, t) - \Delta p_{(j+1)2}(0, y, t)) \\
 & + \underbrace{\frac{k_{fv,j-1} w_f}{2L_{j-1} \mu_{j-1}} (\Delta p_{(j-1)2}(0, y, t) - \Delta p_{j2}(0, y, t))}_{\text{flow from aquifer } j-1 \text{ region 2}}.
 \end{aligned} \right. \tag{3.45}
 \end{aligned}$$

Finally, the uppermost aquifer n does not account for flow to an overlying aquifer:

$$\begin{aligned}
 \text{region 1 : } & \left\{ \begin{aligned}
 & \frac{k_n H_n}{\mu_n} \frac{\partial \Delta p_{n1}(0, y, t)}{\partial x} = \frac{k_{fh,n} H_n}{w_f \mu_n} (\Delta p_{n1}(0, y, t) - \Delta p_{n2}(0, y, t)) \\
 & + \frac{k_{fv,n-1} w_f}{2L_{n-1} \mu_n} (\Delta p_{(n-1)1}(0, y, t) - \Delta p_{n1}(0, y, t)),
 \end{aligned} \right. \\
 \text{region 2 : } & \left\{ \begin{aligned}
 & \frac{k_{fh,n} H_n}{w_f \mu_n} (\Delta p_{n1}(0, y, t) - \Delta p_{n2}(0, y, t)) = \frac{k_n H_n}{\mu_n} \frac{\partial \Delta p_{n2}(0, y, t)}{\partial x} \\
 & + \frac{k_{fv,n-1} w_f}{2L_{n-1} \mu_{n-1}} (\Delta p_{(n-1)2}(0, y, t) - \Delta p_{n2}(0, y, t)).
 \end{aligned} \right. \tag{3.46}
 \end{aligned}$$

In order to solve the system of equations in Eq. 3.38, and 3.39 analytically, it is necessary to reduce the partial differential equations with three independent variables (x, y, t) to a system of ordinary differential equations which are coupled through the Neumann boundary conditions in Eq. 3.43 to 3.46. Zeidouni (2012) first brings Equations 3.38 - 3.46 into their dimensionless form before the Laplace transform is used to replace the temporal derivative. Further, the exponential Fourier transform is applied on the Laplace transformed equations to remove the second derivative in the y -coordinate. Thus, only the second derivative in the dimensionless

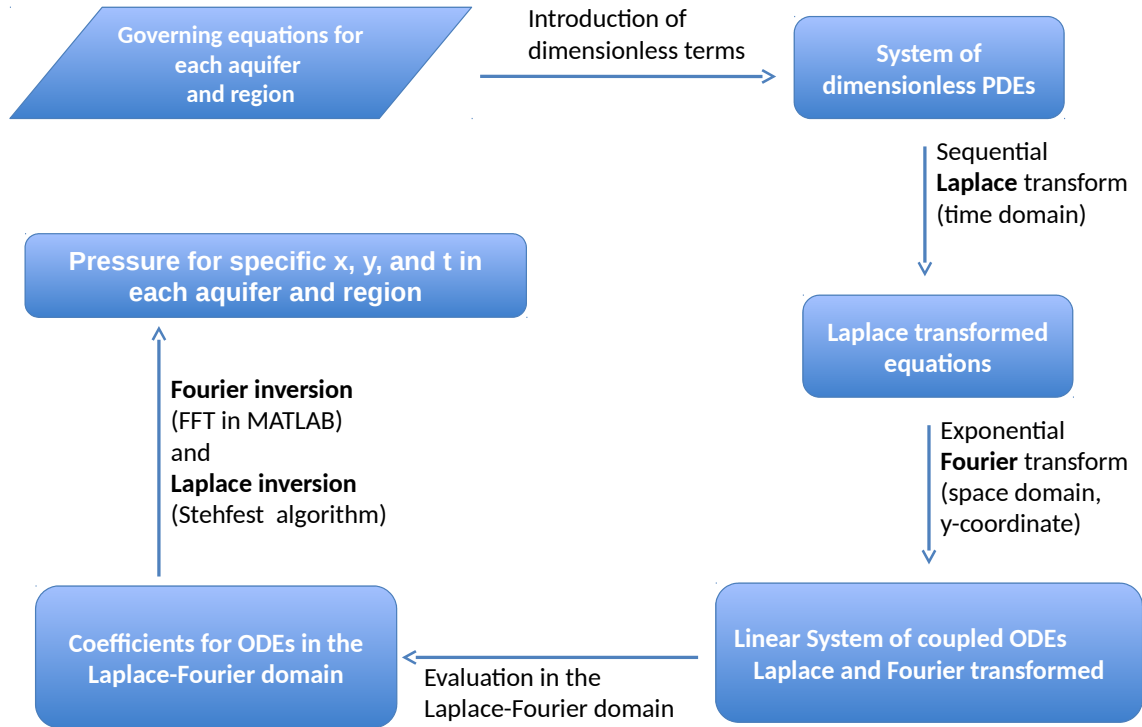


Figure 3.3.: Schematic overview of the solution procedure for the Zeidouni-Method, modified after Scholz (2014). For numerically inverting the Laplace transform the Stehfest algorithm is used (Stehfest, 1970).

x-coordinate remains, and the equations are reduced to a system of linear ordinary differential equations. Once the transformed solution is found, it must be inverted in time and space. This is achieved numerically. An overview of the procedure is given in Fig. 3.3.

The main target variable of this model is usually not the resulting pressure distribution but rather the leakage rate into overlying aquifers. To calculate the leakage, for example into the uppermost aquifer, the following integral relation can be used:

$$\begin{aligned}
 Q_{leakage}(t) = \frac{k_{fv,n-1}w_f}{2L_{n-1}\mu_{n-1}} & \left[\int_{-\infty}^{+\infty} (\Delta p_{(n-1)1}(0, y, t) - \Delta p_{n1}(0, y, t)) dy \right. \\
 & \left. + \int_{-\infty}^{+\infty} (\Delta p_{(n-1)2}(0, y, t) - \Delta p_{n2}(0, y, t)) dy \right].
 \end{aligned} \tag{3.47}$$

In the implementation, finite integral boundaries have to be chosen for y , and the integral is replaced by a sum, with N sampling steps and a sampling distance Δy :

$$Q_{leakage}(t) = \frac{k_{fv,n-1}w_f}{2L_{n-1}\mu_{n-1}} 2 \left[\sum_{i=1}^N (\Delta p_{(n-1)1}(i \cdot \Delta y - \frac{1}{2}\Delta y) - \Delta p_{n1}(i \cdot \Delta y - \frac{1}{2}\Delta y)) \Delta y \right. \\ \left. + \sum_{i=1}^N (\Delta p_{(n-1)2}(i \cdot \Delta y - \frac{1}{2}\Delta y) - \Delta p_{n2}(i \cdot \Delta y - \frac{1}{2}\Delta y)) \Delta y \right]. \quad (3.48)$$

Here, the constant values of x and t have been omitted, i.e. $\Delta p(y)$. Naturally, the integration length ($N \cdot \Delta y$) has to be chosen large enough such that the leakage rate is not significantly influenced by a further extension of the integration domain. Evaluating the solution for too many points can be computationally demanding. The factor of 2 in front of the sum arises due to the symmetry of the solution for $y = 0$.

3.3. Numerical Implementation

In this section, the numerical implementation of the different formulations given in Sec. 3.1.2 is presented. All simulations are carried out with the numerical simulator DuMu^x. The Box-Method is used for spatial discretization and the implicit Euler scheme is used for temporal discretization. The Newton-Raphson method is used to solve the non-linear system of equations. Additional implementations are required for the applications presented in this work. These include a 3D discrete-fracture approach for representing fault zones and infinite-aquifer boundary conditions achieved through a domain extension.

3.3.1. Numerical Simulator DuMu^x

All numerical models used in this work are implemented into the open-source numerical simulator DuMu^x (Flemisch et al., 2011; Schwenck et al., 2015). DuMu^x stands for DUNE for Multi-{Phase, Component, Scale, Physics,...} flow and transport in porous media. The simulator is based on the Distributed and Unified Numerics Environment (DUNE). It is an open-source system and has mainly been developed at the University of Stuttgart since January 2007. DuMu^x is developed in C++ and provides a modular design which makes it ideal for the implementation of porous-media model concepts. DuMu^x was used for a number of problems in the field of CO₂ storage in geological formations (Darcis et al., 2011; Walter et al., 2012, 2013; Kissinger et al., 2014) and was part of several code comparison studies (Nordbotten et al., 2012; Class et al., 2009).

3.3.2. Spatial Discretization: The Box-Method

The Box-Method is a node-centered finite-volume method where the fluxes over a control volume face are approximated by including information from multiple finite volumes (multi-point flux approximation). The degrees of freedom are situated on the nodes of a finite-element grid. A secondary finite-volume grid is constructed over the finite-element grid as shown in Fig. 3.4. The Box-Method is able to handle unstructured grids and anisotropic permeability

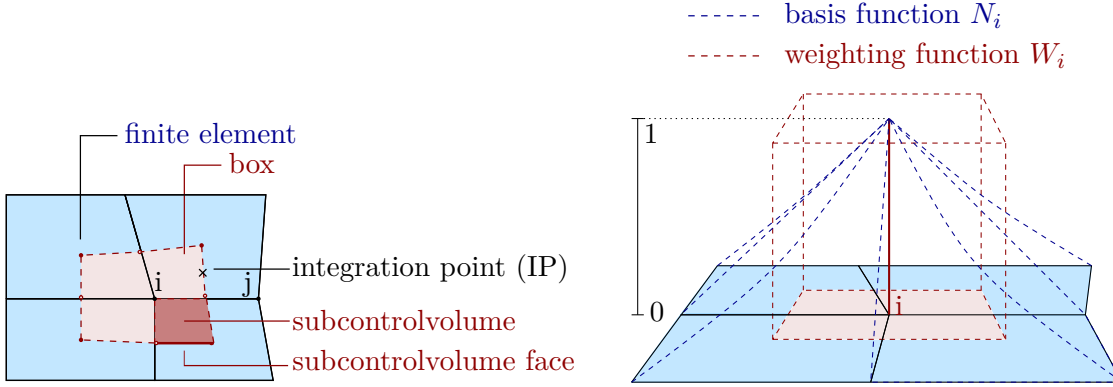


Figure 3.4.: Box constructed on a finite-element grid (left). Basis and weighting function for a node i (right). For 2D quadrilaterals the basis function is bilinear, and for 3D cubes it is trilinear. Figure modified after Darcis (2012).

tensors. The first steps in the derivation are similar to the derivation of the finite-element method. The above balance equations can be generalized to the following:

$$\frac{\partial s(\mathbf{u})}{\partial t} = \text{div}(\mathbf{f}(\mathbf{u})) + q(\mathbf{u}), \quad (3.49)$$

where $\mathbf{u} = \mathbf{u}(\mathbf{x})$ is a primary-variable vector, s is the storage term, \mathbf{f} is a flux vector (advective + dispersive fluxes), and q is a source and sink term dependent on the primary variables. Similar to finite-element methods, an interpolation, $\tilde{\mathbf{u}}(\mathbf{x})$, of discrete primary-variable values, $\hat{\mathbf{u}}$, is used to describe \mathbf{u} in space:

$$\tilde{\mathbf{u}}(\mathbf{x}) = \sum_{i=1}^N N_i(\mathbf{x}) \hat{\mathbf{u}}_i. \quad (3.50)$$

Here, $\hat{\mathbf{u}}$ is the interpolated primary-variable vector, N is the number of nodes, and $N_i(\mathbf{x})$ is known as the basis function which is chosen here to be linear (see Fig. 3.4). The gradient of a primary variable \hat{u} can be expressed in a similar way:

$$\mathbf{grad} \tilde{u}(\mathbf{x}) = \sum_{i=1}^N \mathbf{grad}(N_i(\mathbf{x})) \cdot \hat{u}_i. \quad (3.51)$$

Inserting the interpolated values $\tilde{\mathbf{u}}$ into Eq. 3.49 and integrating the equation over the model domain G leads to a residual ϵ since the original partial differential equation is no longer fulfilled exactly:

$$\int_G \frac{\partial s(\tilde{\mathbf{u}})}{\partial t} dG - \int_G \operatorname{div}(\mathbf{f}(\tilde{\mathbf{u}})) dG - \int_G q(\tilde{\mathbf{u}}) dG = \int_G \epsilon dG. \quad (3.52)$$

Using the method of weighted residuals, weighting functions $W_j = W_j(\mathbf{x})$ for each node are introduced and multiplied with Eq. 3.52 with the aim to minimize ϵ in G . The product of weighting function and ϵ has to vanish:

$$\int_G W_j \epsilon dG \stackrel{!}{=} 0 \quad \text{with} \quad \sum_{j=1}^N W_j = 1, \quad \text{for any point within } G. \quad (3.53)$$

Therefore, Eq. 3.52 is defined for each node j :

$$\int_G W_j \frac{\partial s(\tilde{\mathbf{u}})}{\partial t} dG - \int_G W_j \operatorname{div}(\mathbf{f}(\tilde{\mathbf{u}})) dG - \int_G W_j q(\tilde{\mathbf{u}}) dG = 0. \quad (3.54)$$

The next step is to apply Green's integral theorem to transform the volume integral of the second term into a boundary integral which results in an equation with four terms:

$$\underbrace{\int_G W_j \frac{\partial s(\tilde{\mathbf{u}})}{\partial t} dG}_{(1)} - \underbrace{\int_{\Gamma_G} W_j \cdot \mathbf{f}(\tilde{\mathbf{u}}) \cdot \mathbf{n} d\Gamma_G}_{(2)} + \underbrace{\int_G \mathbf{grad} W_j \cdot \mathbf{f}(\tilde{\mathbf{u}}) dG}_{(3)} - \underbrace{\int_G W_j q(\tilde{\mathbf{u}}) dG}_{(4)} = 0. \quad (3.55)$$

Up to this point, the derivation is similar to a finite-element approach. Equation 3.55 is formulated for the whole domain. Three steps are necessary to derive the Box-Method formulation from this point:

- As the Box-Method is a finite-volume method, local mass conservation for each box is required. Therefore the integration over the model domain G for the volume terms (1, 3, and 4) in Eq. 3.55 is replaced by the integration over the volume of a box V_i . The surface area of a box, i , across which the fluxes are calculated, is denoted by ∂V_i .
- The weighting function W_i is defined as a piecewise constant function, being 1 within V_i and 0 everywhere else (see Fig. 3.4), i.e.:

$$W_j(\mathbf{x}) = \begin{cases} 1 & \mathbf{x} \in V_i \\ 0 & \mathbf{x} \notin V_i. \end{cases} \quad (3.56)$$

With this definition, term (3) vanishes, as $\mathbf{grad}(W_j)$ is zero.

- Mass lumping of the volume terms (1) and (4) is applied. This means that the mass is stored only at the node, and therefore $s(\tilde{\mathbf{u}})$ becomes $s(\hat{\mathbf{u}}_i)$, which is only dependent on the discrete primary-variable vector at the node, and can be written in front of the integral, as it is no longer a function of space. The integral then simplifies to the volume of the box V_i .

The balance equations for a finite volume or box at node i therefore become:

$$V_i \frac{\partial s(\hat{\mathbf{u}}_i)}{\partial t} = \int_{\partial V_i} \mathbf{f}(\tilde{\mathbf{u}}) \cdot \mathbf{n} d\Gamma_{V_i} + V_i \cdot q(\hat{\mathbf{u}}_i). \quad (3.57)$$

Note that the number of equations at a node i depends on the number of primary variables. The time derivative will be discretized in the next section. As for the flux term, it can be split into an advective part and a dispersive part. The integral is replaced by a sum over the number of integration points at a node ($\eta_{IP,i}$):

$$\begin{aligned} \int_{\partial V_i} \mathbf{f}(\tilde{\mathbf{u}}) \cdot \mathbf{n} d\Gamma_{V_i} &= \sum_{IP \in \eta_{IP,i}} \left(\sum_{\alpha} \beta(\hat{\mathbf{u}}_{upw}) \mathbf{f}_{\mathbf{a}}(\tilde{\mathbf{u}}_{IP}) + \sum_{\alpha} \mathbf{f}_{\mathbf{d}}(\tilde{\mathbf{u}}_{IP}) \right) \cdot \mathbf{n}_{IP} A_{IP} \\ \text{with } \mathbf{f}_{\mathbf{a}}(\tilde{\mathbf{u}}_{IP}) &= -\bar{\mathbf{K}} \left(\mathbf{grad}(p_{\alpha})_{IP} - \bar{\varrho}_{\alpha} \mathbf{g} \right) \\ \text{and } \mathbf{f}_{\mathbf{d}}(\tilde{\mathbf{u}}_{IP}) &= -(\varrho_{\alpha}^m)_{IP} \mathbf{D}_{\text{disp}} \mathbf{grad}(x_{\alpha}^{\kappa})_{IP}. \end{aligned} \quad (3.58)$$

Here IP is the index of an integration point. Since discrete primary-variable values of $\hat{\mathbf{u}}$ are not available at an integration point, the interpolated primary-variable values at the coordinates of the integration point, i.e. $\tilde{\mathbf{u}}_{IP}$ or $\mathbf{grad} \tilde{\mathbf{u}}_{IP}$, are interpolated using Eq. 3.50 and 3.51. These interpolated values allow for the evaluation of the advective ($\mathbf{f}_{\mathbf{a}}$) and the dispersive flux ($\mathbf{f}_{\mathbf{d}}$) functions for each phase α . \mathbf{n}_{IP} and A_{IP} are the outer normal vector and the area of the sub-control volume face, respectively. In front of the advective-flux function, the term $\beta(\hat{\mathbf{u}}_{upw})$ is the product of those parameters whose values require an upwinding in order to avoid oscillations in advection dominated problems. In this work, a first order fully upwind weighting function is used for all models. This means that the parameters within β are evaluated with the primary variables of the upstream node, i.e.

$$upw = \begin{cases} i & \mathbf{f}_{\mathbf{a}} \cdot \mathbf{n}_{ij} \geq 0 \\ j & \mathbf{f}_{\mathbf{a}} \cdot \mathbf{n}_{ij} < 0. \end{cases} \quad (3.59)$$

Additionally, $\mathbf{f}_{\mathbf{a}}$ and $\mathbf{f}_{\mathbf{d}}$ both contain the permeability (\mathbf{K}) and the hydromechanic dispersion tensor (\mathbf{D}_{disp}). For these parameters, a harmonic average is calculated at the integration point, if the permeability and porosity are assigned at the node (box). If these properties are assigned on the element, no averaging is required. The density at the integration point within

the Darcy velocity ($\bar{\rho}_\alpha$) is the arithmetic mean of the adjacent nodes i and j .

Neumann boundary conditions are evaluated within the flux term (Eq. 3.58). This means that Neumann boundary fluxes are also allowed to be solution dependent, i.e. being a function of $\tilde{\mathbf{u}}_{IP}$. Dirichlet boundary conditions at a node i are treated by replacing the balance equation for a primary-variable vector $\hat{\mathbf{u}}_i$ with:

$$\hat{\mathbf{u}}_i - \hat{\mathbf{u}}_D = 0. \quad (3.60)$$

Here, $\hat{\mathbf{u}}_D$ are the fixed Dirichlet values. Mixed boundary conditions for different primary variables at a node i are also possible.

3.3.3. Temporal Discretization: The Implicit Euler Scheme

To account for a general time discretization, the time differential ∂t is replaced by a finite difference operator Δt . Eq. 3.57 can be extended as:

$$\begin{aligned} & V_i \frac{s(\hat{\mathbf{u}}_i^{n+1})}{\Delta t^n} - \theta \int_{\partial V_i} \mathbf{f}(\tilde{\mathbf{u}}^{n+1}) \cdot \mathbf{n} \, d\Gamma_{V_i} - V_i \cdot q(\hat{\mathbf{u}}_i^{n+1}) \\ & - \left[V_i \frac{s(\hat{\mathbf{u}}_i^n)}{\Delta t^n} - (1 - \theta) \int_{\partial V_i} \mathbf{f}(\tilde{\mathbf{u}}^n) \cdot \mathbf{n} \, d\Gamma_{V_i} - V_i \cdot q(\hat{\mathbf{u}}_i^n) \right] = 0, \end{aligned} \quad (3.61)$$

where n denotes the time step index, and θ is a weighting coefficient ($0 \leq \theta \leq 1$). $\theta = 0$ corresponds to an explicit scheme where all functions are evaluated with the primary variables of the previous time step (n). $\theta = 1$ yields the fully implicit scheme which is first order accurate in time (Helmig, 1997; Diersch and Kolditz, 2002) and unconditionally stable. In this work the fully implicit scheme is used for all numerical simulations. Equation 3.61 is rewritten here:

$$V_i \frac{s(\hat{\mathbf{u}}_i^{n+1}) - s(\hat{\mathbf{u}}_i^n)}{\Delta t^n} = \int_{\partial V_i} \mathbf{f}(\tilde{\mathbf{u}}^{n+1}) \cdot \mathbf{n} \, d\Gamma_{V_i} + V_i \cdot q(\hat{\mathbf{u}}_i^{n+1}). \quad (3.62)$$

3.3.4. The Newton-Raphson Method

Equation 3.62 is generally non-linear, as the constitutive parameters, such as densities, viscosities, relative permeabilities etc. are all functions of the primary variables. In order to solve a system of non-linear equations, an iterative scheme, such as the Newton-Raphson method, applied in this work, can be used. First, Eq. 3.62 is reformulated into a residual form:

$$r_i = V_i \frac{s(\hat{\mathbf{u}}_i^{n+1}) - s(\hat{\mathbf{u}}_i^n)}{\Delta t^n} - \int_{\partial V_i} \mathbf{f}(\tilde{\mathbf{u}}^{n+1}) \cdot \mathbf{n} \, d\Gamma_{V_i} - V_i \cdot q(\hat{\mathbf{u}}_i^{n+1}). \quad (3.63)$$

For a system with N nodes and P primary variables per node, the resulting number of equations is $N \times P$. The Jacobian matrix \mathbf{J} is obtained by forming partial derivatives of each equation r_i with respect to each connected primary variable \hat{u}_j . The partial derivatives for \mathbf{J} are calculated numerically. The linearized equation system for the Newton-Raphson method is:

$$\mathbf{J}(\hat{\mathbf{u}}^k) \Delta \hat{\mathbf{u}}^k = \mathbf{r}(\hat{\mathbf{u}}^k) \quad (3.64)$$

with $\Delta \hat{\mathbf{u}}^k = \hat{\mathbf{u}}^{k+1} - \hat{\mathbf{u}}^k,$

where the time step index is omitted and the iteration index k is introduced. The iteration is repeated until a convergence criterion is fulfilled. A convergence criterion can be an error norm such as the L^2 norm applied on the residual vector, or the prescribed demand for several digits accuracy in the calculated primary variables. The latter approach is used in this work, and is formulated in the following manner:

$$\epsilon > \max \left(\frac{\Delta \hat{u}_1^k}{0.5(\hat{u}_1^{k+1} + \hat{u}_1^k)}, \dots, \frac{\Delta \hat{u}_N^k}{0.5(\hat{u}_N^{k+1} + \hat{u}_N^k)} \right). \quad (3.65)$$

The Newton-Raphson method is described in more detail for multi-phase flow problems in Helmig (1997).

3.3.5. Fault-Zone Representation Using a Discrete-Fracture Approach

The implementation of a discrete-fracture model on top of the existing models discretized with the Box-Method is shown here. In the context of this work it is used for the representation of fault zones.

In the application presented in Chapter 5, complex multi-layer geological systems have to be discretized. The grids used for these kinds of systems are usually horizontally aligned with the geological layers. However, there are vertical discontinuities such as fault zones or salt domes which can play a crucial role for the flow field, as they can be impermeable or permeable to horizontal or vertical flow. Fault zones can be considered as planar discontinuities, where their width is much smaller than their height or length. In large-scale models, the width of a fault zone can therefore be much smaller than the horizontal discretization length. Describing a fault zone in detail would require severe grid refinement, not only leading to an increased computational effort but also requiring additional work during the grid generation. In order to avoid this grid refinement but still be able to describe the relevant characteristics of a fault zone, a discrete-fracture approach is implemented. Within this approach a fracture or fault zone can be described with three parameters: fracture width, fracture permeability and fracture porosity. Fig. 3.5 shows the discretization of a fault zone in a horizontal layer.

Using a lower-dimensional implementation the fractures are defined on the element faces.

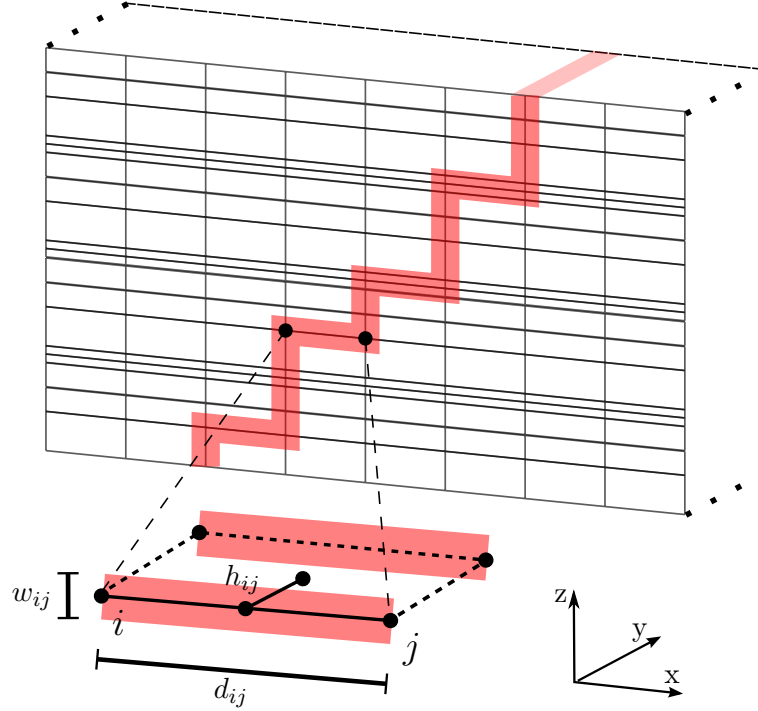


Figure 3.5.: Grid with variable vertical discretization length and a fault zone shown in red. Note that the width of the fault zone (w_{ij}) may be greater than the vertical discretization length. The bottom shows a zoom on a fracture element face, containing the nodes i and j from the above grid, in x and y direction. The fault-zone width w_{ij} is an input parameter of the fracture model. d_{ij} is the distance between nodes i and j and h_{ij} is the distance between the midpoint of the line connecting nodes i and j and the center of the element face. Both d_{ij} and h_{ij} are calculated from the geometry of the element face.

Nodes connected by a fracture consider both matrix and fracture flow as well as matrix and fracture storage. No additional primary variables are used with the underlying assumption that pressures and mole or mass fractions in the fracture and matrix are the same. Saturations within the fracture and matrix can be different using an interface condition as discussed in Tatomir (2013). However, this will not be treated further, since it is not relevant for the applications presented below. Within the fracture, Darcy's law is assumed to be valid. The general equation for fracture flow at a node i for this implementation is:

$$W_f V_{f,i} \frac{\partial s_f(\hat{\mathbf{u}}_i)}{\partial t} = \int_{\partial V_{f,i}} \mathbf{f}_f(\bar{\mathbf{u}}) \cdot \mathbf{n} d\Gamma_{V_{f,i}}, \quad (3.66)$$

where the subscript f denotes fracture-specific parameters and W_f is a weighting factor ($0 \leq W_f \leq 1$) used for the storage within the fracture. Similar to Eq. 3.58 the discretized flux

term can be expressed as follows:

$$\int_{\partial V_{f,i}} \mathbf{f}_f(\tilde{\mathbf{u}}) \cdot \mathbf{n} d\Gamma_{V_{f,i}} = \sum_{j \in \eta_i} \left(\sum_{\alpha} \beta(\hat{\mathbf{u}}_{upw}) \mathbf{f}_a(\hat{\mathbf{u}}_i, \hat{\mathbf{u}}_j) \right) \mathbf{n}_{ij} \frac{w_{ij}}{2} h_{ij} \quad (3.67)$$

$$\text{with } \mathbf{f}_a(\hat{\mathbf{u}}_i, \hat{\mathbf{u}}_j) = -\bar{k}_f \left(\frac{p_i - p_j}{d_{ij}} \mathbf{n}_{ij} - \bar{\varrho}_\alpha \mathbf{g} \right).$$

Here η_i is a set of nodes that are connected to i via a fracture. d_{ij} , w_{ij} , and h_{ij} are the geometrical parameters describing the fracture geometry, as shown in Fig. 3.5. Fracture flow only comprises advective flow using a two-point flux approximation. The scalar fracture permeability \bar{k}_f is again a harmonic average of the permeability of nodes i and j . Adding Eq. 3.66 to Eq. 3.57 yields:

$$W_m V_i \frac{\partial s(\hat{\mathbf{u}}_i)}{\partial t} + W_f V_{f,i} \frac{\partial s_f(\hat{\mathbf{u}}_i)}{\partial t} = \int_{\partial V_i} \mathbf{f}(\tilde{\mathbf{u}}) \cdot \mathbf{n} d\Gamma_{V_i} + \int_{\partial V_{f,i}} \mathbf{f}_f(\tilde{\mathbf{u}}) \cdot \mathbf{n} d\Gamma_{V_{f,i}} + V_i \cdot q(\hat{\mathbf{u}}_i), \quad (3.68)$$

where W_m ($0 \leq W_m \leq 1$) is another weighting factor for the storage term of the matrix. The weighting factors for the storage terms of the fracture and the matrix can be used to manipulate the transport velocity within the fracture. For example, setting W_f to one and W_m to zero would decrease the retention time of a component or phase within the fracture as the available storage volume of the matrix in a box containing a fracture is neglected. This can be considered a conservative assumption with respect to the arrival time of a transported contaminant. Table 3.1 gives an overview of the fully discretized equations used in this work.

Table 3.1.: List of fully discretized equations. Note that in this work the 2p model is not used in combination with the fracture module, hence the equations for the 2p model only account for matrix flow. The matrix and fracture weighting factors (W_m and W_f) are only implemented for the component balance equations of salt in the 1p2c and 2p3c model.

Model	Discretized equation
1p2c total mole balance	$V_i \frac{(\phi \varrho_w^m)_i^{n+1} - (\phi \varrho_w^m)_i^n}{(\Delta t)^n} + (V_f \phi_f)_i \frac{(\varrho_w^m)_i^{n+1} - (\varrho_w^m)_i^n}{(\Delta t)^n} =$ $+ \sum_{IP \in \eta_{IP,i}} \left[- \left(\frac{\varrho_w^m}{\mu_w} \right)_{upw} \bar{\mathbf{K}} (\mathbf{grad}(p_w)_{IP} - \bar{\varrho}_w \mathbf{g}) \right]^{n+1} \mathbf{n}_{IP} A_{IP}$ $+ \sum_{j \in \eta_i} \left[- \left(\frac{\varrho_w^m}{\mu_w} \right)_{upw} \bar{k}_f \left(\frac{p_{w,i} - p_{w,j}}{d_{ij}} \mathbf{n}_{ij} - \bar{\varrho}_w \mathbf{g} \right) \right]^{n+1} \mathbf{n}_{ij} \frac{w_{ij}}{2} h_{ij}$ $+ V_i \cdot (q(\hat{\mathbf{u}}))_i^{n+1}$

Table 3.1.: List of fully discretized equations. Note that in this work the 2p model is not used in combination with the fracture module, hence the equations for the 2p model only account for matrix flow. The matrix and fracture weighting factors (W_m and W_f) are only implemented for the component balance equations of salt in the 1p2c and 2p3c model.

Model	Discretized equation
1p2c component balance salt	$ \begin{aligned} & W_m V_i \frac{(\phi \varrho_w^m x_w^S)_i^{n+1} - (\phi \varrho_w^m x_w^S)_i^n}{(\Delta t)^n} + W_f (V_f \phi_f)_i \frac{(\varrho_w^m x_w^S)_i^{n+1} - (\varrho_w^m x_w^S)_i^n}{(\Delta t)^n} = \\ & + \sum_{IP \in \eta_{IP,i}} \left[- \left(\frac{\varrho_w^m x_w^S}{\mu_w} \right)_{upw} \bar{\mathbf{K}} (\mathbf{grad} (p_w)_{IP} - \bar{\varrho}_w \mathbf{g}) \right. \\ & \left. - (\varrho_w^m)_{IP} \bar{\mathbf{D}}_{w,pm}^S \mathbf{grad} (x_w^S)_{IP} \right]^{n+1} \mathbf{n}_{IP} A_{IP} \\ & + \sum_{j \in \eta_i} \left[- \left(\frac{\varrho_w^m x_w^S}{\mu_w} \right)_{upw} \bar{k}_f \left(\frac{p_{w,i} - p_{w,j}}{d_{ij}} \mathbf{n}_{ij} - \bar{\varrho}_w \alpha \mathbf{g} \right) \right]^{n+1} \mathbf{n}_{ij} \frac{w_{ij}}{2} h_{ij} \\ & + V_i \cdot (q(\hat{\mathbf{u}}))_i^{n+1} \\ & \text{primary variables } \hat{\mathbf{u}} : p_w, x_w^S \end{aligned} $
2p phase balance $\alpha = \text{brine or CO}_2$	$ \begin{aligned} & V_i \frac{(\phi \varrho_\alpha S_\alpha)_i^{n+1} - (\phi \varrho_\alpha S_\alpha)_i^n}{(\Delta t)^n} = \\ & + \sum_{IP \in \eta_{IP,i}} \left[- \left(\frac{\varrho_\alpha k_{r\alpha}}{\mu_\alpha} \right)_{upw} \bar{\mathbf{K}} (\mathbf{grad} (p_\alpha)_{IP} - \bar{\varrho}_\alpha \mathbf{g}) \right]^{n+1} \mathbf{n}_{IP} A_{IP} \\ & + V_i \cdot (q_\alpha(\hat{\mathbf{u}}))_i^{n+1} \\ & \text{primary variables } \hat{\mathbf{u}} : p_w, S_n \end{aligned} $

Table 3.1.: List of fully discretized equations. Note that in this work the 2p model is not used in combination with the fracture module, hence the equations for the 2p model only account for matrix flow. The matrix and fracture weighting factors (W_m and W_f) are only implemented for the component balance equations of salt in the 1p2c and 2p3c model.

Model	Discretized equation
2p3c component balance $\kappa = \text{H}_2\text{O}$ or CO_2	$V_i \frac{\sum_{\alpha} \left(\phi \varrho_{\alpha}^m S_{\alpha} x_{\alpha}^{\kappa} \right)_i^{n+1} - \left(\phi \varrho_{\alpha}^m S_{\alpha} x_{\alpha}^{\kappa} \right)_i^n}{(\Delta t)^n}$ $+ (V_f \phi_f)_i \frac{\sum_{\alpha} \left(\left(\varrho_{\alpha}^m S_{\alpha} x_{\alpha}^{\kappa} \right)_i^{n+1} - \left(\varrho_{\alpha}^m S_{\alpha} x_{\alpha}^{\kappa} \right)_i^n \right)}{(\Delta t)^n} =$ $+ \sum_{IP \in \eta_{IP,i}} \left[\sum_{\alpha} \left(- \left(\frac{\varrho_{\alpha}^m k_{r\alpha} x_{\alpha}^{\kappa}}{\mu_{\alpha}} \right)_{upw} \bar{\mathbf{K}} \left(\mathbf{grad} (p_{\alpha})_{IP} - \bar{\varrho}_{\alpha} \mathbf{g} \right) \right.$ $\left. - \sum_{\alpha} \left(- \left(\varrho_{\alpha}^m \right)_{IP} \bar{\mathbf{D}}_{\alpha,pm}^{\kappa} \mathbf{grad} (x_{\alpha}^{\kappa})_{IP} \right) \right]^{n+1} \mathbf{n}_{IP} A_{IP}$ $+ \sum_{j \in \eta_i} \left[- \left(\frac{\varrho_{\alpha}^m x_{\alpha}^{\kappa}}{\mu_{\alpha}} \right)_{upw} \bar{k}_f \left(\frac{p_{\alpha,i} - p_{\alpha,j}}{d_{ij}} \mathbf{n}_{ij} - \bar{\varrho}_{\alpha} \mathbf{g} \right) \right]^{n+1} \mathbf{n}_{ij} \frac{w_{ij}}{2} h_{ij}$ $+ V_i \cdot (q^{\kappa}(\hat{\mathbf{u}}))_i^{n+1}$
2p3c component balance $\kappa = \text{salt}$	$W_m V_i \frac{\sum_{\alpha} \left(\phi \varrho_{\alpha}^m S_{\alpha} x_{\alpha}^{\kappa} \right)_i^{n+1} - \left(\phi \varrho_{\alpha}^m S_{\alpha} x_{\alpha}^{\kappa} \right)_i^n}{(\Delta t)^n}$ $+ W_f (V_f \phi_f)_i \frac{\sum_{\alpha} \left(\left(\varrho_{\alpha}^m S_{\alpha} x_{\alpha}^{\kappa} \right)_i^{n+1} - \left(\varrho_{\alpha}^m S_{\alpha} x_{\alpha}^{\kappa} \right)_i^n \right)}{(\Delta t)^n} =$ $+ \sum_{IP \in \eta_{IP,i}} \left[\sum_{\alpha} \left(- \left(\frac{\varrho_{\alpha}^m k_{r\alpha} x_{\alpha}^{\kappa}}{\mu_{\alpha}} \right)_{upw} \bar{\mathbf{K}} \left(\mathbf{grad} (p_{\alpha})_{IP} - \bar{\varrho}_{\alpha} \mathbf{g} \right) \right.$ $\left. - \sum_{\alpha} \left(- \left(\varrho_{\alpha}^m \right)_{IP} \bar{\mathbf{D}}_{\alpha,pm}^{\kappa} \mathbf{grad} (x_{\alpha}^{\kappa})_{IP} \right) \right]^{n+1} \mathbf{n}_{IP} A_{IP}$ $+ \sum_{j \in \eta_i} \left[- \left(\frac{\varrho_{\alpha}^m x_{\alpha}^{\kappa}}{\mu_{\alpha}} \right)_{upw} \bar{k}_f \left(\frac{p_{\alpha,i} - p_{\alpha,j}}{d_{ij}} \mathbf{n}_{ij} - \bar{\varrho}_{\alpha} \mathbf{g} \right) \right]^{n+1} \mathbf{n}_{ij} \frac{w_{ij}}{2} h_{ij}$ $+ V_i \cdot (q^{\kappa}(\hat{\mathbf{u}}))_i^{n+1}$ <p>primary variables $\hat{\mathbf{u}} : p_w, S_n / x_w^{CO_2} / x_n^{H_2O}, x_w^S$</p>

The 3D implementation of the discrete-fracture approach is done in a general way to ensure that it can easily be coupled to the different model types (1p2c, 2p, 2p3c) used in this work. It is therefore an extension and generalization of the implementation by Tatomir (2013) which

is 2D and specific to the 2p model in DuMu^x. Additionally, the implementation is valid for different element types, such as simplex or hexahedral grids.

An alternative approach to the representation of fault zones that avoids refinement could be an upscaling procedure coming from a fine grid fully describing the geometry of the fault zone, for example, a multiple interacting continua (MINC) approach, as described in Tatomir (2013). However, some effort is required as well to implement a generalized method for converting the complex geometrical information of the fault zone into effective parameters.

3.3.6. Infinite-Aquifer Boundary Conditions

Another necessary implementation for this work is the extension of an arbitrary domain, henceforth called the inner domain, by an outer domain. This outer domain extends to a certain radius, ensuring that the pressure buildup within the inner domain is not underestimated due to its boundaries being too close to the injection point.

A saline aquifer confined by barrier layers on top and bottom is generally characterized by lateral dimensions much larger than the vertical ones. During the injection of CO₂ into such an aquifer, the lateral extent, that is subject to pressure increases is much larger than the lateral extent of the CO₂ plume. Models primarily concerned with the shape and fate of the CO₂ plume often use Dirichlet boundary conditions for pressure on the lateral boundaries at distances too small, such that the actual pressure buildup would reach further than the model boundaries. This means that the resistance to lateral flow is reduced and the pressures that evolve are underestimated. When predicting the CO₂-plume shape, this usually does not pose a significant problem. However, if the primary aim of the model is characterizing brine flow at large distances from the injection point, as will be the case in Chapter 5, lateral Dirichlet boundary conditions will lead to an underestimation of the vertical migration of brine through vertical discontinuities in the barrier layers.

As far-field information of saline aquifers is usually sparse, assumptions have to be made. One possible assumption is an infinite extent of the aquifer. This means that the pressure at infinite distance from the injection remains unchanged. In this work, this condition is approximated by extending the model domain (inner domain) by a circular outer domain with a coarser grid. The discretization length of the outer domain may increase as a function of the radius. An example of an inner and an outer domain is given in Fig. 3.6. As the discretization length of the outer domain can be chosen much coarser, the additional computational demand can be kept within reasonable limits. The effect on the results however is significant, as will be shown in Chapter 5.

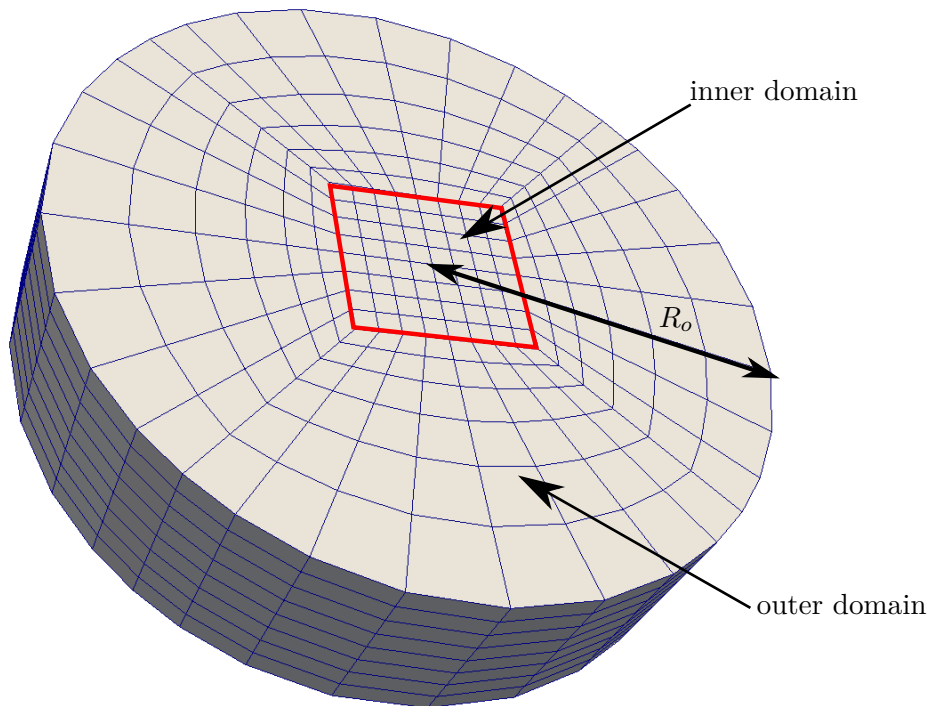


Figure 3.6.: An inner domain within the red frame is surrounded by an outer domain with radius R_o .

The required outer radius R_o is a function of the system parameters:

- diffusivity of the injection aquifer,
- leakage into upper and lower aquifers,
- injection rate, and
- injection duration.

In this work, the outer radius R_o is determined by increasing R_o until convergence in the results is reached. The domain extension module, can be applied to any domain, with a convex outer boundary, and is implemented into DuMu^x.

Alternatively, there exist analytical solutions which can be coupled to a numerical model at its boundary. In the context of groundwater modeling, Kipp (1986) uses the term aquifer influence functions (AIF) and implemented them into the simulator HST3D (Kipp, 1987). However, the concept originates from the field of petroleum engineering (Van Everdingen and Hurst, 1949), where such methods are still used to estimate the inflow from an outer aquifer into an oil reservoir during extraction. The AIF approach requires only one additional

primary variable per boundary node. However, the assumptions made are more severe, as the underlying analytical model was developed for a circular domain, putting restrictions on arbitrary inner model shapes as well as stratified aquifer systems.

4. Basin-Scale Screening for CO₂ Storage Efficiency¹

This chapter deals with a screening method for determining suitable areas for CO₂ storage based on their storage efficiency. The storage efficiency is a measure of how efficient a reservoir can be utilized. In literature (e.g. Okwen et al. (2010)), the term storage efficiency is often defined as the volume of injected CO₂ divided by the pore space (see Eq. 3.35), which is referred to here as volumetric storage efficiency. However, in this work the storage efficiency is defined in terms of the mass of CO₂ in place, which is the target variable used here for comparing different reservoirs. The database used for the screening covers regionalized data for depth, temperature conditions and salt concentrations of the Middle Buntsandstein rock unit in the North German Basin. As proposed by Kopp et al. (2009a), the gravitational number, Gr (see Eq. 3.19), is used as a qualitative indicator for storage efficiency to determine more or less favorable areas for CO₂ injection. Unfortunately, a reservoir database similar to the U.S. National Petroleum Council public database (NPC, 1984) used by Kopp et al. (2009a,b) is not available for the North German Basin. No regionalized data for the permeability, the porosity and the reservoir thickness are available. However, the initial fluid properties (viscosities and densities of brine and CO₂) can be estimated from measured depth contours, temperature profiles, and salt concentrations.

In Sec 4.1, the relevant driving forces influencing storage efficiency are explained. The available database is described in Sec. 4.2, followed by a description of the numerical model's setup in Sec. 4.3. Results of the regional calculation of the Gravitational Number (Gr) for the Middle Buntsandstein rock unit are presented in Sec. 4.4.1. Based on these results, several data points of the database are selected for more detailed numerical investigations with the aim of:

- quantifying the impact of varying depths, temperature conditions, and salt concentrations in the Middle Buntsandstein on storage efficiency (Sec. 4.4.2),
- testing the Gr -criterion as a qualitative screening criterion for storage efficiency and comparing the results to the screening method proposed by Okwen et al. (2010) (Sec. 4.4.2),

¹The main parts of this chapter have been published in Kissinger et al. (2014).

- investigating the effect of Gr-criterion on the amount of residually trapped CO₂ (Sec. 4.4.3).

Moreover, in Sec. 4.4.4, three different regions are selected which are characterized by different values of Gr (high, medium, and low). For these regions, published data for reservoir thickness and porosity are gathered as input for the numerical simulations. The aim of these simulations is to check:

- if Gr, based on the initial fluid properties, has a recognizable effect on storage efficiency when area-specific distributions of reservoir thickness and porosity are considered as well.

4.1. The Gravitational Number as a Qualitative Indicator for Storage Efficiency

In an injection scenario, where CO₂ is injected via a vertical injection well into resident brine held in a confined homogeneous reservoir, the CO₂ plume shape is characterized by the following driving forces:

- Viscous forces (or advective forces). The injection causes a displacement of resident brine away from the injection well.
- Gravitational (or buoyant forces). Due to the density difference between the two fluid phases, an upward flow of the lighter CO₂ phase is induced (gravity segregation) as well as horizontal flow of the CO₂ phase along the cap-rock due to a horizontal pressure gradient at the tip of the CO₂ tongue (buoyant drive).
- Capillary forces. Capillary pressure gradients lead to the development of a capillary fringe at the interface between the two phases depending on the capillary pressure-saturation relationship.

The influence of these driving forces and especially the ratio of gravitational to advective forces has been investigated in many subsurface applications. Examples include: steam injection into oil reservoirs (Rapoport, 1955; Lookeren, 1983; Li and Lake, 1995), steam injection into fully water-saturated porous media in the context of soil remediation (Ochs et al., 2010), or CO₂ storage (Nordbotten and Celia, 2006, 2012; Nazarian et al., 2013; Taku Ide et al., 2007; Kopp et al., 2010). Also, other related subsurface applications, like geothermal systems (cold water injection) or the storage of methane in subsurface formations, have similarities, where the ratios between their driving forces help to describe the spreading behavior of the injected fluid. There are many established dimensionless groups that are useful in the characterization of a

reservoir (Rapoport, 1955; Li and Lake, 1995; Zhou et al., 1997).

In the context of CO₂ injection, Kopp et al. (2009a) define the dimensionless capillary number (Ca) and the gravitational number (Gr) using a fractional flow formulation, as presented in Sec. 3.1.2, and shown here again. The Capillary Number is defined as:

$$Ca = \frac{kp_{cr}}{\mu_n v_{cr} l_{cr}} = \frac{\text{capillary forces}}{\text{viscous forces}}. \quad (4.1)$$

Further, the Gravitational Number is defined as:

$$Gr = \frac{(\rho_w - \rho_n)gk}{\mu_n v_{cr}} = \frac{\text{gravitational forces}}{\text{viscous forces}}, \quad (4.2)$$

where k is the scalar intrinsic permeability, p_{cr} is a characteristic capillary pressure, μ_n is the dynamic viscosity of CO₂, l_{cr} is a characteristic length of the system, v_{cr} is a characteristic Darcy velocity, ρ_w is the brine density, ρ_n is the CO₂ density and g is the acceleration due to gravity. Kopp et al. (2009a) suggest using Ca and Gr for qualitatively ranking different reservoirs according to their storage efficiency. Through numerical simulations, they show that advective forces, dominating over gravitational forces (small values of Gr), and capillary forces, dominating over advective forces (large values of Ca), lead to a higher storage efficiency. They further conclude that Gr has a stronger influence on storage efficiency than Ca for large system dimensions. This conclusion is also confirmed by Nordbotten and Celia (2012) who scale capillary pressure with the hydrostatic pressure difference within a formation. They show that capillary pressure generally reduces the saturation of the CO₂ front with increasing distance from the well. This reduction, is caused by a smearing of the front, following a diffusion-like behavior, leading to a reduced plume velocity at the tip, and therefore a higher storage efficiency. Nordbotten and Celia (2012) conclude that if the capillary fringe is small compared to the thickness of the reservoir, capillary forces can be neglected and the assumption of a sharp interface model becomes reasonable. In this work, Ca will not be considered in the estimation of storage efficiency since the database used does not allow for any reliable regional differentiation of capillary pressure-saturation relationships.

In this work Gr is used as a qualitative indicator for storage efficiency, as concluded by Kopp et al. (2009a,b). The ratio between gravitational and advective forces is not constant. Near the injection well advective forces dominate, but with increasing distance from the injection well the advective forces decrease. Thus, sooner or later the two phases will separate and the CO₂ plume will then spread mainly underneath the top of the reservoir. Close to the injection well, where the advective forces are high (i.e. high v_{cr} , see Eq. 4.2), the plume spreads cylindrically. Kopp et al. (2009a) calculate the characteristic velocity v_{cr} in Eq. 4.2 from an average time dependent velocity obtained from simulation results. As this is not an option for the large data set of this study, a priori estimate of v_{cr} is defined, characteristic for the advective forces

in the system. For this purpose the specific volumetric injection rate $\frac{\dot{m}_n}{\rho_n}$ is used, where \dot{m}_n is the specific mass injection rate of CO₂ (i.e. the injection rate divided by the area of the well) in [kg/s/m²]. This results in the following definition of Gr:

$$Gr = \frac{(\rho_w - \rho_n)gk}{\mu_n \frac{\dot{m}_n}{\rho_n}}. \quad (4.3)$$

The smaller the priorly calculated Gravitational Number (Eq. 4.3), the more the advective forces will dominate over the gravitational forces, which leads to a more piston-like displacement. As a result, the storage efficiency is increased, as the CO₂ spreads over a larger fraction of the reservoir. Besides increasing the storage efficiency also the amount of residually trapped CO₂ increases, which is beneficial for storage safety. The effect of Gr on residual trapping was also shown by Taku Ide et al. (2007).

Since there are no data for permeability (k) and the actual specific injection rate (\dot{m}_{CO_2}) used is not known beforehand, these two parameters are set to 1 in order to make it clear that they are not varied in the calculation of the a priori Gr.

As shown in the derivation of the sharp interface model (Eq. 3.30) and the Okwen-Method (Eq. 3.37) the mobility ratio λ is an important factor in the estimation of storage efficiency. When using Gr, as defined in Eq. 4.3, to qualitatively compare different locations, the influence of the brine mobility and therefore the spatial variability of the brine viscosity is neglected. To see if this is a valid assumption, the results are compared to the Okwen-Method, which is explained in detail in Sec. 3.2.1. The main equation for estimating the volumetric storage efficiency $E = \frac{V_{injected}}{V_{formation}}$, based on the mobility ratio λ and the gravitational number Γ , is presented here again:

$$E = (1 - S_{rw}) \frac{1}{\lambda} \quad 0 \leq \Gamma < 0.5,$$

$$E = \frac{2(1 - S_{rw})}{(0.0324\lambda - 0.0952)\Gamma + (0.1778\lambda + 5.9682)\Gamma^{1/2} + 1.6962\lambda - 3.0472}, \quad (4.4)$$

$$0.5 \leq \Gamma \leq 50.$$

Γ is another definition of the gravitational number defined as:

$$\Gamma = \frac{2\pi\Delta\rho gk\lambda_w H^2}{Q_{well}}, \quad (4.5)$$

where H is the reservoir thickness and Q_{well} is the volumetric injection rate. λ and λ_w can be simplified to $\frac{\mu_w}{\mu_n}$ and $\frac{1}{\mu_w}$ respectively, when assuming that the relative permeability of brine

(k_{rw}) is equal to 1 in the fully brine saturated part of the domain, similar to the relative permeability of CO₂ (k_{rn}) in the CO₂ saturated part of the domain.

4.2. Available Data

The database used in this work is compiled by project partners of the Federal Institute for Geosciences and Natural Resources of Germany (BGR). Therefore, the database will only briefly be outlined here, for more details see Kissinger et al. (2014). The screening is carried out for those parts of the Middle Buntsandstein rock unit, which were designated to be worthy of further investigation in the Storage Catalogue of Germany (Müller and Reinhold, 2011). The database includes regionalized data for depth, temperature conditions and salt concentrations for the Middle Buntsandstein on a 1 km × 1 km raster. The depth information is shown in Fig. 4.1 for the top of the Middle Buntsandstein. The temperature conditions are interpolated

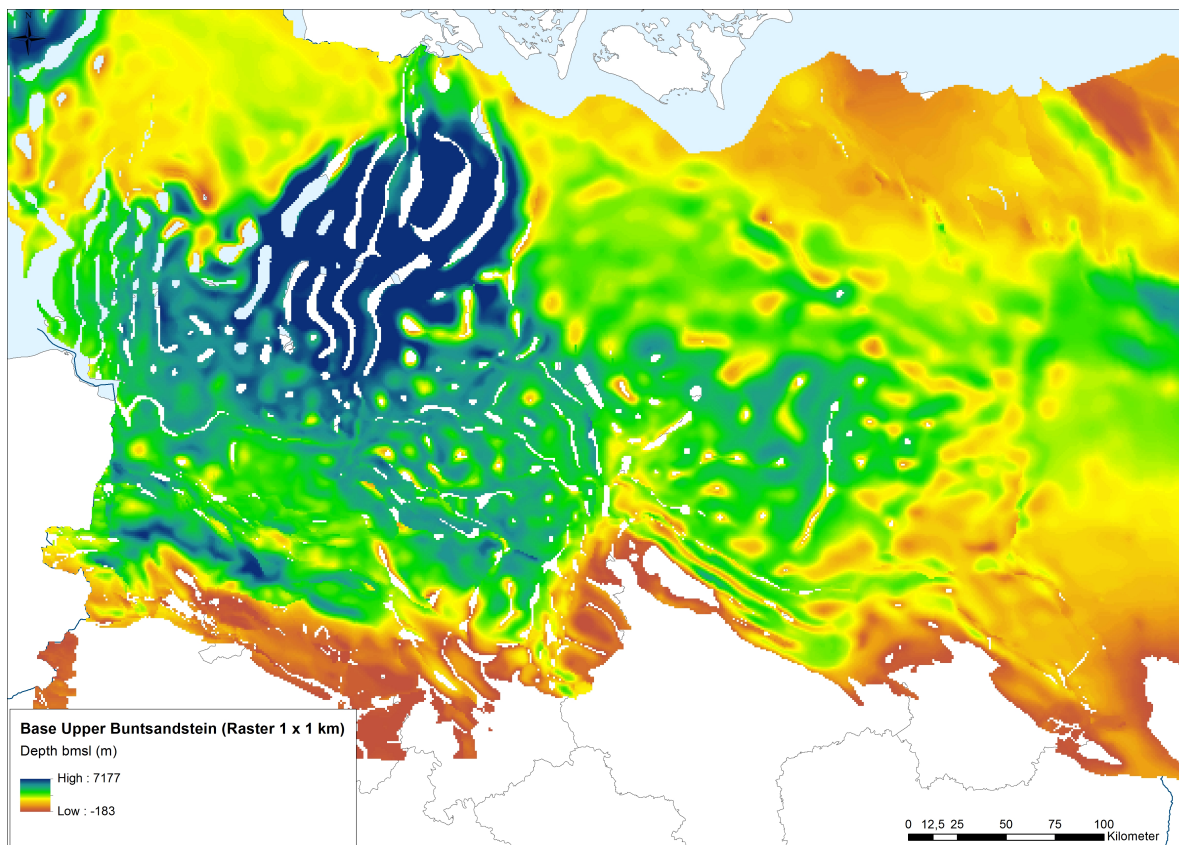


Figure 4.1.: Unpublished depth grid for the base of the Upper Buntsandstein (equivalent to the top of the Middle Buntsandstein) with depths recorded in meters below mean sea level (bmsl). Figure from Kissinger et al. (2014).

from a coarse-scale map of the Leibniz Institute for Applied Geophysics (LIAG, 2012) showing the lateral variation of the mean geothermal gradient in selected regions in Germany. The temperature distribution can be estimated by combining the depth information with the map of the geothermal gradients in the Middle Buntsandstein rock unit. The temperature gradient distribution is shown in Fig. 4.2. No data for the lateral variability of the salt concentrations is

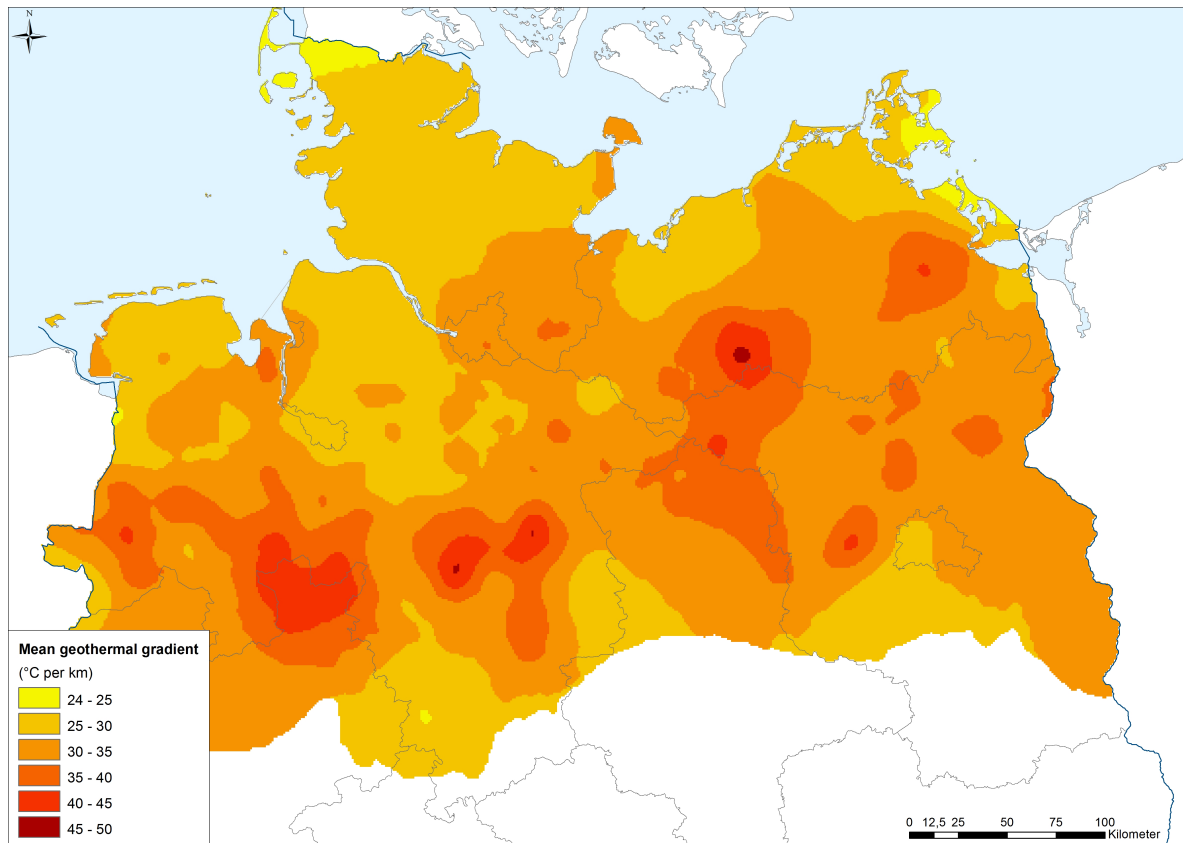


Figure 4.2.: The interpolated distribution of the geothermal gradient for the area of interest (based on (LIAG, 2012)). Figure from Kissinger et al. (2014).

available. Hence, the salt concentrations only vary with depth. For this, an average increase of the salt concentration of 15 g L^{-1} per 100 m is assumed for the formation fluid in the Middle Buntsandstein (Wolfgramm and Seibt, 2008). The salt concentration may not exceed the maximum salt concentration of 360 g L^{-1} .

The density and the viscosity of CO₂ and brine are dependent on the pressure, the temperature, and in the case of brine also on the salinity in the reservoir. The temperature can be directly obtained from the above data. To obtain the pressures and the salinities, hydrostatic conditions are assumed. The pressure is then dependent on the weight of the overlying fluid column. To calculate the hydrostatic pressure, an effective density for the overlying fluid column is iteratively determined by taking the average of the water density under surface conditions and

the brine density in the reservoir, which is a function of salinity, temperature and pressure. As the actual pressures are unknown, this is assumed to be a reasonable estimate. The salinity can thus also be determined from the calculated brine density in the reservoir and the salt concentration at each data point. Figure 4.3 shows the fluid properties of CO₂ and brine, as well as the data points of the database plotted over the independent variables pressure, temperature and salinity. With the calculated values of viscosity and density the gravitational number can be obtained using Eq. 4.3 for each data point. As explained in Sec. 4.1 the permeability and the specific injection rate are not varied in this calculation, and are therefore set to 1.

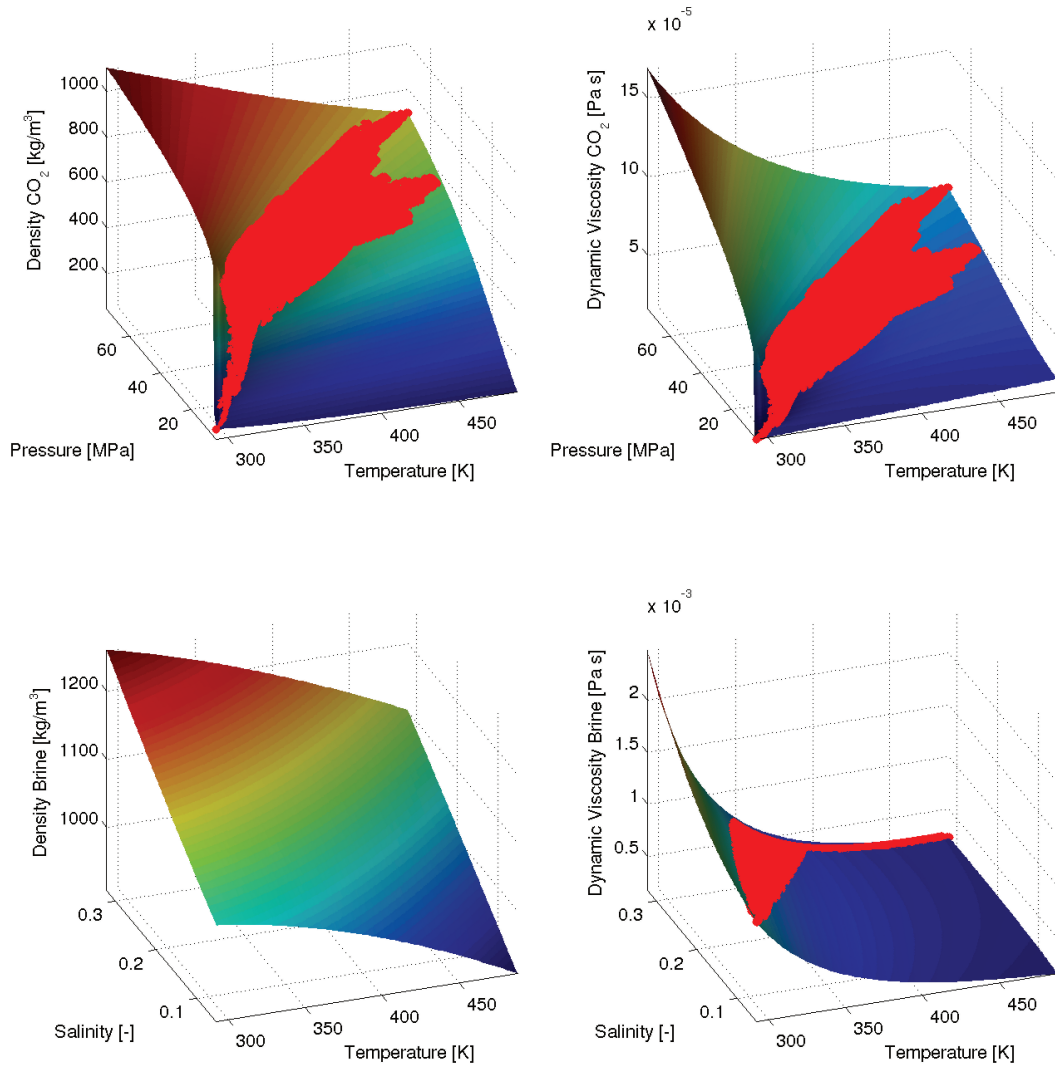


Figure 4.3.: The CO₂ density as a function of pressure and temperature (top left), the CO₂ viscosity as a function of pressure and temperature (top right), the brine density as a function of salinity and temperature (bottom left) and the brine viscosity as a function of salinity and temperature (bottom right). The red points are the data points from the database. They are not plotted with the brine density (bottom left) as they are a function of pressure, salinity and temperature and would therefore not fit on the brine density surface shown here. Figure modified after Kissinger et al. (2014).

4.3. Numerical Model Setup

A numerical simulation study is carried out to determine the simulated storage efficiency for several data points and thereby evaluate the quality of the Gr-criterion as an indicator thereof.

In all simulations, the 2p model is used, considering the brine and the CO₂ phases, as given by Eq. 3.7. All simulations are carried out with the numerical simulator DuMu^x. The numerical implementation is given in Sec. 3.3 with the Box-Method used for spatial discretization and the implicit Euler scheme for temporal discretization. The discretized equations are shown in Table 3.1. The reservoir setup is kept as simple as possible. It consists of a radially symmetric domain as illustrated in Fig. 4.4 with a CO₂ injection well in the middle. The injection rate is 0.1 Mt per year. The reservoir has a thickness of 25 m and is bounded by a low permeable cap

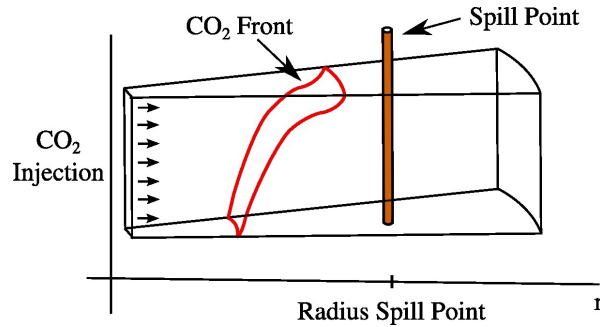


Figure 4.4.: Schematic setup of the model domain for the numerical simulations. Due to symmetry reasons only a small part of the radially symmetric problem is simulated. Figure from Kissinger et al. (2014).

rock at the top and bottom (permeability $1 \times 10^{-19} \text{ m}^2$, porosity 0.01 and 5 m thickness). Top and bottom of the domain have no flow boundary conditions. Dirichlet boundary conditions (constant pressure) are used as a lateral boundary condition (5 km from the injection well). The reservoir is homogenous and has a porosity of 0.2 and a permeability of $1 \times 10^{-13} \text{ m}^2$. For calculating the capillary pressure and the relative permeabilities a Brooks-Corey relationship (Brooks and Corey, 1964) with an entry pressure p_e of 10 000 Pa and a shape parameter λ_{BC} of 2.0, as shown in Fig. 2.5, is used. The residual water saturation S_{rw} is 0.3 and the residual CO₂ saturation S_{rn} is 0.0.

4.4. Results

First, the areal distribution of Gr in the Middle Buntsandstein rock unit is presented in Sec. 4.4.1. In Sec. 4.4.2 numerical simulation studies are carried out to show the effect of varying fluid properties on the storage efficiency. Further, the Gr-criterion and the Okwen-Method are compared to the simulation results. The significance of the Gr-criterion with regard to residual trapping is investigated in 4.4.3. Finally, in Sec. 4.4.4 the significance of the Gr-criterion, based on the initial fluid properties, is compared against the relevance of the

parameters porosity and reservoir thickness for three areas, with a high, medium, and low value of Gr.

4.4.1. Basin-Scale Application of the Gravitational Number

The calculated values of Gr vary from around 4×10^{10} to 1×10^{11} . To display the results in a map, these values have been divided into six classes, as shown in Fig. 4.5. Areas with low values of Gr are assumed to be indicative of a high storage efficiency and are depicted in light green. On the other hand, areas with high values of Gr are assumed to be indicative of a low storage efficiency and are depicted in red.

A comparison between the resulting Gr distribution (Fig. 4.5) with the regional geothermal gradient variations (Fig. 4.2), and the rock unit depths (Fig. 4.1) shows that for areas with shallow to medium depths (800–2000 m), the values of Gr are mainly affected by variations in the geothermal gradient. Thus, low geothermal gradients result in small Gr values whereas high geothermal gradients result in high Gr values. A similar observation can be made for areas with greater depths (2000–4000 m). However, this relation is slightly less pronounced than for the shallow to medium depths. For depths >4000 m, low values of Gr are predominant.

At depths between 800–4000 m, assuming that conditions are not close to or below the critical point of CO₂, only a moderate increase in CO₂ density and viscosity is observed over depth. Both the CO₂ density and the viscosity increase with increasing pressure and decrease with increasing temperature. For an increasing depth the influence of the pressure increase slightly outweighs the influence of the temperature increase. This causes only a moderate reduction of Gr over depth, and strongly relates the values of Gr to the lateral variations in the geothermal gradient.

4.4.2. Comparison of the Gr-Criterion and the Okwen-Method with Respect to Storage Efficiency

For the simulations, different representative data points are chosen which cover various depths and the full range of Gr values. These data points provide the conditions (pressure, temperature and salinity) upon which the initial fluid properties are calculated in the simulations. The varied properties of 7 data points used for the different simulations are presented in Table 4.1. A table containing the input data for all simulations is given in the Appendix in Table A.2. The measure of storage efficiency used in this work is determined by dividing the total mass of injected CO₂ when the plume reaches a spill point (see Fig.4.4), by the maximum lateral

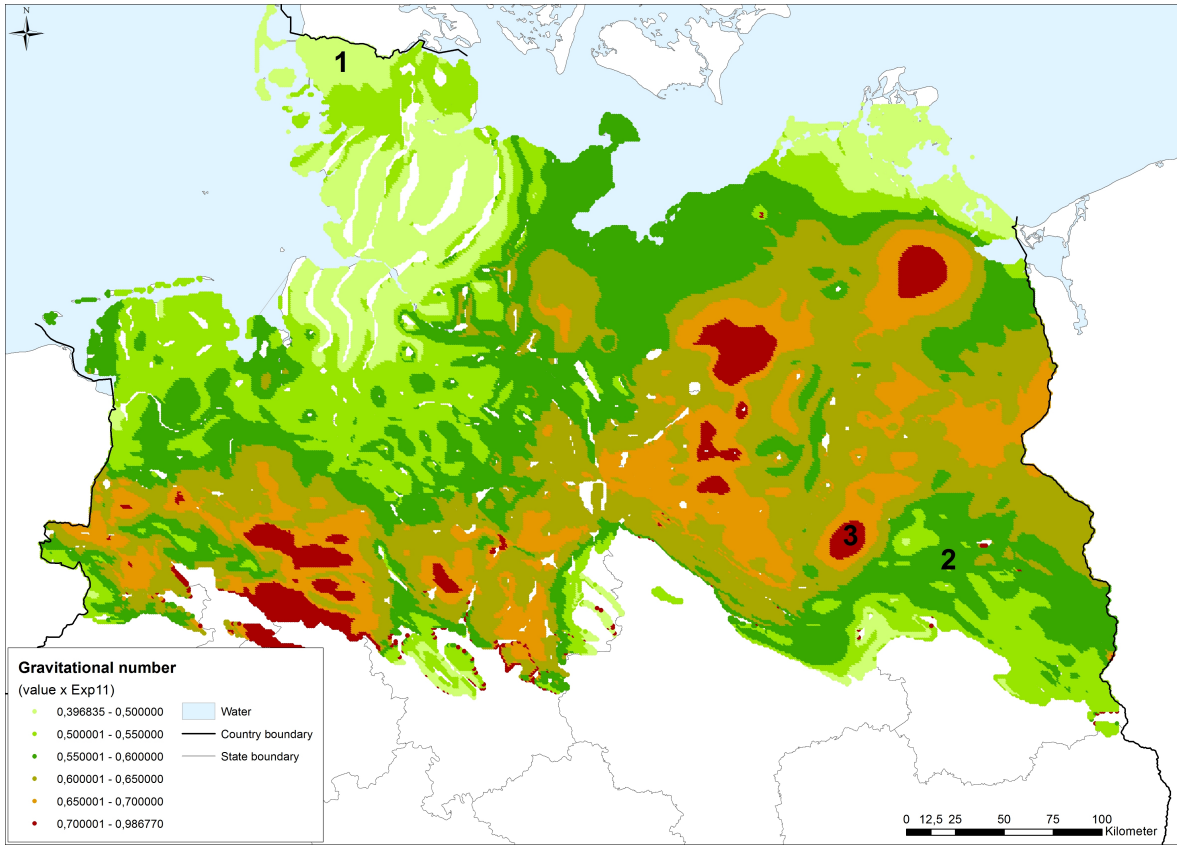


Figure 4.5.: Distribution of Gr for the Middle Buntsandstein rock unit in the North German Basin. The numbers refer to the areas selected in Sec. 4.4.4 (Area 1 = low Gr, Area 2 = medium Gr, Area 3 = high Gr). Figure from Kissinger et al. (2014).

area of the plume (lateral footprint):

$$\text{Storage Efficiency [kg/m}^2\text{]} = \frac{\text{Mass of CO}_2 \text{ in place}}{\pi \cdot (\text{Radius of Spill Point})^2}. \quad (4.6)$$

In this approach, the spill point represents a maximum acceptable extent for the CO₂ plume. The definition of storage efficiency used here is somewhat similar to the value of M_{eff} , which corresponds to the mass of CO₂ in place, that Kopp et al. (2009b) use for comparing the storage efficiency of different sites. The mass in place in this work is additionally divided by the lateral extent of the CO₂ plume (which is the same for all simulations) to emphasize that this value is an efficiency meant for comparing different sites, rather than an actual storage capacity. The injection rate is the same for all simulations. The longer it takes for the CO₂ to reach the spill point, the more CO₂ is injected into the system, and hence the storage efficiency is higher, as a larger part of the reservoir volume is utilized. The spill point is located at a

Table 4.1.: The initial fluid properties of seven different data points as well as Gr and the storage efficiency obtained from the simulations.

Cases	Depth m	ρ_w kg m ⁻³	ρ_n kg m ⁻³	μ_w/μ_n [-]	Gr [-] · 10 ¹⁰	Storage Efficiency kg m ⁻²
1	1492	1140	757	10.4	4.44	381
2	1735	1154	668	15.2	6.01	315
3	2304	1187	611	11.8	7.19	299
4	1865	1150	521	14.5	8.05	230
5	906	1083	371	32.3	9.60	165
6	1776	1161	734	15.2	5.05	362
7	3305	1200	758	9.1	4.98	450

radial distance of 1 km, from the injection well, as in Kopp et al. (2009b).

The simulation results, with corresponding values of Gr, are compared to the results obtained using the Okwen-Method (see Sec. 3.2.1). In order to make the analytical results comparable with the simulation results the volumetric storage efficiency E , defined in Eq. 4.4, is expressed in terms of mass of CO₂ per lateral area:

$$\text{Storage Efficiency [kg/m}^2] = \phi \rho_n H E. \quad (4.7)$$

ϕ is the porosity of 0.2 and H is the thickness of the reservoir of 25 m, which is also used in the simulations. For calculating the gravitational number Γ (see Eq. 4.5) defined by Nordbotten et al. (2005) the reservoir permeability k is the same as in the simulations ($1 \times 10^{-13} \text{ m}^2$) and the volumetric injection rate Q_{well} is obtained by dividing the injection rate (0.1 Mt per year) by the CO₂ density. The range of values of Γ for the points selected for the simulations is 0.24 to 1.34. Looking at Eq. 4.4, this means that the gravitational number Γ has to be considered for some of the data points (i.e. gravitational forces have to be considered for values of Γ greater than 0.5). Figure 4.6 shows the results of the simulations with the storage efficiency over Gr (left hand side) and the storage efficiency obtained by using Eq 4.7 (right hand side). On the left an inversely proportional linear trend relates high Gr to small storage efficiencies in the system for the simulations with depths ranging between 1000–2000 m. For the simulations, where the thermodynamic conditions of the reservoir are close to the critical point of CO₂ ($T_{crit} = 304.25 \text{ K}$ and $P_{crit} = 7.39 \text{ MPa}$, points marked in red in the left plot of Fig. 4.6), the storage efficiency is strongly underestimated by the a priori calculated Gr-criterion. This is due to the injection-induced pressure increase, which leads to strong deviations of the CO₂ density and viscosity from the initial thermodynamic conditions in the reservoir. For the points with depths greater than 2000 m, an increase of storage efficiency is observed when compared to the points between 1000 m and 2000 m. This can be explained by looking at cases

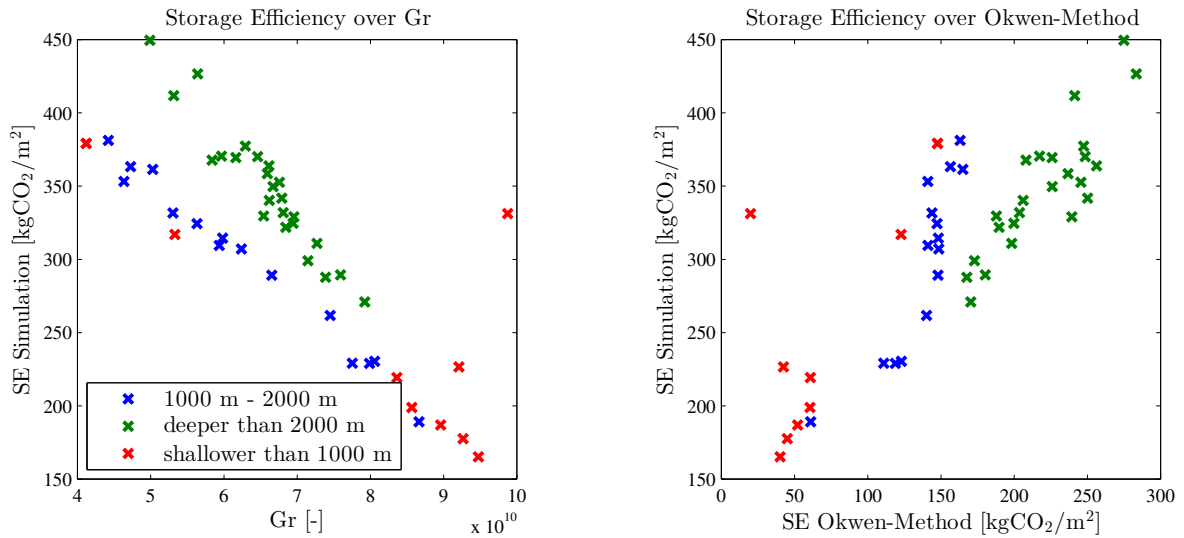


Figure 4.6.: **Left:** Simulation results in terms of storage efficiency (SE) for 49 data points over Gr. **Right:** The same simulation results plotted over storage efficiency obtained from the Okwen-Method using Eq. 3.37 and 4.7. Figure modified after Kissinger et al. (2014).

6 and 7 given in Table 4.1 (Note: The cases 6 and 7 are also included in Fig. 4.6). These cases have the same Gr value but different viscosity ratios. The brine viscosity is not considered in the Gr formula and decreases with increasing depth, due to the increasing temperature. This in turn leads to smaller viscosity ratios. The closer the viscosity values of brine and CO₂ are, the higher is the sweep efficiency due to the steeper CO₂ front profile. The increase in sweep efficiency results in a higher simulated storage efficiency for the deep cases (>2000 m) compared to the shallow to medium depth cases (1000–2000 m). The right hand side of Fig. 4.6 shows that the storage efficiency calculated with the Okwen-Method is generally smaller than the storage efficiency from the simulation results. This can be explained by the sharp interface assumption on which the analytical solution is based. In the simulations, capillary pressure reduces the saturation, and the relative permeability at the tip of the CO₂ plume leading to an increase in storage efficiency as explained in Sec. 4.1. However, numerical dispersion can also lead to smaller saturations at the plume tip, and could therefore be another reason for a reduced velocity at the tip of the CO₂ tongue, as reported in Møll Nilsen et al. (2011). In contrast, the CO₂ tongue in the sharp interface model moves faster as it has the maximum CO₂ saturation, and the maximum relative permeability of CO₂. Similar to the Gr-criterion, the sharp interface model underestimates the storage efficiency of shallow points (< 1000 m). For depths between 1000–2000 m the results of the Okwen-Method still seem to be influenced by the injection-induced pressure, which results in an underestimation of storage efficiency, compared to the simulation results. For depths greater than 2000 m the Okwen-Method is in

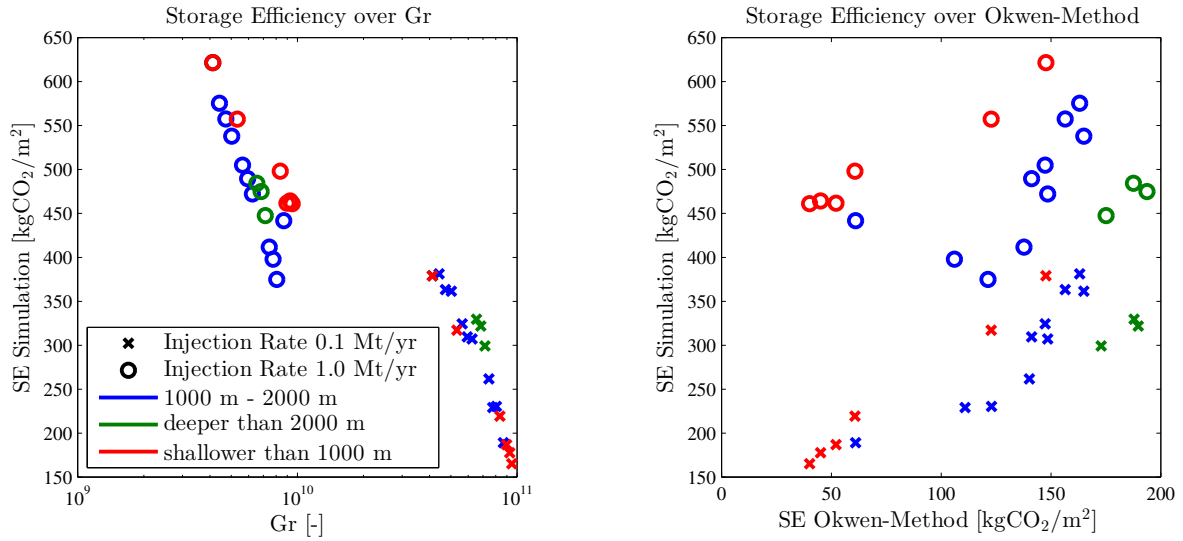


Figure 4.7.: **Left:** Simulation results for two injection rates (0.1 and 1.0 Mt per year) plotted over Gr. Note the logarithmic scaling of Gr. **Right:** The same simulation results plotted over storage efficiency (SE) obtained from the Okwen-Method using Eq. 3.37 and 4.7. Figure modified after Kissinger et al. (2014).

better qualitative agreement with the simulation results than for smaller depths. To conclude, the highest storage efficiencies in the simulations are obtained for the cases where the CO₂ density and the viscosity are high and the brine viscosity is low. This finding is in agreement with the results from the Okwen-Method. This implies that deep formations (below 2000 m) show the best storage efficiency.

20 of the above simulations with equi-distant values of Gr and depths up to 2500 m are repeated with an increased injection rate of 1.0 Mt per year. Obviously, this corresponds to a decrease in the values of Gr by a factor of 10. For the Okwen-Method this corresponds to a mean Γ of 0.045 for the 20 simulations with an injection rate of 1.0 Mt per year (i.e. volumetric storage efficiency is only dependent on the mobility ratio λ) and a mean Γ of 0.45 for the 20 simulations with an injection rate of 0.1 Mt per year (Γ has to be considered in some of the cases). It must be noted that a Γ of 0.045 is extremely small as the injection rate compared to the formation thickness is very high. However, these simulations should illustrate the effect of the injection-induced pressure increase on storage efficiency. The results are presented in Fig. 4.7. The the left hand side plot shows the simulated storage efficiency obtained with the high and the low injection rate. A discontinuity in the Gr values between data points having a similar storage efficiency (between 350 and 400 kgCO₂/m²) is recognizable. For a qualitative ranking, as proposed by Kopp et al. (2009a), which would also include regionalized data for the permeability, this suggests that reservoirs where high viscous forces are expected would be

falsely favored by the Gr-criterion. However, the general trend of a low Gr value corresponding to high storage efficiency within each injection regime (Gr of 10^9 and 10^{10}) is confirmed. For the Okwen-Method, the increased injection rate leads to a strong underestimation of storage efficiency, which is again related to the increased impact of the injection-induced pressure on the initial fluid properties.

4.4.3. Testing the Significance of the Gr-Criterion with Respect to Residual Trapping

Next, the effect of the initial fluid properties on the amount of residually trapped CO₂ is investigated. Generally, more CO₂ will be trapped if the sweep efficiency is increased. The amount of trapped CO₂ is calculated using the Land model (Land, 1968):

$$S_t^* = \frac{S_{max}^*}{1 + CS_{max}^*}, \quad (4.8)$$

where S_t^* is the saturation of the residually trapped CO₂, S_{max}^* is the maximum saturation reached during the drainage process, and C is the land trapping coefficient which is given by:

$$C = \frac{1}{S_t} - \frac{1}{S_{max}}, \quad (4.9)$$

where S_t is highest possible residually trapped CO₂ saturation, here assumed to be 0.3, and S_{max} is the maximum possible CO₂ saturation in the porous medium, here assumed to be 0.7. The highest CO₂ saturation S_{max}^* at every node in the domain is reached at the end of the simulation, since CO₂ is injected at a constant rate and the saturation values only increase over time. This simple approach for determining the residually trapped CO₂ saturation is chosen, as the aim is only to qualitatively compare the different simulations. The residual CO₂ saturation is then calculated for the 20 simulations shown in Fig. 4.7 for the case of the low injection rate (i.e. 0.1 Mt per year). The results are presented in Fig. 4.8. Here, Gr is again used as an indicator for the residually trapped CO₂. The amount of residually trapped CO₂ (green circles) shows a similar but weaker inversely proportional trend compared to the total CO₂ storage efficiency (residually trapped and mobile CO₂, blue crosses). The value of Gr clearly influences the amount of residually trapped CO₂ in the reservoir.

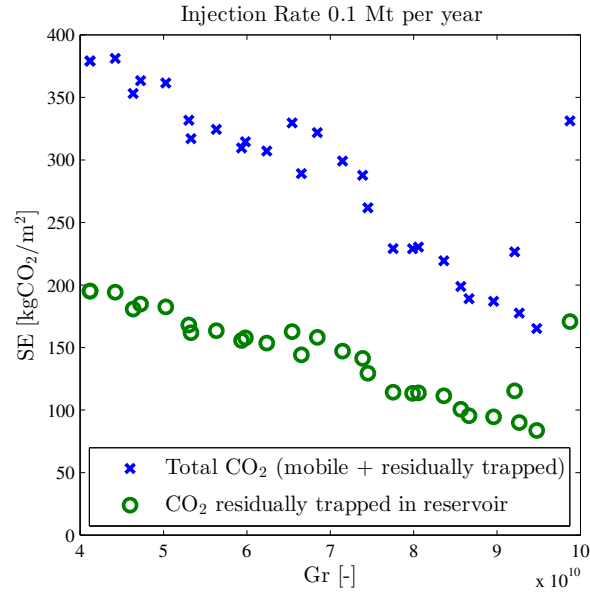


Figure 4.8.: Comparison of storage efficiency (SE) and the residually trapped CO₂ mass (also given in terms of storage efficiency, i.e. kg/m²). Figure modified after Kissinger et al. (2014).

4.4.4. Testing the Significance of the Gr-Criterion with Respect to Porosity and Reservoir Thickness

Permeability, reservoir thickness and porosity are crucial parameters to assess the significance of reservoir units (Reinhold et al., 2011). However, in this study permeability cannot be considered since there is not sufficient data available to reliably account for its basin-wide variability. An analysis of the significance of the Gr-criterion can only be carried out with respect to the variation of the parameters reservoir thickness and porosity. Three areas of high, medium, and low values of Gr were selected by the project partners of the BGR, where data for the reservoir thickness and the porosity are available. More information regarding the sources of these data is given in Kissinger et al. (2014). The locations of these areas are shown in Fig. 4.5. The characteristic parameters of the three areas are listed in Table 4.2.

Area 1 (Mean Gr value: 4.85×10^{10}) represents regions with a small value of Gr. According to the database, the thickness varies between 6 and 20 m. The porosity values range from 0.11 to 0.30.

Area 2 (Mean Gr value: 5.73×10^{10}) is related to regions with medium values of Gr. For this area the thickness varies between 5 and 20 m, whereas porosity data ranges from 0.06 to 0.25.

Area 3 (Mean Gr value: 7.27×10^{10}) represents regions with the highest Gr values. For this region an average thickness of 10 m and porosities between 0.04 to 0.08 are reported.

In order to deal with the variability of the porosity and thickness data in the three areas,

Table 4.2.: The characteristics of the three different areas. Note that for Area 1 and 3 there are only ranges of a minimum and maximum value for porosity and thickness. For Area 2 the data points are listed in the the appendix in Table A.1. The values for pressure, temperature, salinity and Gr are the mean values for each area and are used as initial conditions for the simulations.

	Area 1	Area 2	Area 3
Data Type	Range	9 data points	Range
Porosity [-]	0.11 - 0.30	0.06 - 0.25	0.04 - 0.08
Thickness [m]	6 - 20	5 - 20	10
Gr [-] · 10 ¹⁰	4.85	5.73	7.27
Pressure [MPa]	21.4	18.9	19.0
Temperature [K]	331	335	351
Salinity [$\frac{\text{kg Salt}}{\text{kg Brine}}$]	0.25	0.23	0.23

Monte-Carlo simulations are carried out. For Areas 1 and 3, where only a range of porosity and thickness values (maximum and minimum) is available, a uniform distribution of these parameters within their ranges is assumed. By means of an arbitrary polynomial chaos expansion in combination with the probabilistic collocation method, presented in for example Oladyskhin et al. (2011b), Oladyskhin et al. (2011a) and Oladyskhin and Nowak (2012), these data are integrated into the modeling process. The result is a polynomial from which the mean storage efficiency as well as the standard deviation of the storage efficiency in the two areas can be calculated. For Area 2, nine data pairs of porosity and thickness (see appendix in Table A.1) are available, for which nine simulations were performed to calculate the mean storage efficiency and the standard deviation. For all areas, the storage efficiency is now a function of the area-specific porosity, the reservoir thickness distribution, and the mean initial fluid properties. The mean initial fluid properties used here are obtained from the area-specific mean temperature, pressure and salinity values given in Table 4.2. The numerical simulation setup is the same as described in Sec. 4.3, except that the porosity and thickness of the aquifers are varied according to the area-specific probability distribution.

Figure 4.9 shows the results of the simulations. The plot on the left shows the mean storage efficiency along with its standard deviation for each area over the mean Gr value of this area. The results show a clear trend of decreasing storage efficiency with increasing Gr. The standard deviations of Area 1 (low) and Area 2 (medium) are much higher than for Area 3, due to the small range of porosities (4-8 %) and the constant thickness (10 m) in Area 3. In Fig. 4.9 left, the storage efficiency is a function of both Gr (i.e. initial fluid properties) and the joint probability functions of porosity and thickness for each area. Therefore, it is not obvious which of the two has the highest influence on storage efficiency. Thus, additional simulations are carried out where the Gr value is kept constant, i.e. the same initial fluid properties for

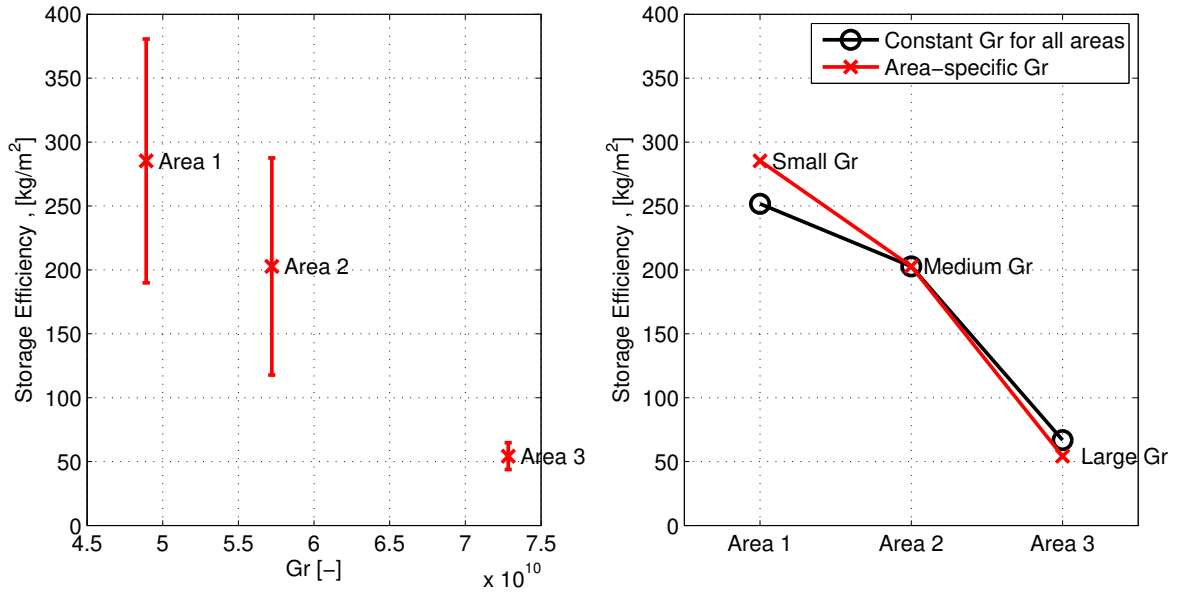


Figure 4.9.: **Left:** Storage efficiency over Gr. The cross marker represents the mean storage efficiency and the bars indicate the standard deviation. **Right:** Mean storage efficiency for the three areas with constant Gr for all areas (black curve) and area-specific Gr (red curve). Note: the three means for the area-specific case (red cross marker) on the right plot are identical to the three means on the left plot (red cross marker). Figure modified after Kissinger et al. (2014).

the three areas. Here the Gr value of Area 2 is chosen for the three areas. Figure 4.9 (right) compares the simulated mean storage efficiencies for the constant Gr case (i.e. Gr value of Area 2) with the previously performed simulations with the area-specific Gr values (red line). It can be seen that the trend is mainly caused by the different distributions of porosity and thickness of the three areas. The trend improves due to the area-specific value of Gr, i.e. a small value of Gr leads to an increase of storage efficiency compared to the constant Gr case and a high value of Gr leads to a decrease of storage efficiency compared to the constant Gr case. This is the expected behavior which is in agreement with the findings of Sec. 4.3. For Area 1, the contribution of Gr to the storage efficiency is much higher than for Area 3. To conclude, the expected qualitative influence of the Gr criterion on storage efficiency in the three areas is supported by the simulation results. However, the clear trend seen on the left hand plot of Fig. 4.9 is mainly caused by the different distributions of porosity and thickness. Only between Area 1 and Area 2 can a significant increase of storage efficiency be contributed to the different Gr values.

4.5. Discussion

There are different criteria that can be used for a basin-scale site screening for CO₂ sequestration. Among others, the Gr-criterion (Kopp et al., 2009a) or the analytical solution by Okwen et al. (2010) can be useful criteria to consider for estimating storage efficiency. Due to an insufficient regional database of hydrogeological parameters, such as permeability porosity, and reservoir thickness, the input data here are restricted to reservoir depth, temperature conditions, and salt concentrations. For this study, only the Middle Buntsandstein rock unit is considered. However, the Gr-criterion or the Okwen-Method may also be applied to other storage units within the Storage Catalogue of Germany.

As the simulations in Sec. 4.4.2 show, the Gr-criterion may be used to distinguish areas with more or less favorable initial fluid properties. Care should be taken when comparing areas of small to medium depths (1000–2000 m) to areas of large depths (>2000 m). As the simulations have shown, the decrease in brine viscosity with depth due to increasing temperature leads to a smaller viscosity ratio which increases the storage efficiency. This behavior cannot be described with the Gr-criterion. The Okwen-Method, also considers the variation in brine viscosity, and therefore shows a more consistent trend for larger depths. An additional advantage of the Okwen-Method is that it can be used to quantify storage efficiency, in contrast to the Gr-criterion which only allows for a qualitative ranking. If, for example, data for the porosity were regionally available, this data could easily be incorporated in the Okwen-Method. The simulations further show, that changes in pressure, caused by the injection, lead to an underestimation of storage efficiency in areas having conditions close to the critical point of CO₂. But also for the depth range of 1000–2000 m, the Okwen-Method seems to underestimate storage efficiency, due to these changes in the CO₂ fluid properties.

For the simulations with a higher injection rate (factor 10 increase), the viscous forces increase and therefore, the values of Gr decrease by the same factor. However, the storage efficiency does not increase as much as would be expected from the Gr-criterion. For a qualitative ranking, which would include regionalized data for the permeability, that may vary over orders of magnitude, the Gr-criterion may falsely favor regions with a very low permeability (i.e. very high viscous forces) over regions with a higher permeability. This ambiguity has to be considered when choosing appropriate methods for a basin-scale screening, also bearing in mind that such methods or criteria should be transparent and comprehensible to stakeholders. Therefore, the use of Gr as a screening criterion should be restricted to ranking regions with more or less favorable initial fluid properties for CO₂ storage. The Okwen-Method clearly underestimates the storage efficiency for the cases with an increased injection rate, as it cannot account for the effect of the injection-induced pressure increase on the fluid properties of CO₂. Considering a case where regionalized data for permeability would be available, low per-

meabilities could reduce the injectivity, and therefore also the storage efficiency. Thus, an additional constraint on pressure, which should not exceed the fracturing pressure would be required. Areas could be excluded by using the method proposed by Mathias et al. (2008, 2009), which allows for the determination of the maximum pressure buildup during a CO₂ injection. Considering the plume extent which is also used as a constraint in this work (i.e. spill point), the reservoir geometry plays an important role (e.g. dipping or anticlinal) that may significantly influence storage efficiency as well (Goater et al., 2013). This discussion makes it clear that criteria like the Gr-criterion or the Okwen-Method can only be part of a larger set of criteria that have to be evaluated.

The effect of the Gr-criterion on the amount of residually trapped CO₂ described in Sec. 4.4.2 is recognizable and confirms the expected increase in residually trapped CO₂ for systems with lower Gr values compared to systems with higher Gr values. Hence, a low Gr value is likely to be beneficial for long term storage safety.

The simulations in Sec. 4.4.4 illustrate that changes in storage efficiency, due to variable porosities and reservoir thicknesses, are larger than the changes between a low, a medium, and a high value of Gr. Nevertheless, the influence on storage efficiency caused by different values of Gr (i.e. different initial fluid properties) may still be in the same range as the influence of the area-specific distributions of porosity and reservoir thickness. It must be noted that the database of porosity and reservoir thickness used here is not very large and that more data would be necessary to get the complete picture. However, the simulations may still help to gain an insight on the effect of the variability of these parameters.

4.6. Conclusion

The main results and findings of this chapter are summarized briefly below:

- The simulations show that the variations of depth, temperature conditions and salt concentrations, as found in the Middle Buntsandstein rock unit of the North German Basin have a noticeable influence on the CO₂ and brine densities and viscosities, and thus on storage efficiency.
- Storage efficiency is highest for depths greater than 2000 m where the CO₂ density and the viscosity are high and the brine viscosity is low. This result is in agreement with the Okwen-Method and simulations by Kopp et al. (2009b) for deep reservoirs with a small viscosity ratio (μ_w/μ_n).

-
- The regional Gr distribution for the Middle Buntsandstein rock unit is mainly affected by the regional variations of the geothermal gradient.
 - With some restrictions both Gr and the Okwen-Method can be used as indicators for storage efficiency.
 - The simulations confirm the trend of decreasing Gr values leading to an increasing storage efficiency. Low values of Gr leading to a more compact CO₂ plume are in agreement with findings in Nazarian et al. (2013), where a similar formulation of Gr was used.
 - At depths greater than 2000 m, the Gr-criterion starts to underestimate storage efficiency, as the effect of a decreasing brine viscosity is not considered. Here, the Okwen-Method shows a more continuous trend.
 - The Gr approach and the Okwen-Method both underestimate the storage efficiency for thermodynamic conditions close to or below the critical point of CO₂, as the fluid properties of CO₂ are very sensitive to pressure changes caused by the injection.
 - Smaller Gr values lead to more residually trapped CO₂ in the reservoir, and to more storage security. This result is in qualitative agreement with the findings of Taku Ide et al. (2007).
 - Comparing the contribution of the initial fluid properties on storage efficiency to the contribution of the parameters porosity and reservoir thickness, shows that the porosity and the reservoir thickness are more important. However, the contribution of the initial fluid properties can still be in the same range as that of the other two parameters.

5. Large-Scale Investigation of Brine Displacement¹

In this chapter, the focus lies on the effects of large-scale brine migration due to CO₂ injection in a realistic (but not real) geological structure in the North German Basin. The latter is the most relevant region regarding CO₂ storage capacity in Germany (Knopf et al., 2010). The geological model comprises layers from the Lower Buntsandstein up to potential drinking water horizons in shallow, freshwater aquifers along with characteristic geological features of the North German Basin. In contrast to earlier work for example by Kempka et al. (2013), the model presented here fully couples flow in shallow aquifers with deep saline aquifers considering variable-density flow. As uncertainty is inherent to hydrogeological problems, a classification of different types of uncertainty is made in Sec. 5.1, which helps in categorizing the results presented later. The data available for the geological model and the numerical model setup are presented in Sec. 5.2 and 5.3, respectively. The reliability of the numerical model is then tested for (i) large scale pressure propagation due to injection with the Zeidouni-Method (Sec. 5.4.1) and (ii) variable-density flow using experimental data from the popular saltpool benchmark (Sec. 5.4.2). The results section has the following aims:

- Definition of target variables, suitable for the analysis of brine displacement (Sec. 5.5.1).
- Analysis of different scenarios in order to identify relevant components of the geological model controlling brine displacement (Sec. 5.5.2).
- Comparative analysis of model simplifications, in order to develop an understanding what assumptions in the model may be relevant and when, i.e. to design the optimal model with respect to required accuracy, computational costs, data availability and the uncertainty in these data (Sec. 5.5.3).

¹Large parts of this chapter will be published in Kissinger et al. (2017).

5.1. Uncertainty Categorization and Brine Displacement

Every model result is inherently subject to uncertainty, mainly from input data and from model assumptions. The type of uncertainty can be categorized along with a qualitative or quantitative estimation of the model uncertainty. Communicating uncertainty in simulation results is a crucial aspect for decision making. The approach by Walker et al. (2003), for the classification of uncertainties, is followed here, similarly to Walter et al. (2012), who have adopted this approach in the context of risk estimation for CO₂ storage. Walker et al. (2003) categorize the uncertainties into different levels on a scale (see Fig. 5.1) where determinism (a hypothetical state where everything is known) is on the far left end of the scale. The first level of uncertainty is statistical uncertainty which accounts for all model parameters that can be described by statistical terms, for example, a probability density function (PDF). In the hydrogeological context this can be, for example, a probability density function of

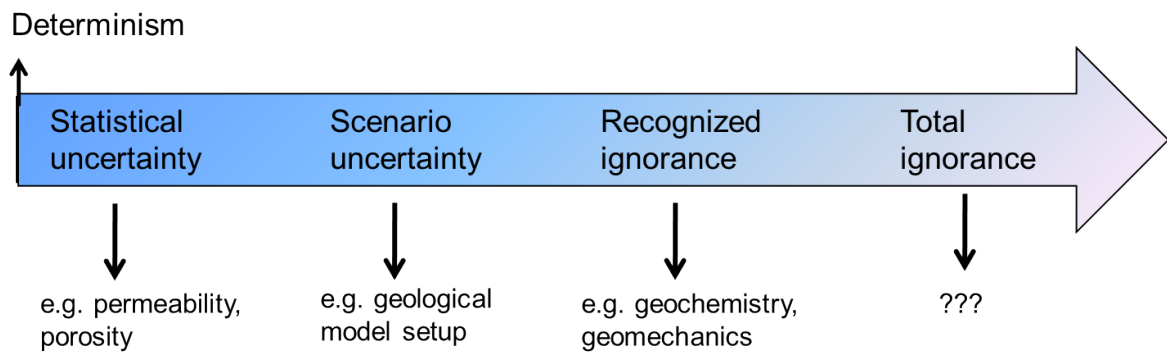


Figure 5.1.: Levels of uncertainty after Walker et al. (2003), modified by Walter et al. (2012).

permeability or porosity. The second level is defined as scenario uncertainty and includes parameters which cannot readily be described by statistical terms. This could be the existence of a certain geological feature, like the presence of a permeable fault zone at a certain location, or the type of boundary condition chosen on the lateral boundaries, etc. The next level is recognized ignorance which is defined by Walker et al. (2003) as fundamental uncertainties about mechanisms and functionalities. Recognized ignorance is any uncertainty caused by neglecting certain physical processes within the model concept. It will also be referred to as model uncertainty in this work. A model is always an abstraction of reality, as complex as necessary and as simple as possible. In contrast to the last category, total ignorance, which stands for all uncertainties that have simply not been recognized yet, model uncertainty can be reduced by comparing models of different conceptual complexity. The analysis presented below will focus on scenario uncertainty, and model uncertainty (i.e. recognized ignorance).

5.2. Available Data

The geological model was set up by the project partners of the Federal Institute for Geosciences and Natural Resources of Germany (BGR) within the CO2BRIM project. More details of the setup can be found in Class et al. (2015) or in Kissinger et al. (2017).

In this section only an overview of the geological model and its parametrization will be given. The model consists of 12 layers, from the Zechstein at the base, to the Quaternary near the surface, and has a geological setup typical for the North German Basin (NGB). The injection horizon is known as the Solling layer and is part of the Middle Buntsandstein. Figure 5.2 shows the top of the Solling layer along with the Zechstein in blue which pierces the Solling where the salt wall is located. The depth of the Solling layer varies enormously. The injection point shown in Fig. 5.2 is located at a depth of 1651 m. The parametrization of the sediments flanking the salt wall is highly uncertain. According to LBEG (2014) "the contact zone between salt domes and the CO₂-sequestration horizon is assumed to be a zone of weakness, similar to geological faults". This is of course a matter of debate. Making a conservative assumption, the sediments near the salt wall are considered permeable in this work, and are treated like a permeable fault zone. The injection horizon Solling is located beneath the Upper Buntsandstein barrier,

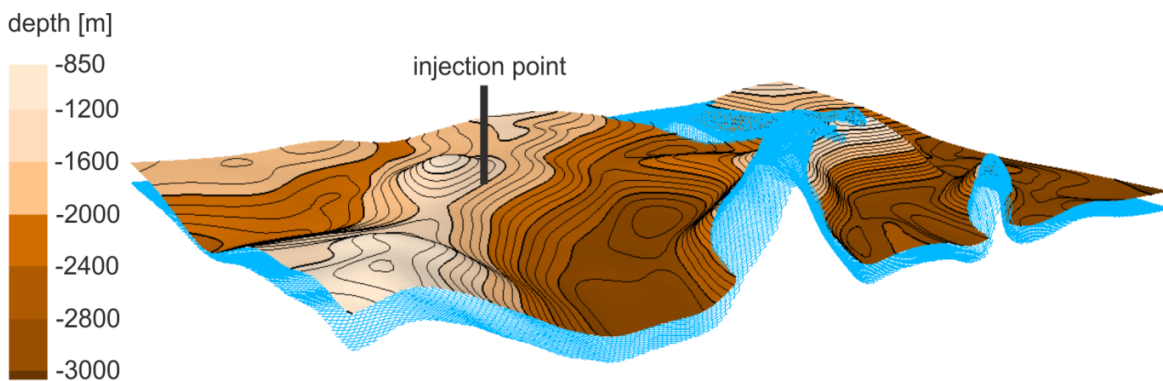


Figure 5.2.: Top of the Solling injection horizon discontinuous where the salt wall penetrates the layer. The top of the Zechstein salt is displayed with a blue mesh. The injection point at the flank of the anticlinal structure in about 1651 m depth is projected on top of the Solling injection horizon. Vertical exaggeration is 2:1. Figure from Kissinger et al. (2017).

which is one of the two main barriers in the geological model. The other primary barrier is the Rupelian clay barrier, which is considered a hydraulic barrier between shallow freshwater and deep saline aquifers. The top of the Rupelian clay barrier is shown in Fig. 5.3. Depicted in blue is the top of the underlying Cretaceous layer which pierces the Rupelian clay barrier at several locations. The two more round-shaped discontinuities are termed here as hydrogeological windows in the Rupelian clay barrier. The long discontinuity in the middle of the domain

is caused by the salt wall lifting the Cretaceous layer. These three discontinuities play an important role in the exchange between saline water and freshwater. In the context of CO₂ storage, they can be considered potential pathways for saltwater. The Upper Buntsandstein barrier is discontinuous at the locations where it is penetrated by the salt wall, similar to the injection horizon Solling shown in Fig. 5.2. The top of the geological model consists of

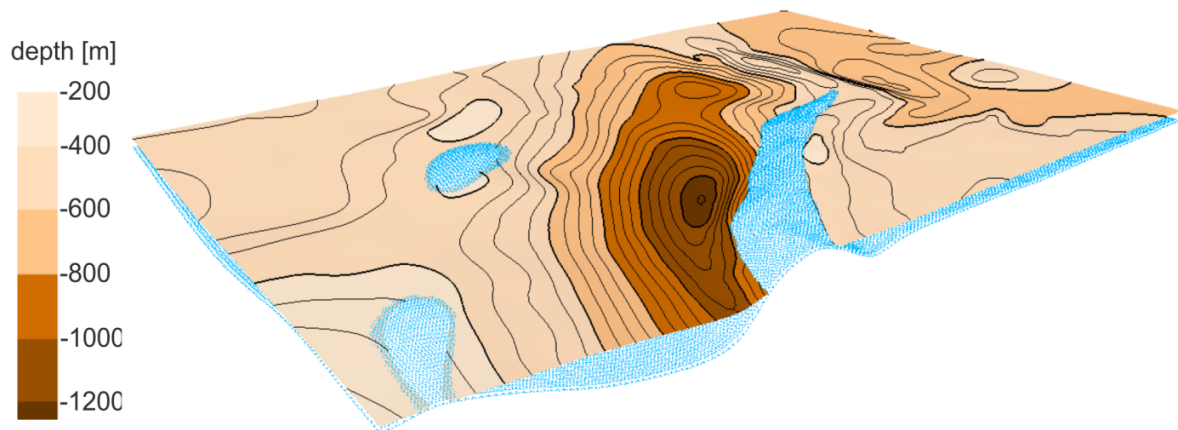


Figure 5.3.: Top of the Rupelian clay barrier with discontinuities where Cretaceous sediments penetrate the Rupelian clay barrier. The top of the Cretaceous is displayed as blue mesh. Vertical exaggeration is 2:1. Figure from Kissinger et al. (2017).

groundwater isolines from an upper freshwater aquifer. In order to simulate the groundwater flow in the shallow aquifers data of the main rivers derived from the associated catchment area are used, see Fig. 5.4. Both datasets (groundwater isolines and data on rivers) were prepared to be used as upper boundary conditions on top of the model (data provided by LUGV (2012); LUGV (2014)).

The different layers and the grid are shown in Fig. 5.5. The grid consists of hexahedral elements with a constant horizontal discretization length of 300 m × 300 m. The vertical resolution depends on the thickness of each layer resolved in the model, and varies between 10 and 300 m. The smallest vertical resolution, 10 m, is found within the injection horizon Solling. Each layer is assumed to be homogeneous, i.e. having a single permeability and porosity value assigned to it. The parametrization of the layers is given in Table 5.1. Data for lithological composition and the corresponding hydrogeological parameters are derived from regional literature data and numerical simulation studies (Larue, 2010; Reutter, 2011; Schäfer et al., 2011; Noack et al., 2013). Since the Zechstein layer is impermeable, it is not included in the numerical model, except for the parts where the salt wall penetrates the above layers. As can be seen in Table 5.1, the Quaternary unit is split into two parts. Compared to the bottom section of this Quaternary unit (Quaternary 2), the top section (Quaternary 1) has a higher

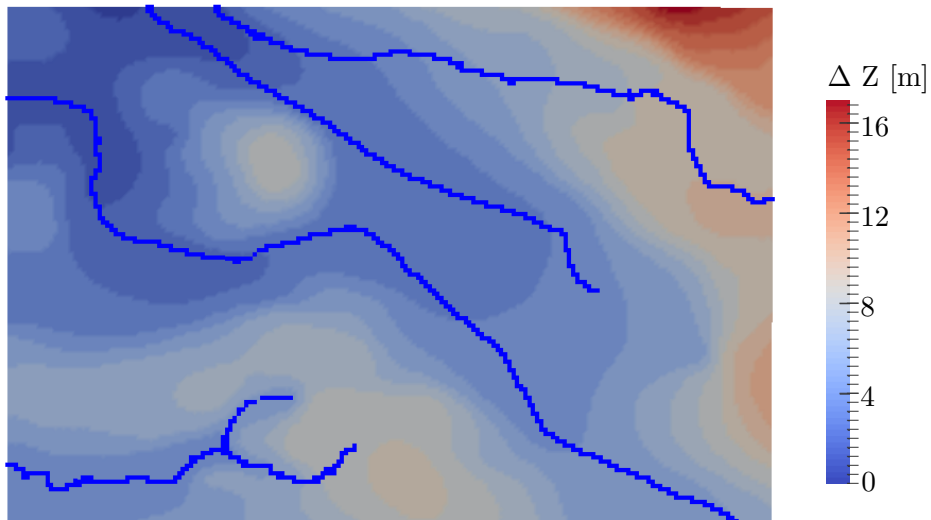


Figure 5.4.: Top view on the groundwater table. The rivers are highlighted in blue. The elevation values are normalized to the minimum elevation of the groundwater table. Figure from Kissinger et al. (2017).

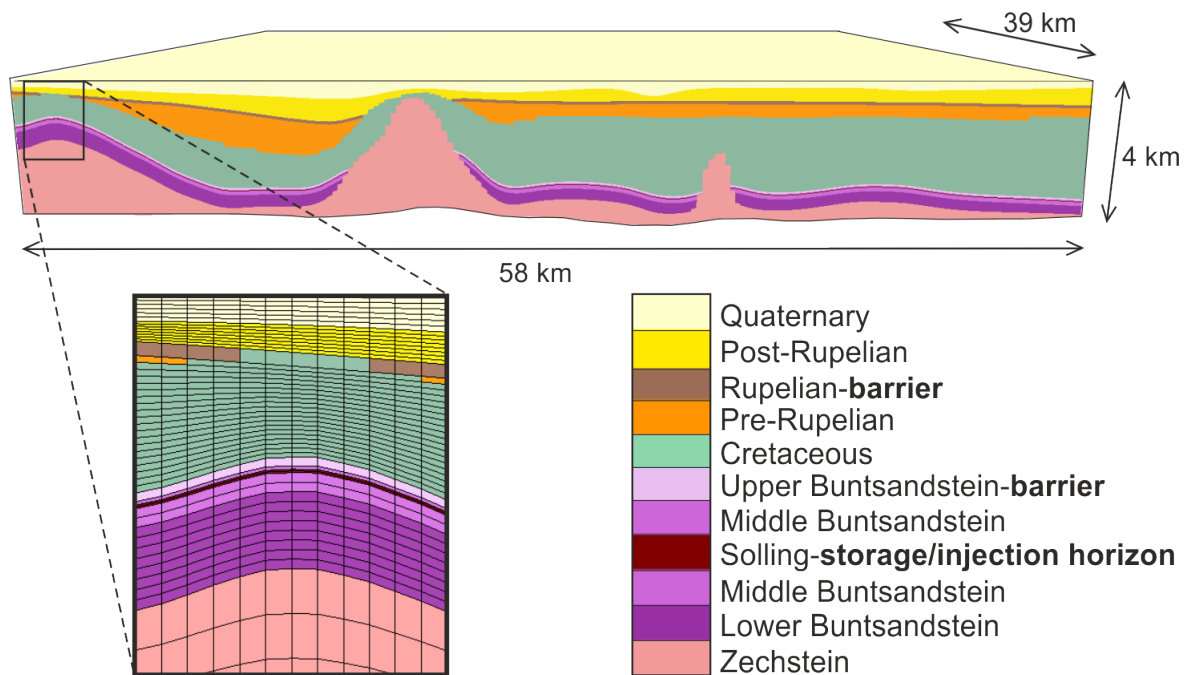


Figure 5.5.: Perspective view on the 3D geological model with zoom in on the anticlinal structure showing the mesh of the 3D volume model. Vertical exaggeration 2:1. Here Quaternary 1 and 2 are combined in the Quaternary layer. Figure from Kissinger et al. (2017).

permeability. This is the result of a stationary calibration performed in order to obtain a

Table 5.1.: Properties of the model layers according to Larue (2010); Reutter (2011); Schäfer et al. (2011); Noack et al. (2013).

Layer	Lithology	Thickness [m]	Porosity [%]	Permeability [m ²]
Quaternary 1	sand, gravel	100	20	6×10^{-11}
Quaternary 2	sand, gravel	200	20	1×10^{-12}
(Tertiary) Post-Rupelian	sand, silt	400	15	1×10^{-13}
(Tertiary) Rupelian clay barrier	clay	80	10	1×10^{-18}
(Tertiary) Pre-Rupelian	sand, sandstone	350	10	1×10^{-13}
Cretaceous	chalk, claystone	900	7	1×10^{-14}
Upper Buntsandstein barrier	salt, anhydrite, claystone	50	4	1×10^{-18}
Upper Middle Buntsandstein	siltstone	20	4	1×10^{-16}
Solling	sandstone	20	20	1.1×10^{-13}
Lower Middle Buntsandstein	siltstone	110	4	1×10^{-16}
Lower Buntsandstein	clay- and siltstone	350	4	1×10^{-16}
Permian Zechstein	rock salt	-	0.1	1×10^{-20}
Fault zone	-	50	30	1×10^{-12}

reasonable pressure distribution in agreement with the groundwater isolines and the recharge boundary conditions applied at the top of the Quaternary 1 (boundary conditions will be discussed in more detail in the next section). Further, the fault zone permeability and porosity of the reference setting are shown in the table. The location and implementation of the fault zone will be discussed in Sec. 5.3.

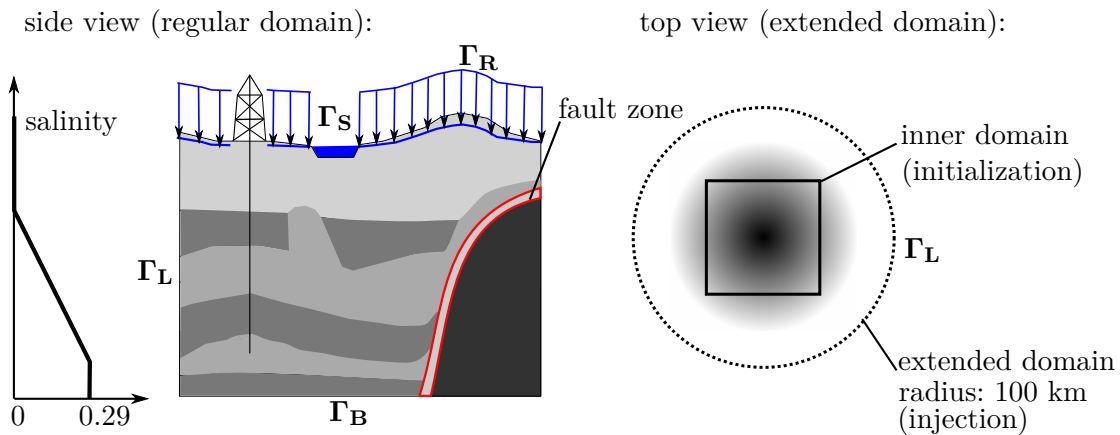
5.3. Numerical Model Setup

For the analysis of model simplifications (model uncertainty) below, four different models will be used to investigate brine migration in the geological setting, that was previously introduced in Sec. 5.2. These models are described in detail in Chapter 3. The reference model is the single-phase (brine), two-component (water and salt) model, referred to here as 1p2c model. The 1p2c model accounts for variable-density flow, due to salt transport. The model simplifies the injection process, as brine is injected instead of CO₂. The single-phase (brine) single-component (water) model, referred to here as 1p1c model, is a simplification of the 1p2c model, where salt transport is neglected and salt is instead considered to be a pseudo component. This means that locally varying salinities within the domain can be defined. This will affect the fluid properties (density and viscosity), but these salinities are held constant during the simulation (similar to the geothermal gradient). The third model accounts for

two-phase flow (brine and CO_2) as well as three-component (water, CO_2 and salt) transport and is referred to as the 2p3c model. This model is the most complex model considered, as it takes into account the injection and transport of CO_2 , as well as the salt transport. The 1p1c, 1p2c, and the 2p3c models are solved numerically, using the Box-Method for spatial discretization, and using the Implicit-Euler scheme for temporal discretization. They are implemented in the numerical simulator DuMu^x (see Sec. 3.3). The fourth model used is the Zeidouni-Method discussed in Sec. 3.2.2. It is used for two reasons: (i) to verify the numerical models in terms of discretization and system length, and, (ii) as a model simplification, where salt transport is neglected, brine is injected instead of CO_2 , and the geometry is significantly simplified.

5.3.1. Boundary and Initial Conditions for the Numerical Models

Realistic boundary and initial conditions are required for a sound prediction of brine flow due to CO_2 injection. In this section, the boundary conditions for the numerical models (1p1c, 1p2c, and 2p3c) are explained. The boundary conditions are illustrated in Fig. 5.6. On the



Γ_R Recharge: fresh water flux 100 mm/a **Γ_L Lateral:**
 Γ_S Stream: Atm. pressure, zero salinity initialization run - no flow (inner domain)
 Γ_B Bottom: no flow for water, sal. = 0.29 injection run - infinite aquifer (extended)

Figure 5.6.: Boundary and initial conditions of the domain. Also shown is the position of the fault zone situated on the flank of the salt wall in red.

top boundary (Γ_R), a constant water recharge of 100 mm/year is set (Neumann boundary condition) except for the nodes located at a river (Γ_S), where a constant atmospheric pressure is set (Dirichlet boundary condition). The rivers act as a sink in the system. Figure 5.4 shows the top view of the domain with the location of the rivers and the elevation of the groundwater table. Note that the differences in the elevation of the groundwater table are rather small

(17 m). It is assumed that full hydraulic contact exists between the rivers and the groundwater. Four episodes are distinguished in the numerical simulations:

1. Pre-initialization episode (1 s)
2. Initialization episode (300 000 years)
3. Injection episode (50 years)
4. Post-injection episode (50 years)

The first two episodes are required to establish a quasi-stationary base flow. The pre-initialization episode is needed to determine the pressure field, which is dependent on the geothermal gradient, the recharge boundary conditions, and the initial salt distribution, prescribed for this episode as a pseudo component. This means that only the pressure is variable in the pre-initialization run. A stationary pressure field can be established with a single time step. This is achieved by reducing the value of the storage term at every node by several orders of magnitude via a reduction of the porosities. The initial salt distribution below the Rupelian Clay Barrier is assumed to follow a linear increase of salinity with depth, with a maximum salinity of 0.29 kg–Salt/kg–Brine, see Fig. 5.6 (left).

The initialization episode (second episode) is required to obtain a quasi-stationary salt distribution. The porosities are set again to their normal values and salt transport is included. The pressure field determined from the pre-initialization episode is used as an initial condition for the pressure. Salt may enter the system for the 2p3c and the 1p2c models at the bottom boundary, where a fixed maximum salinity of 0.29 is set. The salt wall acts as another source of salt for the 1p2c and the 2p3c models with a fixed maximum salinity of 0.29 assigned to it. However, the maximum salinity is not assigned to the nodes in the fault zone, which is located at the interface between the salt wall and the surrounding layers. At the fault zone, the salinity is allowed to change. Given the initial salt distribution (linear salt gradient) a non-linear system (variable-density flow) is then solved forward in time. A theoretical steady state, which would be possible given the boundary and initial conditions is not reached as the simulations are terminated after a certain time (300 000 years for the cases considered here). The 1p1c model only requires the pre-initialization run, as this model neglects salt transport and treats the salt component as a pseudo component. Both initialization episodes consider the lateral boundaries to be closed.

After the initialization episode, the pressure and the salt distribution are quasi-stationary on the time scale of the injection and post-injection episodes (100 years). This means that during this period, without injection, no recognizable changes in the concentration field occur. The results from the initialization episode (i.e. pressure and salinity distribution) serve as an initial condition for the injection episode. To allow pressure propagation beyond the inner domain

during the injection episode, the domain is extended laterally. For this, the grid extension described in Sec. 3.3.6 is applied for the layers with a permeability greater than $1 \times 10^{-15} \text{ m}^2$ beneath the Rupelian clay barrier (i.e. Pre-Rupelian, Cretaceous and Solling layers). The grid extension is also illustrated on the right hand side of Fig. 5.6. The layers are extended to a distance of 100 km from the center of gravity of the inner domain. All other lateral boundaries remain closed. As will be shown in Sec. 5.4 this distance is sufficient to make the boundaries of the inner domain act as infinite aquifers.

5.3.2. Fault Zone Representation Using a Discrete-Fracture Model

In the geological model, a fault zone with a width of 50 m is considered near the salt wall. Since the horizontal discretization length of the numerical models is about 300 m, representing the geometry of the fault zone accurately would require a grid refinement over large areas. This would substantially increase the computational costs. In order to avoid the grid refinement, the fault zone is implemented with a discrete fracture approach, by defining the fault zone as a single large fracture, as described in Sec. 3.3.5. A fracture can be described by three parameters: fracture width, fracture permeability, and fracture porosity. Additionally, in Sec. 3.3.5 the matrix and fracture weighting factors W_m and W_f are introduced. Setting W_m to zero, and W_f to one, leads to faster transport velocities, as the storage volume on the fracture nodes is reduced. The effect of this assumption is investigated in Sec. 5.5. In the reference case, W_m is set to zero, i.e. decreasing the retention time of the salt component within the fault zone. The position of the fault zone is illustrated in the schematic shown in Fig. 5.6 and in Fig. 5.12, marked in red.

5.4. Numerical Model Reliability

To make sure that the 1p2c reference model, is adequate for the problem setting, different functionalities of the 1p2c model are tested in this section using the Zeidouni-Method for large-scale pressure evolution, and the experimental results of the saltpool benchmark for variable-density flow.

5.4.1. Large-Scale Pressure Propagation During Injection

The driving force for brine migration during the injection period is the displacement of brine caused by the injected fluid. To adequately capture the far-field pressure buildup and brine leakage through the fault zone, the Zeidouni-Method is used. With this method, a reference

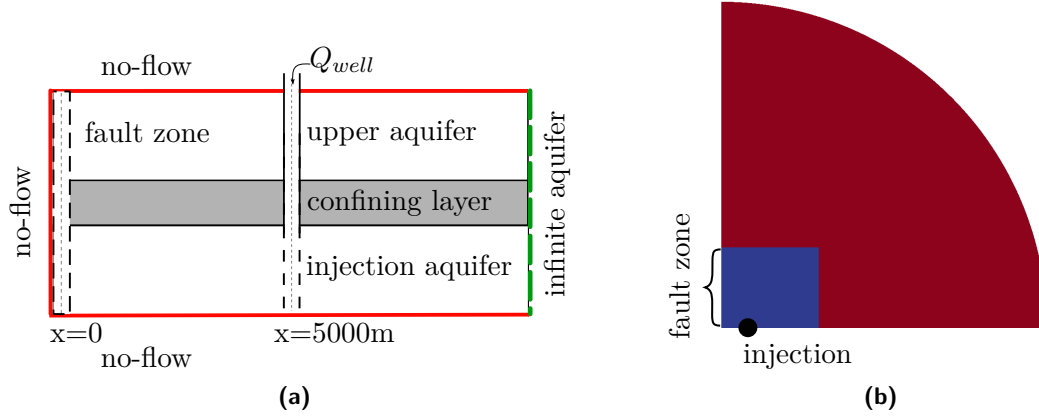


Figure 5.7.: a) Cross-section of the domain showing the lateral and top boundary conditions as well as the injection well and the fault zone (modified after Scholz (2014)).

b) Top view on the upper aquifer showing the inner domain (30 km × 25 km) in blue and the domain extension with an outer radius of 100 km in red. Due to the symmetry of the line connecting the injection and the fault zone only half of the domain is simulated.

solution is obtained for a simple test case comprising two aquifers separated by a completely impermeable layer, and connected by a vertically permeable fault zone. The model setup is illustrated in Fig. 5.7 and the relevant parameters are given in Table 5.2.

For this setting two scenarios are evaluated. The first scenario considers a closed top boundary in the upper aquifer (Neumann scenario), and the second scenario considers the upper aquifer to act as a Dirichlet boundary (Dirichlet scenario). This is achieved by increasing the permeability of the upper aquifer by several orders of magnitude, thereby increasing its diffusivity D_u ($D_u = \frac{k_u}{\mu_u \phi_u C_t}$). Here C_t is the sum of the compressibility of the porous medium and the water compressibility. The numerical model is verified against the analytical solution for different radii of the domain extension, as well as different horizontal discretization lengths. Hexahedral elements are used with a constant vertical discretization length of 50 m. The simulations are named according to their horizontal discretization length and the radius of the outer domain, for example: D300-R100 translates into a horizontal discretization length of 300 m × 300 m and an outer radius of 100 km.

The results for the comparison of different domain lengths are shown in Fig. 5.8. Here, the leakage rates over the fault zone are plotted over time. The leakage rate is normalized by the injection rate. The results show that for both the Neumann and Dirichlet scenario, a good agreement with the analytical solution is reached for all radii. The cases for an outer radius of 100 and 150 km are not distinguishable. The solution for the 50 km case shows a slightly smaller leakage rate. Thus, for the simulations presented below, where the complex geological model is used, an outer radius of 100 km is deemed to be sufficient.

Table 5.2.: Input parameters for the analytical and the numerical model.
* denotes parameters only relevant for the numerical simulation.

Parameter	Unit	Value
Injection rate	kg s^{-1}	10.87
Injection period	year	50
Injection well fault distance	m	5000
Water viscosity	Pa s	1×10^{-3}
Water compressibility	Pa^{-1}	4.5×10^{-10}
Aquifer permeabilities	m^2	1×10^{-13}
Aquifer porosities	-	0.2
Porous medium compressibility	Pa^{-1}	4.5×10^{-10}
Aquifer thicknesses	m	50
Barrier permeability*	m^2	1×10^{-25}
Barrier porosity*	-	0.001
Barrier thickness	m	50
Fault permeability	m^2	1×10^{-12}
Fault porosity*	-	0.01
Fault thickness	m	50

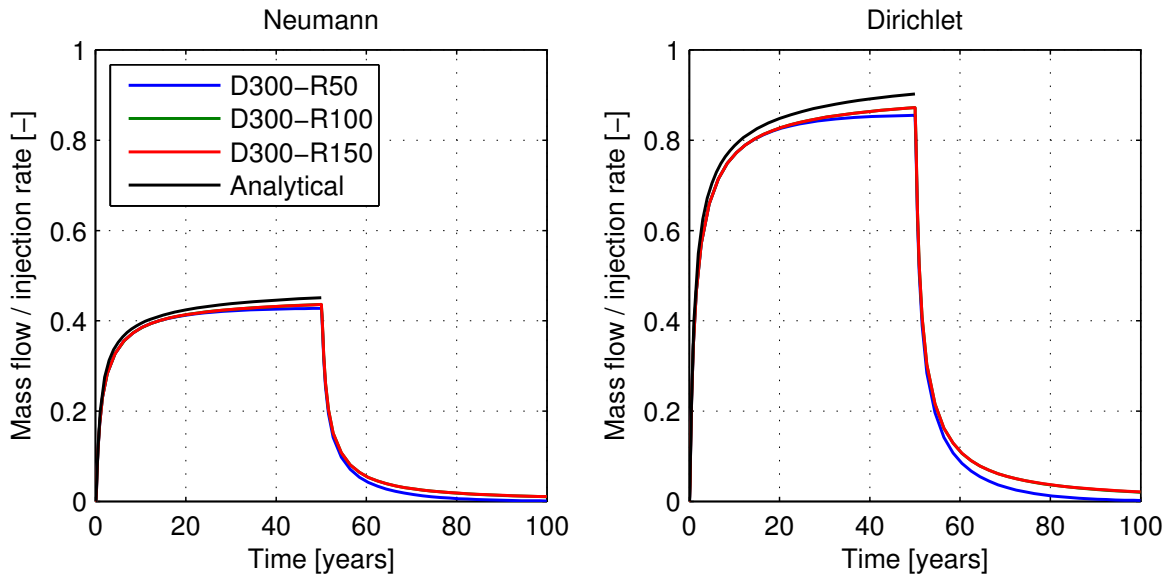


Figure 5.8.: Comparison of domain radii for 50, 100 and 150 km. **Left:** Neumann case with the upper aquifer closed on top. **Right:** Dirichlet case where the top aquifer has a constant pressure (very large diffusivity).

The comparison of the different horizontal discretization lengths, for both the Neumann and the Dirichlet scenario are shown in Fig. 5.9. The results show that all three horizontal discretization lengths sufficiently approximate the analytical solution. While the solution

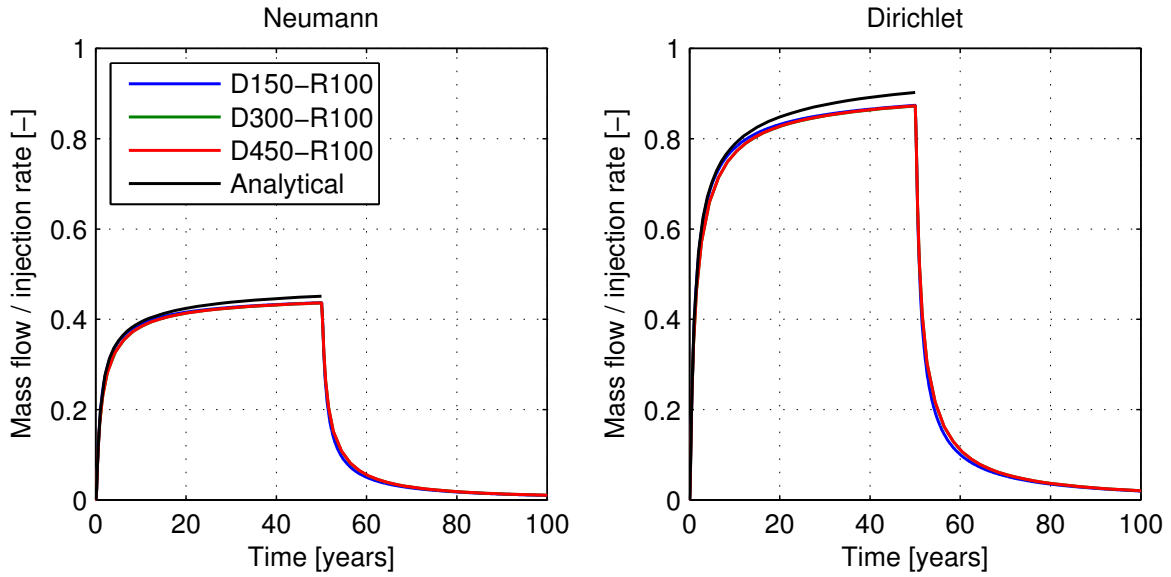


Figure 5.9.: Comparison of different horizontal discretization lengths for 150, 300 and 450 m. **Left:** Neumann case with the upper aquifer closed on top. **Right:** Dirichlet case where the top aquifer has a constant pressure (very large diffusivity).

curves of the 300 m and 450 m discretizations are not distinguishable from each other, the solution for the 150 m case follows the analytical solution more closely. This is likely due to the strongly decreased horizontal discretization length, leading to smaller time steps, whose size is constrained by the convergence of the linear solver. A reason for the numerical simulations not exactly fitting the analytical solution may lie in the near injection region, where the relatively coarse discretization can lead to an increased numerical dispersion. However, with an outer domain radius of 100 km and a horizontal discretization length of $300\text{ m} \times 300\text{ m}$, the results are still in good agreement, with only a 3.3% deviation from the Zeidouni-Method at the end of the injection, for both the Dirichlet and the Neumann scenario. The horizontal discretization length for the complex geological model is $300\text{ m} \times 300\text{ m}$ as previously discussed in Sec. 5.2. Given the results shown here, this horizontal discretization length is a good compromise between model accuracy, the need to sufficiently resolve the geology, and the computational feasibility.

5.4.2. Upconing with Variable Brine Density: The Saltpool Experiment

The saltpool experiment is a popular benchmark for testing numerical simulators for their ability to deal with variable-density flow. As discussed previously in Sec. 2.7 the saltpool

experiment was first conducted by Oswald and Kinzelbach (2004). It considers a stable layering of freshwater above saltwater. The experimental setup is shown in Fig. 5.10. It includes an

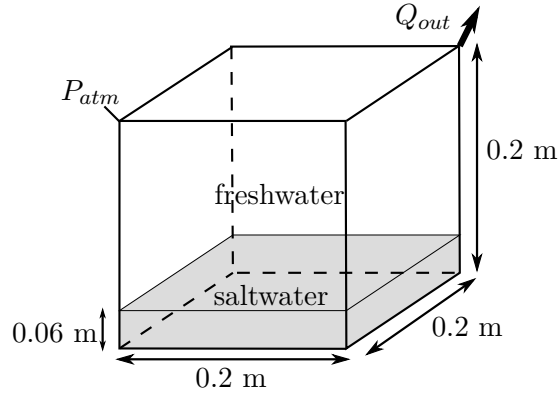


Figure 5.10.: Setup of the saltpool benchmark.

inlet where freshwater enters the domain, and an outlet where water and salt leave the domain. The inlet and outlet are each described by one node in the numerical model. For the inlet node, the pressure is set to atmospheric pressure, and the salinity is set to zero (Dirichlet boundary condition). At the outlet, a constant outflow rate is assigned (Neumann boundary condition), which allows the components water and salt to leave the system. The density is considered to be a linear function of the salinity X^S :

$$\varrho = \varrho_{ref}(1 + \alpha X^S), \quad (5.1)$$

where ϱ_{ref} (1000 kg m^{-3}) is the reference density and α is the so-called solute expansion coefficient (Diersch and Kolditz, 2002). Also, the viscosity of the saltwater is a function of the salinity:

$$\mu = \mu_{ref}(1 + 1.85X^S - 4.1(X^S)^2 + 44.5(X^S)^3), \quad (5.2)$$

where μ_{ref} ($1 \times 10^{-3} \text{ Pa s}$) is the reference viscosity. The grid consists of equi-distant hexahedral elements. All remaining input parameters of the model setup are given in Table 5.3. Two cases are simulated: a low (0.01) and a high salinity case (0.1). These salinities correspond to the salinity of the saltwater layer (see Fig. 5.10). The simulations for the low and the high salinity cases are carried out for different levels of grid refinement: 50^3 , 100^3 , and 125^3 elements. On the equidistant grid this corresponds to a discretization length of 4 mm, 2 mm, and 1.6 mm respectively.

The results for the two salinity cases are presented in Fig. 5.11. The diagonal cross-sections, between inlet and outlet, shown in a) and b) clearly illustrate the different flow behavior for the low and high salinity case. For the low salinity case, the freshwater flow enters the saltwater layer, whereas for the high salinity case, the layering stays almost intact, with the 50% isoline

Table 5.3.: Input parameters for the saltpool benchmark as given in Oswald and Kinzelbach (2004).

Parameter	Unit	Value
Extraction rate (low case)	$\text{m}^3 \text{s}^{-1}$	1.89×10^{-6}
Extraction rate (high case)	$\text{m}^3 \text{s}^{-1}$	1.83×10^{-6}
Extraction period	s	9000
Water viscosity	Pa s	see Eq. 5.2
Solute expansion coefficient α (low case)	-	0.76
Solute expansion coefficient α (high case)	-	0.735
Permeability	m^2	9.77×10^{-10}
Porosity	-	0.372
Longitudinal dispersion	m	1.2×10^{-3}
Transversal dispersion	m	1.2×10^{-4}
Initial salt layer height	m	0.06
Initial salt layer salinity (low case)	-	0.01
Initial salt layer salinity (high case)	-	0.1

being horizontal. The main target variable considered in this case is the salinity at the outlet. Figure 5.11 c) and d) show the salinity over time for the low and high salinity case compared to the experimental results. For both cases, the qualitative behavior of the evolution of the salinity over time is in good agreement with the experimental results. Different grid resolutions are compared, and it can be seen that for 100^3 and 125^3 elements the results are almost grid convergent for both salinity cases. However, the quantitative agreement, especially for the high salinity case, is not satisfactory. Simulated results for the saltpool benchmark can be found in several publications (Bastian et al., 2001; Diersch and Kolditz, 2002; Johannsen et al., 2002; Oswald and Kinzelbach, 2004). Simulations carried out by Bastian et al. (2001) with the original values from Oswald and Kinzelbach (2004), also used here (see Table 5.3), indicate an overestimation for both the high and the low salinity case. This is especially true for the high salinity case, as the salinity at the outlet observed by Bastian et al. (2001) with these values is higher by a factor of almost two. Simulated results for the high salinity case shown in Oswald and Kinzelbach (2004) cannot even reproduce the experimental results qualitatively, with the salinity at the outlet continuously increasing over time. To obtain a good agreement, Johannsen et al. (2002) had to fit the values for transversal dispersion (α_t), permeability, and porosity, through inverse modeling. This explains the strong deviations observed here too. Additionally, Johannsen et al. (2002), Bastian et al. (2001), and Diersch and Kolditz (2002) stress the importance of using a consistent velocity approximation as proposed by Knabner et al. (1998), which is not implemented in DuMu^x. A consistent velocity approximation will mainly decrease the velocity dependent dispersion (see Sec. 2.6.3), due to erroneous fluxes arising from linearly approximating the pressure between two nodes, which in the case of variable-density flow is

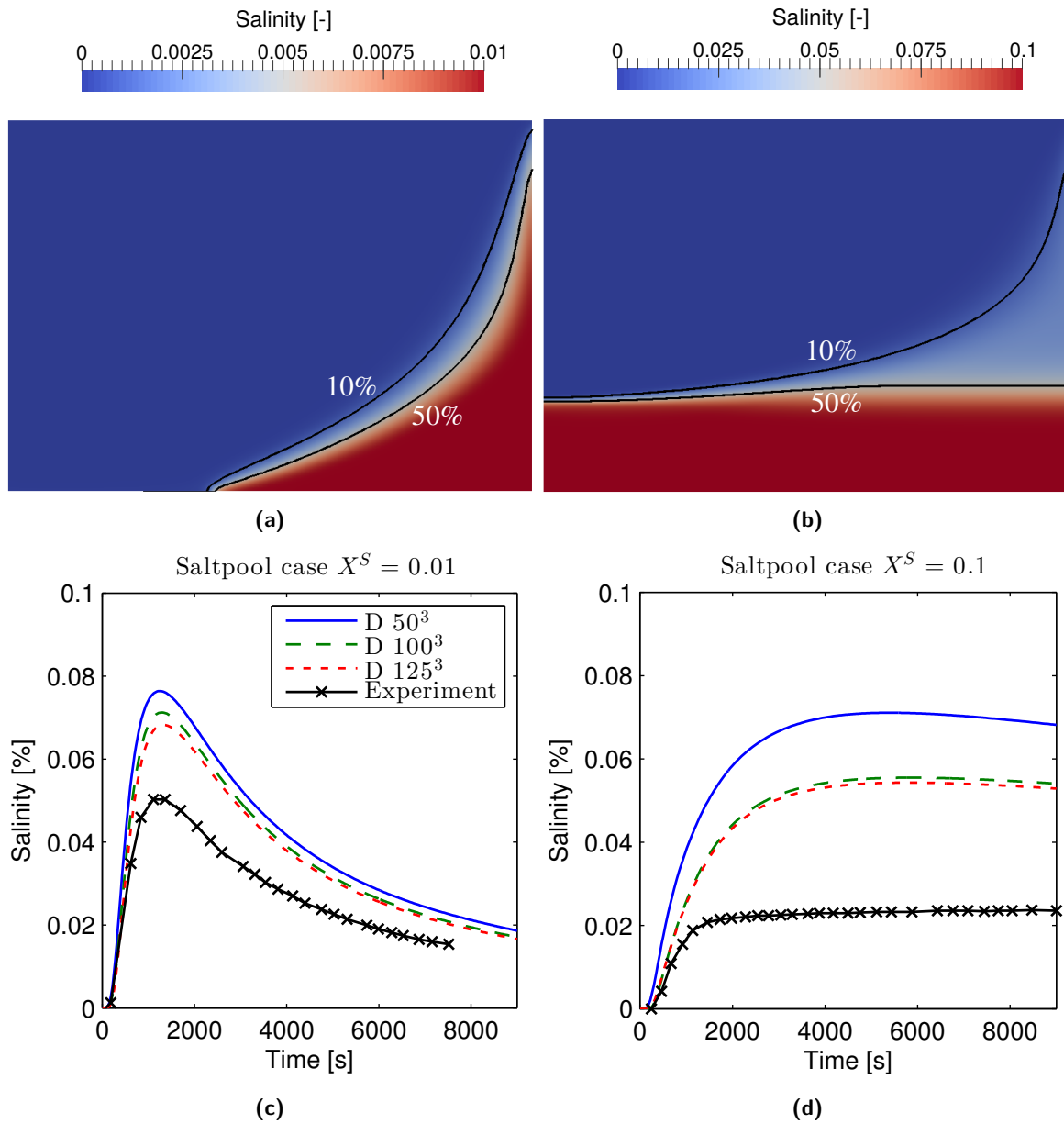


Figure 5.11.: a) and b): diagonal vertical cross-sections between inlet and outlet showing the salinity after 9000 s. Also shown are the 10 % and 50 % isolines for the low (0.01) and high (0.1) salinity case. c) and d): salinity at outlet over time for the low (0.01) and high (0.1) salinity case, with 50^3 , 100^3 and 125^3 elements.

generally a non-linear function. Additionally, the full upwind-weighting and the first order temporal discretization scheme used here (see Sec. 3.3), may contribute to the overestimation. To conclude: the main reason for the observed overestimation of salinities at the outlet can be related to the false parametrization of the benchmark, as seen in Johannsen et al. (2002)

and Bastian et al. (2001). A second reason for this observed overestimation of salinity may be related to the implementation of variable-density flow in DuMu^x. Both issues should be investigated in future work. For the simulations of large scale brine displacement presented below, the results of the saltpool benchmark imply that when considering concentrations as a target variable, these concentrations will be strongly influenced by the highly uncertain parametrization, especially with regard to the dispersivities. However, the overall flow field will react much less sensitively to the variation of salinities, especially to those with a small value. This argument is supported by the qualitative agreement between the experimental results and the simulation results of the saltpool benchmark.

The simulation of the high density case with 125^3 elements is only feasible, with a massive parallelization. The wall clock time for this case was 10 hours on 120 processes. Unfortunately, a massive parallelization could not be applied to the simulations of the complex geological model presented below. The heterogeneities and high aspect ratios of the elements made a convergence of the parallel linear solver impossible.

5.5. Results

The results section is divided into three parts. (i) definition of appropriate target variables, (ii) the results of the scenario analysis (scenario uncertainty), and, (iii) the comparison of models of different physical complexity (model uncertainty).

5.5.1. Definition of Target Variables

First, the target variables which will be used to compare the results within this section are defined. The choice of an effective and efficient conceptual model is closely connected to the target variable considered.

- **Flow into target aquifers:** The target aquifers are defined as all layers located above the Rupelian clay barrier, i.e. the Post-Rupelian, Quaternary 2 and Quaternary 1 layers. Different areas are distinguished, over which the flow into the target aquifers is summed up: (i) flow near the salt wall, which comprises flow through the fault zone and flow through the Cretaceous dragged up by the salt wall (for ease of notation, both are referred to as flow through the fault zone), and (ii) flow through the hydrogeological windows in the Rupelian clay barrier. Figure 5.12 shows a view on the interface between the Rupelian clay barrier and the Post-Rupelian layer. Further, the total salt flow into the more shallow Quaternary 1 and 2 layers is also considered.

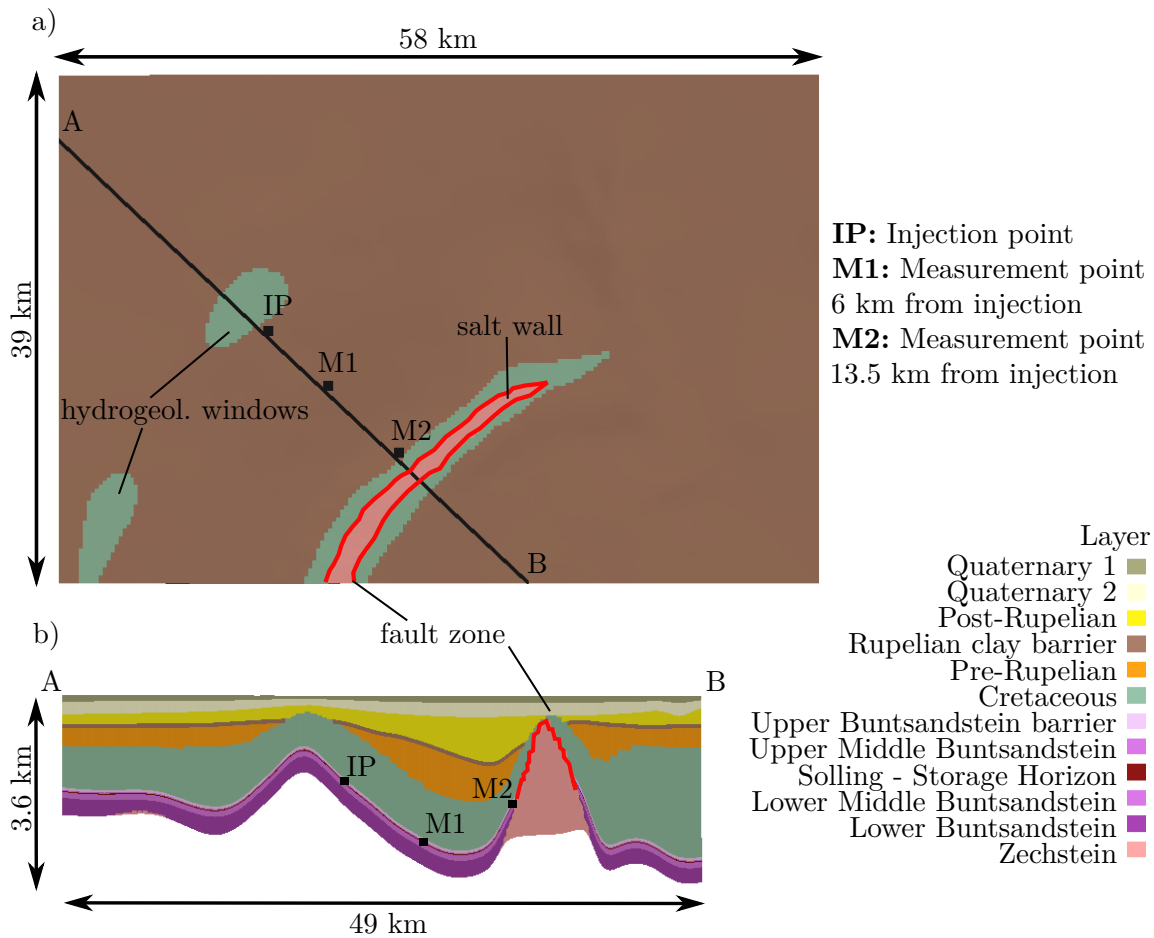


Figure 5.12.: a) Top view on the Rupelian clay barrier. Also shown are the two hydrogeological windows in the Rupelian clay barrier and the salt wall piercing through the barrier layer. The fault zone on the salt wall is highlighted in red. b) shows a cross-section (vertical exaggeration 4:1) along line A-B with approximate locations of the injection point (IP) and the two measurement points for pressure (M1 and M2).

- **Pressure increase at selected locations:** Injection-induced pressure increase is monitored at two locations (M1 and M2) in the injection horizon Solling. They are located on a straight line between the injection point and the nearest point on the salt wall: (i) M1 approximately 6 km from the injection and (ii) M2 approximately 13.5 km from the injection directly at the fault zone on the salt wall, see Fig. 5.12.
- **Concentration changes in target aquifers:** The injection-induced changes in the salt concentration will be shown on the top of the Rupelian clay barrier as shown in Fig. 5.12 a), and on the top of the Post-Rupelian layer.

Table 5.4.: List of parameters for the 1p2c model for the reference scenario. The two-phase flow specific parameters are additionally required for the 2p3c model.

Parameter	Unit	Value
Compressibility solid phase	Pa^{-1}	4.5×10^{-10}
Depth injection	m	1651
Temperature gradient	K m^{-1}	0.03
Temperature top	K	281.15 (9 °C)
Density CO ₂ at injection point	kg m^{-3}	687
Density brine at injection point	kg m^{-3}	1078
Injection rate CO ₂	kg s^{-1}	15.9 (0.5 Mt/year)
Volume equivalent injection rate brine	kg s^{-1}	24.9
Recharge at top boundary	$\text{kg s}^{-1} \text{m}^{-2}$	3.17×10^{-6} (100 mm/year)
Initial salt gradient	kg m^{-4}	0.15 (15 g/L/100 m)
Maximum salinity	-	0.292
Longitudinal dispersivity	m	0.0
Transversal dispersivity	m	0.0
Matrix weighting factor W_m	-	0
Fracture weighting factor W_m	-	1.0
Two phase flow specific parameters:		
Brooks and Corey shape parameter λ	-	2.0
Residual water saturation	-	0.2
Residual CO ₂ saturation	-	0.05

5.5.2. Scenario Uncertainty

In this section different scenarios are evaluated. In each scenario, a key parameter is varied. All of these parameters are highly uncertain and are varied over a range of values to obtain a span of possible results. The model used in this section is the 1p2c model. All scenarios are evaluated against a reference scenario, which is not chosen because it is the most likely geological setup but is rather chosen because all processes under investigation occur on a recognizable scale. The setup of the reference scenario is given in Table 5.1, where the porosities and permeabilities of the geological model are shown, and Table 5.4, where the remaining parameters are listed. Except for the first scenario study, where parameters of the initialization episode are varied, all following scenario studies use the same initial pressure and salinity distribution. These values are obtained from the reference scenario, and are used as initial conditions for the injection episode.

Scenario Study 1: Initial Salt Distribution

In this scenario, parameters for the initialization run are varied which results in different salt distributions prior to the injection of CO₂. As described in Sec. 5.3.1, an initial salt

gradient serves as the initial condition for the initialization run which covers 300.000 years. This gradient starts at a depth of 645 m, which is the average depth of the Rupelian clay barrier layer. Once the solubility limit of salt is reached at a certain depth, the salinity is not increased further (see Fig. 5.6).

First, three different scenarios with different gradients are considered: low, medium, and high. The gradient is either decreased to 10 (low) or increased to 20 (high) from the reference value of 15 g/L/100 m (medium). Figure 5.13 shows the salt distribution for the medium scenario (reference) before and after the initialization run when a quasi-stationary system has established. The salinity distribution has considerably changed after the initialization run from the initial salt gradient. The less dense brine has migrated above the Rupelian clay barrier while the more dense brine collects at the bottom of the domain. The salt distribution changes the most during the first 50 000 years. The initialization run shows that upconing in the target aquifers occurs near rivers. The rivers act as a sink since the lowest potential in the system (atmospheric pressure, zero salinity) is assigned there. The 10 g/L isoline follows the Rupelian clay barrier layer, except for where the depth of the Rupelian clay barrier layer strongly increases near the salt wall.

The increases in concentration after 50 years of injection (i.e. the end of the injection) are shown in Fig. 5.14 for the low, medium and high scenario. While concentration changes of up to about 4 g/L occur on the top of the Rupelian clay barrier, maximum concentration changes on the top of the Post-Rupelian directly below the Quaternary 2 are an order of magnitude smaller, about 0.25 g/L. The largest changes occur close to the fault zone and at the hydrogeological window above the injection horizon. Generally, the concentration changes due to the injection increase from the low to the high scenario as the salt concentrations are higher and, therefore, more salt can be displaced by the injection. This is illustrated in Fig. 5.15. Here, the total salt flow into the target aquifers is compared to the flow over the fault zone, the hydrogeological windows and the intact Rupelian clay barrier. It becomes clear that the main contribution to the total salt flow comes from the region near the salt wall (fault zone). This is to be expected, as the permeable fault zone is situated here, and the highest salt concentrations in the target aquifers prior to the injection, are found here, due to the strong increase in depth of the Rupelian clay barrier (see Fig. 5.13). The hydrogeological windows have only a minor contribution to the total salt flow into the target aquifers. Also shown in Fig. 5.15 is the medium scenario without injection. This scenario shows a constant salt flow throughout the injection and post-injection episode, confirming that quasi-stationary conditions can be assumed during this period.

In addition to the initial salt gradient, the initial salt distribution is dependent on other parameters such as dispersion, diffusion and the permeability of the aquifers below the Rupelian clay barrier (i.e. Cretaceous and Pre-Rupelian layer). These parameters are varied in further scenarios, whose results, along with a short explanation of the varied parameters in each

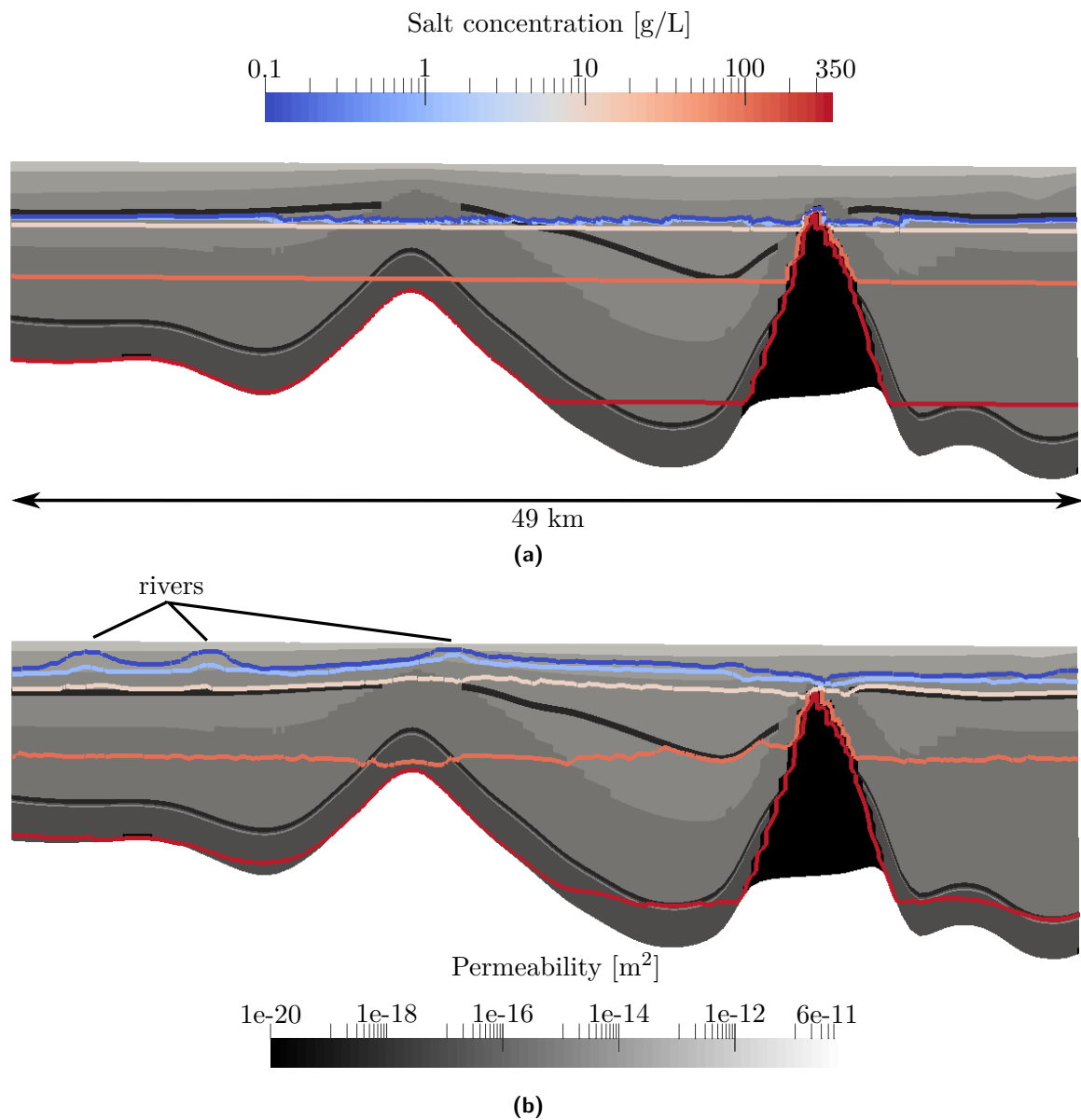


Figure 5.13.: (a): Initial salt distribution for the reference scenario before the initialization run along the cross-section shown in Fig. 5.12 (vertical exaggeration 4:1). (b): Salt distribution for the reference scenario after an initialization run of 300 000 years. Six concentration isolines are shown which correspond to the entries in the legend (0.01, 0.1, 1, 10, 100 and 300). The permeability of the different layers is also shown. Please note the logarithmic scale of concentration and permeability.

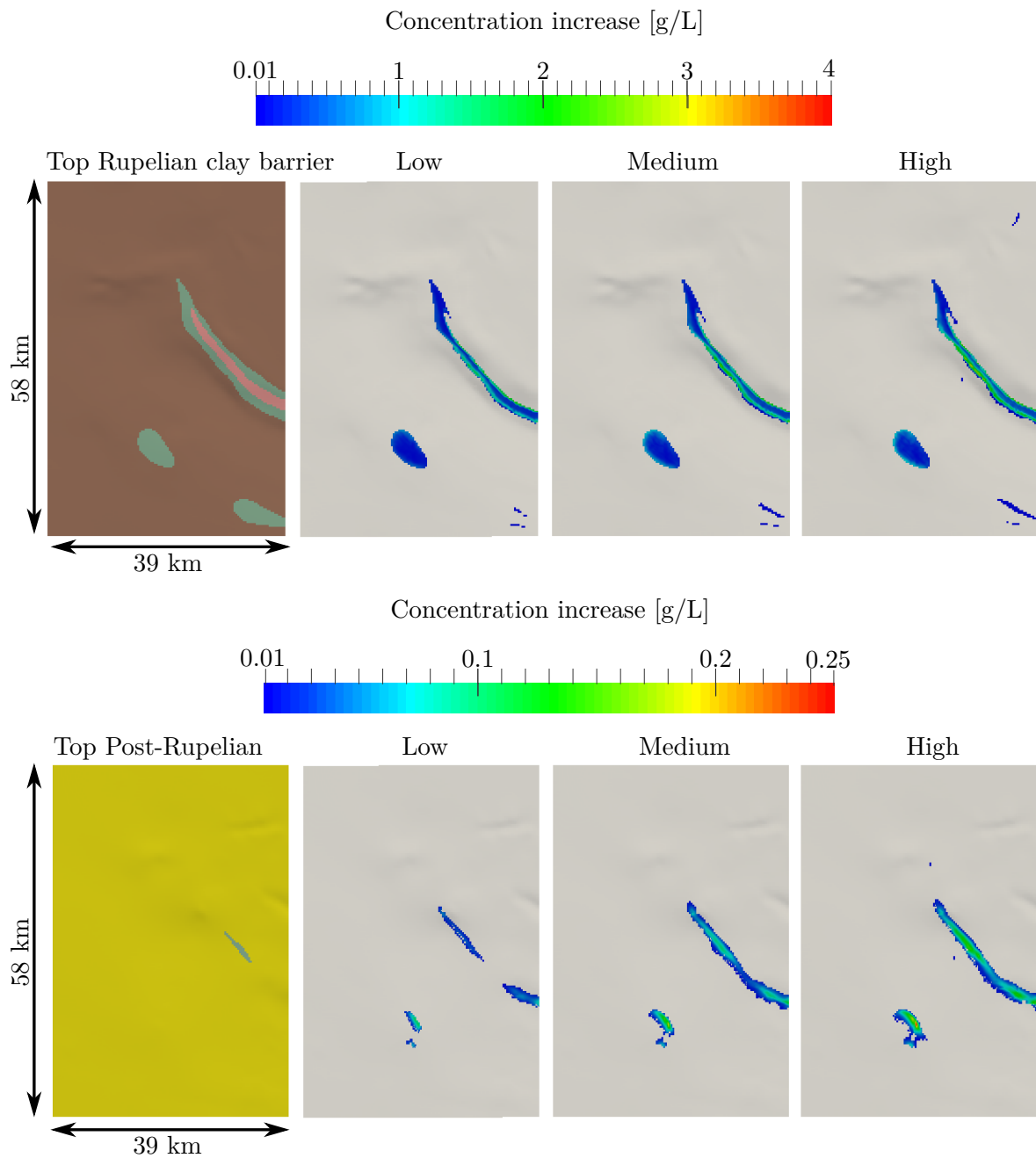


Figure 5.14.: **Top row:** View on top of the Rupelian clay barrier for three different scenarios low, medium and high with increasing initial salt gradients. The results show the salt concentration increase after 50 years of injection. Concentration increases below 0.01 g/L are not shown. **Bottom row:** View on top of the Post-Rupelian for the three scenarios. Also see Fig. 5.12 for orientation. Note the different scales for the top and bottom row.

scenario, are shown in Fig. 5.16. Figure 5.16 a) shows that there are significant variations in the results for the different scenarios. The previously discussed initial salt gradient (Scenarios

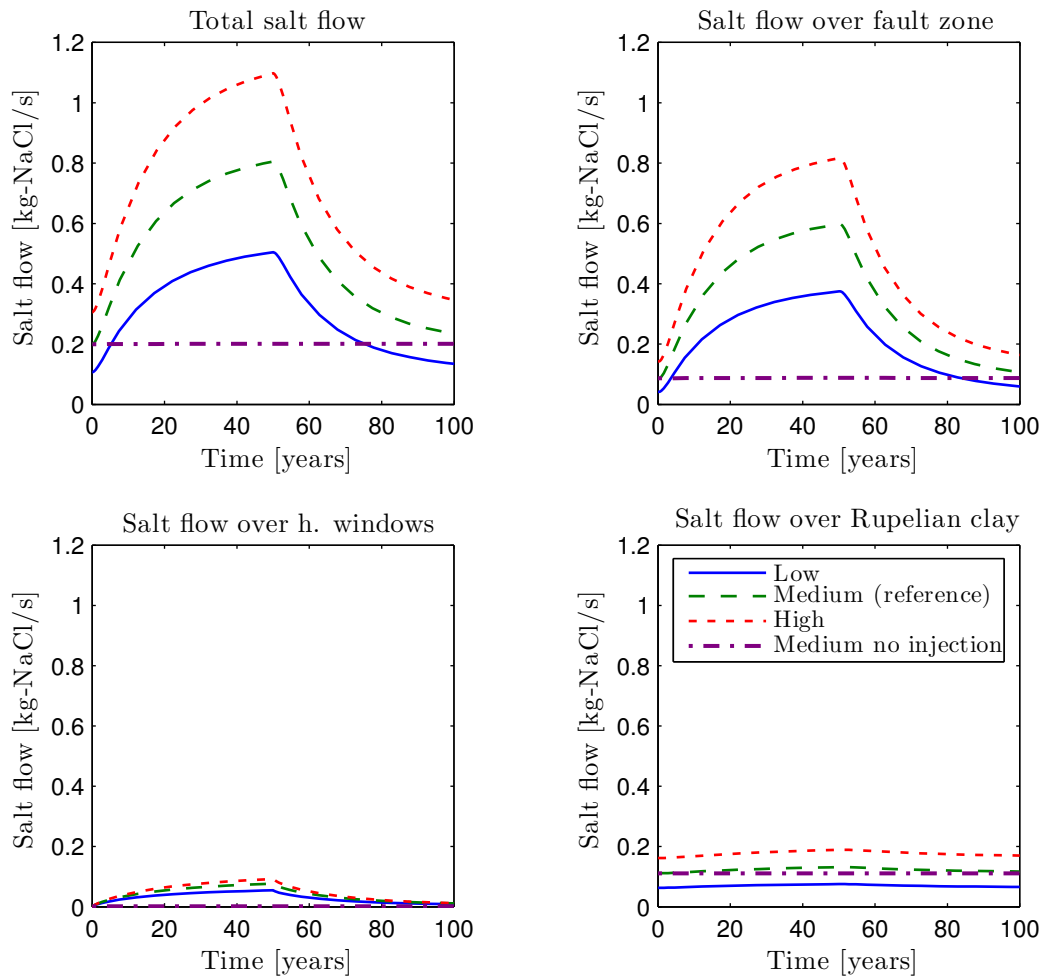


Figure 5.15.: Total salt flow into target aquifers (top left) over the injection and post-injection period split into salt flow over fault zone (top right), salt flow over hydrogeological windows (bottom left) and salt flow over the intact Rupelian clay barrier (bottom right).

2 and 3), the dispersion (large dispersion: Scenario 4), and the reduction of permeability of the Cretaceous and Pre-Rupelian (Scenario 6), all have a significant effect on the salt distribution after the initialization. Therefore, the varied parameters also influence the amount of salt that is additionally displaced due to the injection on top of the base flow. Scenario 6 illustrates that the permeabilities of the Cretaceous and Pre-Rupelian layers control the magnitude of exchange between freshwater and saltwater in locations where the Rupelian Clay barrier is discontinuous. Considering for example the reference scenario (Scenario 1) in Fig. 5.16 (a), (b), and (c) shows the decline in the impact of the injection on the amount of displaced salt in comparison to the amount displaced by the base flow over the injection period. The contribution of the injection becomes gradually smaller for the shallower aquifers, while the

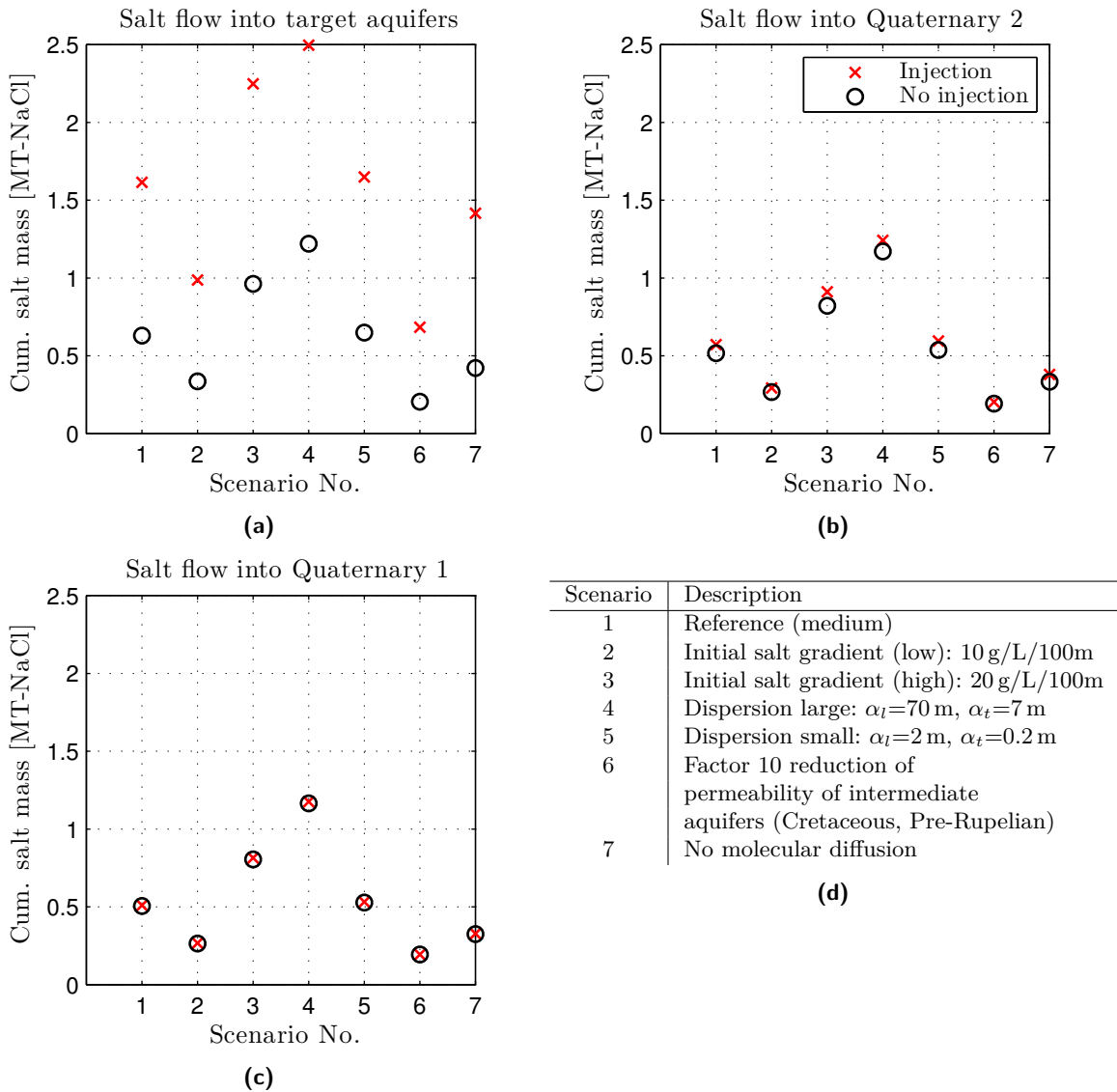


Figure 5.16.: The cumulative salt flow for a period of 100 years (injection + post injection) into the Tertiary Post-Rupelian layer (a), Quaternary 2 layer (b) and Quaternary 1 layer (c) with and without injection. The scenario numbers along with short explanations of the varied parameters are given in (d).

base flow stays more or less constant across the target aquifers. This can be explained by the low salt concentrations found in the bottom of the Quaternary 1 and 2 aquifers, prior to the injection, compared to higher salt concentrations at the bottom of the Tertiary Post-Rupelian layer (Fig. 5.16 (a)). The base flow (i.e no injection) of salt is almost the same across all layers of the target aquifers for a specific scenario. This again shows that, for each variation of a parameter, a quasi-stationary solution has evolved with a constant salt flow across the target

aquifers.

Scenario Study 2: Boundary Conditions

In this section, three different boundary conditions for the lateral boundaries of the inner domain are compared. The reference scenario uses a domain extension which results in an infinite aquifer behavior, as already described above. The other two scenarios use a no-flow and a Dirichlet boundary condition (hydrostatic) respectively, on the lateral boundary of the inner domain. The results of these scenarios are shown in Fig. 5.17. It can be seen that the

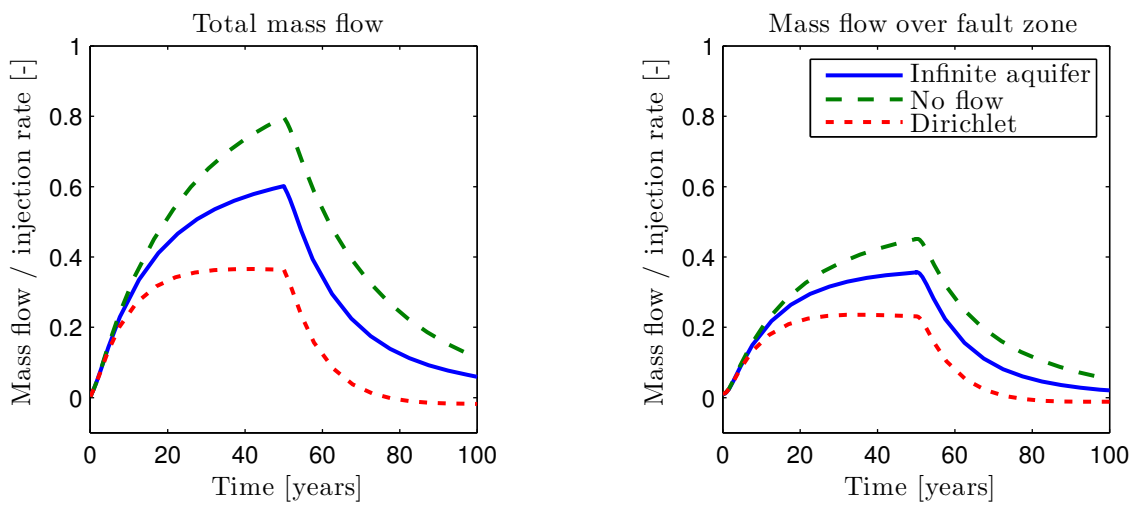


Figure 5.17.: **Left:** Total mass flow into the target aquifers normalized by the injection rate. **Right:** Mass flow over fault zone into the target aquifers.

choice of the lateral boundary conditions strongly influences the overall flow regime. For the no flow scenario considerably more fluid is displaced vertically than for the Dirichlet scenario. The reference scenario with an infinite aquifer boundary condition is somewhere in the middle of the other two scenarios. This is expected as more storage capacity for the displaced brine is available in the extended aquifers than for the no flow scenario and a stronger resistance to flow at the lateral boundaries is established than in the case of the Dirichlet scenario. For the infinite aquifer scenario, the total flow into the target aquifers reaches a level of about 60% of the injection rate. The rest is stored within the compressible fluid and rock phases.

Scenario Study 3: Barrier Rock Permeability

Within this scenario, the permeability of the layer confining the injection layer, i.e. Upper Buntsandstein barrier, is varied over several orders of magnitude. The results are presented in

Fig. 5.18. The higher the Upper Buntsandstein barrier permeability is, the more diffuse leakage

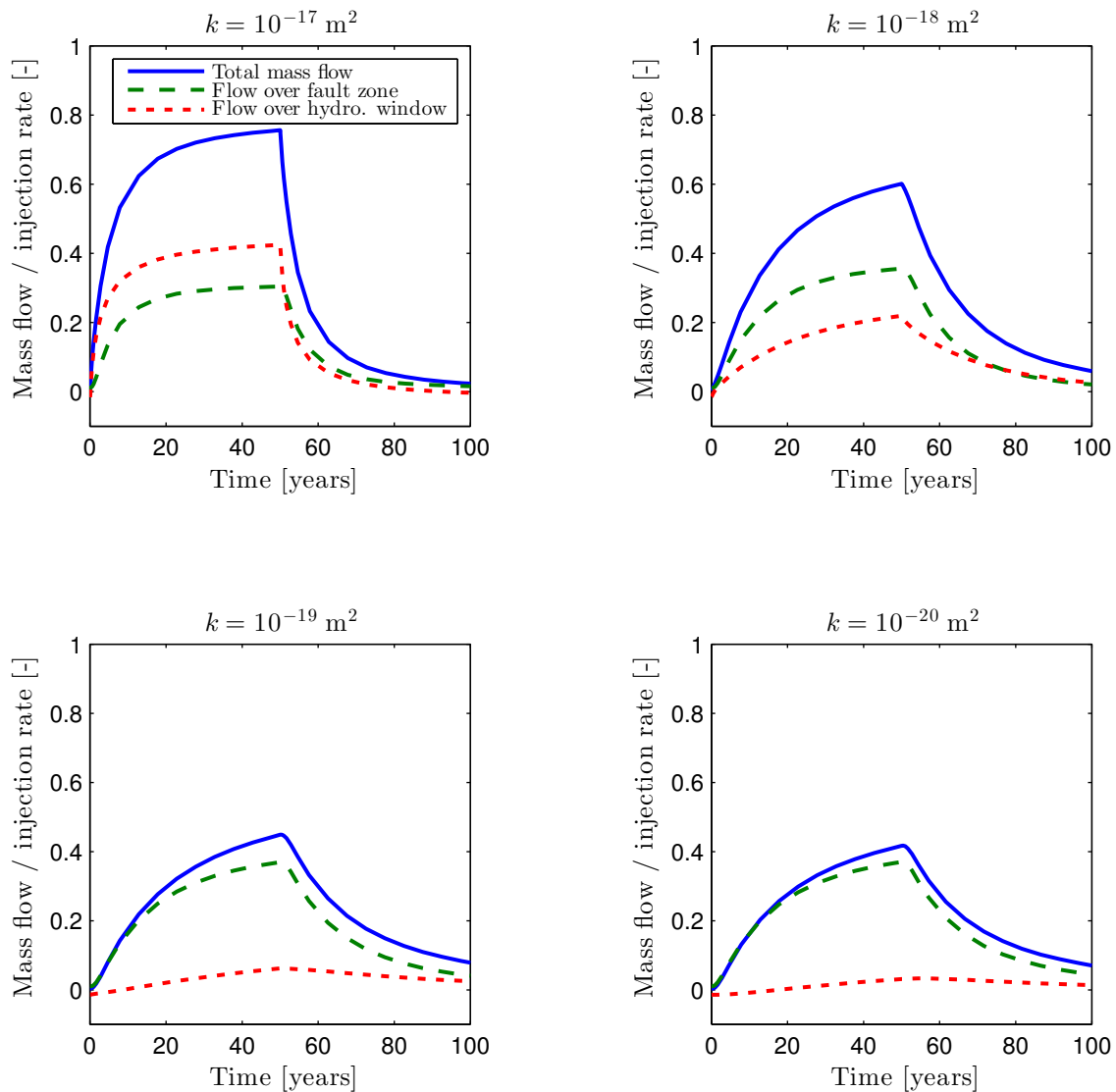


Figure 5.18.: Mass flow normalized by the brine injection rate into the target aquifers, for different permeabilities of the Upper Buntsandstein barrier. The upper right scenario with a permeability of $1 \times 10^{-18} \text{ m}^2$ corresponds to the reference scenario.

through the hydrogeological window in the Rupelian clay barrier directly above the injection point will occur, as this is the path of least resistance for the displaced fluid. The flow field completely changes when decreasing the barrier permeability and focused leakage through the fault zone becomes the predominant leakage path. The overall amount of displaced fluid into the target aquifers decreases with decreasing barrier permeability. Diffuse leakage becomes smaller with lower barrier rock permeabilities in the range of $1 \times 10^{-20} \text{ m}^2$ and $1 \times 10^{-19} \text{ m}^2$.

The simulations show the importance of the Upper Buntsandstein barrier permeability in controlling the leakage pathways.

Scenario Study 4: Fault Zone Transmissibility and the Effect of the Matrix Weighting Factor on Salt Transport

In this section, the fault-zone transmissibility and the matrix weighting factor are varied. The transmissibility is varied by changing the permeability of the fault zone for two cases: (i) A case with high diffuse migration, where the permeability of the barrier rock is similar to the reference case ($1 \times 10^{-18} \text{ m}^2$) and (ii) A case with high focused migration through the fault zone, where the permeability of the barrier rock is low ($1 \times 10^{-20} \text{ m}^2$). The results are presented in Fig. 5.19. While varying the fault zone permeability only has a small effect where

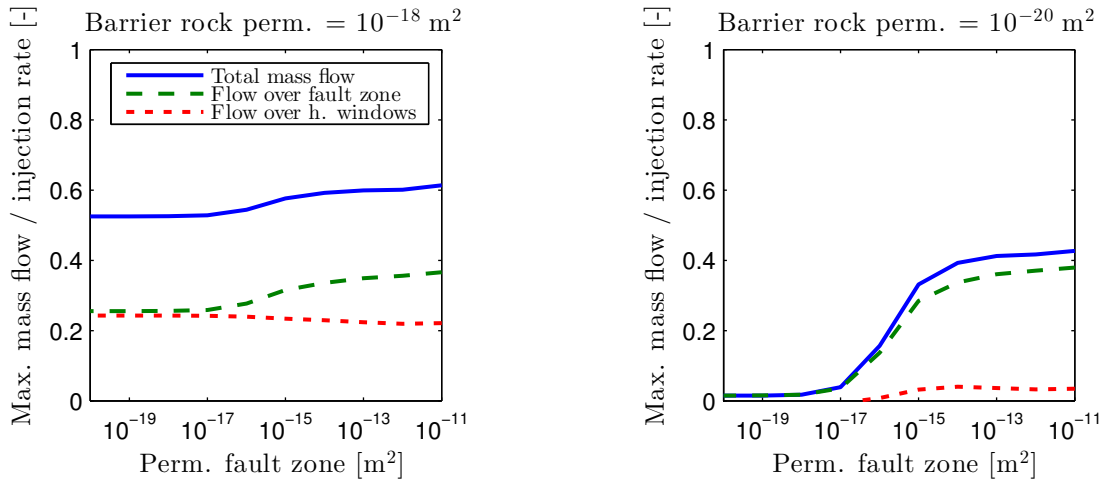


Figure 5.19.: Maximum mass flow reached after 50 years of injection normalized by the brine injection rate into the target aquifers over the fault zone permeability, for two different permeabilities of the Upper Buntsandstein barrier. **Left:** High barrier permeability, high diffuse migration over barrier; **right:** Low barrier permeability, high focused migration over fault zone.

diffuse migration is dominant (left figure). The effect is considerably higher for the case with focused migration (right figure), especially for fault zone permeabilities between 1×10^{-17} and $1 \times 10^{-14} \text{ m}^2$. For higher fault zone permeabilities, the flow is less sensitive to changes in the permeability as the resistance of the fault zone becomes small compared to the resistance within the injection layer. The right figure also shows that if neither a diffuse nor focused vertical pathway exists reaching the target aquifers, migration does not occur.

As discussed previously, the fault zone is treated as a discrete fracture (see Sec. 3.3.5 and 5.3.2). The matrix weight factor controls the amount of matrix storage at a fracture node, as this

node is shared by the fracture and the matrix. If set to zero, the storage of the salt component only comprises the fracture storage term and the storage term of the matrix is neglected at the node. The effect of the matrix weighting factor for the fault zone is compared for two scenarios: $W_m = 0$, i.e. fracture storage only, which is the reference scenario, and $W_m = 1$, i.e. the fracture and the matrix storage term are considered at the node. The results are presented in Fig. 5.20. For the reference scenario ($W_m = 0$), the left plot shows that the volume flow is

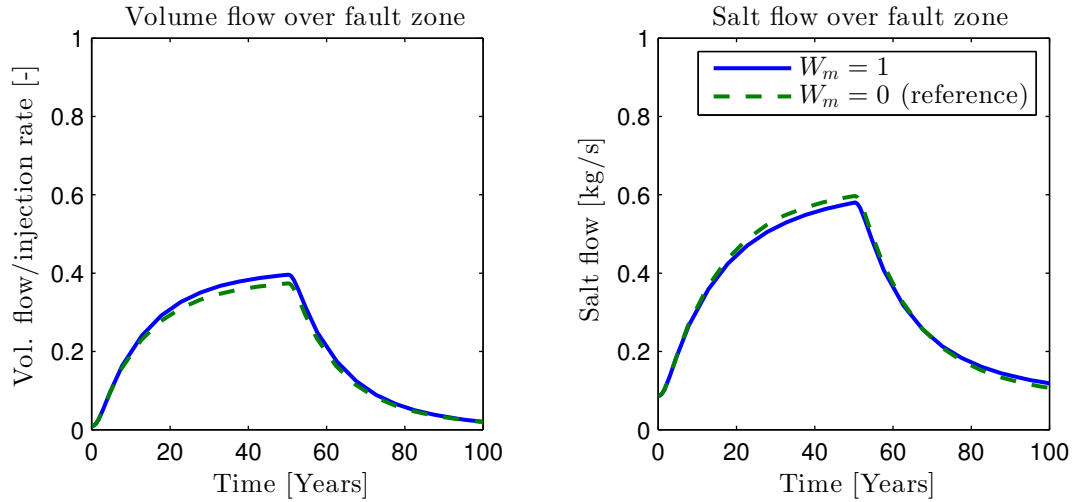


Figure 5.20.: **Left:** Volumetric flow normalized by injection rate into target aquifers through the fault zone. **Right:** Salt flow into target aquifers through fault zone.

lower and the salt flow on the right plot is slightly higher. This is conservative, as required, with respect to an increased transport velocity for the salt component (see Sec. 3.3.5). If W_m is set to zero, the transport velocity (per area of fluid) of the salt increases. This then means that the weight and therefore gravitational force of the brine column within the fault zone will increase faster. This leads to an increase in the resistive forces, meaning higher pressures are required in order to push the heavy brine upwards. This increased resistance explains why the overall volume flow is lower for the reference scenario. This effect is a consequence of the variable-density transport of salt. However, the overall effect of the matrix weighting factor is rather small but can be higher for scenarios where focused leakage through the fault zone is predominant, i.e. for permeabilities of the Upper Buntsandstein barrier smaller than $1 \times 10^{-19} \text{ m}^2$.

5.5.3. Model Uncertainty (Recognized ignorance)

The results of four different model comparisons are shown in this section. All comparisons are carried out against the 1p2c model with the parametrization of the reference scenario given in Table 5.1 and Table 5.4. As a target variable, the volume flow into the target aquifers is chosen, as this indicates how well the flow fields match. In some comparisons, the pressure buildup at the measurement points M1 and M2, shown in Fig. 5.12, is also used.

Model Comparison 1: Neglecting Salt Transport

In this comparison, the effects of neglecting salt transport and therefore neglecting the effects of variable-density flow are investigated, by applying the 1p1c model which neglects salt transport, as opposed to the 1p2c reference model. In the 1p1c model, the salinity is set as a pseudo component (similar to temperature) influencing the brine density and viscosity, but held as a fixed value throughout the simulation. A constant salinity gradient of 15 g/L/100 m is assigned in the 1p1c model, similar to the condition shown in Fig. 5.13 a). Since the 1p1c model does not require the initialization episode, the results are much faster to obtain than in case of the 1p2c reference model. Brine is injected at a rate of 25.2 kg/s in the 1p1c model which is the volume equivalent rate corresponding to the 24.9 kg/s injected in the 1p2c model due to different densities at the injection point (1p1c: 1091 kg/m³; 1p2c: 1078 kg/m³). The aim is to investigate whether both models lead to a similar flow fields. The results for the flow into the target aquifer are shown in Fig. 5.21. The total volume flow is higher by approximately 5% for the 1p1c model than that of the 1p2c model. For the 1p1c model, the volume flow over the fault zone and the hydrogeological windows starts at a value below, and above zero, respectively (see Fig. 5.21). This is caused by the base flow induced by the recharge boundary conditions on the top boundary. For the reference 1p2c model, the overall exchange of water between the target aquifers and the layers below the Rupelian clay barrier is much smaller than for the 1p1c, as the saltwater needs to be moved against the gravitational forces. For the 1p1c model, the base flow and the injection-induced flow have the same order of magnitude, whereas base flow in the 1p2c model is negligible compared to the injection-induced flow. On the bottom row of Fig. 5.21, the pressure increase at M1 and M2 are shown (see Fig. 5.12 for the approximate locations). The pressure increase at 6 km from the injection (M1) is almost the same for both models, as the brine viscosity in the injection layer is similar. However, at the fault zone, the pressure increase for the 1p2c is higher by a factor of approximately three, compared with the 1p1c model. This is due to the increasing weight of the ascending brine within the fault zone, leading to an increasing resistance. This is a result of salt transport and the associated density changes.

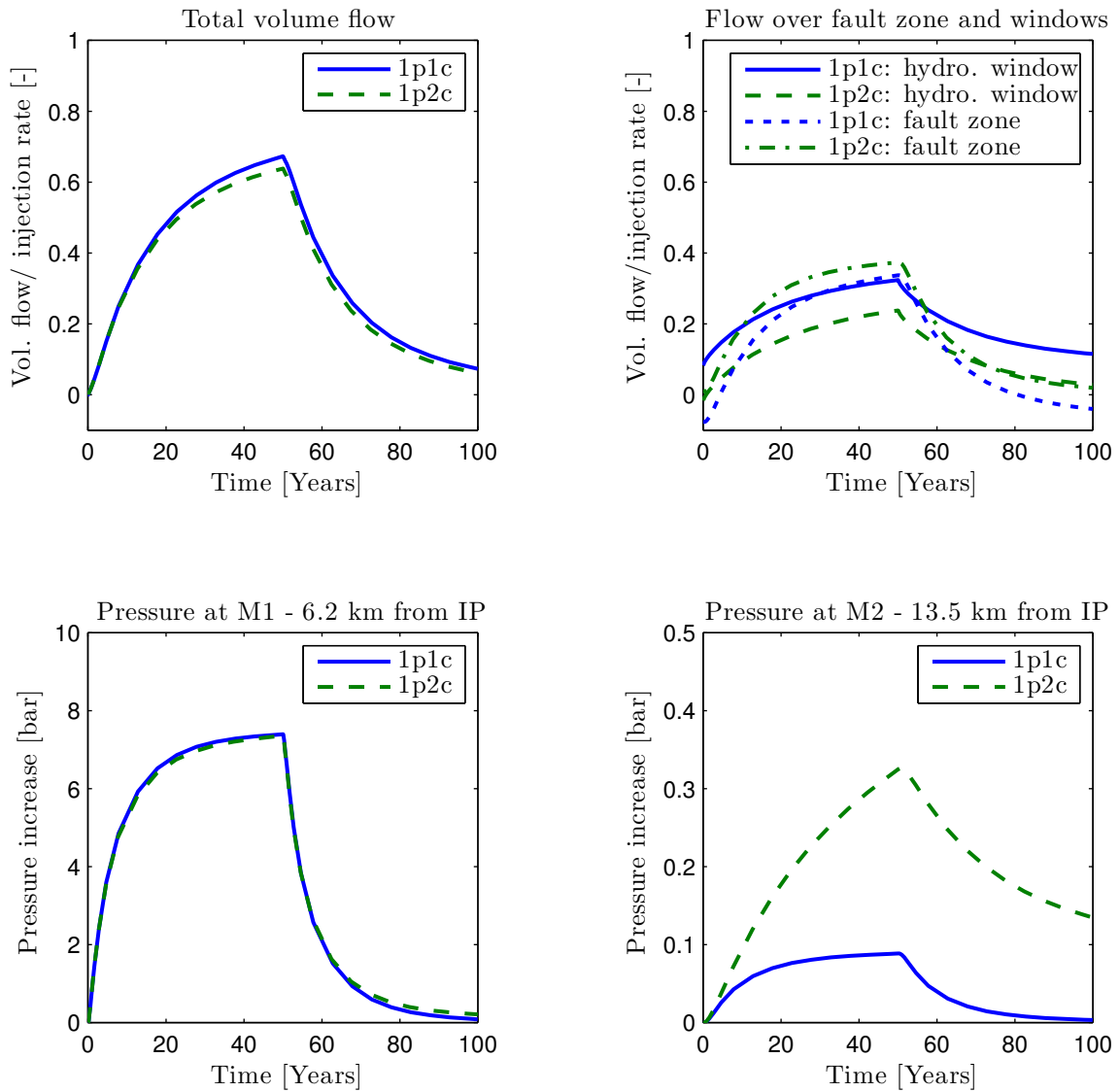


Figure 5.21.: **Top:** Volume flow over time into the target aquifers for the 1p1c and the 1p2c model. **Bottom:** Pressure increase due to injection at M1 and M2.

Model Comparison 2: CO₂ Versus Water Injection

In this section, the 1p2c and the 2p3c model are compared. In the 2p3c model, CO₂ instead of brine is injected at a rate of 15.9 kg/s, see Table 5.4. As the injection point is located on the flank of the anticline, buoyancy forces drive the CO₂ upwards (see Fig. 5.12 for the approximate position of the injection point). The resulting volume flows are shown in Fig. 5.22 for both models. After 50 years (end of injection), the total volume flow into the target aquifer for the 1p2c model is higher by approximately 7.5% in comparison to the results from the

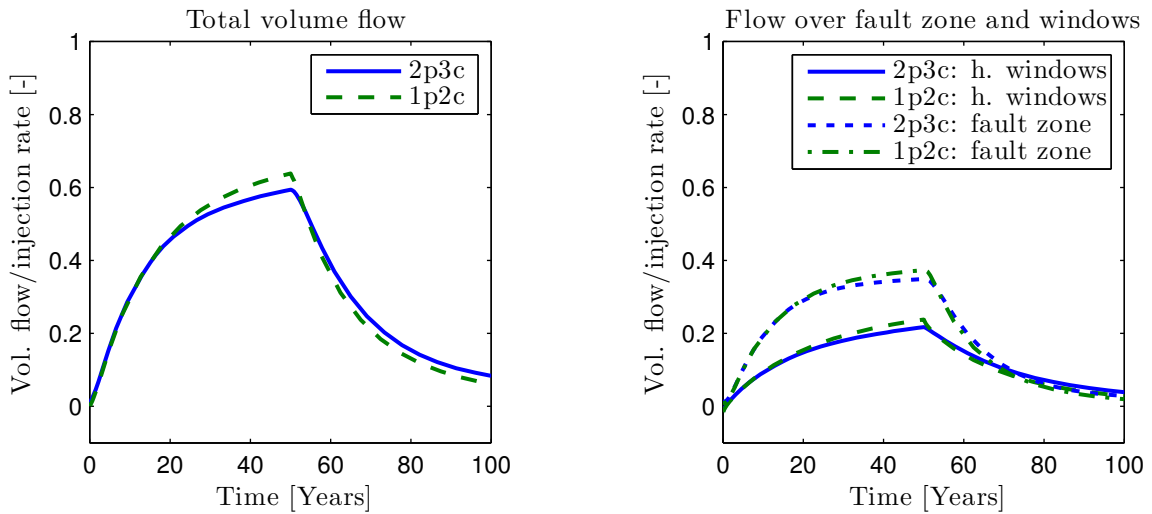


Figure 5.22.: Volume flow over time into the target aquifers for the 2p3c and the 1p2c model.

2p3c model. The right figure shows that the volume flow across the hydrogeological windows and the fault zone are in good agreement for both models. The the slightly reduced volume flow for the 2p3c model compared to the 1p2c model is due to the rise in pressure near the injection, which causes the density of CO_2 to increase, leading to a smaller brine flow into the target aquifers.

Model Comparison 3: Simplifying the Geometry

This comparison deals with a major simplification of the geometry. The reference 1p2c model is called “complex case“, while the simplified geometry is referred to as “generic case“. In the generic case, the complex geometry is converted into a simple stratified system with the layering orthogonal to the direction of gravity as shown in Fig. 5.23. The target aquifers are removed and replaced by a Dirichlet boundary condition with a constant hydrostatic pressure and zero salinity above the Rupelian clay barrier. Therefore, no base flow establishes as hydrostatic conditions are assumed within the domain, along with a linear salinity gradient similar to the one prescribed initially for the complex case before the initialization run (15 g/L). Due to the simple geometry and boundary conditions no initialization run is required prior to the injection. The salt wall is implemented at the boundary of the model domain along with the fault zone marked in red in Fig. 5.23. The lateral boundary conditions are infinite aquifers, like those in the complex model. The geometrical information required for the generic model’s setup consists only of the layer thicknesses, the distances of geological features, and the areas of the hydrogeological windows. They are estimated based on the complex geometry.

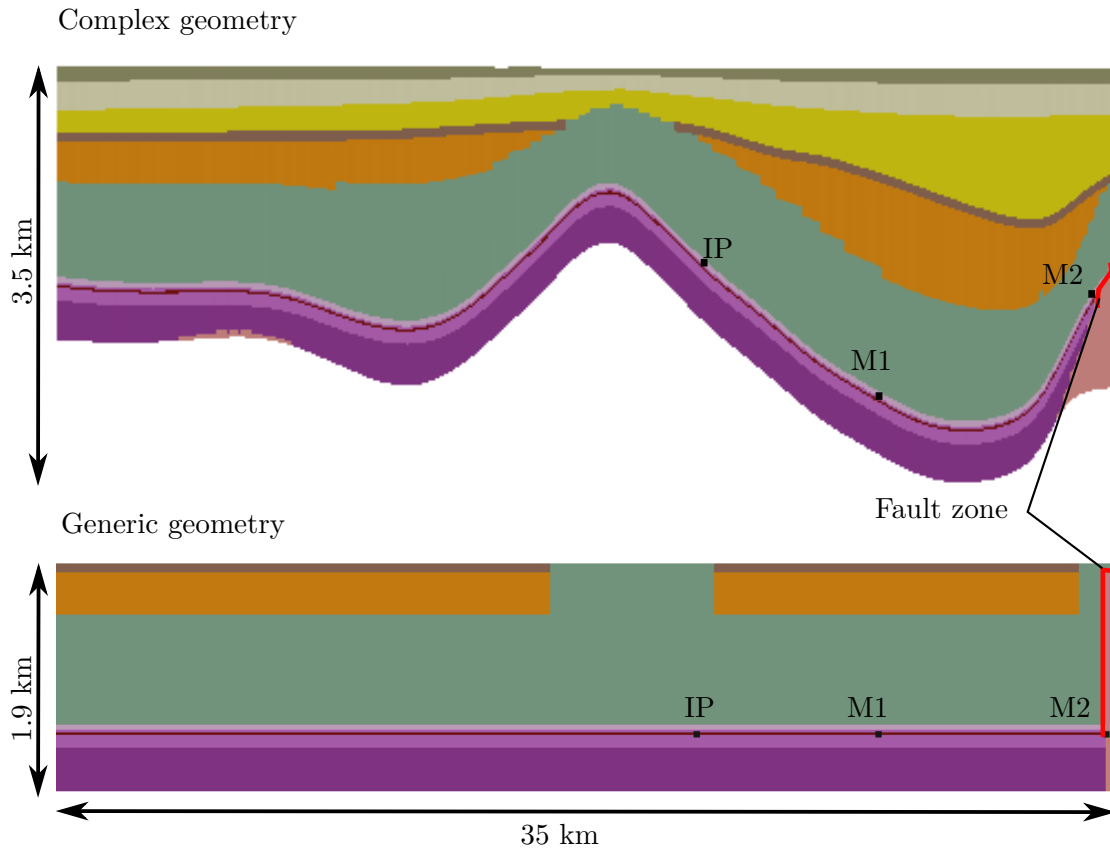


Figure 5.23.: Cross-section of the complex and generic geometry (vertical exaggeration 4:1) along the same cross-section, as shown in Fig. 5.12.

The injection point, and the measurement points M1 and M2, are at a depth of 2100 m in the generic case. Again brine is injected at a rate of 25.8 kg/s in the generic model which is the volume equivalent rate corresponding to the 24.9 kg/s injected in the complex model due to different densities at the injection point (generic: 1117 kg/m³; complex 1078 kg/m³). The resulting volume flows into the target aquifers are given in the top row of Fig. 5.24. The total brine flow across the top boundary (equivalent to the flow into the target aquifers) is 10% higher for the generic model, than for the complex model at the end of the injection. The flow across the fault zone and the hydrogeological windows (see Fig. 5.24 top right) is different for the generic and complex case, with the generic model having higher flow through windows and less flow through the fault zone, than the complex model. The bottom row of Fig. 5.24 shows the pressure buildup at the measurement points M1 and M2. In general, the pressure in the injection horizon is higher for the generic case. A possible reason for the elevated pressure may lie in a higher average brine viscosity in the injection horizon in the generic case. The brine viscosity generally decreases with increasing depth due to an increasing temperature. Looking at Fig. 5.2, it becomes clear that a large part of the Solling horizon, between the injection

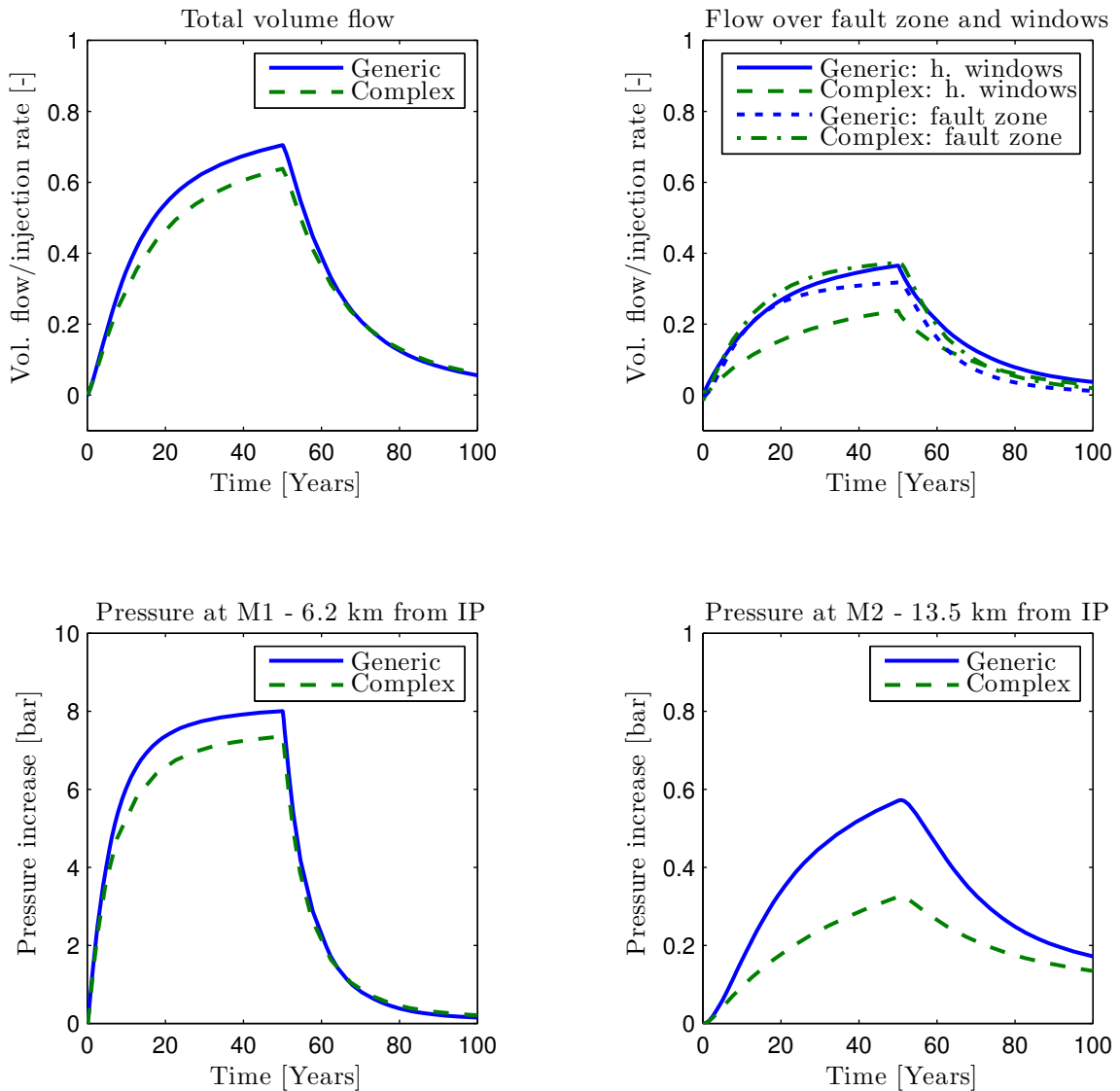


Figure 5.24.: Volume flow normalized by the injection rate over time into the target aquifers for the generic and the complex model.

point and the fault zone at the salt wall, is below a depth 2800m, which is considerably deeper, than the depth of M1 and M2 (2100m) in the generic case. However, other effects may contribute to the observed difference of flow across the individual pathways, such as the simplified representation of the geometry of the Cretaceous and the Pre-Rupelian, which can shift the path of least resistance, or the neglected target aquifers in the generic case, which can decrease the overall resistance of the system.

Table 5.5.: Averaged values for the permeability, porosity, viscosity and diffusivity of the injection horizon and the intermediate aquifer for the Zeidouni-Method.

Parameter	Unit	Injection horizon	Intermediate aquifer
Thickness H_j	m	500	1250
Permeability k_j	m^2	4.50×10^{-15}	3.52×10^{-14}
Porosity ϕ_j	-	0.046	0.078
Viscosity μ_j	Pa s	6.70×10^{-4}	7.51×10^{-4}
Diffusivity D_j	-	0.161	0.664
Total compressibility $C_{t,j}$	Pa^{-1}	9×10^{-10}	9×10^{-10}

Model Comparison 4: Analytical Solution

In this model comparison the Zeidouni-Method for single-phase injection in a multi-layer system with a fault zone (see Sec. 3.2.2) is compared to all other models presented previously in this section. The Zeidouni-Method considers the barrier layers as completely impermeable. Therefore, the layers are only coupled through the fault zone. Similar to the generic model introduced in the previous section, the target aquifers are removed and replaced by a Dirichlet boundary condition, which is achieved by setting the diffusivity of the topmost aquifer to a very high value in the Zeidouni-Method. Only aquifers, not barriers, can be considered with the Zeidouni-Method. However, the injection horizon Solling (thickness 20 m), is embedded between the semi-permeable Upper Middle Buntsandstein (thickness 20 m) and the Lower Middle and Lower Buntsandstein (thickness 110 m and 350 m, respectively) which have a permeability of $1 \times 10^{-16} \text{ m}^2$ and a porosity of 4%, see Table 5.1. These layers contribute to the storage potential and therefore decrease the diffusivity ($D_j = \frac{k_j}{\mu_j \phi_j C_{t,j}}$) of the injection horizon. Hence, permeability and porosity of the injection horizon are recalculated for the Zeidouni-Method by taking an arithmetic average of the four layers of the Middle Buntsandstein, weighted by the specific layer thicknesses. Similarly, the permeability and porosity of the intermediate Cretaceous and Pre-Rupelian layers are averaged to obtain one layer. The resulting parameters are given in Table 5.5. The viscosity of the injection horizon is similar to the viscosity at the injection point in the generic model. The viscosity of the intermediate layer is again a weighted average of the average viscosities in the Cretaceous and Pre-Rupelian layers obtained from the generic model. The setup is shown in Fig. 5.25. A volumetric rate of $0.0231 \text{ m}^3/\text{s}$ is injected for 50 years which is equivalent to the volumetric rate of the 1p2c model.

The results for all models are shown in Fig. 5.26. The Zeidouni-Method can only consider flow through the fault zone, therefore the total flow into the target aquifers and the flow through the fault zone is the same for the Zeidouni-Method. Additionally, the Upper Buntsandstein barrier is considered completely impermeable in the Zeidouni-Method. Therefore, the results

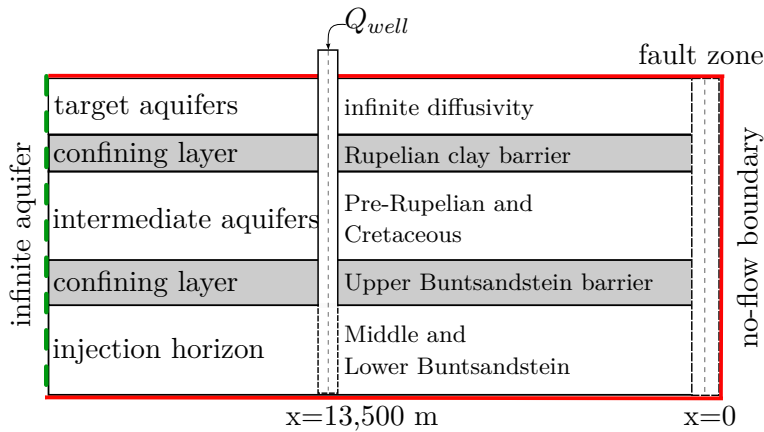


Figure 5.25.: Model setup for the Zeidouni-Method with two permeable layers (injection horizon and intermediate aquifers) and the target aquifers with infinite diffusivity.

of the Zeidouni-Method are the same if this parameter is varied, as shown in Fig. 5.26. For a permeability of $1 \times 10^{-18} \text{ m}^2$ of the Upper Buntsandstein barrier, diffuse migration is significant, as seen in the top row. The total volumetric flow is underestimated by the Zeidouni-Method whereas the volumetric flow over the fault zone is overestimated. The case when focused migration over the fault zone is predominant (bottom row Fig 5.26) is in better agreement with the assumptions of the Zeidouni-Method. Here, the volumetric flow into the target aquifers is higher for the Zeidouni-Method than for the numerical models. The main reason for this is the different realization of the injection horizon. In the numerical model, the semi-permeable layers surrounding the Solling injection horizon provide additional storage potential which reduces the diffusivity of the injection complex. In the Zeidouni-Method, a reduction of the diffusivity is achieved by reducing the permeability of the injection horizon through the averaging process described above. However, this procedure is not physically equivalent with the numerical model and may therefore not generally be expected to deliver similar results. Neglecting the layers surrounding the Solling for the Zeidouni-Method would lead to a very large diffusivity of 0.913 causing a strong overestimation of the volume flow into the target aquifers. This overestimation is shown in the right plot of the bottom row in Fig. 5.26.

Table 5.6 summarizes the comparison between the different models. It shows the cumulative displaced volumes into the target aquifers during the injection period. The overall agreement is best for the low Upper Buntsandstein barrier permeability ($1 \times 10^{-20} \text{ m}^2$), where focused leakage over the fault zone is the main vertical migration pathway. If both diffuse migration over the barrier rock, and focused migration over the fault zone occur, a larger variation in the results can be observed, as the distribution of flow among the different pathways varies. Considering both cases of high and low diffuse migration, the best agreement is observed

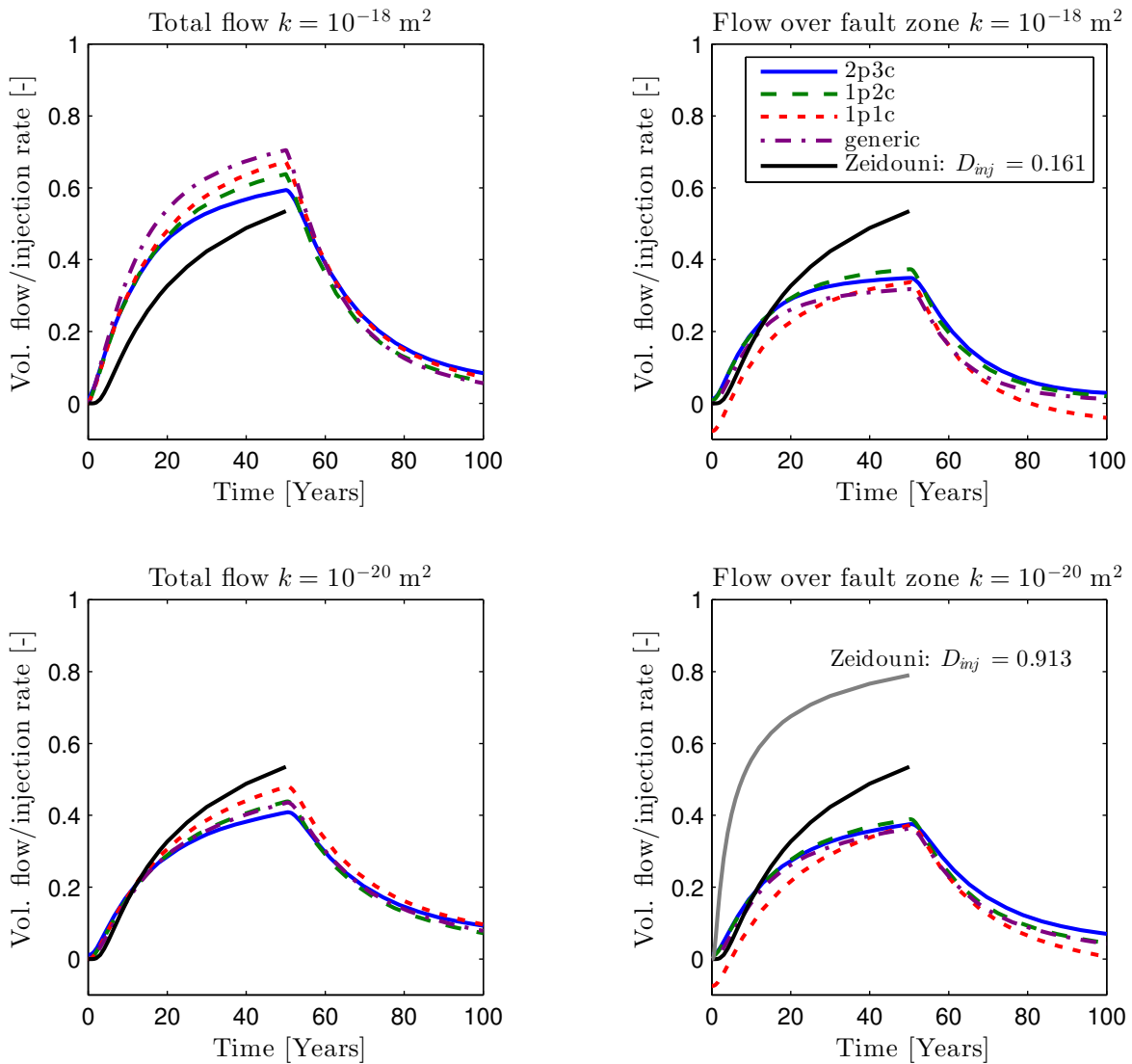


Figure 5.26.: **Top row:** Total volume flow into target aquifers (left) and volume flow over fault zone (right) for an Upper Buntsandstein barrier permeability of $1 \times 10^{-18} \text{ m}^2$. **Bottom row:** Total volume flow into target aquifers (left) and volume flow over fault zone (right) for an Upper Buntsandstein barrier permeability of $1 \times 10^{-20} \text{ m}^2$. Also shown in the right figure is the Zeidouni-Method for the case of a high injection horizon diffusivity.

between the 2p3c and the 1p2c model with regard to a similar distribution of flow among the different pathways. However, if the base flow is deducted from the 1p1c model, as shown by the values in brackets in Table 5.6, the displaced volumes of the 1p1c model are only slightly higher than those of 2p3c and 1p2c models, and therefore the agreement of the results improves

considerably. The generic model underestimates the flow through the fault zone especially for the case of high diffuse migration (Upper Buntsandstein barrier permeability $1 \times 10^{-18} \text{ m}^2$).

Table 5.6.: Fluid volumes displaced into the target aquifers during 50 years of injection over different vertical pathways. The volumes are normalized by the injected volume. Two scenarios are considered: (i) High diffuse leakage through the Upper Buntsandstein barrier (UBS) ($k = 10^{-18} \text{ m}^2$) and (ii) low diffuse leakage through the UBS ($k = 10^{-20} \text{ m}^2$). The values in brackets for the 1p1c model are the displaced volumes obtained when deducting the base flow.

Model type	UBS $k = 10^{-18} \text{ m}^2$			UBS $k = 10^{-20} \text{ m}^2$		
	Total ume	vol-	Fault zone Windows	Total ume	vol-	Fault zone Windows
2p3c	0.44		0.27 0.15	0.28		0.27 0.00
1p2c	0.45		0.28 0.16	0.29		0.27 0.01
1p1c	0.47		0.22 (0.29) (0.17)	0.31		0.22 (0.29) (0.01)
Generic	0.51		0.23 0.26	0.29		0.25 0.03
Zeidouni- Method	0.33		0.33 0.00	0.33		0.33 0.00

5.6. Discussion

The analysis on scenario uncertainty first and foremost shows that, if concentration changes in the target aquifers are considered as the target variable for estimating damage due to CO_2 injection, there is a need to have good knowledge of the salt distribution prior to the injection, which is in qualitative agreement with findings by Tillner et al. (2013), Tillner et al. (2016), Kempka et al. (2013), and Walter et al. (2013). As the results (see Fig. 5.14 and 5.15) show, two conditions need to be fulfilled in order for notable changes in concentration to occur: (i) the permeability is high enough such that flow occurs (this is true where the Rupelian clay barrier is discontinuous) and (ii) initially elevated concentrations have to be present prior to the injection. For the geological model considered in this work, this is especially true for the region near the salt wall. This implies that it is unlikely to observe sudden and strong increases in the salt concentration due to CO_2 injection at locations where elevated concentrations have not been an issue before. Further, notable changes in concentration occur only locally.

The results obtained in the simulations, where salt concentration changes are the target variable, are not only dependent on the hydrogeological parametrization but also on the salt distribution present prior to the injection. As illustrated in Fig. 5.16, there is large uncertainty

regarding different parameters for the initialization run which directly pass on to the results obtained after the injection. There is still room for further investigating the uncertainties, with regard to the model complexity and the parametrization, of models aiming to determine natural pressure, temperature and salinity distributions on a regional scale. For example, the transport of heat is not considered within this work, although a constant geothermal gradient influencing the fluid properties is assumed. A variable temperature distribution can have a strong influence on the base flow and the salt distribution that establishes during the initialization run (Kaiser et al., 2013; Noack et al., 2013). Thereby, the salt wall, which has a higher thermal conductivity than the surrounding layers (Magri et al., 2009a) plays an important role. Future work should evaluate the influence of heat transport on the initial salt distribution. Magri et al. (2009a) model the evolution of the salt and the temperature field near a salt dome with a 2D numerical model. They introduce a so called “transition zone“ between the salt wall and the surrounding layers. Permeability and porosity values of the transition zone are higher than those of the the salt wall but lower than those of the surrounding layers. They show that the transition zone slows down the flow of salt into the surrounding layers. The transition zone can be considered equivalent to the fault zone in this work. LBEG (2014) suspect the existence of permeable pathways similar to a fault zone near a salt wall. Making this assumption, and considering the results of Magri et al. (2009a), implies that the salt would dissolve and propagate faster from the salt wall, when considering a permeable fault zone surrounding the salt wall. To this end, there remain many open questions with regard to a realistic parametrization of the near salt wall region.

A massive parallelization could help to overcome the high computational demand of the initialization run, especially if heat transport is to be considered as well. Using the parallel capabilities of DuMu^x is not feasible in the current state of the implementation, for the type of system considered in this chapter. The reason lies in the implementation of the parallelization of the linear solver, which proves to be very sensitive to the high aspect ratios of the elements and the layered heterogeneities. These seem to cause badly conditioned matrices on the individual processes. A domain decomposition algorithm, which takes into account the connectivity between the degrees of freedom, or in other words which “knows“ about the heterogeneities may improve the convergence of the parallel linear solver. For realistic large scale models, considering salt and heat transport, a robust parallelization is necessary for future work.

A key aspect when considering the injection of CO₂ is the definition of realistic boundary conditions. Assuming Dirichlet conditions at the lateral boundaries during the injection will lead to an underestimation of the vertical migration of brine. Incorporating no-flow boundaries within the inner domain, or extending the model to obtain infinite aquifer conditions will allow significantly higher vertical brine flow, as shown in Fig. 5.17. If the top boundary above the target aquifers was considered a no-flow boundary, brine flow into the target aquifers would be significantly smaller, similar to the results found by Walter et al. (2012, 2013) or Cihan

et al. (2013) where the displaced brine distributes more into the intermediate aquifers below the target aquifers.

Of similar relevance is the diffuse migration across the barrier layers, especially the barrier layer sealing the injection layer, (here: Upper Buntsandstein barrier). The results presented here show that if the permeability of the Upper Buntsandstein barrier is increased, the vertical leakage of brine increases as well, because the overall vertical resistance decreases. Significant diffuse migration across the barrier will change the flow regime in the intermediate layers (Cretaceous, Pre-Rupelian) resulting in focused migration, in locations where the Rupelian clay barrier is discontinuous (hydrogeological windows), even if the Upper Buntsandstein barrier below is intact (see Fig. 5.18). Diffuse vertical migration is significant for permeabilities higher than $1 \times 10^{-19} \text{ m}^2$, which is in good agreement with findings in Birkholzer et al. (2009).

Varying the fault zone transmissibility shows that the injection-induced upward flow is most sensitive to this parameter when diffuse migration is small, and the resistance from the injection point to the fault zone is in the same range as the resistance over the length of the fault zone. The sensitivity of the leakage rate with respect to the fault zone transmissibility is small for fault zone permeabilities higher than $1 \times 10^{-14} \text{ m}^2$, even when increasing the fault zone permeability over several orders of magnitude. Therefore, when assuming a highly permeable fault zone, a simplified geometrical representation of the fault zone, as used in this work, should be sufficient. Focused vertical leakage of highly saline water, which mixes with less saline water in the fault zone, leads to an additional resistance against flow. This resistance is caused by the increasing weight of the saltwater column in the fault zone. The faster the transport velocity of salt, the faster the resistance will increase. As a result of this resistance, the volume flow through the fault zone decreases. This effect is shown in Fig. 5.20, where the storage term of the fault zone nodes is manipulated with the matrix weighting factor (W_m). A high storage in the fault zone ($W_m = 1$) will decrease the transport velocity of the salt, and the resistance, which results in an increased volume flow and a decreased salt flow over the fault zone, when compared to the reference scenario with a low fault zone storage ($W_m = 0$). A new hydrostatic equilibrium, which means that the injection-induced flow over the fault ceases entirely due to the increasing gravitational force, such as discussed in Oldenburg and Rinaldi (2010), is not observed in any of the simulations in this work.

Next, the effect of different model assumptions (model uncertainty) is discussed. In the first model comparison, the transport of salt and, thus, variable-density flow, is neglected. The corresponding 1p1c model does not require a complex and costly initialization run. Obviously, concentration changes cannot be considered as a target variable, but still relevant information on volume flow into the target aquifers can be obtained, which may be a useful target variable for optimizing a pressure management concept. In the 1p1c model, the total volume flow is only slightly higher than in the 1p2c model (see Fig. 5.21, top left). However, when looking at the individual flow paths (see Fig. 5.21, top right), it is observed that the base flow in

the 1p1c model is much higher than in the 1p2c model. The base flow in the 1p1c model is still smaller than the injection-induced flow, but it has the same order of magnitude. In the 1p2c model, the exchange of fluid between the saltwater and freshwater aquifers is reduced, as an effect of the additional resistance caused by an increase in the gravitational force, when saltwater is transported upwards. If the base flow is deducted from the leakage rates, the agreement between the 1p1c and the 1p2c reference model, regarding the displaced volumes into the target aquifers, significantly improves (see Table. 5.6). When looking at the pressures (bottom row of Fig. 5.21) at the measurement point M1 (6.2 km from the injection), which are in very good agreement for the two models, it becomes clear that the overall resistance in the injection layer is met, by making the salinity a pseudo component. In contrast, the pressure increase at M2 (13.5 km from the injection at the fault zone) is about three times as high for the 1p2c model as for the 1p1c model, which can be attributed to the increased resistance due to the focused vertical transport of salt through the fault zone. Hence, the transport of salt is important to consider if pressure increase is a target variable.

The second assumption that was investigated concerns the effect of injecting brine instead of supercritical CO₂ at a volume-equivalent rate. The total volume displaced into the target aquifers during 50 years of injection is 4.7% higher for the 1p2c model than for the 2p3c model (see Table 5.6, high diffuse leakage scenario). With regard to the distribution of flow among the vertical pathways (hydrogeological windows and fault zone), the models are in good agreement. The injection of brine instead of CO₂ is therefore a reasonable conservative assumption that simplifies the physics considerably. This assumption has also been previously discussed in the literature for example by Cihan et al. (2013).

The next assumption deals with simplifying the complex geometry of the geological model. A simpler generic geological model may be advantageous in many cases, as the effort of setting up the geological model is reduced and the implementation of geological features is faster. For example, if the uncertainty in the location of fault zones were included within a risk assessment approach, a simpler generic geological model would allow for a faster analysis of this uncertainty. However, if the location of the geological features is known, then it is important to have good estimates of the horizontal and vertical distances and transmissibilities between features since these determine the main flow paths. Additionally, for the geological model considered here, the viscosity differences due to the varying depth of the injection layer in the complex model can lead to a different resistance compared with the generic model. The same arguments hold for analytical solutions which also rely on a simplified geometrical description of the geological model. The results show that the total flow into the target aquifers for the generic geometry is overestimated by about 13% for the high diffuse leakage scenario in comparison to the 1p2c reference model with the complex geological model, see Table 5.6. The results of the generic and the complex geological models are in better agreement for low diffuse migration over the Upper Buntsandstein barrier, also see Table 5.6. As discussed above,

the uncertainty related to the simulated salt distribution prior to the injection is quite high for the complex geological model, and in reality, there will probably not be sufficient data to calibrate the simulation results to. Therefore, using conservative assumptions, as presented in Walter et al. (2012) or Cihan et al. (2013), with a generic geometry can be justified in the light of sparse data availability. The salt concentration at the saltwater - freshwater interface will then strongly influence the results of a risk assessment.

Finally, comparing the results of the numerical models to the Zeidouni-Method (Zeidouni, 2012) reveals first and foremost the importance of considering the semi-permeable layers, here defined as the layers with a permeability of $1 \times 10^{-16} \text{ m}^2$, that surround the injection horizon Solling. Their contribution to the overall storage of displaced brine is high which causes a reduction of vertical flow during the injection period. When including the layers of the Middle and Lower Buntsandstein into the Zeidouni-Method an averaging of the properties of these layers is performed in order to obtain one injection layer with a more realistic diffusivity than the one obtained when solely considering the Solling layer. The results given in Fig. 5.26 show that the Zeidouni-Method underestimates flow for the case when diffuse migration across the Upper Buntsandstein barrier is significant and overestimates flow if focused migration over the fault zone is the dominant migration pathway. The latter scenario is in better agreement with the assumptions of the Zeidouni-Method. Therefore, it can be concluded that the Zeidouni-Method is conservative with respect to flow over the fault zone for the geological setup considered in this work and the scenario of low diffuse migration. As such, the Zeidouni-Method can be used to quickly assess the consequences of changing certain parameters in the geological model. This is especially useful for investigating statistical uncertainty (see Fig. 5.1) with Monte-Carlo methods, where many different realizations are required. The analytical model presented in Cihan et al. (2011) is also capable of handling diffuse migration over barrier layers. Hence, a comparison with this model would be very interesting, and would improve the overall understanding of this complex problem.

5.7. Conclusion

The main findings of this chapter are summarized below:

- Notable, in the sense of non-negligible, increases in salt concentration in the target aquifers are locally constrained to regions, where initially elevated concentrations are present prior to the injection, and where permeabilities are high enough to support sufficient flow. Hence, the quality of the prediction of concentration changes strongly depends on how well the initial salt distribution is known.

- An inherent problem to modeling is the assignment of boundary conditions. Lateral and top boundary conditions strongly determine the amount of displaced brine into the target aquifers. Lateral Dirichlet boundary conditions at insufficient distance from the injection will lead to a strong underestimation of vertical flow. Setting the top boundary condition as *open* - as opposed to a closed boundary at the top - strongly increases the amount of fluid that is displaced into the target aquifers.
- The Upper Buntsandstein barrier permeability plays a crucial role in determining the amount of diffuse leakage. Diffuse migration over the Upper Buntsandstein barrier can result in focused leakage in locations where the Rupelian clay barrier is discontinuous.
- Due to the low sensitivity of the fault zone permeability on the leakage rates, the representation of the fault zone, using a discrete fracture approach, based on a crude approximation of the geometry of the fault zone, and without requiring additional degrees of freedom, is a good compromise between accuracy and the computational demand.
- During injection (constant injection rate), salt transport decreases the overall vertical flow due to the additional resistance caused by the increase in the gravitational force. However, the effect of salt transport on vertical flow is not as significant as the pressure increase near the fault zone observed when considering salt transport. Hence, if pressure increase is a target variable, for example in studies considering fault reactivation, salt transport should be considered.
- Injecting an equivalent volume of brine, instead of CO₂ is a conservative assumption which leads to slightly increased brine flow into the target aquifers.
- Simplifying the geometry can lead to comparable results with regard to total vertical brine migration with much less effort required for the setup of the geological model. For real systems, where the uncertainty of the geological model both in parametrization and geometry is high, this implies that a simplified representation of the geometry for the simulations can be considered a feasible and justified approach.
- A comparison with the Zeidouni-Method shows the importance of semi-permeable layers ($1 \times 10^{-16} \text{ m}^2$) surrounding the injection horizon Solling. For a realistic estimate of vertical migration, the storage potential for displaced brine of these layers needs to be considered.

6. Summary and Outlook

6.1. Summary

Carbon Dioxide, Capture and Storage (CCS) is considered to be a cost-effective technology for mitigating climate change. A necessary requirement for a successful implementation of CCS is the public acceptance of the technology. The affected public needs to be aware of, and accept the risks that are associated with the subsurface storage of CO₂. This demands the use of transparent and comprehensible criteria in a site-selection and characterization process.

This work deals with two aspects of a multi-level site-selection and characterization process. The first aspect is related to a basin-scale screening method, allowing for a qualitative ranking of different areas with respect to storage efficiency. This aspect is part of the first level of a site-selection and characterization process with the aim of identifying suitable storage sites, which are then characterized in more detail on the following levels. The second aspect investigates the displacement of resident brine during the injection of CO₂, on the basis of a realistic, but not real, large-scale storage site in the North German Basin. Saltwater intrusion in freshwater aquifers is one of the major risks associated with CO₂ storage. The investigation of brine displacement should be part of a higher level of a site-selection and characterization process, where suitable sites have been selected and more site-specific data are available. For both aspects (basin-scale screening and investigation of brine displacement), models with varying complexity are analyzed, as well as the relevant processes and parameters. This section summarizes the key findings of this work by formulating a set of questions to which answers are provided, that have been found based on the results and conclusions of this dissertation.

Basin-Scale Screening with Regard to Storage Efficiency

Is the storage efficiency significantly influenced by the initial fluid properties in the reservoir? The basin-scale database available in this work comprises regionalized data for depth, temperature conditions, and salt concentrations in the Middle Buntsandstein rock unit. These data are sufficient to estimate the initial fluid properties (viscosities and densities) of brine

and CO₂. However, other relevant parameters like the permeability, the porosity, and the reservoir thickness are not available on the basin scale. Therefore, numerical simulations are conducted to test whether the effect of the initial fluid properties on the storage efficiency is significant enough, such that a screening approach based on these data will provide useful information. The results obtained from these simulations, at different locations in the Middle Buntsandstein, suggest that there is a notable influence of the initial fluid properties on the calculated storage efficiency. Therefore, a screening approach based on the available database can provide valuable information for identifying suitable areas for CO₂ storage. In order to assess the significance of the initial fluid properties, in comparison to the parameters porosity and the reservoir thickness, different areas in the Middle Buntsandstein rock unit are selected, where data for porosity and reservoir thickness are available. Monte-Carlo simulations taking into account the area-specific data for porosity and reservoir thickness are performed. The results indicate that the influence of the initial fluid properties on the storage efficiency is less important than the influence of the parameters porosity and reservoir thickness, but can be in the same range.

What are favorable conditions for a high storage efficiency? Based on the initial fluid properties, the regional variations of the geothermal gradient have a strong influence on the storage efficiency. This becomes clear, when comparing the regional variations of the geothermal gradient with the distribution of the gravitational number (Gr), as an indicator for storage efficiency (Fig. 4.2 and 4.5) in the Middle Buntsandstein. High geothermal gradients lead to high values of Gr and therefore to a low storage efficiency and vice versa. Additionally, the storage efficiency is also influenced by the viscosity ratio ($\frac{\mu_w}{\mu_n}$), which decreases with depth leading to a more piston-like displacement, of the CO₂ front. The simulations show the increase in storage efficiency, related to lower viscosity ratios, for depths greater than 2000 m.

Which screening methods can be used for determining suitable areas for CO₂ storage? Two screening methods, the Gr-criterion and the Okwen-Method, are analyzed in this work. Both methods can be used to rank different areas according to their storage efficiency. The Gr-criterion and the Okwen-Method are compared to the simulation results of a full-fledged numerical model accounting for two-phase flow, in order to test their suitability as indicators for storage efficiency. The main finding is, that both methods show an acceptable qualitative agreement with the simulation results for large parts of the considered range of pressure, temperature, and salinity conditions found in the Middle Buntsandstein rock unit. At depths between 900–2000 m the Gr-criterion shows a clearer trend than the Okwen-Method, relating low values of Gr to high storage efficiencies and vice versa. However, for depths greater than 2000 m, the agreement between the Okwen-Method and the simulations is better, than

for the Gr-criterion, because the Okwen-Method considers both the brine, and the CO₂ viscosity. For thermodynamical conditions close to the critical point (i.e. depths <900 m), both methods (Gr-criterion and Okwen-Method) strongly underestimate the trend observed in the simulations, because of the effect of the injection-induced pressure on the fluid properties of CO₂. The deviation of the Gr-criterion and the Okwen-Method to the simulation results has to be evaluated bearing in mind the uncertainties in the hydrogeological parameters (permeability, porosity, reservoir thickness, capillary pressure-saturation relationships, and relative permeabilities), which are assumed higher than the model uncertainty related to the screening method used. The Okwen-Method produces quantitative estimates for the storage efficiency, as opposed to the Gr-criterion, which can only be used for a qualitative ranking. This has the advantage that parameters like the porosity (if regionalized data were available on the basin scale) can be directly included in the approach, for example for storage capacity estimates. Both, the Gr-criterion and the Okwen-Method, do not consider pressure constraints on storage efficiency. However, pressure constraints are important to consider, as a high demand for CO₂ storage space will lead to high injection rates. The injection-induced pressure increase should not compromise the integrity of the barrier rock or the reservoir. Therefore, combining, for example the Okwen-Method with a method taking into account injection-induced pressure constraints will lead to more realistic estimates. This is further discussed in the outlook (Sec. 6.2).

Large-Scale Brine Displacement Along Vertical Pathways

Which parts of the target aquifers are prone to salinity increases due to CO₂ injection?

Notable, in the sense of non-negligible, increases in salt concentration in the target aquifers are locally constrained to regions, where initially elevated concentrations are present prior to the injection, and where permeabilities are high enough to support sufficient flow (i.e. at the fault zone and the hydrogeological windows). Hence, the quality of the prediction of concentration changes strongly depends on how well the initial salt distribution is known.

Which are the relevant components of the geological model controlling saltwater migration into the target aquifers?

Vertical leakage of saltwater into the target aquifers due to CO₂ injection requires vertical pathways, where diffuse or focused leakage can occur. In the geological model considered in Chapter 5, diffuse leakage can occur over the Upper Buntsandstein barrier, which is situated above the injection horizon Solling. Focused leakage can occur over the hydrogeological windows in the Rupelian clay barrier and the permeable fault zone on the salt wall, which connects the target aquifers to the injection horizon. The permeability

of these leakage pathways along with other key components of the geological model are varied, not in a statistical sense, but on the entire range of plausible values, thereby creating a span of possible results. This allows, to some extent, a generalization of the conclusions drawn here to other sites, at least within the North German Basin. In Chapter 5, the following scenario studies have been conducted:

- The effect of the initial quasi-stationary salt distribution on the salt concentration increase after the injection.
- Different lateral boundary condition types (Dirichlet, no-flow, and infinite aquifer).
- Diffuse leakage during the injection, controlled by the permeability of the Upper Buntsandstein barrier.
- Focused leakage during the injection, controlled by the fault zone permeability.

If the salt concentration increases in the target aquifers, caused by the injection of CO₂, are the target variable, the results are highly dependent on the salt distribution prior to the injection. If, on the other hand, the injection-induced volumetric leakage rate into the target aquifers is the target variable, the salt distribution prior to the injection hardly influences the results.

Lateral and top boundary conditions strongly determine the amount of displaced fluid into the target aquifers. Lateral Dirichlet boundary conditions at insufficient distance from the injection will lead to an underestimation of the vertically displaced saltwater. The combination of:

- permeable pathways (i.e. fault zone, and hydrogeological windows),
- Dirichlet boundary conditions on the top of the domain (i.e. rivers),
- and lateral no-flow or infinite aquifer boundary conditions

leads to a significant amount of the injected volume being displaced into the target aquifers. The permeability of the Upper Buntsandstein barrier has a strong influence on the overall flow field. For values between 1×10^{-20} to 1×10^{-19} m² focused leakage over the fault zone is the dominant leakage pathway. However, if the permeability is between 1×10^{-18} to 1×10^{-17} m² diffuse leakage over the barrier is the major vertical leakage pathway. This diffuse leakage then leads to focused leakage into the target aquifers over the hydrogeological windows in the Rupelian Clay barrier. This implies that discontinuities in the Rupelian clay barrier play an important role as leakage pathways, if diffuse leakage over the Upper Buntsandstein barrier is significant.

The leakage rates are less sensitive to the fault zone permeability compared to the Upper

Buntsandstein barrier permeability, especially if diffuse migration over the barrier is significant. For low diffuse migration over the barrier, the strongest sensitivity of the fault zone permeability is observed, when the resistance within the injection horizon from the injection point up to the fault zone is in a similar range, as the resistance over the length of the fault zone. Also important, although not specifically investigated in the scenario studies, are the semi-permeable layers ($1 \times 10^{-16} \text{ m}^2$) surrounding the injection horizon. For a realistic estimate of vertical saltwater migration, the storage potential of these layers, with regard to the displaced brine, needs to be considered. The layers decrease the diffusivity of the whole injection complex, thereby attenuating the upward leakage (see Fig. 5.26 bottom right, Zeidouni-Method for high diffusivity).

What are suitable model simplifications for analyzing brine migration and when can they be applied?

Models with varying physical complexity can be used for analyzing brine migration due to CO_2 injection. More complex models will generally increase the computational demand and require more data. The choice of the model should therefore depend on the target variable of interest. In Chapter 5 different target variables describing the effects of CO_2 storage are considered: salt concentration increases in the target aquifers, pressure increase at selected locations in the injection horizon, and the leakage rates into the target aquifers. Further, different assumptions with regard to the physical complexity of different models are tested, for the above target variables. The simplification of model complexity follows two aims: (i) improving the understanding of the relevant processes by switching assumptions on and off, and (ii) reducing the model uncertainty, by quantifying the effects of different model simplifications on different target variables. The following model simplifications are considered:

- Injecting brine instead of CO_2 .
- Neglecting the effect of salt transport, and therefore also variable-density flow effects.
- Simplifying the complex geometry of the geological model into a simple layered system, with straight, horizontal layers.
- Using the analytical Zeidouni-Method to evaluate leakage across the fault zone.

The analysis in Chapter 5 shows that the first model simplification, where an equivalent volume of brine is injected instead of CO_2 , is a conservative assumption which leads to slightly increased brine flow into the target aquifers. This assumption considerably simplifies the physics and is a good choice if an accurate description of the CO_2 plume or the pressure increase near the injection well is not necessary. This is the case for the analysis in Chapter 5, where only far-field effects are considered. The main advantage of the other model simplifications,

is that no initialization run is required, to establish a quasi-stationary system. This greatly speeds up the analysis, as the initialization run has by far the highest computational demand. However, this also means that a realistic salt distribution cannot establish, and therefore salt concentration increases in the target aquifers cannot be considered as a target variable. Instead the leakage rate into the target aquifers, and the pressure within the injection horizon remain as target variables. Information regarding the leakage rates can be important, for example for optimizing pressure management concepts. The pressure increase in the injection horizon can be an important criterion to control injection rates, for example to avoid geomechanical failure in fault zones.

Considering the leakage rates into the target aquifers as the target variable, the results of most model simplifications show an acceptable agreement (see Table 5.6 and Fig. 5.26). Although there are deviations in the leakage rates for the individual models, the impact of variable hydrogeological parameters on the results is assumed to be much greater, justifying the use of simplified models. Only the Zeidouni-Method clearly underestimates the total leakage, when diffuse leakage over the Upper Buntsandstein barrier is dominant, as diffuse leakage cannot be accounted for with this method.

Neglecting salt transport significantly reduces the pressure increase observed at the fault zone, compared to the models which consider salt transport. This pressure increase is related to the increasing weight of the fluid column, when dissolved salt migrates upwards along the fault zone. Hence, if pressure increase is a target variable, for example in studies considering fault reactivation, salt transport should be considered.

6.2. Outlook

Basin-Scale Screening with Regard to Storage Efficiency

Combining analytical solutions for calculating storage efficiency and capacity. The literature dealing with estimating CO₂ storage efficiency (Sec. 1.2.1) shows that storage efficiency is not only constrained by the technically accessible pore volume, but also by the pressure buildup around the injection well. Analytical solutions exist for both of these constraints. One example, the Okwen-Method, discussed in this work in Chapter 4, can be used to assess the technically accessible storage volume. Another analytical solution, proposed by Mathias et al. (2009), is applicable for determining a sustainable injection rate, constrained by a maximum pressure buildup at the injection well. A sustainable injection rate can thus be determined, serving as an input parameter for the Okwen-Method, used for determining the

storage efficiency. The great advantage of combining these two analytical approaches is that the computational costs are negligible, while the most relevant physical effects are included. Additionally, both methods rely on similar assumptions, such as open aquifers, and a vertical injection well. Given the database available in this work for the Middle Buntsandstein rock unit, which includes only depth, temperature conditions, and salt concentrations, it is obvious that critical input parameters such as permeability, porosity, compressibility, and reservoir thickness are missing. These parameters could, as a first assumption, be replaced by constant values based on reasonable assumptions.

Using the arbitrary polynomial chaos expansion to calculate storage efficiency and capacity.

The method proposed here combines the advantages of a full-fledged numerical model with the speed of evaluating a polynomial for obtaining results. Using a numerical model, storage efficiency can be constrained by a maximum pressure at the injection well, as well as a spill point criterion similar to the simulations carried out in Chapter 4. Based on input data with an arbitrary distribution, the arbitrary Polynomial Chaos Expansion (aPCE) (Oladyshkin et al., 2011a,b; Oladyshkin and Nowak, 2012) uses the results of several simulation runs, to create a polynomial function, approximating the numerical model with regard to a target variable (here: storage efficiency). The number of simulation runs is constrained by the number of variable input parameters (N), and by the degree of the polynomial (d):

$$\text{No. Simulations} = \frac{(N + d)!}{N!d!}.$$

For example considering a database of six parameters (depth temperature, salinity, porosity, permeability, and reservoir thickness), and a third order polynomial, this would result in 84 simulation runs, which should not pose a considerable problem, assuming a similar setup of the numerical model as in Sec. 4.3. Once the polynomial is obtained, storage efficiency can be calculated for the rest of the database at a negligible cost.

Combining the evaluation of storage efficiency for the North German Basin with structural traps.

Knopf et al. (2010) identified 408 discrete structures suitable for storing CO₂ in Germany. These discrete structures could be combined with the basin-scale calculation of Gr for the Middle Buntsandstein rock unit in the North German Basin which is carried out in this work. The Gr-criterion could then help in selecting the most suitable structures. Alternatively, one of above methods (combination of analytical solutions or arbitrary Polynomial Chaos Expansion) could be used for quantifying the storage efficiencies within these structures.

Combination of suitable structural traps with large CO₂ point sources in the North German Basin. In a last step, the information regarding storage efficiency or capacity for the structural traps can be combined with information about the positions of large CO₂ point sources, such as coal-fired power plants, within an economic distance of the structural traps. This would be an important step towards determining the matched capacity within the North German Basin. Of course, this step is far beyond the actual scope of this work, and for defining an economic distance many additional technical, social, economic and legislative criteria would have to be reviewed, besides storage efficiency.

Large-Scale Brine Displacement Along Vertical Pathways

Improving the convergence of parallel simulations in DuMu^x for layered heterogeneous systems. As discussed in Sec. 5.6, solving large layered heterogeneous systems with the help of massive parallelization in DuMu^x is constrained by the convergence of the iterative linear solver (for parallel runs the Bi-conjugate Gradient Stabilized method, with an algebraic multigrid method for preconditioning is used (Blatt and Bastian, 2007)). As a matter of fact, all the simulations carried out in Chapter 5, had to be performed on a single process, except for the homogeneous saltpool benchmark (Sec. 5.4.2). For parallel simulations the linear solver shows poor convergence for: (i) high aspect ratios of the elements (in this work: horizontal:vertical - 30:1), and (ii) heterogeneity due to the horizontal layering, i.e. homogeneous permeability within a layer, but different permeabilities for each layer. This leads to badly conditioned matrices on the individual processes. As a result, the convergence of parallel simulations, reacts very sensitive to the number of processes used, and the method used for the domain decomposition. A possible solution could be a domain decomposition algorithm, which takes into account the geological model, and therefore the connectivity between the degrees of freedom, such that the degrees of freedom with a strong connectivity preferably stay within one process. In other words, using an algorithm for domain decomposition that is aware of the heterogeneities may improve the convergence of the parallel linear solver.

Improving the efficiency and accuracy of the 1p2c model with regard to variable-density flow. Although the 1p2c model is capable of dealing with variable-density flow, as shown for the saltpool benchmark in Sec. 5.4.2, there is still room for increasing the efficiency and accuracy of the model. For many applications involving variable-density flow, the so-called Boussinesq assumption is considered a valid simplification (e.g. Diersch and Kolditz (2002)). The Boussinesq assumption calls for the division of the mass balance equations of the 1p2c model (Eq. 3.1.2) by the brine density, removing the brine density from all of the terms

except the gravity term of the Darcy velocity. The Boussinesq assumption can improve the convergence, as the non-linearities decrease.

For improving the accuracy of the model, many authors (Bastian et al., 2001; Diersch and Kolditz, 2002; Johannsen et al., 2002) stress the importance of using a consistent velocity approximation as proposed by Knabner et al. (1998), which is not implemented in DuMu^x. A consistent velocity approximation will mainly decrease the velocity dependent dispersion. Without this approximation, the transport of salt can be overestimated. This was also reported for the saltpool benchmark (Diersch and Kolditz, 2002). The overestimation of dispersive fluxes is the result of the erroneous velocities that arise during the linear approximation of the pressure between two degrees of freedom, which, considering the case of variable-density flow, is generally a non-linear function.

Including heat transport for determining the initial conditions. The salt distribution prior to the injection of CO₂ is a key parameter, when salt concentration changes are the target variable. As discussed in Sec. 5.6, there is large uncertainty regarding this parameter, especially close to structures like salt domes, which are a potential source of salt in the system. Both the temperature, and the salt distribution may strongly influence the flow field near these structures (Magri et al., 2009a,b). In the simulations carried out in this work a constant geothermal gradient is assumed. In future work, energy transport should be considered in order to obtain more realistic distributions of pressure, temperature and salinity.

Using the geological model presented in this work as a benchmark setting. The geological model presented in Chapter 5 includes characteristics of the North German Basin, such as the salt wall structure and the hydrogeological windows in the Rupelian clay barrier. The geometry of the layers is very complex. For example, the depth of the injection horizon Solling varies between 850 to 3000 m. Diffuse leakage across the Upper Buntsandstein barrier, focused leakage over the fault zone on the salt wall, and the importance of the semi-permeable layers ($1 \times 10^{-16} \text{ m}^2$), surrounding the injection horizon Solling have to be taken into account for calculating vertical leakage. In other words, the geological model is very challenging, and therefore it is a suitable testing ground for different models. Future work in this field should focus on setting up a benchmark or model comparison study to test different numerical, and analytical models, for example the analytical model presented in Cihan et al. (2011), with regard to the volumetric leakage rates reaching the target aquifers. With this, important insights into the applicability of different models for estimating leakage could be gained. This is particularly relevant for operators who have to carry out a risk assessment or develop a pressure management strategy.

Basin-scale model for the evaluation of pressure buildup caused by multiple CO₂ injections.

To this day, no basin-scale geological model of the North German Basin exists. Assuming such a model will exist in the future, the overall pressure buildup due to basin-wide CO₂ storage at multiple injection sites could be estimated. The information that can be gained by a basin-scale model is very relevant. On the one hand, a more realistic estimation of storage efficiency constrained by a maximum pressure buildup can be attained, and on the other hand a better assessment of brine migration on the basin scale can be made. The results and conclusions of Chapter 5 may prove to be valuable input for the design of an efficient basin-scale numerical model. The basin-scale model should include the over- and underburden, as these are required for a realistic estimation of pressure buildup. Injecting brine instead of CO₂, is a conservative assumption that significantly simplifies the physical complexity. A coarse discretization (300 × 300 m), as used in this work, should be sufficient, if near well conditions are not the primary interest. If the pressures at the injection well are required a well model can be applied. An accurate description of the geometry of vertical discontinuities, such as fault zones or salt domes is not required, which reduces the overall computational demand. A realistic description of the base flow (i.e. naturally occurring flow without injection) will make the model significantly more complex. The reasons being, that such a model would require recharge and river boundary conditions, as well as an initialization run, to obtain a quasi-stationary state. Just for estimating leakage rates and pressure buildup this effort is not necessary. Similar to the generic geometry case discussed in Chapter 5, the target aquifers may be replaced by a horizontal Dirichlet boundary condition, where no recharge enters the system. Salt transport, and the effects of variable-density flow, may then be included without an initialization run, for example by assigning a linear increase of salt with depth. Generally, a strategy where models of varying complexity are used side by side may prove advantageous when reducing model uncertainty. Simple models may be used for inverse modeling to estimate parameters or to optimize pressure management concepts. Complex models can be used to validate these simple models or estimate model errors.

Bibliography

- Bachu, S. Screening and ranking of sedimentary basins for sequestration of CO₂ in geological media in response to climate change. *Environmental Geology*, 44(3):277–289, 2003.
- Bachu, S., Bonijoly, D., Bradshaw, J., Burruss, R., Holloway, S., Christensen, N. P., and Mathiassen, O. M. CO₂ storage capacity estimation: Methodology and gaps. *International Journal of Greenhouse Gas Control*, 1(4):430–443, 2007.
- Bannick, C., Engelmann, B., Fendler, R., Frauenstein, J., Ginzky, H., Hornemann, C., Ilvonen, O., Kirschbaum, B., Penn-Bressel, G., Rechenberg, J., Richter, S., Roy, L., and Wolter, R. Grundwasser in Deutschland. Technical report, Bundesministerium für Umwelt, Naturschutz und Reaktorsicherheit (BMU), 2008.
- Bastian, P., Johannsen, K., Lang, S., Wieners, C., Reichenberger, V., and Wittum, G. High-accuracy simulation of density driven flow in porous media. Technical report, Interdisziplinäres Zentrum für Wissenschaftliches Rechnen Technical Simulation Group Universität Heidelberg, Heidelberg, 2001.
- Batzle, M. and Wang, Z. Seismic properties of pore fluids. *Geophysics*, 57(11):1396–1408, 1992.
- Bear, J. *Dynamics of fluids in porous media*. Dover Publ Inc, 1988. ISBN 9780486656755.
- Bear, J. *Encyclopedia of Hydrological Sciences*, volume 4. John Wiley & Sons, Ltd, Chichester, UK, 2005. ISBN 0471491039.
- Bielinski, A. *Numerical Simulation of CO₂ Sequestration in Geological Formations*. PhD thesis, Institut für Wasserbau, Universität Stuttgart, 2006.
- Birkholzer, J. T. and Zhou, Q. Basin-scale hydrogeologic impacts of CO₂ storage: Capacity and regulatory implications. *International Journal of Greenhouse Gas Control*, 3(6):745–756, 2009.

- Birkholzer, J. T., Zhou, Q., and Tsang, C.-F. Large-scale impact of CO₂ storage in deep saline aquifers: A sensitivity study on pressure response in stratified systems. *International Journal of Greenhouse Gas Control*, 3(2):181–194, 2009.
- Birkholzer, J. T., Cihan, A., and Zhou, Q. Impact-driven pressure management via targeted brine extraction - Conceptual studies of CO₂ storage in saline formations. *International Journal of Greenhouse Gas Control*, 7:168–180, 2012.
- Birkholzer, J. T., Oldenburg, C. M., and Zhou, Q. CO₂ migration and pressure evolution in deep saline aquifers. *International Journal of Greenhouse Gas Control*, 40:203–220, 2015.
- Blatt, M. and Bastian, P. The Iterative Solver Template Library. *Applied Parallel Computing. State of the Art in Scientific Computing*, 4699:666–675, 2007.
- Brooks, R. J. and Corey, A. T. Hydraulic properties of porous media. *Hydrology Papers*, 3, 1964.
- Bruckner, T., Bashmakov, I. A., Mulugetta, Y., Chum, H., Navarro, A. D., Edmonds, J., Faaij, A., Fungtammasan, B., Garg, A., Hertwich, E., and Others. Energy systems. In *Mitigation of Climate Change. Contribution of Working Group III to the Fifth Assessment Report of the Intergovernmental Panel on Climate Change*, chapter 7, pages 511–597. Cambridge University Press, 2014.
- Celia, M. A. and Nordbotten, J. M. Practical modeling approaches for geological storage of carbon dioxide. *Ground Water*, 47(5):627–638, 2009.
- Celia, M. A., Nordbotten, J. M., Court, B., Dobossy, M., and Bachu, S. Field-scale application of a semi-analytical model for estimation of CO₂ and brine leakage along old wells. *International Journal of Greenhouse Gas Control*, 5(2):257–269, 2011.
- Cihan, A., Zhou, Q., and Birkholzer, J. T. Analytical solutions for pressure perturbation and fluid leakage through aquitards and wells in multilayered-aquifer systems. *Water Resources Research*, 47(10), 2011.
- Cihan, A., Birkholzer, J. T., and Zhou, Q. Pressure buildup and brine migration during CO₂ storage in multilayered aquifers. *Ground water*, 51(2):252–67, 2013.
- Clarke, L., Jiang, K., Akimoto, K., Babiker, M., Blanford, G., Fisher-Vanden, K., Hourcade, J.-C., Krey, V., Kriegler, E., Löschel, A., and Others. Assessing transformation pathways. *Climate Change 2014: Mitigation of Climate Change. Contribution of Working Group III to the Fifth Assessment Report of the Intergovernmental Panel on Climate Change*, pages 413–510, 2014.

- Class, H., Ebigo, A., Helmig, R., Dahle, H. K., Nordbotten, J. M., Celia, M. A., Audigane, P., Darcis, M., Ennis-King, J., Fan, Y., Flemisch, B., Gasda, S. E., Jin, M., Krug, S., Labregere, D., Naderi Beni, A., Pawar, R. J., Sbai, A., Thomas, S. G., Trenty, L., and Wei, L. A benchmark study on problems related to CO₂ storage in geologic formations. *Computational Geosciences*, 13(4):409–434, 2009.
- Class, H., Kissinger, A., Knopf, S., Konrad, W., Noack, V., and Scheer, D. Schlussbericht Mehrstufige und regionale Charakterisierung potentieller CO₂-Speicherformationen unter besonderer Berücksichtigung von Soleaufstiegsrisiken - ein integrierter natur- und sozialwissenschaftlicher Ansatz. Technical report, 2015.
- Darcis, M. *Coupling Models of Different Complexity for the Simulation of CO₂ Storage in Deep Saline Aquifers*. PhD thesis, Institut für Wasser- und Umweltsystemmodellierung, Universität Stuttgart, 2012.
- Darcis, M., Class, H., Flemisch, B., and Helmig, R. Storage in Deep Saline Aquifers. *Oil & Gas Science and Technology – Revue d’IFP Energies nouvelles*, 66(1):93–103, 2011.
- Diersch, H.-J. G. and Kolditz, O. Variable-density flow and transport in porous media: approaches and challenges. *Advances in Water Resources*, 25(8-12):899–944, 2002.
- Dooley, J. J. Estimating the supply and demand for deep geologic CO₂ storage capacity over the course of the 21 st Century : A meta-analysis of the literature. *Energy Procedia*, 37: 5141–5150, 2013.
- Eom, J., Edmonds, J., Krey, V., Johnson, N., Longden, T., Luderer, G., Riahi, K., and Van Vuuren, D. P. The impact of near-term climate policy choices on technology and emission transition pathways. *Technological Forecasting and Social Change*, 90:73–88, 2015.
- Fenghour, A., Wakeham, W. A., and Vesovic, V. The Viscosity of Carbon Dioxide. *Journal of Physical and Chemical Reference Data*, 27(1):31, 1998.
- Flemisch, B., Darcis, M., Erbertseder, K., Faigle, B., Mosthaf, K., Lauser, A., Müthing, S., Nuske, P., Tatomir, A., Wolf, M., and Helmig, R. DUMUX: DUNE for multi-{phase, component, scale, physics, ...} flow and transport in porous media. *Advances in Water Resources*, 34(9):1102–1112, 2011.
- Gläser, D. *Simulation der Konvektionsströmung bei der Speicherung von CO₂ in tiefen Gesteinsformationen*. Bachelor’s thesis, Institut für Wasser- und Umweltsystemmodellierung, Universität Stuttgart, 2011.

- Goater, A. L., Bijeljic, B., and Blunt, M. J. Dipping open aquifers - The effect of top-surface topography and heterogeneity on CO₂ storage efficiency. *International Journal of Greenhouse Gas Control*, 17:318–331, 2013.
- Goodman, A., Bromhal, G., Strazisar, B., Rodosta, T., and Guthrie, G. Comparison of Publicly Available Methods for Development of Geologic Storage Estimates for Carbon Dioxide in Saline Formations. Technical Report March, U.S. Department of Energy, National Energy Technology Laboratory, Morgantown, 2013.
- Helmig, R. *Multiphase flow and transport processes in the subsurface: A contribution to the modeling of hydrosystems*. Springer, 1997.
- Huang, X., Bandilla, K. W., Celia, M. A., and Bachu, S. Basin-scale modeling of CO₂ storage using models of varying complexity. *International Journal of Greenhouse Gas Control*, 20 (2014):73–86, 2014.
- IEA. Energy Technology Perspectives 2012. Technical report, International Energy Agency, 2012a.
- IEA. Medium-Term Coal Market Report 2012. Technical report, International Energy Agency, 2012b.
- IEA. Technology Roadmap Carbon Capture and Storage. Technical report, International Energy Agency, 2013.
- IPCC. Climate Change 2014: Synthesis Report. Contribution of Working Groups I, II and III to the Fifth Assessment Report of the Intergovernmental Panel on Climate Change. page 151 pp, 2014.
- Johannsen, K., Kinzelbach, W., Oswald, S., and Wittum, G. The saltpool benchmark problem – numerical simulation of saltwater upconing in a porous medium. *Advances in Water Resources*, 25(3):335–348, 2002.
- Kaiser, B. O., Cacace, M., and Scheck-Wenderoth, M. Quaternary channels within the Northeast German Basin and their relevance on double diffusive convective transport processes: Constraints from 3-D thermohaline numerical simulations. *Geochemistry, Geophysics, Geosystems*, 14(8):3156–3175, 2013.
- Kempka, T., Herd, R., Huenges, E., Jahnke, C., Janetz, S., Jolie, E., Kühn, M., Magri, F., Möller, M., Munoz, G., Ritter, O., Schafrik, W., Schmidt-Hattenberger, C., Tillner, E., Voigt, H. J., and Zimmermann, G. brine: CO₂ - Speicherung in Ostbrandenburg:

- Implikationen für eine synergetische geothermische Energiegewinnung und Konzeptionierung eines Frühwarnsystems gegen Grundwasserversalzung. Technical report, 2013.
- Kipp, K. L. Adaptation of the Carter-Tracy Water Influx Calculation to Groundwater Flow Simulation. *Water Resources Research*, 22(3):423–428, 1986.
- Kipp, K. L. A Computer Code for Simulation of Heat and Solute Transport in 3D ground Water flow, 1987.
- Kissinger, A., Noack, V., Knopf, S., Scheer, D., Konrad, W., and Class, H. Characterization of reservoir conditions for CO₂ storage using a dimensionless Gravitational Number applied to the North German Basin. *Sustainable Energy Technologies and Assessments*, 7:209–220, 2014.
- Kissinger, A., Noack, V., Knopf, S., Konrad, W., Scheer, D., and Class, H. Regional-scale brine migration along vertical pathways due to CO₂ injection in the North German Basin – Part 1: a simulated case study using models of varying complexity. *in preparation*, 2017.
- Knabner, P., Tapp, C., and Thiele, K. Adaptive finite volume discretization of density driven flows in porous media. *Acta Math. Univ. Comenianae*, Di(May), 1998.
- Knopf, S., May, F., Müller, C., and Gerling, P. Neuberechnung möglicher Kapazitäten zur CO₂-Speicherung in tiefen Aquifer-Strukturen. *Energiewirtschaftliche Tagesfragen*, 60(4): 76–80, 2010.
- Kopp, A., Class, H., and Helmig, R. Investigations on CO₂ storage capacity in saline aquifers Part 1. Dimensional analysis of flow processes and reservoir characteristics. *International Journal of Greenhouse Gas Control*, 3(3):263–276, 2009a.
- Kopp, A., Class, H., and Helmig, R. Investigations on CO₂ storage capacity in saline aquifers - Part 2: Estimation of storage capacity coefficients. *International Journal of Greenhouse Gas Control*, 3(3):277–287, 2009b.
- Kopp, A., Binning, P., Johannsen, K., Helmig, R., and Class, H. A contribution to risk analysis for leakage through abandoned wells in geological CO₂ storage. *Advances in Water Resources*, 33(8):867–879, 2010.
- Land, C. S. Calculation of imbibition relative permeability for two and three-phase flow from rock properties. *Society of Petroleum Engineers Journal*, 8(2):149–156, 1968.
- Larue, J. Endlagerung im Tonstein, Entwicklung eines synthetischen Tonsteinstandortes, Teil 2: Standortcharakterisierung. Abschlussberichte zum Vorhaben 3607R02538 „planerische Grundsatzfragen“. Technical report, GRS-A-3535, Köln, 2010.

- LBEG (Landesamt für Bergbau, Energie und Geologie). CO₂-Speicherung, accessed October 2014. URL http://www.lbeg.niedersachsen.de/energie_rohstoffe/co2speicherung/co2-speicherung-935.html.
- Li, D. and Lake, L. Scaling fluid flow through heterogeneous permeable media. *SPE Advanced Technology Series*, 3(1):188–197, 1995.
- LIAG (Leibniz-Institut für Angewandte Geophysik). Deutschlandkarte des geothermischen Gradienten, 2012. URL <http://www.liag-hannover.de/de/s/s4/forschungsfelder/temperaturfeld-im-untergrund-deutschlands/ergebnis.html>.
- Lookeren, J. Calculation Methods for Linear and Radial Steam Flow in Oil Reservoirs. *Society of Petroleum Engineers Journal*, 23(3):427–439, 1983.
- LUGV (Landesamt für Umwelt, Gesundheit und Verbraucherschutz). Hydroisohypsen des oberen genutzten Grundwasserleiters des Landes Brandenburg für das Frühjahr 2011, Daten des LUGV Brandenburg, <http://www.mlul.brandenburg.de/cms/detail.php/bb1.c.310481.de>, accessed September 2014.
- LUGV (Landesamt für Umwelt, Gesundheit und Verbraucherschutz). Gewässernetz im Land Brandenburg [gewnet25_*.shp] Version 4.0. - Daten des LUGV Brandenburg, <http://www.mlul.brandenburg.de/cms/detail.php/bb1.c.310481.de>, accessed September 2014.
- Magri, F., Bayer, U., Maiwald, U., Otto, R., and Thomson, C. Impact of transition zones, variable fluid viscosity and anthropogenic activities on coupled fluid-transport processes in a shallow salt-dome environment. *Geofluids*, 9(3):182–194, 2009a.
- Magri, F., Bayer, U., Pekdeger, A., Otto, R., Thomsen, C., and Maiwald, U. Salty groundwater flow in the shallow and deep aquifer systems of the Schleswig-Holstein area (North German Basin). *Tectonophysics*, 470(1-2):183–194, 2009b.
- Mathias, S. A., Hardisty, P. E., Trudell, M. R., and Zimmerman, R. W. Approximate Solutions for Pressure Buildup During CO₂ Injection in Brine Aquifers. *Transport in Porous Media*, 79(2):265–284, 2008.
- Mathias, S. A., Hardisty, P. E., Trudell, M. R., and Zimmerman, R. W. Screening and selection of sites for CO₂ sequestration based on pressure buildup. *International Journal of Greenhouse Gas Control*, 3(5):577–585, 2009.

- Metz, B., Davidson, O., de Coninck, H., Loos, M., and Meyer, L. IPCC Special Report on Carbon Dioxide Capture and Storage. Technical report, Intergovernmental Panel on Climate Change (IPCC), 2005.
- Møll Nilsen, H., Herrera, P. A., Ashraf, M., Ligaarden, I., Iding, M., Hermanrud, C., Lie, K.-A., Nordbotten, J. M., Dahle, H. K., and Keilegavlen, E. Field-case simulation of CO₂-plume migration using vertical-equilibrium models. *Energy Procedia*, 4:3801–3808, 2011.
- Müller, C. and Reinhold, K. (Hrsg.) Informationssystem Speichergesteine für den Standort Deutschland - eine Grundlage zur klimafreundlichen geotechnischen und energetischen Nutzung des tieferen Untergrundes (Speicher-Kataster Deutschland). Technical report, Bundesanstalt für Geowissenschaften und Rohstoffe (BGR), Berlin/Hannover, 2011.
- Nazarian, B., Held, R., Høier, L., and Ringrose, P. Reservoir Management of CO₂ Injection: Pressure Control and Capacity Enhancement. *Energy Procedia*, 37:4533–4543, 2013.
- NETL. Carbon Sequestration Atlas of the United States and Canada, Third Edition. Technical report, U.S. Department of Energy, Office of Fossil Energy, National Energy Technology Laboratory, 2010.
- Noack, V., Scheck-Wenderoth, M., Cacace, M., and Schneider, M. Influence of fluid flow on the regional thermal field: results from 3D numerical modelling for the area of Brandenburg (North German Basin). *Environmental Earth Sciences*, 70(8):3523–3544, 2013.
- Nordbotten, J., Flemisch, B., Gasda, S., Nilsen, H., Fan, Y., Pickup, G., Wiese, B., Celia, M., Dahle, H., Eigestad, G., and Pruess, K. Uncertainties in practical simulation of CO₂ storage. *International Journal of Greenhouse Gas Control*, 9:234–242, 2012.
- Nordbotten, J. M. and Celia, M. A. Similarity solutions for fluid injection into confined aquifers. *Journal of Fluid Mechanics*, 561:307, 2006.
- Nordbotten, J. M. and Celia, M. A. *Geological Storage of CO₂: Modeling Approaches for Large-scale Simulation*. John Wiley and Sons, New York, 2012.
- Nordbotten, J. M., Celia, M. A., and Bachu, S. Injection and storage of CO₂ in deep saline aquifers: Analytical solution for CO₂ plume evolution during injection. *Transport in Porous Media*, 58(3):339–360, 2005.
- Nordbotten, J. M., Kavetski, D., Celia, M. A., and Bachu, S. Model for CO₂ leakage including multiple geological layers and multiple leaky wells. *Environmental science & technology*, 43(3):743–9, 2009.

- NPC. U.S. National Petroleum Council Public Database, 1984. URL <http://www.netl.doe.gov>.
- Nuske, K. P. *Beyond Local Equilibrium - Relaxing local equilibrium assumptions in multiphase flow in porous media*. PhD thesis, Institut für Wasser- und Umweltsystemmodellierung, Universität Stuttgart, 2014.
- Ochs, S. O., Class, H., Färber, A., and Helmig, R. Methods for predicting the spreading of steam below the water table during subsurface remediation. *Water Resources Research*, 46(5), 2010.
- Okwen, R. T., Stewart, M. T., and Cunningham, J. A. Analytical solution for estimating storage efficiency of geologic sequestration of CO₂. *International Journal of Greenhouse Gas Control*, 4(1):102–107, 2010.
- Oladyshkin, S. and Nowak, W. Data-driven uncertainty quantification using the arbitrary polynomial chaos expansion. *Reliability Engineering & System Safety*, 106:179–190, 2012.
- Oladyshkin, S., Class, H., Helmig, R., and Nowak, W. An integrative approach to robust design and probabilistic risk assessment for CO₂ storage in geological formations. *Computational Geosciences*, 15(3):565–577, 2011a.
- Oladyshkin, S., Class, H., Helmig, R., and Nowak, W. A concept for data-driven uncertainty quantification and its application to carbon dioxide storage in geological formations. *Advances in Water Resources*, 34(11):1508–1518, 2011b.
- Oldenburg, C. M. and Rinaldi, A. P. Buoyancy Effects on Upward Brine Displacement Caused by CO₂ Injection. *Transport in Porous Media*, 87(2):525–540, 2010.
- Oswald, S. and Kinzelbach, W. Three-dimensional physical benchmark experiments to test variable-density flow models. *Journal of Hydrology*, 290(1-2):22–42, 2004.
- Papafotiou, A. *Numerical Investigations of the Role of Hysteresis in Heterogeneous Two-Phase Flow Systems*. PhD thesis, Institut für Wasserbau, Universität Stuttgart, 2008.
- Rapoport, L. Scaling laws for use in design and operation of water-oil flow models. *American Institute of Mining, Metallurgical, and Petroleum Engineers, Transactions*, 204:143–150, 1955.
- Reinhold, K., Müller, C., and Riesenberger, C. Informationssystem Speichergesteine für den Standort Deutschland - Synthese -. Technical report, Bundesanstalt für Geowissenschaften und Rohstoffe (BGR), Hannover, 2011.

- Reutter, E. Hydrostratigrafische Gliederung Niedersachsens. *Geofakten*, 21, 2011.
- Schäfer, F., Walter, L., Class, H., and Müller, C. The regional pressure impact of CO₂ storage: a showcase study from the North German Basin. *Environmental Earth Sciences*, 65(7): 2037–2049, 2011.
- Scholz, S. *Analytical Solution for Determining Brine Leakage Along a Salt Wall*. Bachelor's thesis, Institut für Wasser- und Umweltsystemmodellierung, Universität Stuttgart, 2014.
- Schwenck, N., Beck, M., Becker, B., Class, H., Fetzner, T., Flemisch, B., Grüninger, C., Hommel, J., Jambhekar, V., Kissinger, A., Koch, T., Schneider, M., Schröder, N., Seitz, G., and Weishaupt, K. DuMuX 2.8.0, 2015.
- Shan, C., Javandel, I., and Witherspoon, P. A. Characterization of leaky faults: Study of water flow in aquifer-fault-aquifer systems. *Water Resources Research*, 31(12):2897–2904, 1995.
- Span, R. and Wagner, W. A New Equation of State for Carbon Dioxide Covering the Fluid Region from the Triple-Point Temperature to 1100 K at Pressures up to 800 MPa. *Journal of Physical and Chemical Reference Data*, 25(6):1509, 1996.
- Stehfest, H. Algorithm 368: Numerical inversion of Laplace transforms [D5]. *Communications of the ACM*, 13(1):47–49, 1970.
- Szulczewski, M. L., MacMinn, C. W., Herzog, H. J., and Juanes, R. Lifetime of carbon capture and storage as a climate-change mitigation technology. *Proceedings of the National Academy of Sciences of the United States of America*, 109(14):5185–9, 2012.
- Taku Ide, S., Jessen, K., and Orr, F. M. Storage of CO₂ in saline aquifers: Effects of gravity, viscous, and capillary forces on amount and timing of trapping. *International Journal of Greenhouse Gas Control*, 1(4):481–491, 2007.
- Tatomir, A. *From discrete to continuum concepts of flow in fractured porous media*. PhD thesis, Institut für Wasser- und Umweltsystemmodellierung, Universität Stuttgart, 2013.
- Taylor, R. and Krishna, R. *Multicomponent Mass Transfer*, volume 60. 1995. ISBN 0471574171.
- Tillner, E., Kempka, T., Nakaten, B., and Kühn, M. Brine migration through fault zones: 3D numerical simulations for a prospective CO₂ storage site in Northeast Germany. *International Journal of Greenhouse Gas Control*, 19:689–703, 2013.
- Tillner, E., Langer, M., Kempka, T., and Kühn, M. Fault damage zone volume and initial salinity distribution determine intensity of shallow aquifer salinisation in subsurface storage. *Hydrology and Earth System Sciences*, 20(3):1049–1067, 2016.

- Van Everdingen, A. and Hurst, W. The Application of the Laplace Transformation to Flow Problems in Reservoirs. *Journal of Petroleum Technology*, 1(12):305–324, 1949.
- Walker, W., Harremoës, P., Rotmans, J., van der Sluijs, J., van Asselt, M., Janssen, P., and Kraayer von Krauss, M. Defining Uncertainty: A Conceptual Basis for Uncertainty Management in Model-Based Decision Support. *Integrated Assessment*, 4(1):5–17, 2003.
- Walter, L., Binning, P. J., Oladyshkin, S., Flemisch, B., and Class, H. Brine migration resulting from CO₂ injection into saline aquifers - An approach to risk estimation including various levels of uncertainty. *International Journal of Greenhouse Gas Control*, 9:495–506, 2012.
- Walter, L., Binning, P. J., and Class, H. Predicting salt intrusion into freshwater aquifers resulting from CO₂ injection – A study on the influence of conservative assumptions. *Advances in Water Resources*, 62:543–554, 2013.
- Wolff, M. *Multi-Scale Modeling of Two-Phase Flow in Porous Media Including Capillary Pressure Effects*. PhD thesis, Institut für Wasser- und Umweltsystemmodellierung, Universität Stuttgart, 2013.
- Wolfgramm, M. and Seibt, A. Zusammensetzung von Tiefenwässern in Deutschland und ihre Relevanz für geothermische Anlagenteile. In *GTV-Tagung in Karlsruhe 2008*, pages 503 – 516, 2008.
- Zeidouni, M. Analytical model of leakage through fault to overlying formations. *Water Resources Research*, 48(12), 2012.
- Zhou, D., Fayers, F. J., and Orr Jr, F. Scaling of multiphase flow in simple heterogeneous porous media. *SPE Reservoir Engineering*, (April):559–569, 1997.
- Zhou, Q., Birkholzer, J. T., Tsang, C. F., and Rutqvist, J. A method for quick assessment of CO₂ storage capacity in closed and semi-closed saline formations. *International Journal of Greenhouse Gas Control*, 2(4):626–639, 2008.

A. Further Information for Simulations in Chapter 4

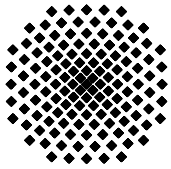
This document contains supplementary data for Chapter 4. The first table shows nine data pairs of porosity and reservoir thickness for Area 2, used for the simulations in Sec. 4.4.4, see also Table 4.2. The second table shows the initial conditions and the results of the simulations in Sec. 4.4.2.

Table A.1.: 9 data pairs of porosity and reservoir thickness for Area 2. Note: for the simulations an average is taken, where value ranges are given.

Index	Porosity [-]	Reservoir thickness [m]
1	0.20	10
2	0.14-0.2	10
3	0.10	5
4	0.14-0.15	20
5	0.25	15-20
6	0.20	10
7	0.15-0.19	10
8	0.06-0.16	20
9	0.18	20

Table A.2.: Initial conditions and results of the simulations in Sec. 4.4.2.

Index	Temperature [K]	Pressure [MPa]	Salinity [kgNaCl/kgBrine]	Density Brine [kg/qm]	Density CO2 [kg/qm]	Viscosity Brine [Pa.s]	Viscosity CO2 [Pa.s]	Gr [°]	Storage Efficiency [kg/sm]
1	305	9,70	0,13	1091	742	1,04E-3	6,20E-5	4,10E+10	379
2	305	9,70	0,13	1091	742	1,04E-3	6,20E-5	4,10E+10	379
3	318	15,66	0,20	1140	757	1,00E-3	6,40E-5	4,44E+10	381
4	310	10,82	0,14	1100	716	9,92E-4	5,80E-5	4,65E+10	353
5	320	15,26	0,19	1136	735	9,65E-4	6,10E-5	4,73E+10	364
6	363	35,67	0,30	1200	758	6,00E-4	6,60E-5	4,98E+10	450
7	329	18,83	0,23	1161	734	9,15E-4	6,10E-5	5,05E+10	362
8	323	14,75	0,19	1130	695	9,08E-4	5,60E-5	5,30E+10	332
9	357	31,13	0,30	1202	740	6,53E-4	6,30E-5	5,33E+10	412
10	311	10,13	0,14	1093	669	9,56E-4	5,20E-5	5,36E+10	317
11	330	16,93	0,21	1145	685	8,57E-4	5,50E-5	5,62E+10	325
12	387	38,66	0,30	1186	700	4,45E-4	5,90E-5	5,65E+10	427
13	354	27,03	0,30	1203	709	6,84E-4	5,90E-5	5,83E+10	368
14	332	16,73	0,21	1143	664	8,30E-4	5,30E-5	5,88E+10	310
15	361	28,69	0,30	1199	696	6,16E-4	5,80E-5	5,93E+10	371
16	337	18,33	0,23	1154	668	8,06E-4	5,30E-5	6,01E+10	315
17	371	30,49	0,30	1194	678	5,42E-4	5,60E-5	6,13E+10	370
18	341	19,17	0,23	1158	655	7,68E-4	5,20E-5	6,22E+10	307
19	389	34,59	0,30	1183	656	4,37E-4	5,40E-5	6,29E+10	378
20	398	35,60	0,30	1178	637	3,99E-4	5,20E-5	6,50E+10	370
21	394	33,87	0,31	1180	631	4,15E-4	5,20E-5	6,54E+10	359
22	360	25,45	0,30	1196	659	6,27E-4	5,30E-5	6,55E+10	330
23	420	38,91	0,31	1163	606	3,30E-4	5,00E-5	6,63E+10	364
24	345	19,20	0,24	1157	627	7,26E-4	4,90E-5	6,65E+10	289
25	372	28,50	0,30	1193	647	5,33E-4	5,20E-5	6,66E+10	340
26	388	32,13	0,30	1183	631	4,41E-4	5,10E-5	6,70E+10	350
27	452	42,00	0,32	1140	558	2,71E-4	4,70E-5	6,78E+10	342
28	376	28,65	0,30	1190	631	5,05E-4	5,10E-5	6,79E+10	332
29	416	37,18	0,31	1166	599	3,40E-4	4,90E-5	6,80E+10	353
30	368	26,45	0,30	1195	636	5,62E-4	5,10E-5	6,84E+10	322
31	378	28,41	0,30	1189	621	4,95E-4	5,00E-5	6,92E+10	325
32	450	40,26	0,32	1141	546	2,74E-4	4,60E-5	6,93E+10	329
33	367	24,71	0,29	1187	611	5,66E-4	4,80E-5	7,19E+10	299
34	390	29,35	0,30	1181	588	4,32E-4	4,70E-5	7,28E+10	311
35	371	24,58	0,29	1184	591	5,40E-4	4,70E-5	7,31E+10	288
36	359	20,54	0,25	1160	574	6,20E-4	4,40E-5	7,50E+10	262
37	387	27,24	0,30	1183	569	4,48E-4	4,50E-5	7,62E+10	289
38	346	16,30	0,21	1133	537	6,90E-4	4,10E-5	7,66E+10	229
39	393	26,77	0,31	1179	538	4,19E-4	4,30E-5	7,87E+10	271
40	359	18,71	0,23	1146	525	6,09E-4	4,00E-5	8,00E+10	229
41	364	19,68	0,24	1151	521	5,77E-4	4,00E-5	8,05E+10	231
42	315	9,34	0,13	1085	473	8,87E-4	3,40E-5	8,35E+10	219
43	320	10,09	0,14	1090	459	8,45E-4	3,30E-5	8,61E+10	199
44	323	10,60	0,14	1093	452	8,17E-4	3,30E-5	8,62E+10	189
45	319	9,75	0,13	1087	426	8,47E-4	3,10E-5	8,91E+10	187
46	311	8,37	0,11	1077	403	9,24E-4	2,90E-5	9,19E+10	227
47	318	9,41	0,13	1084	396	8,53E-4	2,90E-5	9,22E+10	178
48	318	9,26	0,13	1083	371	8,49E-4	2,70E-5	9,59E+10	165
49	301	6,86	0,10	1065	281	1,04E-3	2,20E-5	9,84E+10	331



Institut für Wasser- und Umweltsystemmodellierung Universität Stuttgart

Pfaffenwaldring 61
70569 Stuttgart (Vaihingen)
Telefon (0711) 685 - 64717/64749/64752/64679
Telefax (0711) 685 - 67020 o. 64746 o. 64681
E-Mail: iws@iws.uni-stuttgart.de
<http://www.iws.uni-stuttgart.de>

Direktoren

Prof. Dr. rer. nat. Dr.-Ing. András Bárdossy
Prof. Dr.-Ing. Rainer Helmig
Prof. Dr.-Ing. Silke Wieprecht
Prof. Dr.-Ing. Wolfgang Nowak

Vorstand (Stand 1.3.2016)

Prof. Dr. rer. nat. Dr.-Ing. A. Bárdossy
Prof. Dr.-Ing. R. Helmig
Prof. Dr.-Ing. S. Wieprecht
Prof. Dr. J.A. Sander Huisman
Jürgen Braun, PhD
apl. Prof. Dr.-Ing. H. Class
Dr.-Ing. H.-P. Koschitzky
Dr.-Ing. M. Noack
Prof. Dr.-Ing. W. Nowak
Dr. rer. nat. J. Seidel
Dr.-Ing. K. Terheiden
Dr.-Ing. habil. Sergey Oladyshkin

Emeriti

Prof. Dr.-Ing. habil. Dr.-Ing. E.h. Jürgen Giesecke
Prof. Dr.h.c. Dr.-Ing. E.h. Helmut Kobus, PhD

Lehrstuhl für Wasserbau und Wassermengenwirtschaft

Leiter: Prof. Dr.-Ing. Silke Wieprecht
Stellv.: Dr.-Ing. Kristina Terheiden
Versuchsanstalt für Wasserbau
Leiter: Dr.-Ing. Markus Noack

Lehrstuhl für Hydromechanik und Hydrosystemmodellierung

Leiter: Prof. Dr.-Ing. Rainer Helmig
Stellv.: apl. Prof. Dr.-Ing. Holger Class

Lehrstuhl für Hydrologie und Geohydrologie

Leiter: Prof. Dr. rer. nat. Dr.-Ing. András Bárdossy
Stellv.: Dr. rer. nat. Jochen Seidel
Hydrogeophysik der Vadosen Zone
(mit Forschungszentrum Jülich)
Leiter: Prof. Dr. J.A. Sander Huisman

Lehrstuhl für Stochastische Simulation und Sicherheitsforschung für Hydrosysteme

Leiter: Prof. Dr.-Ing. Wolfgang Nowak
Stellv.: Dr.-Ing. habil. Sergey Oladyshkin

VEGAS, Versuchseinrichtung zur Grundwasser- und Altlastensanierung

Leitung: Jürgen Braun, PhD, AD
Dr.-Ing. Hans-Peter Koschitzky, AD

Verzeichnis der Mitteilungshefte

- 1 Röhnisch, Arthur: *Die Bemühungen um eine Wasserbauliche Versuchsanstalt an der Technischen Hochschule Stuttgart*, und Fattah Abouleid, Abdel: *Beitrag zur Berechnung einer in lockeren Sand gerammten, zweifach verankerten Spundwand*, 1963
- 2 Marotz, Günter: *Beitrag zur Frage der Standfestigkeit von dichten Asphaltbelägen im Großwasserbau*, 1964
- 3 Gurr, Siegfried: *Beitrag zur Berechnung zusammengesetzter ebener Flächentragwerke unter besonderer Berücksichtigung ebener Stauwände, mit Hilfe von Randwert- und Lastwertmatrizen*, 1965
- 4 Plica, Peter: *Ein Beitrag zur Anwendung von Schalenkonstruktionen im Stahlwasserbau*, und

- Petrikat, Kurt: *Möglichkeiten und Grenzen des wasserbaulichen Versuchswesens*, 1966
- 5 Plate, Erich: *Beitrag zur Bestimmung der Windgeschwindigkeitsverteilung in der durch eine Wand gestörten bodennahen Luftschicht*, und
Röhnisch, Arthur; Marotz, Günter: *Neue Baustoffe und Bauausführungen für den Schutz der Böschungen und der Sohle von Kanälen, Flüssen und Häfen; Gesteungskosten und jeweilige Vorteile*, sowie
Unny, T.E.: *Schwingungsuntersuchungen am Kegelstrahlschieber*, 1967
- 6 Seiler, Erich: *Die Ermittlung des Anlagenwertes der bundeseigenen Binnenschiffahrtsstraßen und Talsperren und des Anteils der Binnenschiffahrt an diesem Wert*, 1967
- 7 *Sonderheft anlässlich des 65. Geburtstages von Prof. Arthur Röhnisch mit Beiträgen von* Benk, Dieter; Breitling, J.; Gurr, Siegfried; Haberhauer, Robert; Honekamp, Hermann; Kuz, Klaus Dieter; Marotz, Günter; Mayer-Vorfelder, Hans-Jörg; Miller, Rudolf; Plate, Erich J.; Radomski, Helge; Schwarz, Helmut; Vollmer, Ernst; Wildenhahn, Eberhard; 1967
- 8 Jumikis, Alfred: *Beitrag zur experimentellen Untersuchung des Wassernachschubs in einem gefrierenden Boden und die Beurteilung der Ergebnisse*, 1968
- 9 Marotz, Günter: *Technische Grundlagen einer Wasserspeicherung im natürlichen Untergrund*, 1968
- 10 Radomski, Helge: *Untersuchungen über den Einfluß der Querschnittsform wellenförmiger Spundwände auf die statischen und rammtechnischen Eigenschaften*, 1968
- 11 Schwarz, Helmut: *Die Grenztragfähigkeit des Baugrundes bei Einwirkung vertikal gezogener Ankerplatten als zweidimensionales Bruchproblem*, 1969
- 12 Erbel, Klaus: *Ein Beitrag zur Untersuchung der Metamorphose von Mittelgebirgsschneedecken unter besonderer Berücksichtigung eines Verfahrens zur Bestimmung der thermischen Schneequalität*, 1969
- 13 Westhaus, Karl-Heinz: *Der Strukturwandel in der Binnenschiffahrt und sein Einfluß auf den Ausbau der Binnenschiffskanäle*, 1969
- 14 Mayer-Vorfelder, Hans-Jörg: *Ein Beitrag zur Berechnung des Erdwiderstandes unter Ansatz der logarithmischen Spirale als Gleitflächenfunktion*, 1970
- 15 Schulz, Manfred: *Berechnung des räumlichen Erddruckes auf die Wandung kreiszylindrischer Körper*, 1970
- 16 Mobasseri, Manoutschehr: *Die Rippenstützmauer. Konstruktion und Grenzen ihrer Standsicherheit*, 1970
- 17 Benk, Dieter: *Ein Beitrag zum Betrieb und zur Bemessung von Hochwasserrück-*

- haltebecken*, 1970
- 18 Gál, Attila: *Bestimmung der mitschwingenden Wassermasse bei überströmten Fischbauchklappen mit kreiszylindrischem Staublech*, 1971, vergriffen
- 19 Kuz, Klaus Dieter: *Ein Beitrag zur Frage des Einsetzens von Kavitationserscheinungen in einer Düsenströmung bei Berücksichtigung der im Wasser gelösten Gase*, 1971, vergriffen
- 20 Schaak, Hartmut: *Verteilleitungen von Wasserkraftanlagen*, 1971
- 21 *Sonderheft zur Eröffnung der neuen Versuchsanstalt des Instituts für Wasserbau der Universität Stuttgart mit Beiträgen von* Brombach, Hansjörg; Dirksen, Wolfram; Gál, Attila; Gerlach, Reinhard; Giesecke, Jürgen; Holthoff, Franz-Josef; Kuz, Klaus Dieter; Marotz, Günter; Minor, Hans-Erwin; Petrikat, Kurt; Röhnisch, Arthur; Rueff, Helge; Schwarz, Helmut; Vollmer, Ernst; Wildenhahn, Eberhard; 1972
- 22 Wang, Chung-su: *Ein Beitrag zur Berechnung der Schwingungen an Kegelstrahlschiebern*, 1972
- 23 Mayer-Vorfelder, Hans-Jörg: *Erdwiderstandsbeiwerte nach dem Ohde-Variationsverfahren*, 1972
- 24 Minor, Hans-Erwin: *Beitrag zur Bestimmung der Schwingungsanfachungsfunktionen überströmter Stauklappen*, 1972, vergriffen
- 25 Brombach, Hansjörg: *Untersuchung strömungsmechanischer Elemente (Fluidik) und die Möglichkeit der Anwendung von Wirbelkammerelementen im Wasserbau*, 1972, vergriffen
- 26 Wildenhahn, Eberhard: *Beitrag zur Berechnung von Horizontalfilterbrunnen*, 1972
- 27 Steinlein, Helmut: *Die Eliminierung der Schwebstoffe aus Flußwasser zum Zweck der unterirdischen Wasserspeicherung, gezeigt am Beispiel der Iller*, 1972
- 28 Holthoff, Franz Josef: *Die Überwindung großer Hubhöhen in der Binnenschifffahrt durch Schwimmerhebwerke*, 1973
- 29 Röder, Karl: *Einwirkungen aus Baugrundbewegungen auf trog- und kastenförmige Konstruktionen des Wasser- und Tunnelbaues*, 1973
- 30 Kretschmer, Heinz: *Die Bemessung von Bogenstaumauern in Abhängigkeit von der Talform*, 1973
- 31 Honekamp, Hermann: *Beitrag zur Berechnung der Montage von Unterwasserpipelines*, 1973
- 32 Giesecke, Jürgen: *Die Wirbelkammertriode als neuartiges Steuerorgan im Wasserbau*, und
Brombach, Hansjörg: *Entwicklung, Bauformen, Wirkungsweise und Steuereigenschaften von Wirbelkammerverstärkern*, 1974

- 33 Rueff, Helge: *Untersuchung der schwingungserregenden Kräfte an zwei hintereinander angeordneten Tiefschützen unter besonderer Berücksichtigung von Kavitation*, 1974
- 34 Röhnisch, Arthur: *Einpreßversuche mit Zementmörtel für Spannbeton - Vergleich der Ergebnisse von Modellversuchen mit Ausführungen in Hüllwellrohren*, 1975
- 35 *Sonderheft anlässlich des 65. Geburtstages von Prof. Dr.-Ing. Kurt Petrikat mit Beiträgen von:* Brombach, Hansjörg; Erbel, Klaus; Flinspach, Dieter; Fischer jr., Richard; Gàl, Attila; Gerlach, Reinhard; Giesecke, Jürgen; Haberhauer, Robert; Hafner Edzard; Hausenblas, Bernhard; Horlacher, Hans-Burkhard; Hutarew, Andreas; Knoll, Manfred; Krummet, Ralph; Marotz, Günter; Merkle, Theodor; Miller, Christoph; Minor, Hans-Erwin; Neumayer, Hans; Rao, Syamala; Rath, Paul; Rueff, Helge; Ruppert, Jürgen; Schwarz, Wolfgang; Topal-Gökceli, Mehmet; Vollmer, Ernst; Wang, Chung-su; Weber, Hans-Georg; 1975
- 36 Berger, Jochum: *Beitrag zur Berechnung des Spannungszustandes in rotations-symmetrisch belasteten Kugelschalen veränderlicher Wandstärke unter Gas- und Flüssigkeitsdruck durch Integration schwach singulärer Differentialgleichungen*, 1975
- 37 Dirksen, Wolfram: *Berechnung instationärer Abflußvorgänge in gestauten Gerinnen mittels Differenzenverfahren und die Anwendung auf Hochwasserrückhaltebecken*, 1976
- 38 Horlacher, Hans-Burkhard: *Berechnung instationärer Temperatur- und Wärmespannungsfelder in langen mehrschichtigen Hohlzylindern*, 1976
- 39 Hafner, Edzard: *Untersuchung der hydrodynamischen Kräfte auf Baukörper im Tiefwasserbereich des Meeres*, 1977, ISBN 3-921694-39-6
- 40 Ruppert, Jürgen: *Über den Axialwirbelkammverstärker für den Einsatz im Wasserbau*, 1977, ISBN 3-921694-40-X
- 41 Hutarew, Andreas: *Beitrag zur Beeinflußbarkeit des Sauerstoffgehalts in Fließgewässern an Abstürzen und Wehren*, 1977, ISBN 3-921694-41-8, vergriffen
- 42 Miller, Christoph: *Ein Beitrag zur Bestimmung der schwingungserregenden Kräfte an unterströmten Wehren*, 1977, ISBN 3-921694-42-6
- 43 Schwarz, Wolfgang: *Druckstoßberechnung unter Berücksichtigung der Radial- und Längsverschiebungen der Rohrwandung*, 1978, ISBN 3-921694-43-4
- 44 Kinzelbach, Wolfgang: *Numerische Untersuchungen über den optimalen Einsatz variabler Kühlsysteme einer Kraftwerkskette am Beispiel Oberrhein*, 1978, ISBN 3-921694-44-2
- 45 Barczewski, Baldur: *Neue Meßmethoden für Wasser-Luftgemische und deren Anwendung auf zweiphasige Auftriebsstrahlen*, 1979, ISBN 3-921694-45-0

- 46 Neumayer, Hans: *Untersuchung der Strömungsvorgänge in radialen Wirbelkammerverstärkern*, 1979, ISBN 3-921694-46-9
- 47 Elalfy, Youssef-Elhassan: *Untersuchung der Strömungsvorgänge in Wirbelkammerdiolen und -drosseln*, 1979, ISBN 3-921694-47-7
- 48 Brombach, Hansjörg: *Automatisierung der Bewirtschaftung von Wasserspeichern*, 1981, ISBN 3-921694-48-5
- 49 Geldner, Peter: *Deterministische und stochastische Methoden zur Bestimmung der Selbstdichtung von Gewässern*, 1981, ISBN 3-921694-49-3, vergriffen
- 50 Mehlhorn, Hans: *Temperaturveränderungen im Grundwasser durch Brauchwasserleitungen*, 1982, ISBN 3-921694-50-7, vergriffen
- 51 Hafner, Edzard: *Rohrleitungen und Behälter im Meer*, 1983, ISBN 3-921694-51-5
- 52 Rinnert, Bernd: *Hydrodynamische Dispersion in porösen Medien: Einfluß von Dichteunterschieden auf die Vertikalvermischung in horizontaler Strömung*, 1983, ISBN 3-921694-52-3, vergriffen
- 53 Lindner, Wulf: *Steuerung von Grundwasserentnahmen unter Einhaltung ökologischer Kriterien*, 1983, ISBN 3-921694-53-1, vergriffen
- 54 Herr, Michael; Herzer, Jörg; Kinzelbach, Wolfgang; Kobus, Helmut; Rinnert, Bernd: *Methoden zur rechnerischen Erfassung und hydraulischen Sanierung von Grundwasserkontaminationen*, 1983, ISBN 3-921694-54-X
- 55 Schmitt, Paul: *Wege zur Automatisierung der Niederschlagsermittlung*, 1984, ISBN 3-921694-55-8, vergriffen
- 56 Müller, Peter: *Transport und selektive Sedimentation von Schwebstoffen bei gestautem Abfluß*, 1985, ISBN 3-921694-56-6
- 57 El-Qawasmeh, Fuad: *Möglichkeiten und Grenzen der Tropfbewässerung unter besonderer Berücksichtigung der Verstopfungsanfälligkeit der Tropfelemente*, 1985, ISBN 3-921694-57-4, vergriffen
- 58 Kirchenbaur, Klaus: *Mikroprozessorgesteuerte Erfassung instationärer Druckfelder am Beispiel seegangsbelasteter Baukörper*, 1985, ISBN 3-921694-58-2
- 59 Kobus, Helmut (Hrsg.): *Modellierung des großräumigen Wärme- und Schadstofftransports im Grundwasser*, Tätigkeitsbericht 1984/85 (DFG-Forschergruppe an den Universitäten Hohenheim, Karlsruhe und Stuttgart), 1985, ISBN 3-921694-59-0, vergriffen
- 60 Spitz, Karlheinz: *Dispersion in porösen Medien: Einfluß von Inhomogenitäten und Dichteunterschieden*, 1985, ISBN 3-921694-60-4, vergriffen
- 61 Kobus, Helmut: *An Introduction to Air-Water Flows in Hydraulics*, 1985, ISBN 3-921694-61-2

- 62 Kaleris, Vassilios: *Erfassung des Austausches von Oberflächen- und Grundwasser in horizontalebene Grundwassermodellen*, 1986, ISBN 3-921694-62-0
- 63 Herr, Michael: *Grundlagen der hydraulischen Sanierung verunreinigter Porengrundwasserleiter*, 1987, ISBN 3-921694-63-9
- 64 Marx, Walter: *Berechnung von Temperatur und Spannung in Massenbeton infolge Hydratation*, 1987, ISBN 3-921694-64-7
- 65 Koschitzky, Hans-Peter: *Dimensionierungskonzept für Sohlbelüfter in Schußrinnen zur Vermeidung von Kavitationsschäden*, 1987, ISBN 3-921694-65-5
- 66 Kobus, Helmut (Hrsg.): *Modellierung des großräumigen Wärme- und Schadstofftransports im Grundwasser*, Tätigkeitsbericht 1986/87 (DFG-Forschergruppe an den Universitäten Hohenheim, Karlsruhe und Stuttgart) 1987, ISBN 3-921694-66-3
- 67 Söll, Thomas: *Berechnungsverfahren zur Abschätzung anthropogener Temperaturanomalien im Grundwasser*, 1988, ISBN 3-921694-67-1
- 68 Dittrich, Andreas; Westrich, Bernd: *Bodenseeufererosion, Bestandsaufnahme und Bewertung*, 1988, ISBN 3-921694-68-X, vergriffen
- 69 Huwe, Bernd; van der Ploeg, Rienk R.: *Modelle zur Simulation des Stickstoffhaushaltes von Standorten mit unterschiedlicher landwirtschaftlicher Nutzung*, 1988, ISBN 3-921694-69-8, vergriffen
- 70 Stephan, Karl: *Integration elliptischer Funktionen*, 1988, ISBN 3-921694-70-1
- 71 Kobus, Helmut; Zilliox, Lothaire (Hrsg.): *Nitratbelastung des Grundwassers, Auswirkungen der Landwirtschaft auf die Grundwasser- und Rohwasserbeschaffenheit und Maßnahmen zum Schutz des Grundwassers*. Vorträge des deutsch-französischen Kolloquiums am 6. Oktober 1988, Universitäten Stuttgart und Louis Pasteur Strasbourg (Vorträge in deutsch oder französisch, Kurzfassungen zweisprachig), 1988, ISBN 3-921694-71-X
- 72 Soyeaux, Renald: *Unterströmung von Stauanlagen auf klüftigem Untergrund unter Berücksichtigung laminarer und turbulenter Fließzustände*, 1991, ISBN 3-921694-72-8
- 73 Kohane, Roberto: *Berechnungsmethoden für Hochwasserabfluß in Fließgewässern mit überströmten Vorländern*, 1991, ISBN 3-921694-73-6
- 74 Hassinger, Reinhard: *Beitrag zur Hydraulik und Bemessung von Blocksteinrampen in flexibler Bauweise*, 1991, ISBN 3-921694-74-4, vergriffen
- 75 Schäfer, Gerhard: *Einfluß von Schichtenstrukturen und lokalen Einlagerungen auf die Längsdispersion in Porengrundwasserleitern*, 1991, ISBN 3-921694-75-2
- 76 Giesecke, Jürgen: *Vorträge, Wasserwirtschaft in stark besiedelten Regionen; Umweltforschung mit Schwerpunkt Wasserwirtschaft*, 1991, ISBN 3-921694-76-0

- 77 Huwe, Bernd: *Deterministische und stochastische Ansätze zur Modellierung des Stickstoffhaushalts landwirtschaftlich genutzter Flächen auf unterschiedlichem Skalenniveau*, 1992, ISBN 3-921694-77-9, vergriffen
- 78 Rommel, Michael: *Verwendung von Kluftdaten zur realitätsnahen Generierung von Kluftnetzen mit anschließender laminar-turbulenter Strömungsberechnung*, 1993, ISBN 3-92 1694-78-7
- 79 Marschall, Paul: *Die Ermittlung lokaler Stofffrachten im Grundwasser mit Hilfe von Einbohrloch-Meßverfahren*, 1993, ISBN 3-921694-79-5, vergriffen
- 80 Ptak, Thomas: *Stofftransport in heterogenen Porenaquiferen: Felduntersuchungen und stochastische Modellierung*, 1993, ISBN 3-921694-80-9, vergriffen
- 81 Haakh, Frieder: *Transientes Strömungsverhalten in Wirbelkammern*, 1993, ISBN 3-921694-81-7
- 82 Kobus, Helmut; Cirpka, Olaf; Barczewski, Baldur; Koschitzky, Hans-Peter: *Versucheinrichtung zur Grundwasser und Altlastensanierung VEGAS, Konzeption und Programmrahmen*, 1993, ISBN 3-921694-82-5
- 83 Zang, Weidong: *Optimaler Echtzeit-Betrieb eines Speichers mit aktueller Abflußregenerierung*, 1994, ISBN 3-921694-83-3, vergriffen
- 84 Franke, Hans-Jörg: *Stochastische Modellierung eines flächenhaften Stoffeintrages und Transports in Grundwasser am Beispiel der Pflanzenschutzmittelproblematik*, 1995, ISBN 3-921694-84-1
- 85 Lang, Ulrich: *Simulation regionaler Strömungs- und Transportvorgänge in Karst-aquiferen mit Hilfe des Doppelkontinuum-Ansatzes: Methodenentwicklung und Parameteridentifikation*, 1995, ISBN 3-921694-85-X, vergriffen
- 86 Helmig, Rainer: *Einführung in die Numerischen Methoden der Hydromechanik*, 1996, ISBN 3-921694-86-8, vergriffen
- 87 Cirpka, Olaf: *CONTRACT: A Numerical Tool for Contaminant Transport and Chemical Transformations - Theory and Program Documentation -*, 1996, ISBN 3-921694-87-6
- 88 Haberlandt, Uwe: *Stochastische Synthese und Regionalisierung des Niederschlages für Schmutzfrachtberechnungen*, 1996, ISBN 3-921694-88-4
- 89 Croisé, Jean: *Extraktion von flüchtigen Chemikalien aus natürlichen Lockergesteinen mittels erzwungener Luftströmung*, 1996, ISBN 3-921694-89-2, vergriffen
- 90 Jorde, Klaus: *Ökologisch begründete, dynamische Mindestwasserregelungen bei Ausleitungskraftwerken*, 1997, ISBN 3-921694-90-6, vergriffen
- 91 Helmig, Rainer: *Gekoppelte Strömungs- und Transportprozesse im Untergrund - Ein Beitrag zur Hydrosystemmodellierung-*, 1998, ISBN 3-921694-91-4, vergriffen

- 92 Emmert, Martin: *Numerische Modellierung nichtisothermer Gas-Wasser Systeme in porösen Medien*, 1997, ISBN 3-921694-92-2
- 93 Kern, Ulrich: *Transport von Schweb- und Schadstoffen in staugeregelten Fließgewässern am Beispiel des Neckars*, 1997, ISBN 3-921694-93-0, vergriffen
- 94 Förster, Georg: *Druckstoßdämpfung durch große Luftblasen in Hochpunkten von Rohrleitungen* 1997, ISBN 3-921694-94-9
- 95 Cirpka, Olaf: *Numerische Methoden zur Simulation des reaktiven Mehrkomponententransports im Grundwasser*, 1997, ISBN 3-921694-95-7, vergriffen
- 96 Färber, Arne: *Wärmetransport in der ungesättigten Bodenzone: Entwicklung einer thermischen In-situ-Sanierungstechnologie*, 1997, ISBN 3-921694-96-5
- 97 Betz, Christoph: *Wasserdampfdestillation von Schadstoffen im porösen Medium: Entwicklung einer thermischen In-situ-Sanierungstechnologie*, 1998, ISBN 3-921694-97-3
- 98 Xu, Yichun: *Numerical Modeling of Suspended Sediment Transport in Rivers*, 1998, ISBN 3-921694-98-1, vergriffen
- 99 Wüst, Wolfgang: *Geochemische Untersuchungen zur Sanierung CKW-kontaminierter Aquifere mit Fe(0)-Reaktionswänden*, 2000, ISBN 3-933761-02-2
- 100 Sheta, Hussam: *Simulation von Mehrphasenvorgängen in porösen Medien unter Einbeziehung von Hysterese-Effekten*, 2000, ISBN 3-933761-03-4
- 101 Ayros, Edwin: *Regionalisierung extremer Abflüsse auf der Grundlage statistischer Verfahren*, 2000, ISBN 3-933761-04-2, vergriffen
- 102 Huber, Ralf: *Compositional Multiphase Flow and Transport in Heterogeneous Porous Media*, 2000, ISBN 3-933761-05-0
- 103 Braun, Christopherus: *Ein Upscaling-Verfahren für Mehrphasenströmungen in porösen Medien*, 2000, ISBN 3-933761-06-9
- 104 Hofmann, Bernd: *Entwicklung eines rechnergestützten Managementsystems zur Beurteilung von Grundwasserschadensfällen*, 2000, ISBN 3-933761-07-7
- 105 Class, Holger: *Theorie und numerische Modellierung nichtisothermer Mehrphasenprozesse in NAPL-kontaminierten porösen Medien*, 2001, ISBN 3-933761-08-5
- 106 Schmidt, Reinhard: *Wasserdampf- und Heißluftinjektion zur thermischen Sanierung kontaminierter Standorte*, 2001, ISBN 3-933761-09-3
- 107 Josef, Reinhold.: *Schadstoffextraktion mit hydraulischen Sanierungsverfahren unter Anwendung von grenzflächenaktiven Stoffen*, 2001, ISBN 3-933761-10-7

- 108 Schneider, Matthias: *Habitat- und Abflussmodellierung für Fließgewässer mit unscharfen Berechnungsansätzen*, 2001, ISBN 3-933761-11-5
- 109 Rathgeb, Andreas: *Hydrodynamische Bemessungsgrundlagen für Lockerdeckwerke an überströmbaren Erddämmen*, 2001, ISBN 3-933761-12-3
- 110 Lang, Stefan: *Parallele numerische Simulation instationärer Probleme mit adaptiven Methoden auf unstrukturierten Gittern*, 2001, ISBN 3-933761-13-1
- 111 Appt, Jochen; Stumpp Simone: *Die Bodensee-Messkampagne 2001, IWS/CWR Lake Constance Measurement Program 2001*, 2002, ISBN 3-933761-14-X
- 112 Heimerl, Stephan: *Systematische Beurteilung von Wasserkraftprojekten*, 2002, ISBN 3-933761-15-8, vergriffen
- 113 Iqbal, Amin: *On the Management and Salinity Control of Drip Irrigation*, 2002, ISBN 3-933761-16-6
- 114 Silberhorn-Hemming, Annette: *Modellierung von Kluftaquifersystemen: Geostatistische Analyse und deterministisch-stochastische Kluftgenerierung*, 2002, ISBN 3-933761-17-4
- 115 Winkler, Angela: *Prozesse des Wärme- und Stofftransports bei der In-situ-Sanierung mit festen Wärmequellen*, 2003, ISBN 3-933761-18-2
- 116 Marx, Walter: *Wasserkraft, Bewässerung, Umwelt - Planungs- und Bewertungsschwerpunkte der Wasserbewirtschaftung*, 2003, ISBN 3-933761-19-0
- 117 Hinkelmann, Reinhard: *Efficient Numerical Methods and Information-Processing Techniques in Environment Water*, 2003, ISBN 3-933761-20-4
- 118 Samaniego-Eguiguren, Luis Eduardo: *Hydrological Consequences of Land Use / Land Cover and Climatic Changes in Mesoscale Catchments*, 2003, ISBN 3-933761-21-2
- 119 Neunhäuserer, Lina: *Diskretisierungsansätze zur Modellierung von Strömungs- und Transportprozessen in geklüftet-porösen Medien*, 2003, ISBN 3-933761-22-0
- 120 Paul, Maren: *Simulation of Two-Phase Flow in Heterogeneous Poros Media with Adaptive Methods*, 2003, ISBN 3-933761-23-9
- 121 Ehret, Uwe: *Rainfall and Flood Nowcasting in Small Catchments using Weather Radar*, 2003, ISBN 3-933761-24-7
- 122 Haag, Ingo: *Der Sauerstoffhaushalt staugeregelter Flüsse am Beispiel des Neckars - Analysen, Experimente, Simulationen -*, 2003, ISBN 3-933761-25-5
- 123 Appt, Jochen: *Analysis of Basin-Scale Internal Waves in Upper Lake Constance*, 2003, ISBN 3-933761-26-3

- 124 Hrsg.: Schrenk, Volker; Batereau, Katrin; Barczewski, Baldur; Weber, Karolin und Koschitzky, Hans-Peter: *Symposium Ressource Fläche und VEGAS - Statuskolloquium 2003, 30. September und 1. Oktober 2003*, 2003, ISBN 3-933761-27-1
- 125 Omar Khalil Ouda: *Optimisation of Agricultural Water Use: A Decision Support System for the Gaza Strip*, 2003, ISBN 3-933761-28-0
- 126 Batereau, Katrin: *Sensorbasierte Bodenluftmessung zur Vor-Ort-Erkundung von Schadensherden im Untergrund*, 2004, ISBN 3-933761-29-8
- 127 Witt, Oliver: *Erosionsstabilität von Gewässersedimenten mit Auswirkung auf den Stofftransport bei Hochwasser am Beispiel ausgewählter Stauhaltungen des Oberrheins*, 2004, ISBN 3-933761-30-1
- 128 Jakobs, Hartmut: *Simulation nicht-isothermer Gas-Wasser-Prozesse in komplexen Kluft-Matrix-Systemen*, 2004, ISBN 3-933761-31-X
- 129 Li, Chen-Chien: *Deterministisch-stochastisches Berechnungskonzept zur Beurteilung der Auswirkungen erosiver Hochwasserereignisse in Flusstauhaltungen*, 2004, ISBN 3-933761-32-8
- 130 Reichenberger, Volker; Helmig, Rainer; Jakobs, Hartmut; Bastian, Peter; Niessner, Jennifer: *Complex Gas-Water Processes in Discrete Fracture-Matrix Systems: Upscaling, Mass-Conservative Discretization and Efficient Multilevel Solution*, 2004, ISBN 3-933761-33-6
- 131 Hrsg.: Barczewski, Baldur; Koschitzky, Hans-Peter; Weber, Karolin; Wege, Ralf: *VEGAS - Statuskolloquium 2004*, Tagungsband zur Veranstaltung am 05. Oktober 2004 an der Universität Stuttgart, Campus Stuttgart-Vaihingen, 2004, ISBN 3-933761-34-4
- 132 Asie, Kemal Jabir: *Finite Volume Models for Multiphase Multicomponent Flow through Porous Media*. 2005, ISBN 3-933761-35-2
- 133 Jacoub, George: *Development of a 2-D Numerical Module for Particulate Contaminant Transport in Flood Retention Reservoirs and Impounded Rivers*, 2004, ISBN 3-933761-36-0
- 134 Nowak, Wolfgang: *Geostatistical Methods for the Identification of Flow and Transport Parameters in the Subsurface*, 2005, ISBN 3-933761-37-9
- 135 Süß, Mia: *Analysis of the influence of structures and boundaries on flow and transport processes in fractured porous media*, 2005, ISBN 3-933761-38-7
- 136 Jose, Surabhin Chackiath: *Experimental Investigations on Longitudinal Dispersive Mixing in Heterogeneous Aquifers*, 2005, ISBN: 3-933761-39-5
- 137 Filiz, Fulya: *Linking Large-Scale Meteorological Conditions to Floods in Mesoscale Catchments*, 2005, ISBN 3-933761-40-9

- 138 Qin, Minghao: *Wirklichkeitsnahe und recheneffiziente Ermittlung von Temperatur und Spannungen bei großen RCC-Staumauern*, 2005, ISBN 3-933761-41-7
- 139 Kobayashi, Kenichiro: *Optimization Methods for Multiphase Systems in the Sub-surface - Application to Methane Migration in Coal Mining Areas*, 2005, ISBN 3-933761-42-5
- 140 Rahman, Md. Arifur: *Experimental Investigations on Transverse Dispersive Mixing in Heterogeneous Porous Media*, 2005, ISBN 3-933761-43-3
- 141 Schrenk, Volker: *Ökobilanzen zur Bewertung von Altlastensanierungsmaßnahmen*, 2005, ISBN 3-933761-44-1
- 142 Hundecha, Hirpa Yeshewatersfa: *Regionalization of Parameters of a Conceptual Rainfall-Runoff Model*, 2005, ISBN: 3-933761-45-X
- 143 Wege, Ralf: *Untersuchungs- und Überwachungsmethoden für die Beurteilung natürlicher Selbstreinigungsprozesse im Grundwasser*, 2005, ISBN 3-933761-46-8
- 144 Breiting, Thomas: *Techniken und Methoden der Hydroinformatik - Modellierung von komplexen Hydrosystemen im Untergrund*, 2006, 3-933761-47-6
- 145 Hrsg.: Braun, Jürgen; Koschitzky, Hans-Peter; Müller, Martin: *Ressource Untergrund: 10 Jahre VEGAS: Forschung und Technologieentwicklung zum Schutz von Grundwasser und Boden*, Tagungsband zur Veranstaltung am 28. und 29. September 2005 an der Universität Stuttgart, Campus Stuttgart-Vaihingen, 2005, ISBN 3-933761-48-4
- 146 Rojanschi, Vlad: *Abflusskonzentration in mesoskaligen Einzugsgebieten unter Berücksichtigung des Sickerraumes*, 2006, ISBN 3-933761-49-2
- 147 Winkler, Nina Simone: *Optimierung der Steuerung von Hochwasserrückhaltebecken-systemen*, 2006, ISBN 3-933761-50-6
- 148 Wolf, Jens: *Räumlich differenzierte Modellierung der Grundwasserströmung alluvialer Aquifere für mesoskalige Einzugsgebiete*, 2006, ISBN: 3-933761-51-4
- 149 Kohler, Beate: *Externe Effekte der Laufwasserkraftnutzung*, 2006, ISBN 3-933761-52-2
- 150 Hrsg.: Braun, Jürgen; Koschitzky, Hans-Peter; Stuhmann, Matthias: *VEGAS-Statuskolloquium 2006*, Tagungsband zur Veranstaltung am 28. September 2006 an der Universität Stuttgart, Campus Stuttgart-Vaihingen, 2006, ISBN 3-933761-53-0
- 151 Niessner, Jennifer: *Multi-Scale Modeling of Multi-Phase - Multi-Component Processes in Heterogeneous Porous Media*, 2006, ISBN 3-933761-54-9
- 152 Fischer, Markus: *Beanspruchung eingeeerdeter Rohrleitungen infolge Austrocknung bindiger Böden*, 2006, ISBN 3-933761-55-7

- 153 Schneck, Alexander: *Optimierung der Grundwasserbewirtschaftung unter Berücksichtigung der Belange der Wasserversorgung, der Landwirtschaft und des Naturschutzes*, 2006, ISBN 3-933761-56-5
- 154 Das, Tapash: *The Impact of Spatial Variability of Precipitation on the Predictive Uncertainty of Hydrological Models*, 2006, ISBN 3-933761-57-3
- 155 Bielinski, Andreas: *Numerical Simulation of CO₂ sequestration in geological formations*, 2007, ISBN 3-933761-58-1
- 156 Mödinger, Jens: *Entwicklung eines Bewertungs- und Entscheidungsunterstützungssystems für eine nachhaltige regionale Grundwasserbewirtschaftung*, 2006, ISBN 3-933761-60-3
- 157 Manthey, Sabine: *Two-phase flow processes with dynamic effects in porous media - parameter estimation and simulation*, 2007, ISBN 3-933761-61-1
- 158 Pozos Estrada, Oscar: *Investigation on the Effects of Entrained Air in Pipelines*, 2007, ISBN 3-933761-62-X
- 159 Ochs, Steffen Oliver: *Steam injection into saturated porous media – process analysis including experimental and numerical investigations*, 2007, ISBN 3-933761-63-8
- 160 Marx, Andreas: *Einsatz gekoppelter Modelle und Wetterradar zur Abschätzung von Niederschlagsintensitäten und zur Abflussvorhersage*, 2007, ISBN 3-933761-64-6
- 161 Hartmann, Gabriele Maria: *Investigation of Evapotranspiration Concepts in Hydrological Modelling for Climate Change Impact Assessment*, 2007, ISBN 3-933761-65-4
- 162 Kebede Gurmessa, Tesfaye: *Numerical Investigation on Flow and Transport Characteristics to Improve Long-Term Simulation of Reservoir Sedimentation*, 2007, ISBN 3-933761-66-2
- 163 Trifković, Aleksandar: *Multi-objective and Risk-based Modelling Methodology for Planning, Design and Operation of Water Supply Systems*, 2007, ISBN 3-933761-67-0
- 164 Götzing, Jens: *Distributed Conceptual Hydrological Modelling - Simulation of Climate, Land Use Change Impact and Uncertainty Analysis*, 2007, ISBN 3-933761-68-9
- 165 Hrsg.: Braun, Jürgen; Koschitzky, Hans-Peter; Stuhmann, Matthias: *VEGAS – Kolloquium 2007*, Tagungsband zur Veranstaltung am 26. September 2007 an der Universität Stuttgart, Campus Stuttgart-Vaihingen, 2007, ISBN 3-933761-69-7
- 166 Freeman, Beau: *Modernization Criteria Assessment for Water Resources Planning; Klamath Irrigation Project, U.S.*, 2008, ISBN 3-933761-70-0

- 167 Dreher, Thomas: *Selektive Sedimentation von Feinstschwebstoffen in Wechselwirkung mit wandnahen turbulenten Strömungsbedingungen*, 2008, ISBN 3-933761-71-9
- 168 Yang, Wei: *Discrete-Continuous Downscaling Model for Generating Daily Precipitation Time Series*, 2008, ISBN 3-933761-72-7
- 169 Kopecki, Ianina: *Calculational Approach to FST-Hemispheres for Multiparametrical Benthos Habitat Modelling*, 2008, ISBN 3-933761-73-5
- 170 Brommundt, Jürgen: *Stochastische Generierung räumlich zusammenhängender Niederschlagszeitreihen*, 2008, ISBN 3-933761-74-3
- 171 Papafotiou, Alexandros: *Numerical Investigations of the Role of Hysteresis in Heterogeneous Two-Phase Flow Systems*, 2008, ISBN 3-933761-75-1
- 172 He, Yi: *Application of a Non-Parametric Classification Scheme to Catchment Hydrology*, 2008, ISBN 978-3-933761-76-7
- 173 Wagner, Sven: *Water Balance in a Poorly Gauged Basin in West Africa Using Atmospheric Modelling and Remote Sensing Information*, 2008, ISBN 978-3-933761-77-4
- 174 Hrsg.: Braun, Jürgen; Koschitzky, Hans-Peter; Stuhmann, Matthias; Schrenk, Volker: *VEGAS-Kolloquium 2008 Ressource Fläche III*, Tagungsband zur Veranstaltung am 01. Oktober 2008 an der Universität Stuttgart, Campus Stuttgart-Vaihingen, 2008, ISBN 978-3-933761-78-1
- 175 Patil, Sachin: *Regionalization of an Event Based Nash Cascade Model for Flood Predictions in Ungauged Basins*, 2008, ISBN 978-3-933761-79-8
- 176 Assteerawatt, Anongnart: *Flow and Transport Modelling of Fractured Aquifers based on a Geostatistical Approach*, 2008, ISBN 978-3-933761-80-4
- 177 Karnahl, Joachim Alexander: *2D numerische Modellierung von multifraktionalem Schwebstoff- und Schadstofftransport in Flüssen*, 2008, ISBN 978-3-933761-81-1
- 178 Hiester, Uwe: *Technologieentwicklung zur In-situ-Sanierung der ungesättigten Bodenzone mit festen Wärmequellen*, 2009, ISBN 978-3-933761-82-8
- 179 Laux, Patrick: *Statistical Modeling of Precipitation for Agricultural Planning in the Volta Basin of West Africa*, 2009, ISBN 978-3-933761-83-5
- 180 Ehsan, Saqib: *Evaluation of Life Safety Risks Related to Severe Flooding*, 2009, ISBN 978-3-933761-84-2
- 181 Prohaska, Sandra: *Development and Application of a 1D Multi-Strip Fine Sediment Transport Model for Regulated Rivers*, 2009, ISBN 978-3-933761-85-9

- 182 Kopp, Andreas: *Evaluation of CO₂ Injection Processes in Geological Formations for Site Screening*, 2009, ISBN 978-3-933761-86-6
- 183 Ebigbo, Anozie: *Modelling of biofilm growth and its influence on CO₂ and water (two-phase) flow in porous media*, 2009, ISBN 978-3-933761-87-3
- 184 Freiboth, Sandra: *A phenomenological model for the numerical simulation of multiphase multicomponent processes considering structural alterations of porous media*, 2009, ISBN 978-3-933761-88-0
- 185 Zöllner, Frank: *Implementierung und Anwendung netzfreier Methoden im Konstruktiven Wasserbau und in der Hydromechanik*, 2009, ISBN 978-3-933761-89-7
- 186 Vasin, Milos: *Influence of the soil structure and property contrast on flow and transport in the unsaturated zone*, 2010, ISBN 978-3-933761-90-3
- 187 Li, Jing: *Application of Copulas as a New Geostatistical Tool*, 2010, ISBN 978-3-933761-91-0
- 188 AghaKouchak, Amir: *Simulation of Remotely Sensed Rainfall Fields Using Copulas*, 2010, ISBN 978-3-933761-92-7
- 189 Thapa, Pawan Kumar: *Physically-based spatially distributed rainfall runoff modeling for soil erosion estimation*, 2010, ISBN 978-3-933761-93-4
- 190 Wurms, Sven: *Numerische Modellierung der Sedimentationsprozesse in Retentionsanlagen zur Steuerung von Stoffströmen bei extremen Hochwasserabflussereignissen*, 2011, ISBN 978-3-933761-94-1
- 191 Merkel, Uwe: *Unsicherheitsanalyse hydraulischer Einwirkungen auf Hochwasserschutzdeiche und Steigerung der Leistungsfähigkeit durch adaptive Strömungsmodellierung*, 2011, ISBN 978-3-933761-95-8
- 192 Fritz, Jochen: *A Decoupled Model for Compositional Non-Isothermal Multiphase Flow in Porous Media and Multiphysics Approaches for Two-Phase Flow*, 2010, ISBN 978-3-933761-96-5
- 193 Weber, Karolin (Hrsg.): *12. Treffen junger WissenschaftlerInnen an Wasserbauinstituten*, 2010, ISBN 978-3-933761-97-2
- 194 Bliedernicht, Jan-Geert: *Probability Forecasts of Daily Areal Precipitation for Small River Basins*, 2011, ISBN 978-3-933761-98-9
- 195 Hrsg.: Koschitzky, Hans-Peter; Braun, Jürgen: *VEGAS-Kolloquium 2010 In-situ-Sanierung - Stand und Entwicklung Nano und ISCO -*, Tagungsband zur Veranstaltung am 07. Oktober 2010 an der Universität Stuttgart, Campus Stuttgart-Vaihingen, 2010, ISBN 978-3-933761-99-6

- 196 Gafurov, Abror: *Water Balance Modeling Using Remote Sensing Information - Focus on Central Asia*, 2010, ISBN 978-3-942036-00-9
- 197 Mackenberg, Sylvia: *Die Quellstärke in der Sickerwasserprognose: Möglichkeiten und Grenzen von Labor- und Freilanduntersuchungen*, 2010, ISBN 978-3-942036-01-6
- 198 Singh, Shailesh Kumar: *Robust Parameter Estimation in Gauged and Ungauged Basins*, 2010, ISBN 978-3-942036-02-3
- 199 Doğan, Mehmet Onur: *Coupling of porous media flow with pipe flow*, 2011, ISBN 978-3-942036-03-0
- 200 Liu, Min: *Study of Topographic Effects on Hydrological Patterns and the Implication on Hydrological Modeling and Data Interpolation*, 2011, ISBN 978-3-942036-04-7
- 201 Geleta, Habtamu Itefa: *Watershed Sediment Yield Modeling for Data Scarce Areas*, 2011, ISBN 978-3-942036-05-4
- 202 Franke, Jörg: *Einfluss der Überwachung auf die Versagenswahrscheinlichkeit von Staustufen*, 2011, ISBN 978-3-942036-06-1
- 203 Bakimchandra, Oinam: *Integrated Fuzzy-GIS approach for assessing regional soil erosion risks*, 2011, ISBN 978-3-942036-07-8
- 204 Alam, Muhammad Mahboob: *Statistical Downscaling of Extremes of Precipitation in Mesoscale Catchments from Different RCMs and Their Effects on Local Hydrology*, 2011, ISBN 978-3-942036-08-5
- 205 Hrsg.: Koschitzky, Hans-Peter; Braun, Jürgen: *VEGAS-Kolloquium 2011 Flache Geothermie - Perspektiven und Risiken*, Tagungsband zur Veranstaltung am 06. Oktober 2011 an der Universität Stuttgart, Campus Stuttgart-Vaihingen, 2011, ISBN 978-3-933761-09-2
- 206 Haslauer, Claus: *Analysis of Real-World Spatial Dependence of Subsurface Hydraulic Properties Using Copulas with a Focus on Solute Transport Behaviour*, 2011, ISBN 978-3-942036-10-8
- 207 Dung, Nguyen Viet: *Multi-objective automatic calibration of hydrodynamic models – development of the concept and an application in the Mekong Delta*, 2011, ISBN 978-3-942036-11-5
- 208 Hung, Nguyen Nghia: *Sediment dynamics in the floodplain of the Mekong Delta, Vietnam*, 2011, ISBN 978-3-942036-12-2
- 209 Kuhlmann, Anna: *Influence of soil structure and root water uptake on flow in the unsaturated zone*, 2012, ISBN 978-3-942036-13-9

- 210 Tuhtan, Jeffrey Andrew: *Including the Second Law Inequality in Aquatic Ecodynamics: A Modeling Approach for Alpine Rivers Impacted by Hydropeaking*, 2012, ISBN 978-3-942036-14-6
- 211 Tolossa, Habtamu: *Sediment Transport Computation Using a Data-Driven Adaptive Neuro-Fuzzy Modelling Approach*, 2012, ISBN 978-3-942036-15-3
- 212 Tatomir, Alexandru-Bodgan: *From Discrete to Continuum Concepts of Flow in Fractured Porous Media*, 2012, ISBN 978-3-942036-16-0
- 213 Erbertseder, Karin: *A Multi-Scale Model for Describing Cancer-Therapeutic Transport in the Human Lung*, 2012, ISBN 978-3-942036-17-7
- 214 Noack, Markus: *Modelling Approach for Interstitial Sediment Dynamics and Reproduction of Gravel Spawning Fish*, 2012, ISBN 978-3-942036-18-4
- 215 De Boer, Cjstmir Volkert: *Transport of Nano Sized Zero Valent Iron Colloids during Injection into the Subsurface*, 2012, ISBN 978-3-942036-19-1
- 216 Pfaff, Thomas: *Processing and Analysis of Weather Radar Data for Use in Hydrology*, 2013, ISBN 978-3-942036-20-7
- 217 Lebreuz, Hans-Henning: *Addressing the Input Uncertainty for Hydrological Modeling by a New Geostatistical Method*, 2013, ISBN 978-3-942036-21-4
- 218 Darcis, Melanie Yvonne: *Coupling Models of Different Complexity for the Simulation of CO₂ Storage in Deep Saline Aquifers*, 2013, ISBN 978-3-942036-22-1
- 219 Beck, Ferdinand: *Generation of Spatially Correlated Synthetic Rainfall Time Series in High Temporal Resolution - A Data Driven Approach*, 2013, ISBN 978-3-942036-23-8
- 220 Guthke, Philipp: *Non-multi-Gaussian spatial structures: Process-driven natural genesis, manifestation, modeling approaches, and influences on dependent processes*, 2013, ISBN 978-3-942036-24-5
- 221 Walter, Lena: *Uncertainty studies and risk assessment for CO₂ storage in geological formations*, 2013, ISBN 978-3-942036-25-2
- 222 Wolff, Markus: *Multi-scale modeling of two-phase flow in porous media including capillary pressure effects*, 2013, ISBN 978-3-942036-26-9
- 223 Mosthaf, Klaus Roland: *Modeling and analysis of coupled porous-medium and free flow with application to evaporation processes*, 2014, ISBN 978-3-942036-27-6
- 224 Leube, Philipp Christoph: *Methods for Physically-Based Model Reduction in Time: Analysis, Comparison of Methods and Application*, 2013, ISBN 978-3-942036-28-3
- 225 Rodríguez Fernández, Jhan Ignacio: *High Order Interactions among environmental variables: Diagnostics and initial steps towards modeling*, 2013, ISBN 978-3-942036-29-0

- 226 Eder, Maria Magdalena: *Climate Sensitivity of a Large Lake*, 2013, ISBN 978-3-942036-30-6
- 227 Greiner, Philipp: *Alkoholinjektion zur In-situ-Sanierung von CKW Schadensherden in Grundwasserleitern: Charakterisierung der relevanten Prozesse auf unterschiedlichen Skalen*, 2014, ISBN 978-3-942036-31-3
- 228 Lauser, Andreas: *Theory and Numerical Applications of Compositional Multi-Phase Flow in Porous Media*, 2014, ISBN 978-3-942036-32-0
- 229 Enzenhöfer, Rainer: *Risk Quantification and Management in Water Production and Supply Systems*, 2014, ISBN 978-3-942036-33-7
- 230 Faigle, Benjamin: *Adaptive modelling of compositional multi-phase flow with capillary pressure*, 2014, ISBN 978-3-942036-34-4
- 231 Oladyshkin, Sergey: *Efficient modeling of environmental systems in the face of complexity and uncertainty*, 2014, ISBN 978-3-942036-35-1
- 232 Sugimoto, Takayuki: *Copula based Stochastic Analysis of Discharge Time Series*, 2014, ISBN 978-3-942036-36-8
- 233 Koch, Jonas: *Simulation, Identification and Characterization of Contaminant Source Architectures in the Subsurface*, 2014, ISBN 978-3-942036-37-5
- 234 Zhang, Jin: *Investigations on Urban River Regulation and Ecological Rehabilitation Measures, Case of Shenzhen in China*, 2014, ISBN 978-3-942036-38-2
- 235 Siebel, Rüdiger: *Experimentelle Untersuchungen zur hydrodynamischen Belastung und Standsicherheit von Deckwerken an überströmbaren Erddämmen*, 2014, ISBN 978-3-942036-39-9
- 236 Baber, Katherina: *Coupling free flow and flow in porous media in biological and technical applications: From a simple to a complex interface description*, 2014, ISBN 978-3-942036-40-5
- 237 Nuske, Klaus Philipp: *Beyond Local Equilibrium — Relaxing local equilibrium assumptions in multiphase flow in porous media*, 2014, ISBN 978-3-942036-41-2
- 238 Geiges, Andreas: *Efficient concepts for optimal experimental design in nonlinear environmental systems*, 2014, ISBN 978-3-942036-42-9
- 239 Schwenck, Nicolas: *An XFEM-Based Model for Fluid Flow in Fractured Porous Media*, 2014, ISBN 978-3-942036-43-6
- 240 Chamorro Chávez, Alejandro: *Stochastic and hydrological modelling for climate change prediction in the Lima region, Peru*, 2015, ISBN 978-3-942036-44-3
- 241 Yulizar: *Investigation of Changes in Hydro-Meteorological Time Series Using a Depth-Based Approach*, 2015, ISBN 978-3-942036-45-0

- 242 Kretschmer, Nicole: *Impacts of the existing water allocation scheme on the Limarí watershed – Chile, an integrative approach*, 2015, ISBN 978-3-942036-46-7
- 243 Kramer, Matthias: *Luftbedarf von Freistrahlturbinen im Gegendruckbetrieb*, 2015, ISBN 978-3-942036-47-4
- 244 Hommel, Johannes: *Modeling biogeochemical and mass transport processes in the subsurface: Investigation of microbially induced calcite precipitation*, 2016, ISBN 978-3-942036-48-1
- 245 Germer, Kai: *Wasserinfiltration in die ungesättigte Zone eines makroporösen Hanges und deren Einfluss auf die Hangstabilität*, 2016, ISBN 978-3-942036-49-8
- 246 Hörning, Sebastian: *Process-oriented modeling of spatial random fields using copulas*, 2016, ISBN 978-3-942036-50-4
- 247 Jambhekar, Vishal: *Numerical modeling and analysis of evaporative salinization in a coupled free-flow porous-media system*, 2016, ISBN 978-3-942036-51-1
- 248 Huang, Yingchun: *Study on the spatial and temporal transferability of conceptual hydrological models*, 2016, ISBN 978-3-942036-52-8
- 249 Kleinknecht, Simon Matthias: *Migration and retention of a heavy NAPL vapor and remediation of the unsaturated zone*, 2016, ISBN 978-3-942036-53-5
- 250 Kwakye, Stephen Oppong: *Study on the effects of climate change on the hydrology of the West African sub-region*, 2016, ISBN 978-3-942036-54-2
- 251 Kissinger, Alexander: *Basin-Scale Site Screening and Investigation of Possible Impacts of CO₂ Storage on Subsurface Hydrosystems*, 2016, ISBN 978-3-942036-55-9

Die Mitteilungshefte ab der Nr. 134 (Jg. 2005) stehen als pdf-Datei über die Homepage des Instituts: www.iws.uni-stuttgart.de zur Verfügung.